Head Office: Università degli Studi di Padova

Department of Industrial Engineering, DII

Ph.D. COURSE INDUSTRIAL ENGINEERING

CURRICULUM: MATERIALS ENGINEERING

DOCTORAL CYCLE: XXXVI

BIO-INSPIRED VOLUMETRIC DESIGN METHODS FOR ADDITIVE MANUFACTURING

Coordinator: Prof. Giulio Rosati

Supervisor: Prof. Enrico Bernardo

Co-Supervisor: Prof. Gianpaolo Savio

Ph.D. student: Luca Grigolato

Index

Abstract

Additive manufacturing (AM) technologies allow producing components layer upon layer in a completely different way with respect to the traditional techniques. This new approach enables unprecedented design freedom; indeed, objects with complex shapes inspired by nature, cellular solids and multiple materials can be produced. However, even though the manufacturing technologies are ready for producing such components, the literature emphasized that the available design tools are not appropriate and do not allow taking full advantage of the AM capabilities. For instance, the geometric modeling of lattice structures requires high computational resources, Boolean operations often fail, and the methods are not robust, while the modeling of multimaterial parts require new approaches able to describe the model at each point of the volume, and not only on the boundary.

This research project aims to overcome some of the highlighted limitations by developing new volumetric geometric modeling methods suitable for exploiting the capabilities offered by AM from a bio-inspired point of view.

To reach the objective, several research topics have been addressed. Methods for the geometric modeling of graded components have been proposed. In this context, four different approaches for the realization of graded lattice structures were presented. Based on volumetric representation, those methods explored the possibilities to create graded density lattice structures by modifying the extrusion parameter in material extrusion technologies, by using implicit TPMS functions, by adopting subdivisions surfaces and by means of distance fields techniques. Graded materials were realized based on the introduction of material ratios in the computer numerical control instructions for material extrusion technologies; an analytical model for the elastic modulus of coextruded materials were proposed and validated experimentally. As a combination of modeling, material, and process topics, silicate-based scaffolds were prepared and tested to compare the mechanical properties. Furthermore, another way was explored concerning the utilization of math models and algorithm describing natural phenomena for geometric modeling purposes. A geometric modeling method based on reaction and diffusion systems was proposed for the realization of tree-like supports for AM. In addition, a method based on curve growing algorithm was proposed.

Results showed that the various methods permit to model complex shapes and materials arrangement. The methods for graded lattice structures give a wide range of possibilities, prioritizing the AM process, or the complexity of the shape, or the flexibility of the approach. While methods derived from natural phenomena showed new possibilities and applications. Moreover, the method and application for multimaterial material extrusion technologies proved the feasibility of the approach and open up new investigation routes. Finally, the realization of porous scaffolds showed the critical interplay between design, material, and manufacturing process, which underlines the importance of an integrated approach.

Due to the versatility of AM, the outcomes of the research can be adopted in different fields to obtain customized and multifunctional components, as shown by the presented test cases: in the automotive sector, these innovations can be pivotal in the development of lightweight components that enhance energy absorption, leading to reduced fuel consumption and improved performance and safety. Furthermore, these advancements hold promise for high-performance applications such as heat exchangers and biomedical scaffolds, where fluid dynamics plays a key role concurrently to high strength to density ratio; and eventually in consumer area, especially in sport, where tailored goods and equipment could set a new standard, providing individuals with products that are perfectly suited to their needs, enhancing comfort and performance.

1. Introduction

Since the landmark work of Charles W. Hull and the introduction of the first system by 3D Systems Inc. in 1987, Additive Manufacturing (AM) technologies have been on a continuous ascent. They now hold a position of equal importance alongside traditional manufacturing methods. As per international standards, the defining feature of AM technologies is their capability to fabricate parts from 3D model data, typically through a layer-by-layer approach, distinguishing them from subtractive and formative manufacturing techniques.

The recent advances in AM have indeed revolutionized object fabrication, unlocking a whole new level of complexity. This complexity manifests in a myriad of ways. It encompasses the creation of organic and intricate shapes, such as structurally optimized models (Figure 1.a) or lattice structures (Figure 1.b). Moreover, material complexity allows to produce parts featuring different materials (Figure 1.c) or blends of materials in distinct regions of the same component, resulting in tailored properties. In addition, process parameters variation can lead to different material microstructures, operating on a scale significantly smaller than the macro/meso dimensions of the part. Additionally, functionally integrated designs, like embedded electronics or information (Figure 1.d), can be seamlessly manufactured in a single step and assemblies can be reimagined to incorporate a reduced number of components.

This progress aligns more closely with the natural world. As a result, there's an increasing trend in research within AM and related fields, centered around drawing insights from nature. This bioinspiration provides a rich pool of ideas and potential solutions for designers.

However, the capacity of human imagination and manufacturing capabilities surpasses the current tools available for designing and geometrically modeling the manifold complexities. Presently, the freedom in manufacturing surpasses that in design.
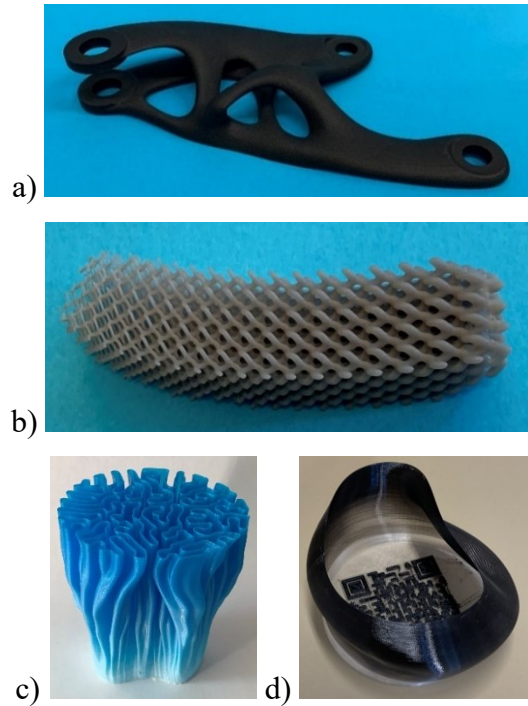
Figure 1. Examples of parts obtained by AM: a) topology optimized shape b) lattice structure with graded beams, c) complex shape printed with multimaterial, d) multimaterial jar with an embedded QR code.

In response to this challenge, researchers, industry professionals, and passionate supporters of AM are actively working to bridge this gap. They are in the process of developing methodologies, approaches, and software tools to streamline the creation of bioinspired objects. Conventional CAD software, it should be noted, exhibit constraints when handling geometrically intricate structures like graded lattices and bioinspired forms, in a manner similar to the constraints encountered with varied material compositions. This stems from the fact that CAD software were initially designed to support traditional manufacturing methods, which necessitate modeling objects with relatively straightforward geometry and uniform composition. On the other hand, CAM and CAE tools face their own limitations in terms of parameter control and model implementation.

In this context, this work aims at developing design and geometric modeling methods and tools to fully exploit material and geometry complexity possibilities offered by AM technologies from a bio-inspired point of view by volumetric approaches. To achieve this objective, the research focused on addressing topics related to shape and material complexities. This encompassed the development of geometric modeling approaches for

graded lattice structures, as well as exploring graded materials and shapes guided by bio-inspired models and algorithms. This is intended as a contribution to showcase some potential and additional approaches in the direction of bio-inspiration.

The thesis is organized as follows. A brief background is given in chapter 2 dealing with the main topics of thesis: additive manufacturing technologies, geometric modeling approaches, and natural phenomena models and algorithms.

The third and fourth chapters delve into the core of the research work, as depicted in Figure 2.

In the third chapter, the focus shifts towards the developed geometric methods for graded structures in terms of shape and material. In the section related to graded shape, four geometric modeling methods are presented for the realization of graded lattice structures. The first method, tailored specifically for material extrusion additive manufacturing techniques, enables the creation of lattices with gradients in relative density by adjusting the extrusion parameter in the G-code file. The second method models triply periodic minimal surfaces (TPMS) implicit functions to produce gradients in size, density and multimorphology. Meanwhile, the third method implements a method for graded density TPMS lattice based on subdivision surface. The fourth method employs a volumetric approach based on distance fields to create graded density lattices. All the previous methods are finally compared, taking into account quantitative and qualitative aspects. In the section related to graded material, one geometric modeling method is presented for the realization of multimaterial components for material extrusion technologies. In addition, the section also encompasses the production, experimental testing, and comparison of porous bioceramic scaffolds. This involves a comprehensive examination of design, material, and manufacturing parameters. Each of these chapters are divided into a 'method development and implementation' section where the method is described and a 'method validation and applications' section that contains test cases and/or experimental tests, except for the porous bioceramic scaffolds.

Moving on to the fourth chapter, the developed geometric methods inspired by natural phenomena math models is described. Two distinct geometric modeling methods have been incorporated into this study. The initial approach revolves around the Reaction-Diffusion model, exploring various patterns it can generate. In this preliminary investigation, a method for creating tree-like supports tailored for AM is introduced. The

second method draws inspiration from another bioinspired concept, known as differential growth. Implemented as a physics-based algorithm, this approach emulates this phenomenon in a three-dimensional context. In the fifth chapter, the work is summed up and the conclusions are drawn.
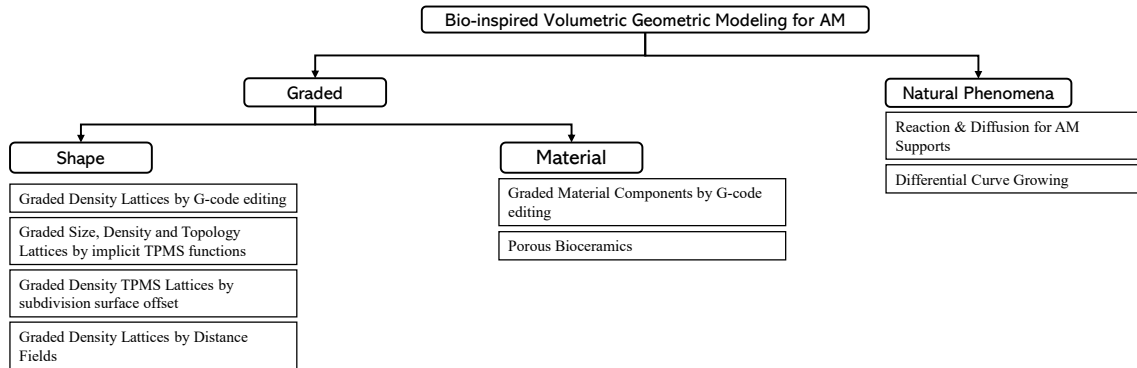
Figure 2. Map of the topics.

2. Background

This chapter lays the contextual foundation for the thesis, covering AM technologies, geometric modeling methods, and the impact of bioinspiration. It places particular emphasis on crucial topics that are central to the thesis, such as volumetric modeling techniques, lattice structures, and math models inspired by natural phenomena. The chapter concludes by providing a summary of relevant issues and limitations.

2.1. Additive Manufacturing

According to ISO/ASTM 52900 standard [1], additive manufacturing is defined as the "process of joining materials to make parts from 3D model data, usually layer upon layer, as opposed to subtractive manufacturing and formative manufacturing methodologies". Before being firstly standardized in 2009 in the ASTM F2792 standard [2], several names were used to refer to this type of process such as 3D printing, rapid prototyping, rapid manufacturing, and solid freeform fabrication.

The layer-by-layer approach used by the AM technologies opens unprecedented design possibilities allowing for freedom in complexity that, most of the time, is impossible to reach with the traditional manufacturing technologies. Four types of complexity can be exploited: shape complexity, hierarchical complexity, material complexity, and functional complexity [3]. Shape complexity allows producing parts with complex geometries, such as lattice structures or internal cooling ducts, thanks to the fact that no machining tools are used; more, the ease in manufacturing different shapes enables the production of customized components, for example in the biomedical field [4], and the production of structurally optimized parts [5]. Hierarchical complexity exploits the AM possibility of controlling the structure of a part at different scales; the nano- and micro-structure of a metal component can be controlled by the processing parameters both in powder bed fusion [6] and direct energy deposition [7] technologies; the meso-structure of a part is modified by introducing cellular structures or solid and voids patterns in certain areas of the part. Material complexity resides in the possibility of producing parts with different materials, or mixtures of them, in different regions, leading to different local properties [8]. Functional complexity comes from the possibility of producing fully functional assemblies and mechanisms, and reducing the number of parts in a component, since part consolidation allows reducing the number of separate parts. These four types

of complexity can be employed simultaneously to fully exploit the AM capabilities. Of course, the design phase of a part becomes fundamental and adequate tools are needed to describe information in a suitable way to further produce the component. Furthermore, the designer needs to be aware of the AM capabilities – and limitations – to design innovative and manufacturable objects.

2.1.1. Technologies

The layer-by-layer approach for producing parts can be obtained by different techniques. According to ASTM F2792 and ISO/ASTM 52900 standards [1,2], these technologies can be subdivided into seven categories, depending on the type of the machine architecture and the physics of the material transformation [9]. The seven categories are: Binder jetting, Directed energy deposition, Material extrusion, Material jetting, Powder bed fusion, Sheet lamination, Vat photopolymerization.

In the binder jetting (BJ) process, powder particles lay in the build platform and are joined together by a liquid binder that is ejected from the print heads, in a line-wise patterning process. The binder is selectively released only on the cross-section of the part, the platform is lowered, a new layer of powder is spread by a coater mechanism, and the procedure is repeated until the entire part is built. The process can be economically scaled by increasing the number of nozzles and a high deposition speed can be reached at a relatively low cost since no high-powered energy sources are used. No supports are needed thanks to the surrounding powder that acts as support itself. Usually, the parts need to undergo post-process operations such as curing, de-powdering, sintering, infiltration, annealing, and finishing, depending on the material and the desired properties [10]. Several materials can be used: ceramics, metals such as 316 stainless steel, Cobalt-chrome, and Inconel 718, biomaterials such as calcium silicate and Hydroxyapatite, and polymers like polylactic acid (PLA) and Polymethyl methacrylate (PMMA) [11].

Directed energy deposition (DED) melts material as it is being deposited. A laser or an electron beam is used as a focused heat source to heat the substrate, melt the substrate, and melt the material that is being deposited into the melt pool of the substrate. In this way, entire near-net-shape parts with complex geometries can be built, or repair and additional features can be added to existing components. Almost exclusively metals are used with DED and the material can be provided as powder or as wire feedstock; powder-

based DED is the most used approach since metals powders are readily available, whereas wire feedstock techniques provide lower resolution but have a higher deposition rate and can build larger structures [12].

Material extrusion (MEX) is probably the most known and diffused AM technology thanks to the low budget machines available in the market. In the MEX process a filament of material is pushed in a hotend by a set of pinch rollers, the filament melts and it can flow out through a nozzle on the baseplate or the previous layer of the part. The machine can control the in-plane position of the nozzle with respect to the baseplate to extrude a single layer; then, the nozzle is raised, or the baseplate is lowered, and the next layer is extruded. Depending on the shape of the part, material support could be necessary if the next layer overhangs with respect to the previous one or if a suspended part like a bridge is created; supports can be produced using the same material as the part or with a different one, usually soluble, if the machine is equipped with a second nozzle. MEX machines mostly work with amorphous thermoplastic polymer since they can be extruded in a viscous paste and the most common ones are PLA, acrylonitrile butadiene styrene (ABS), and polycarbonate (PC) [13]. If high performance is needed, ULTEM 9085 material offers a high strength-to-weight ratio and good fire-, smoke-, and toxicity properties making it suitable for use in aircraft, marine, and ground vehicles [14]. Fiber-reinforced filaments can be used to enhance the mechanical properties of the products: the literature shows the possibility to include carbon fibers, fiberglass, and Kevlar [15]. More, in the biomedical field biocompatible and biodegradable components are obtained by extruding hydrogels in a jellylike form and porous scaffolds can be produced [16].

As in BJ, the material jetting (MJ) process uses print heads to dispense material on a baseplate or the previous layer; the primary distinction between BJ and MJ lies in the process. In MJ, all of the part material is dispensed directly from the print heads, eliminating the need for a powder bed. Depending on the material, UV-curing might be necessary for photopolymers ejected from the nozzles. High speed and scalability are easily achieved by employing print heads with numerous nozzles, and the machine can be equipped with additional print heads for added efficiency. Multiple print heads can also facilitate the creation of multimaterial components or the use of soluble support material alongside the main part material. Commercial MJ systems primarily operate with photopolymers and waxes. Photopolymers enable the production of realistic prototypes

and functional parts, while waxes are employed for crafting investment casting patterns. [17]. In the research field, efforts have been made for printing ceramics [18] and metals [19]. MJ process presents some drawbacks and challenges too: part accuracy for large size parts is not so good due to the need to use large droplets and droplets formation from a continuum volume of liquid and droplets flight path need a perfectly tuned hardware and depend on the material [3].

Powder Bed Fusion (PBF) is a manufacturing process where thermal energy is employed to selectively fuse specific regions within a bed of powdered material. Initially, a layer of powder is uniformly spread across a baseplate using a coating mechanism. Then, the 2D slice of the part geometry is formed by selectively sintering or melting the powders on the plate. Subsequently, the baseplate is lowered by a distance equivalent to the desired layer thickness, and these operations are repeated until the entire component is constructed. The entire process occurs within a chamber that contains a low concentration of oxygen to minimize oxidation, material degradation, and unwanted reactions. While PBF can theoretically utilize any material that can be melted and resolidified, metals and polymers are the most commonly employed, whereas composites and ceramics see less frequent use [20]. When dealing with polymers, different technologies are available, and they differ by the way the thermal energy is provided and the way the sintering of the surrounding powders is prevented; laser sintering (LS) is the most common approach, where a laser selectively sinters the powder only in the space defined by a 3D model [21]; high-speed sintering (HSS) aims at sintering 2D profiles of powder layers by adding carbon black that absorbs infrared radiations and increases the rate of sintering, and using an infrared lamp to sinter without the need for a laser [22]; selective inhibition sintering (SIS) is characterized by the deposition of a sintering-inhibitor liquid along the layer profiles to prevent the sintering of selected areas and the uninhibited powder is sintered by a heated nichrome filament, again, without using a laser [23]; the multi-jet fusion (MJF) technology is a hybrid between HSS and SIS since it uses a so-called "fusing agent" inside the model boundaries to promote the sintering of the powder, and a "detailing agent" on the edges of the model to inhibit the sintering and create fine details and smooth surfaces [24]. Polyamides, especially polyamide 12, are widely used in polymers PBF [25–27], but also thermoplastic polyurethane (TPU) [28], polypropylene (PP) [29], and polyether ether ketone (PEEK) [30] parts can be manufactured. PBF of

polymers does not require supports since the surrounding powder acts as support itself. Moving on to metal PBF technologies, the two main energy sources are a laser beam or an electron beam. The laser beam is adopted in the selective laser melting (SLM) technology, where, similarly to the LS, the laser selectively melts the powders that lay in the powder bed layer after layer [31]. The electron beam replaces the laser in the electron beam melting (EBM) [32]. SLM is cheaper and allows obtaining better surface finish and finer feature details than EBM. EBM is faster and produces less residual stress and distortion in the final part, so it requires fewer support structures; at the same time, EBM works at high temperature, up to 750 °C for titanium and stainless steels [33]: some of the powder particles that surrounds the part could partially sinter and it could be difficult to perform the de-powdering of the part or the cleaning of the internal channels. A wide range of metals can be produced by PBF and the most common are stainless steels [34], aluminum alloys [35], titanium alloys [36], and cobalt-chrome [37]. Since parts produced by metal PBF are prone to distortion, the process planning phase in which the part orientation in the chamber and the supports geometry are optimized is fundamental; furthermore, post-processing operation such as support removal, sandblasting for enhancing the surface finish and removing partially molten powders, and hot isostatic press for reducing the porosity of the final part are required. Regardless the material, the powders must be handled with care, both for the safety of the operators and for the success of the print job.

The Sheet Lamination (SL) process involves cutting sheets of material, stacking them, and then bonding them together to create a part. This method is cost-effective, user-friendly, and well-suited for constructing very large objects. There are two distinct approaches based on the sequence of operations used to create the part: the "bond-then-form" method and the "form-then-bond" method. In the former, the sheet is first bonded to the substrate and then shaped into the desired cross-sectional form. Conversely, in the latter approach, the laminate is initially cut and subsequently bonded to the substrate. [3]. More, different methodologies can be used to achieve the bonding between the layers. Adhesive bonding uses a polymer-based adhesive that can be activated by a heated roller that passes after each sheet is placed [38]; thermal bonding is especially used for metal SL where the temperature is increased to promote the bonding between the sheets [39]; a quicker and less expensive option could be the sheet metal clamping, where the clamping,

or bolting, itself can act as a reference point to position each laminate with respect to the others. Also, ultrasonic metal seam welding has been applied, where a rotating sonotrode moves along the metal foil applying a force and oscillates at a high frequency transversely to the direction of motion [40].

Vat photopolymerization (VPP) is a process in which a liquid polymer that reacts to radiation, i.e., a photopolymer, is contained in a vat, is hit by radiation usually in the ultraviolet wavelength range, and chemically reacts solidifying. As previously said, VPP was the first patented and commercialized AM process with the original name of Stereolithography [41]. In the VPP process, a thin layer of liquid polymer is exposed to light radiation. This layer is situated between the part, attached to a baseplate, and a transparent film that follows the cross-sectional area of the object, positioned between the optics and the plate. The baseplate is then lowered, and the subsequent layer is photopolymerized. Among various AM processes, VPP stands out for its ability to achieve a fine layer resolution, typically around 10 μm, while maintaining reasonable costs. Different configurations can be employed for the photopolymerization process. The "vector scan" method utilizes a laser, along with focusing and adjustment optics, and two galvanometers to meticulously scan each layer of the part point by point, resulting in high accuracy and surface finish. The "mask projection" method employs a dynamic mask to project the bitmap of the cross-section onto the resin surface, enabling the curing of an entire layer at once, thus accelerating the process. The "two-photon" approach involves polymers that necessitate the impact of two photons on the photoinitiator before polymerization commences. This leads to a significant enhancement in the resolution of the final part. [42]. Talking about materials used in the VPP process, the photopolymers resins were first prepared from acrylates but the parts were characterized by geometrical inaccuracy due to shrinkage and curling; so they were substituted by epoxy resins that led to better accuracy, with shrinkage of 1-2% with respect to 5-20% [43]; at the same time, epoxy resins have a slow photospeed and the final parts are brittle. As a compromise, modern resins are epoxy ones with the addition of some acrylate content.

2.1.1.1. AM Technologies for multimaterial printing

Between the 7 categories of AM technologies there are some that allow the realization multi-material components. Multi-material printing, or multimaterial additive

manufacturing (MAMM), is the ability of using multiple material during the printing process.

Not all AM methods are capable or optimized for producing multimaterial parts, for instance BJ and SL lack of significative advancements in recent years. The most suitable categories are the DED, the PBF, the MEX, the MJ and the VPP. Between these categories there are AM technologies with ready and on-the-market solutions for MAMM, i.e., MEX, MJ, PBF and VPP. The most utilized is the MEX process, also due to the low budget printers commercially available. For the other cases, there are only some preliminary studies and attempts for multimaterial printing [44].

Figure 3 depicts the AM technologies capable of multimaterial printing with some significative pros (in green) and cons (in red) for each one.
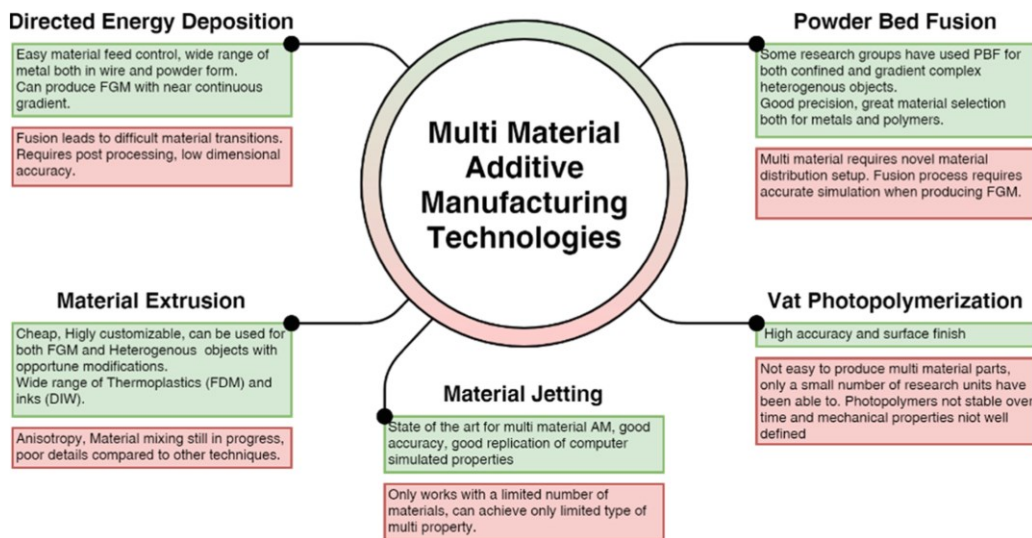
Figure 3. Multimaterial AM technologies.

In the laser metal deposition (LMD), a DED sub-category, the laser beam can melt previously mixed metal powders to obtain graded composition [45]. Wire arc additive manufacturing (WAAM) can use multiple metal wires where the feeding speed is controlled to obtain graded composition [46]. So, with DED it is possible to achieve both confined spaces and gradients with different compositions. Moving to PBF, the design of new selective powder dispensing methods and devices introduced the possibility to produce true gradients and confined multifunctional areas. Zhang et al. [47] combined the delivery of point-by-point selective powder with powder bed fusion for multiple material

SLM. MEX technologies can be upgraded to multimaterial 3D printing by adding several materials flows to the same machine [48]. This is achieved by adding nozzles or by adding extruders that converge in a single nozzle or orifice. Another option to achieve multimaterial in a MEX system is represented by the multimaterial units, from Prusa3D [49] and Mosaic [50]. More, Oxman et al. [51] proposed a method based on direct ink writing (DIW) where the printing platform can mix and extrude two materials, that are liquid at room temperature, and solidify after mixing and deposition. Furthermore, to create a composite structure, a coaxial extrusion of two or more materials can be obtained by using a core–shell or coaxial nozzle, which is a concentric set of coaxial spinnerets composed of an outer and inner needle. MJ technology, particularly the PolyJet system by Stratasys [52], is regarded as the forefront of producing multimaterial objects. This technology allows for various compositions to be achieved by blending different proportions of resins before the curing phase. Additionally, Digital Light Processing (DLP) and Stereolithography (SLA), two VPP technologies, have demonstrated the capability to create multimaterial objects [53]. This is accomplished by employing vats that store entirely different materials or varying compositions of the same material. The pivotal aspect lies in the cleaning process of the substrate, which occurs while the printing platform is mechanically shifted from one material position to another. This process has been successfully employed for both polymers and ceramics materials [54].

2.1.2. General AM Workflow

Regardless the AM technology used for manufacturing a part, some steps are recurrent in the production process. Gibson et al. [3] subdivided the AM process into eight steps: CAD, STL conversion, file transfer to machine and STL manipulation, machine setup, part build, part removal, post-processing, and application. First, the part is geometrically modeled in a computer aided design (CAD) environment. Then, the model is converted in a suitable file format for the AM machine; usually, the STL format is used since it has become the de-facto industry standard: all the software can export such a format and all the machines can deal with it. After the conversion, the STL file is imported into the AM machine and some adjustments like size and orientation are performed. Then, the machine and process parameters are set to obtain a successful build; in this phase, the parameters depend on the AM technology chosen to produce the part. The build is then started and once it ends, the part is removed from the machine. The next phase deals with all the post-

process operations that, again, depends on the adopted technology; for instance, MEX and VP parts may require support removal, whereas metal PBF parts usually undergo sandblasting, thermal cycles, or hot isostatic pressing. The last phase, "Application", considers the utilization of the final part.

Loh et al. [8] proposed a similar workflow, concentrating on the possibility of producing functionally graded additive manufacturing (FGAM) parts, defined as parts in which the material organization gradually varies to achieve an intended function; the flow is divided into five steps: design and modeling, part description, which in turn is divided in material description, product description, and manufacturing description, additive manufacturing, post-processing, and final product. In step 2, they stressed the importance of describing the triptych material-product-manufacturing for obtaining the desired functionality. Loh's workflow also highlights that the "STL conversion" and "File transfer to machine and STL manipulation" phases of Gibson's workflow may be belittling since STL format only carries discretized boundary information that could be insufficient to describe all the characteristics of an object that fully exploits AM capabilities, such as multimaterial.

As reported in Figure 4, a more generic and correct terminology could be "Data exchange", where no file formats are mentioned but the essence of the phase is maintained. Furthermore, the "Qualification" phase has been added, due to the need of assessing the quality of the part concerning structural integrity, surface texture, tolerances, etc.

| Design and modeling | Data exchange | Machine setup | Part manufacturing | Post processing | Qualification | Final product |
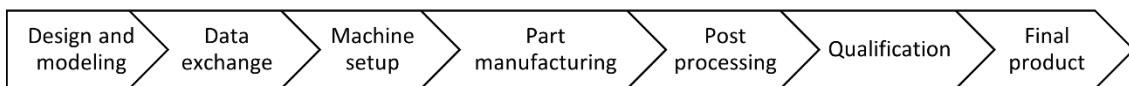
Figure 4. AM workflow, adapted from the ones proposed by Gibson et al. [3] and Loh et al. [8].

2.1.3. Design for Additive Manufacturing

In the "Additive Manufacturing Technologies" book [3], Rosen defined the Design for Additive Manufacturing (DfAM) concept as the set of all the considerations to make to "maximize product performance through the synthesis of shapes, sizes, hierarchical structures, and material compositions, subject to the capabilities of AM technologies". The DfAM is inspired by the design for manufacture and assembly (DfMA) [55], a methodology that focuses on reducing time-to-market and total production costs

concentrating on the ease of the manufacture of the parts of the product and the simplified assembly of the parts into the final product.

To gain a better understanding of DfAM, it is beneficial to begin with DfMA. DfMA is a process in which a designed object undergoes critical evaluation for manufacturability. Design engineers utilize established guidelines to ensure that a product can be manufactured quickly and efficiently at a low cost, while also meeting the quality and functional expectations of the end-user. DfMA primarily focuses on reducing product complexity to lower manufacturing costs. However, with AM, product complexity is only marginally linked to manufacturing costs. AM has deviated somewhat from the principles outlined by DfMA, necessitating its own set of guidelines known as DfAM. The primary prerogatives of AM include product digitization, topology optimization, design freedom at a low cost, product customization, product consolidation, lightweight structures, integrated functions and internal features, multimaterial parts, and optimization of the supply chain. Key considerations in product design with AM encompass AM technology selection, material selection, layer height, build orientation and support structures, hole and channel design, thin features, geometric tolerances, surface quality, and other relevant factors [3].

DfAM can be subdivided in restrictive and opportunistic DfAM. Restrictive DfAM only concentrates on the restrictions of the AM technologies and is basically used as a list of guidelines to design manufacturable parts taking into consideration the limits of the selected AM technique, i.e., the minimum features size, the need of support structures, the need of resin evacuation or de-powdering holes, etc. Opportunistic DfAM, instead, focuses on the unique AM capabilities and aims at introducing in the component all the aforementioned complexities to obtain a better and innovative product. In the literature, researchers followed different approaches to reach this goal. Rosen [56] used a Process – Structure – Property – Behavior framework to describe and model a design; he further divided the Process, Structure, and Property models into geometric and material models. Moving from Geometry to Material and from Property to Process the relevant size scale decreases. More, following the traversal from Behavior to Process the design approach can be seen, where the requirements given by the Behavior are mapped to the properties and the geometry/structure, and finally the manufacturing process is defined; going from the Process to the Behavior the designed part is analyzed, and one can verify if the original

requirements are satisfied. Then he proposed a DfAM system organized in several modules dealing with the modeling, manufacturing simulation, and design behavior analysis phases, as reported in Figure 5.
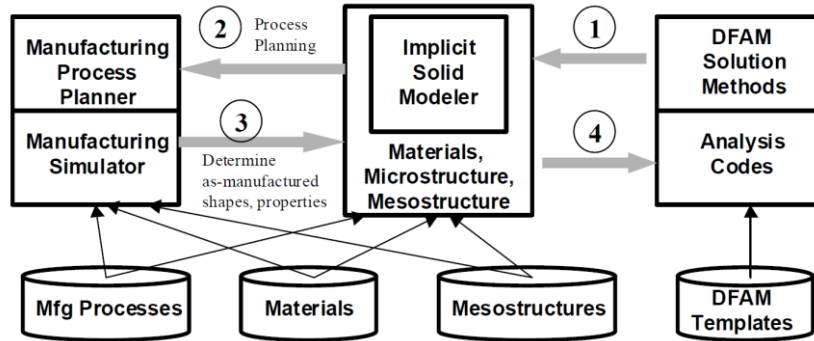
Figure 5. DfAM system proposed by Rosen [56].

2.1.4. File formats for AM

During the development of a part produced by AM technologies, several stages are encountered and, often, several software are used to perform operations such as the part modeling and structural simulation, or the manufacturing process. The product information has to be exchanged between software, and a number of file formats for data exchange are available, each one of them with its pros and cons. The STL file format is the de-facto industry standard for transferring the geometry of the part but is the most limited. It only includes geometrical information about the surface of the component, so it is not possible to carry information about internal characteristics, boundary colors, or any other product and manufacturing information (PMI). When exporting using the STL format, the part is approximated by planar triangles, resulting in the loss of geometrical accuracy [57]. The PLY format is similar to the STL one because it approximates the surface geometry with discrete elements, but it can transport the colors of the textures too. ISO organization developed the STEP AP 242 format under the ISO 10303-242 standard [58]. The second version of the format, released in 2020, introduced several features to cover the whole product development phases, and is now able to deal with AM-related characteristics. Furthermore, according to the STEP AP 242 project webpage [59], the third edition of the standard will take into consideration some other AM capabilities as the heterogeneous materials, the representation of lattice structures, and semantic representation of the PMI for AM. ISO and ASTM organization worked together for

developing a standard format called the Additive Manufacturing Format (AMF) under the standard ISO/ASTM 52915 [60]. The AMF is an XML-based format that describes parts by triangles and can store information about lattice structures, material specifications with mixed and graded materials, and new materials can be defined as compositions of other materials. The AMF file also includes provisional support for voxel-based representation. Due to these characteristics, the AMF is well suited for supporting the design and production of functionally graded parts. Another XML-based format is the 3MF, an open format free of royalties, patents, and licensing, developed by the 3MF consortium [61]. The consortium gathers a group of big players of the AM industry (3D Systems, Autodesk, EOS, General Electric, etc.) whose aim is to represent the physical object in a mark-up format with richer external and internal information supporting several code extensions considering materials and properties, production, and lattices data. A limitation of the 3MF format is that it does not support B-Rep, NURBS, and STEP modeling. Other file formats have been proposed to support the modeling and production of parts that exploit AM features. The FAV (Fabricatable Voxel) format was developed by Fuji Xerox and Keio University, is based on voxels, and can store information about colors, materials, and connection strength through voxels. The SVX (Simple Voxels) format was proposed by Shapeways [62], is voxel-based, and is a ZIP file composed of a series of image slices and a manifest.xml file.

2.2. Geometric modeling and representation

Geometric Modeling is a fundamental step in the AM workflow. Geometric modeling approaches for solids can be classified in 3 main classes (Figure 6): boundary representation (B-Rep), volume representation (V-Rep) and constructive solid geometry (CSG) [63]. In B-rep, solids are described only by their boundary surface. V-rep allows the description of both the surface and the internal portion of an object, and consequently the representation of the internal properties' distribution and not only of the boundaries. CSG is a description of a solid geometry through sequential logical operations (Boolean), starting from simple primitive geometries. Usually, the primitives are homogeneous objects, but if they are heterogeneous, so-called Volumetric-CSG (VCSG) method for the modeling and representation of volumetric heterogeneous objects based on the original CSG approach has been presented in the literature. To visualize, i.e., evaluate, and produce the model, depending on the primitives, it is possible shift to a B-rep or a V-rep.

Almost all the geometric kernels of the CAD 3D software are based on the CSG approach (with homogeneous primitives) for describing and storing the modeling operations, and then they use B-Rep for the visualization of the model.

Both B-rep and V-rep can be both represented by discrete models or by functions (continuous models). In the case of discrete V-rep, spatial decomposition or subdivision can be reached by voxel, octree and polyhedral mesh. Typical discrete representations can be found in computed tomography (CT) image representation, as voxels, or in finite element (FE) method, as polyhedral mesh. Beside discrete representation methods, bi-variate or tri-variate parametric functions are often used in CAD software for intuitively modify shape by moving control points. Usually, bi-variate parametric functions are used for surface representation, while tri-variate are implemented for morphing objects. Implicit and explicit functions can be implemented in CAD software and can be useful in the representation of particular shapes such as minimal surfaces, but do not allow an easy modification of the shape as in the case of parametric functions.

V-Reps are needed when a part presents heterogeneous internal properties and different information are found in different point inside the volume, that a B-Rep can't store.
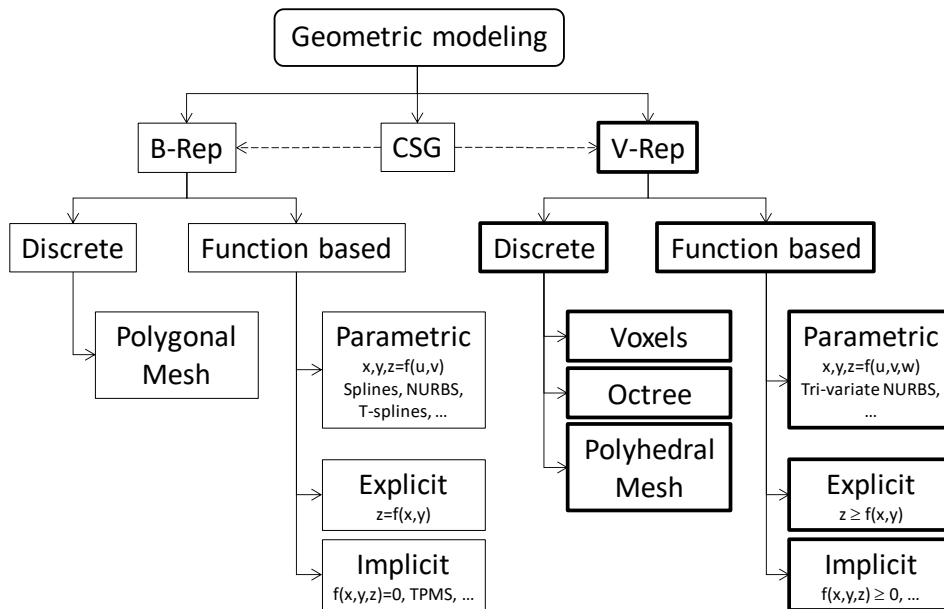

Figure 6. Geometric modeling approaches.

Discrete volumetric models are often classified as evaluated representations or models [64] , since the volumetric information stored in the model is directly available for further

applications, such as numerical analysis and simulation [65]. The easiest way to discretize a volume is to subdivide it in small and equal cubes (i.e., voxels). Octrees is a partition of a three-dimensional space by recursively subdividing a cube into eight cubes; each cube can be inside, outside or in the boundary of an object; for each cube in the boundary the subdivision is repeated until the desired resolution is obtained. The space decomposition can be reached by other approaches that can better follow the external shape or the internal characteristics, using polyhedra. In this case, it is possible to adopt larger elements where the variation in shape or characteristics is low and vice versa. The discrete representation schemes are based on different data structures: for instance, voxel based methods are based on the distribution of the elements inside a tree-dimensional matrix or a vector, octree is based on a tree, while for polyhedral mesh it is necessary to define a list of vertex coordinates, a list of polyhedra, a list of faces, a list of edges and the reciprocal connections [63,66,67].

The most common way to define a geometry in a CAD environment is based on parametric functions. In the volumetric case, these functions map a domain of the parameter space (u,v,w) in the design space (x,y,z). Function adopted for mapping the (u,v,w) space in the (x,y,z), can be simple polynomials, but for an easier geometry management, control points were introduced together with basis function in the Bézier representation. In this formulation, moving a point, the whole geometry is modified. To overcome this limitation, B-splines and NURBS were introduced, where rational non uniform basis functions are recursively defined. Using NURBS, with a single equation, any type of geometry can be obtained. Differently, using explicit or implicit functions, each geometry is represented by a different equation, making difficult modeling complex geometries [66].

The geometric modeling of parts produced by AM technologies can be difficult if adopting the available geometric kernels. For instance, only few CAD software are able to handle volumetric information (commercially available: nTopology, Rhinoceros/Grasshopper, Blender, Houdini), and when modeling cellular structures characterized by a high number of repetition of elements, Boolean operations are needed for joining the elements in one structure; these operations require high computational resources and often fail since the software is not able to compute the intersections between the objects; then filleting operations should be performed for eliminating sharp edges, and

they need to be executed manually. If all the operations are successful, the final part becomes difficult to visualize due to the high number of surfaces to visualize. These issues are shared by all the complex geometries that exploit AM capabilities.

2.2.1. Heterogeneous and functionally graded materials

Our experience with heterogeneous objects far surpasses that with homogeneous ones. Typically, manmade objects exhibit a nearly uniform internal material distribution, allowing them to be modeled as homogeneous solids. Conversely, natural objects are seldom homogeneous; they intricately combine various shapes, materials, and functions. Nature consistently presents us with optimally designed heterogeneous objects, from animal tissues like human bones, to plant structures such as wood, and even geological materials like soil and rocks [68].

When a heterogeneous object is characterized by gradual spatial variation of porosity, material composition and microstructure across the volume, contributing to corresponding changes in material properties, it is called Functionally Graded Material (FGM). FGMs are a class of advanced materials introduced in the 1980s in Japan [69]. Developed for the aerospace industry and meant to be fabricated with the standard manufacturing processes, for example with bulk or surface treatments, FGM can now take advantage of the AM technologies. The fabrication of FGMs in combination with AM leads to the term FGAM [70]. This brings a significant shift from contour modeling, i.e., B-Rep, to volumetric (or performance) modeling since it changes the traditional shape-centric fabrication towards a more property-centric fabrication to obtain multi-functional object. Other properties are for example microstructure, tolerances and operating conditions, which could also be included in a complete model description. In order to define the better distribution of material, new design and optimization approaches are needed.

Currently CAD software are designed to operate with homogeneous solids and not with heterogeneous ones, because the modeling objective until now was to describe mainly geometrical information. Many models exist for representing the outer shape of an object, but modeling the inner composition is still a challenge [71–73]. Since heterogeneous objects modeling is not trivial, because includes more than the shape representation, there are different approaches to model the volumetric property distribution in a solid [64,74],

some of those take advantages from the analogies with other disciplines such as geosciences or colour representation [75].

2.2.1.1.   *Geometric modeling approaches*

2.2.1.1.1.   *Properties assignment approaches*

In general, heterogeneous object geometric modeling requires the connection of properties information, such as material, to the solid model. This procedure includes two concurrent phases: shape modeling and properties assignment [76,77].

Geometric modeling is concerned with both shape representations of the objects and properties assignment that is targeted at defining property composition (values) and distribution (values position) over the geometric domain [64]. The procedures for heterogeneous object modeling can intuitively be sequential or parallel, that is whether the shape is modeled before material distribution, or the geometry and the material are defined simultaneously, respectively.

For heterogeneous/graded objects, the volumetric attribute information consists in a geometrical/physical/chemical etc. property, for instance relative density, with a value and a position in the space. A property information adds dimensions to the model. Conceptually, next to a build space where the geometry is defined, a geometric model for property composition and its distribution is added. Usually, composition and distribution are coupled. Composition represents the "value" of the property at each point of the volume and is stored by a vector m. Composition can be given by a scalar, a vector or a tensor. Distribution models the variation of m in the volume, can be described in various way and can be classified in three main classes [76]. The first one is the extension of conventional geometric modeling approaches to consider property representation, i.e., the property description is dependent to the geometric approach used. This is called geometric model-based. The second class contains schemes wherein the property assignment is based on other geometric information, e.g., coordinate system (Cartesian, Cylindrical, Spherical, etc.). In the last class, special control feature-based schemes, also referred to as primitive features, are used to describe distribution. Other classifications are possible and not in contrast with the previous one [64].

In geometric model-based, geometric modeling approaches are utilized as the basis for modeling the material attribute. In this case, material distribution is geometric

representation dependent. In discrete V-rep, at each voxel, polyhedron or vertex within a boundary, a material composition is assigned [78]. These models permit complex graded modeling with great accuracy that is directly related to the domain resolution, but computational and memory costs can be high [78]. For example, voxels approach can be improved by bringing together adjacent voxel with the same properties, making the spatial-occupancy enumeration more efficient such as in octree encoding. Note that the material distribution inside a voxel is not necessarily homogeneous, for instance, Bernstein polynomials or trilinear functions have been used to represent interpolated material distributions when the material composition is assigned to a vertex. Extensions to pure voxel representation has been proposed by several authors, such as Blouin et al. [79]. A more flexible approach is based on polyhedral mesh. In polyhedral mesh, objects are described with a set of adjacent polyhedra, each represented by a list of vertices. The vertices store their geometric position as well as the material composition, and can be mathematically described as:

$$\text{heterogeneous object} = \{V_i\} = \{T_1, T_2, \ldots T_n\}$$
$$T_k = \{G(v_{k1}, v_{k2}, \ldots, v_{km}), M(v_{k1}, v_{k2}, \ldots, v_{km})\}, \qquad 1 < k < n$$
$$v_{ki} = (x_i, y_i, z_i, m_i)$$

where T_k denotes a representative polyhedron, G and M denote the geometry and material distribution of T_k, v_{ki} is a representative vertex of T_k that stores the coordinates and punctual material information m_i and n is the number of polyhedrons that compose the whole heterogeneous object. The function M is usually an interpolation function used for defining the material distribution inside each polyhedron.

Contrary to space subdivisions, function-based representation utilizes exact geometric data representations, such as B-Rep and F-Rep [80], and rigorous functions (explicit, implicit, parametric) to represent the material distributions. For F-Rep, implicit and explicit functions, it is very challenging to work on different levels of inequalities to manage the distribution of different materials. For example, with an implicit function based strategy it is possible to set a property at each k_i value (a surface) of the f(x,y,z) = k_i. Instead, parametric functions, such as tri-variate NURBS, show several advantages and the approach can be extended for material representation [81,82].

Material distribution can be defined based on geometrical features which differ from the shape of the object. For instance, the definition of properties or material can be referred to the coordinate system and independent from the boundary of a 3D model. This is referred as coordinate system-based. The distribution is defined with respect to a Cartesian, cylindrical or spherical coordinates system with linear or non-linear and discrete or continuous functions. If the material is assigned to a set of equidistant points, the supporting geometric model is equivalent to a voxel model. Doubrovski et al. [83] proposed a methodology based on voxelization modeling in which the resolution is set equal to the AM process. Another example appears when the distribution is controlled by features such as points, curves or surfaces, referred as material features. Material composition at any point in the space model is derived from these control features and distance-based functions. As stated in [64,65] this approach seems to be more intuitive from a user experience point of view. Bidarra et al. [84] defines a feature as a representation of the shape aspect of a product that is mappable to generic shape and functionally significant for the product. Also, features may be entities that are not otherwise present in the shape model. These new reference entities may be point (0-D), line/curve (1-D), or plane/surface (2-D). The material distribution function can be polynomial, exponential, or harmonic functions of the distance from material reference entities [64].

Defining the optimum material distribution function requires extensive knowledge of material data that includes the chemical composition, its characteristics, and the manufacturing constraints [8]. At the present there are no design guidelines on material compatibility, mixing range for materials with variable and non-uniform properties and a framework for optimal property distribution such as choice of spatial, gradient distribution, and the arrangement of transition phases is lacking [8].

A recently developed voxel-based modeling engine called Monolith [85] permits to handle spatial variations directly in material properties, using different approaches to assign the properties to objects such as geometric model-based, coordinate system-based and control features-based. These voxel-based representation fits perfectly within a new class of 3D printers which have multiple print heads capable of depositing different types of material, such as resin, within a single build volume.

2.2.1.1.2. *Volumetric data sources*

As described in the previous paragraph, there are different representation schemes for volumetric models. Regardless of the representation scheme, there are several ways in which volumetric data/properties can be generated or acquired to create heterogeneities and gradients such as functions, measurements, simulations/optimizations or procedural generation [86].

The spatial variation of properties can be defined in the form of a single mathematical function or multiple functions. One of the most interesting functions is the distance function used to generate a distance field. A distance field is a representation where each point of a field stores the distance from the closest point on any object within the domain [87]. In addition to distance, other properties may be derived from the distance field, such as the direction to the surface and the sign, that determine if the point is internal or external to a solid. Given a geometric representation of a solid and a collection of properties, one or more functions parametrized over the distance from specified features are defined. Each function represents some property that varies, usually continuously, from point to point throughout the domain, including the boundary and the interior of the solid [88]. Distance fields exist virtually for all geometric objects, and they may be constructed and/or sampled by a variety of methods, including the one relying on spatial discretization [64,89]. Discrete distance fields are usually stored in voxel grids due to the great simplicity of this representation. The most common types of functions constructed by methods based on spatial discretization appear to be the Euclidean distance function, weighted distance functions, or simple functions of a distance function. Distance fields are recognized as a useful approach within the areas of computer vision, physics, and computer graphics [90,91].

The spatial variation of properties can be derived from volumetric measurements, simulations and procedural generation. Medical imaging is the technique and process of imaging the interior of a body for clinical analysis and medical intervention, as well as visual representation of the shape of some organs or tissues. Technologies such as Computed Tomography (CT), Magnetic Resonance Imaging (MRI), and Ultrasounds use frequency data to obtain spatially encoded information of the body. Usually, many scans are made, obtaining a stack of 2D images which are combined by computers to obtain volumetric data. These data are sampled on a regular array, or a 3D matrix, formed by

grayscale volume elements (voxels) [92] adopting Hounsfield Unit (HU) [93]. Digital Imaging and Communications in Medicine (DICOM) is the standard file format for the communication and management of medical imaging information and related data [94]. All spatially variable data types (volumetric data) derived from numerical simulations are potential sources of information. Between the several approaches, topology optimization TO is the most used, usually to generate optimized shapes. TO is a mathematical method that optimizes the material layout within a specified region for a given set of boundary conditions, so that a certain objective is minimized or maximized [62]. Several reviews on TO methods are available in the literature, which proposes different taxonomies [63]–[67]. TO for discrete structures aims at determining the optimal number, mutual connectivity, and position of trusses and frames. TO of continuum structures seeks to determine the boundary, holes, and cavity locations in the design domain. Among the continuum TO, it is possible to identify density-based methods, hard-kill methods, boundary variation methods, and bio-inspired cellular division-based methods. Indeed, density-based methods return a map of ρ in the design space that can be used as volumetric data source.

Often, volumetric models are converted into surfaces for further applications. The most diffuse algorithms to generate a surface, called surface polygonization algorithms, are marching cubes and dual contouring (Appendix A.4).

2.2.1.2. Graded Lattices Structures

Among the complex structures that can be produced by AM technologies, lattice structures gained a lot of interest in the AM field [78]. Lattice structures or lattices are the common name of cellular materials (or cellular solids) in this field. They are also known as scaffolds in the biomedical field. According to Gibson and Ashby, cellular materials are defined as materials "made up of an interconnected network of solid struts or plates which form the edges and faces of cells" [95]. Lattices are interesting because they have high specific stiffness and strength since they are lightweight; they are good heat exchangers due to the large surface area with respect to the occupied volume; they can absorb and dissipate energy if the structure is designed to undergo large deformations; the large number of internal pores guarantee acoustic insulation too [95,96].

Thanks to their characteristics, cellular structures have been widely adopted by nature as a result of millions of years of evolution; for example, the inner lattice structure of the toucan beak acts as a vascular thermal radiator and as a lightweight part [97], the skeletal microstructure of the sea urchin resembles the Schwartz P-Surface TPMS structure [98], and the internal structure of the human bones is a cellular structure randomly organized.
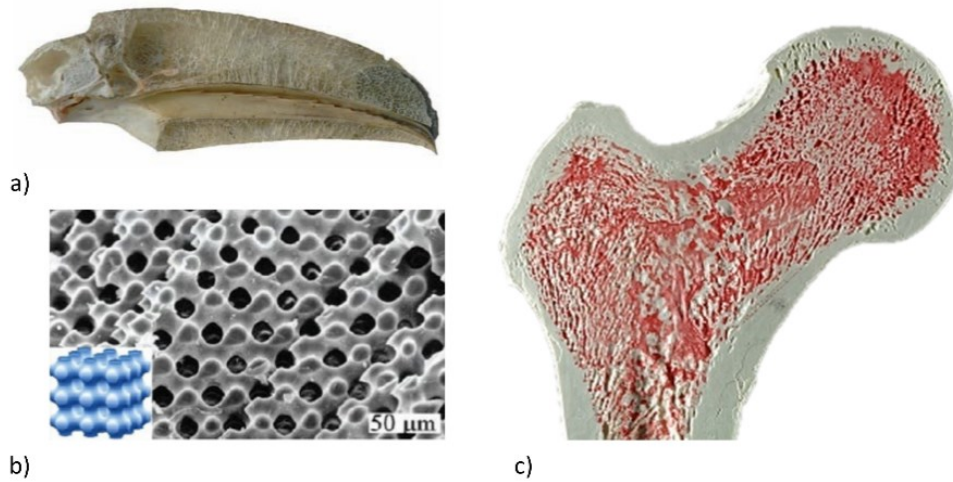

Figure 7. Examples of cellular solids found in nature: a) inner structure of the toucan beak [97], b) skeletal microstructure of the sea urchin [98], and c) internal structure of the human bone.

Before the diffusion of the AM technologies, lattice structures were produced with traditional manufacturing techniques, such as gas foaming, particulate leaching, fiber bonding, and solvent casting. As observed by Leong et al. [99] these manufacturing approaches present limitations: they require manual intervention and the final result is strongly affected by the operator expertise, they are time-consuming since post-processing is needed, toxic organic solvents are used during the production phases so this can be dangerous if the product is intended to be used for biomedical purposes and also time-consuming due to the time required for solvent evaporation, that varies from days to weeks [100]. The most critical issue is the difficulty, if not the impossibility, in controlling the final geometry of the product; the parameters can be tuned and optimize to get closer to the desired result, but limits still remain. With AM technology, instead, better control on the shape of the part is obtained and it is possible to produce cellular solids with almost any desired structure.

From a designer point of view, lattice structures are not easy to model. They are modeled practically in commercial software packages using different approaches. Traditional CAD

software uses B-Rep representation, but recent developments in software are exploring the use of volumetric object representation to generate surfaces and the use of implicit modeling.

2.2.1.2.1.   *Classification*

Lattice structures can be classified according to different properties and characteristics, and several classification schemes have been proposed in the literature. A general classification is given by Ashby [95]. In the case of AM there are other classifications related to lattice geometry and mechanical behavior, highlighting interesting design aspects. Tang et al. [101] classified the lattice structures according to the degree of order of the unit cell, considering lattices at a meso-scale, i.e., where the feature size ranges from 0.1 mm to 10 mm. They identified three groups: disordered, pseudo-periodic, and periodic lattice structures. Disordered lattices are characterized by features of different sizes and shapes and are randomly distributed, pseudo-periodic ones can have the shape of the unit cell changed in different areas of the part according to specific design purposes, and periodic ones are a simple repetition in space of the unit cell. In a following work [102], the classification method was enhanced by proposing three different classification methods.

Savio et al. [96] proposed a geometrical lattice structure classification based on the distribution of the cells in the whole volume, the topology of the cell, the shape of the cell, and the element dimensions of the cell, as illustrated in Figure 8.

Starting from the shape of the structure of the unit cell, cellular material can be divided into regular, pseudo-random, and random. Regular lattices (Figure 9.a) are made by regularly repeating the unit cell along the X-, Y-, and Z-axis. In the pseudo-random structures, the geometry and the size of the cell are modified, but the topology is maintained. These structures can be divided, in turn, into warped and conformal. Warped cellular solids are obtained by deforming the unit cell in different zones of the volume according to the application; for instance, the size of the cells can be driven by the results of FE analyses, where high stresses could require smaller cells, or by the position of the cell with respect to a point, i.e., the closer, the smaller or vice-versa.

Figure 8. Geometrical Lattice structures classification. Adapted from Savio et al. [96].

Starting from the shape of the structure of the unit cell, cellular material can be divided into regular, pseudo-random, and random. Regular lattices (Figure 9.a) are made by regularly repeating the unit cell along the X-, Y-, and Z-axis. In the pseudo-random structures, the geometry and the size of the cell are modified, but the topology is maintained. These structures can be divided, in turn, into warped and conformal. Warped cellular solids are obtained by deforming the unit cell in different zones of the volume according to the application; for instance, the size of the cells can be driven by the results of FE analyses, where high stresses could require smaller cells, or by the position of the cell with respect to a point, i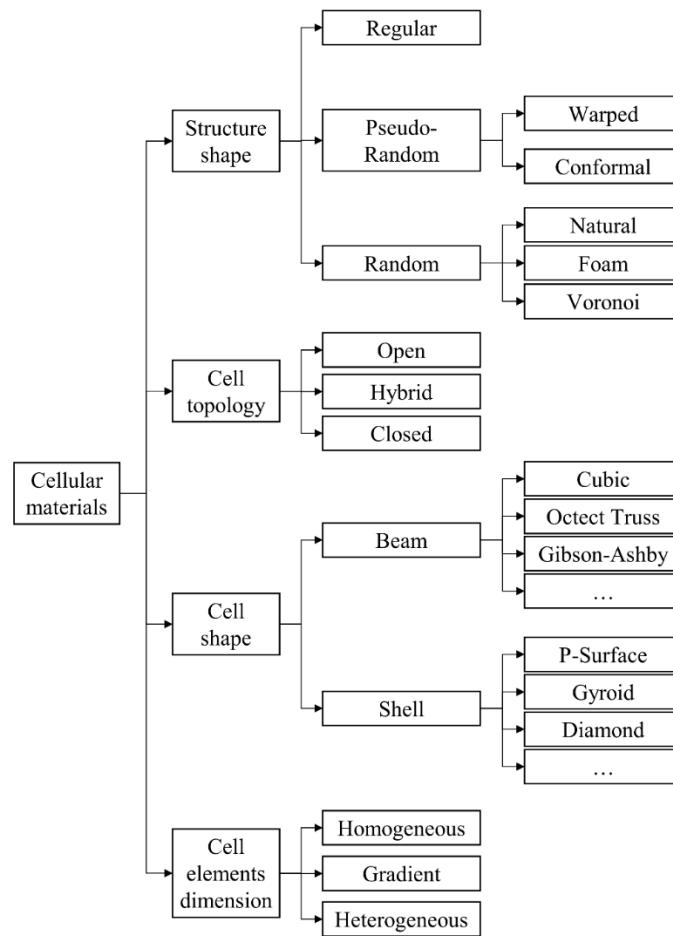.e., the closer, the smaller or vice-versa. Conformal cellular solids present unit cells with different size and geometry to adapt and conform to the external boundary of the model; conformal structures better adapt to freeform shapes since they follow the borders and the cells never interrupt, providing a better stiffness and resistance to the entire model [103]. Figure 9.b shows an example of a simple cubic lattice

conforming to two surfaces. Random structures present a random organization of the cells, and the size and geometry of each cell vary at the same time. As previously said, random lattice structures are frequently found in nature, for example in the cork (the material) or the cancellous bone of human beings, and in the structures produced with traditional manufacturing technologies where it is almost impossible to control the shape of the final part. Random structures are obtained also by adopting the Voronoi diagram, as shown in Figure 9c; a set of points, the seeds, are randomly positioned in the design volume and the space is partitioned in Voronoi cells, where each cell consists of all the points of the plane closer to a seed than to any other [104].
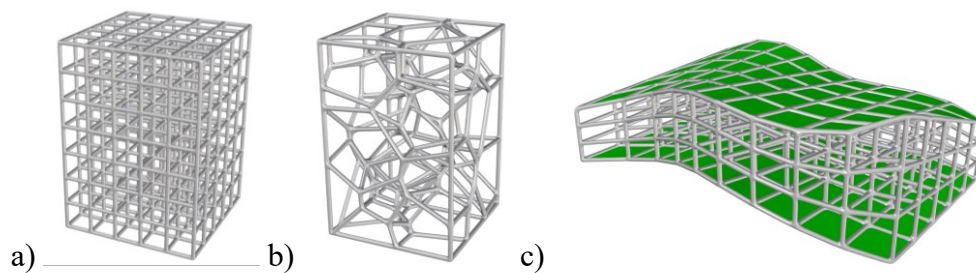

a)   b)   c)

Figure 9. Cellular materials with different structure shapes: a) regular lattices obtained by repeating a simple cubic unit cell along the X-, Y-, and Z-direction; b) Voronoi lattice structure that fills the same box geometry as in a); c) conformal lattice structure in which the cells adapt to the shape of two surfaces.

Another classification of the cellular structures can be done depending on the topology of the cell. The lattice can present an open-cell or a closed-cell organization. In an open-cell structure, the pores and the single cells can "communicate" between each other, whereas in a closed-cell structure, the pores result inaccessible. An open-cell lattice can be preferable for biomedical applications where fluids exchange and tissue regrowth are allowed; closed-cells are better suited in mechanical applications where stiff components are required. In hybrid configurations both open and closed cells can be obtained as well. It must be considered that closed cells cannot be produced with all the AM technologies, for example, in the PBF or VP technologies open cells are needed for evacuating the powder and the resin, respectively.

Furthermore, different cellular materials are obtained by adopting different shapes of the unit cell. A wide class of strut-based unit cells derives from the cubic cell: simple cubic (Figure 10.a), body-centered cubic (Figure 10b), are characterized by an increasing number of beams [105]. The octet-truss cell (Figure 10.c) derives from the face-centered

cubic one and was proven to have higher stiffness and strength if compared to a randomly organized foam [106]. The modified Wallach-Gibson [107] and the modified Gibson-Ashby [108] cells are other two frequently used strut-based cells. Moving on the shell-based unit cells, the triply periodic minimal surfaces (TPMS) are some of the most adopted cells. Minimal surfaces are defined as surfaces with zero mean curvature or surfaces that minimize the surface area for given boundary conditions [109]; if minimal surfaces are repeated and duplicated along the three dimensions, they present a cubic symmetry and are called TPMS. More, TPMSs divide the space into two sub-spaces that never meet. These surfaces are defined by implicit equations; for example, the Gyroid (Figure 10.d) is described by $sin(x) \cdot cos(y) + sin(y) \cdot cos(z) + sin(z) \cdot cos(x) = 0$, and the P-surface (Figure 10.e) is described by $cos(x) + cos(y) + cos(z) = 0$. Thanks to their curvature continuity and mechanical properties, TPMS received a lot of interest in the AM community and have been widely adopted, especially in the biomedical field and heat exchangers application, in which fluid dynamics plays a key role [110,111].
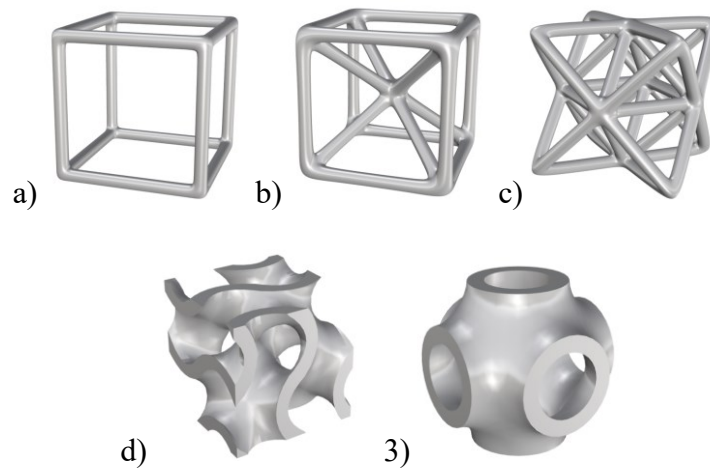
Figure 10. Different types of cell geometry: a) simple cubic, b) body centered cubic, c) octet-truss, e) Gyroid, and f) P-surface.

Another classification criterion hinges on the dimension of the cell elements, specifically the diameter of the beams or the thickness of the shells. When all the elements in the cells of the lattice share the same dimension, the structure is deemed homogeneous. On the other hand, if the elements within the cells have varying dimensions without adhering to a evident pattern, the structure is classified as heterogeneous. Finally, if the size of the elements follows a graded pattern, the cellular material is characterized as a gradient

elements lattice structure; as an example, in Figure 11 the diameter of the beams of the regular lattice structures linearly decreases with respect to the distance of the beams to the point at the top-right of the structure: the closer to the point, the bigger the beam dimension.
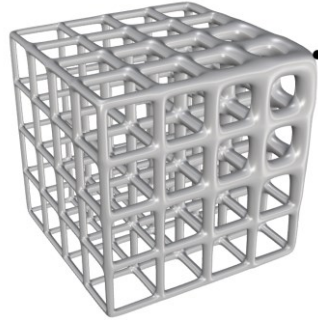
Figure 11. Lattice structure with graded elements size. The closer to the top-right point, the thicker the beam diameter.

Another common classification takes into consideration the lattice deformation criteria and is inspired by the distinction between bending-dominated and stretching-dominated structures [112]. The bending-dominated structures are characterized by low stiffness and the struts and walls tend to bend if loaded, whereas the stretching-dominated structures have a higher stiffness and yield strength than the bending-dominated ones. Due to these properties, bending-dominated structures are more suitable for energy absorption application, whereas stretching-dominated structures are employed in lightweight structure design. The expected compressive behavior of these two types of lattices is presented in Figure 12 [113], where the compressive stress – strain curves are plotted.

Figure 12. Compressive Stress – Strain curves of a) bending-dominated and b) stretching-dominated lattice structures [113].

These two different behaviors are described by the Maxwell stability criterion for 3D lattices based on struts unit cells [107], further generalized by Calladine [114,115] with the equation:

$$M = b - 3j + 6 = s - m$$

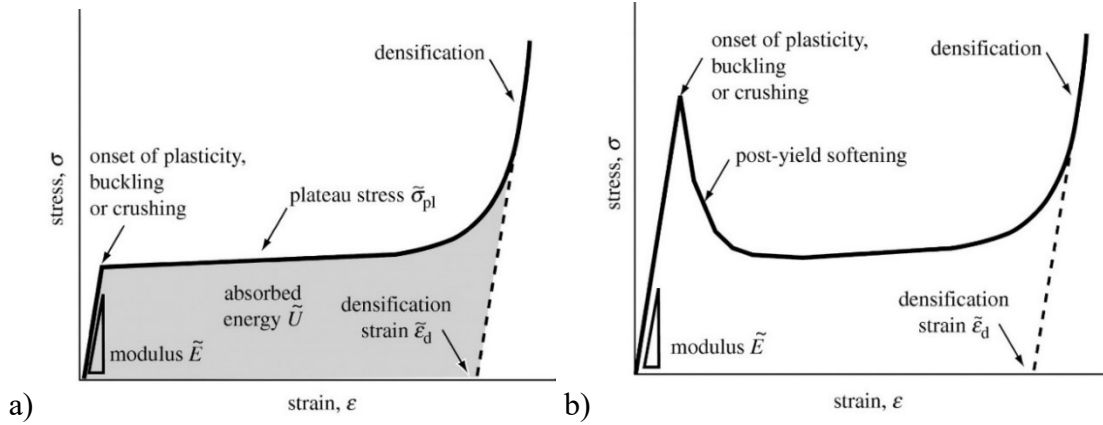where b is the number of struts, j is the number of joints (locked), s is the number of states of self-stress, and m is the number of mechanisms. If $M < 12$ the cell mechanism is defined as bending-dominated, whereas if $M \geq 12$ the cell mechanism is defined as stretching-dominated. It must be highlighted that it is not straightforward to identify the deformation mechanism of a lattice structure directly from Maxwell criterion because the behavior depends on the unit cell topology, orientation, periodicity, and the load direction too [116]. Ashby described the behavior of the bending- and stretching-dominated lattice structures relating the mechanical properties to the relative density, ρ.

2.2.1.2.2. Design

To create lattice-based functional objects, it is possible to operate on several levels of complexity, and properties related for instance to geometry, material, or process characteristics. The geometric characteristic can be tuned by operating on the unit cell shape, the unit cell size, or the unit cell relative density. The material characteristic can be tuned by modifying the material microstructure or by using more than one material, thus changing the composition over the volume. At last, the process can influence the final object by tuning the manufacturing parameters, for instance, temperature or speed,

which influence several characteristics such as actual flow rate, the accuracy of the part, adhesion among layers, and anisotropy.

The most important property of cellular solids is the relative density (ρ), can be defined as:

$$\rho = \frac{V}{V_0}$$

where V is the actual volume of the lattice, and V_0 is the volume of the region occupied by the lattice [117], considering the same density of the materials, or as the ratio between the density of the cellular solid (geometric density)and the corresponding solid material. Indeed, the literature shows that lattice physical properties are related to ρ, that can be derived from the values of cell shape, unit cell size, and thickness [96,118–125]. Consequently, once the cell shape and size have been chosen, a correlation between ρ and thickness can be established.

Generally speaking, every object and, in particular, every lattice structure can be defined as homogeneous or heterogeneous [125,126], thus properties values are respectively constant or variable within the overall volume (i.e. the design space). In contrast with homogeneous lattices, heterogeneous ones are obtained by locally modifying the geometric and/or material properties [5,126–128] and require specific representation approaches [129]. By tuning these characteristics, based on the design requirements, lattice properties can be adjusted as shown in Figure 13. In homogeneous lattices, the unit cell shape (e.g. cubic, kelvin, triply periodic minimal surfaces), cell size (in the range 0.1 to 10 millimeters), and size of the cell elements (i.e., the thickness in shell-based lattices or diameter in beam based lattices), and material (composition and microstructure) are uniform, which means each property has a single value in every point of the design space, whereas, in heterogeneous lattices, at least one property has multiple values. These values can change in two different ways: discrete, where the properties assume a finite number of values, and thus it is considered a discrete heterogeneous lattice, or continuous, where the variation can occur in a continuous (or graded) manner between the predefined limit values. Other characteristics can also influence the lattice properties, such as the fabrication process, summarized in the grey box in Figure 13.

Figure 13. Significant properties of heterogeneous lattice for the purpose of this study. The example shows a P-Surface.

2.2.1.2.3. Modeling

Several approaches for the geometric modeling of lattices, based on different representation schemes, are available in the literature [130]. Among these, some approaches present advantages and have been employed more frequently than others. This is the case of direct polygonal mesh modeling (B-Rep) and implicit (or function-based) modeling (V-Rep) approaches. An example of the first one is given by Savio et al. [131]; as described it is possible to model beam and shell-like structures using low-poly meshes and if needed use a subdivision algorithm to smooth the whole mesh. In this manner minimal surfaces lattices can be also generated by successive approximations and the approach can be extended to graded lattices. On the other hand, implicit modeling represents a flexible solution for lattice structures. Several studies have shown the potentiality of implicit modeling for generating relative density graded, cell size graded and multi-morphology TPMS lattices [132–134]. From an AM point of view, the principal drawback of this approach consists in the conversion, that is needed at some point of the AM workflow, from the function representation into an auxiliary B-rep, such as a mesh (e.g. isosurface polygonization), for subsequent slicing operations. To avoid the auxiliary polygonized representation, the main solutions are the conversion into a stack of raster images, representing each layer in the Z direction, at the machine resolution (which is an acceptable input for some AM technologies) or directly calculating the machine toolpath from the implicit model [135–137]. For this reason, some authors investigated the possibility of modeling the machine toolpath directly by using geometric

entities different from meshes, such as points and curves, especially in the case of MEX technologies [138].

Other works in the literature explored the possibility of modeling cellular solids using the CSG approach. Zeinalabedini et al. [139] modeled a foam-like structure by subtracting randomly organized spheres that overlap each other from the design space; by controlling several parameters such as the range of the size of the spheres and the amount of overlapping between them, they were able to control the relative density of the structures. Similarly, Gagliardi et al. [140] performed the Boolean subtraction between a bulk volume and random spheres to model and simulate foams produced by traditional manufacturing technologies. Ceruti et al. [141] developed a modeling environment inside an open-source CAD software capable of performing Boolean operations to model lightweight sandwich structures and to fill lattice structures inside solid parts.

Lattice structures can be modeled adopting V-Rep approaches as well. Pasko et al. [135] modeled regular and irregular microstructures using function-based modeling via implicit surfaces described by trivariate scalar fields and continuous real functions, calling this approach "Function Representation" (FRep); in particular, they applied the set-theoretic R-functions operations [142] (union, intersection, and subtraction) on the elementary initial objects to build up more complex parts. According to the authors, the proposed FRep approach provides a more robust and dynamic control if compared to the B-Rep methods; more, it is easier to modify the topology of the object due to the FRep parametrization. Aremu et al. [143] addressed the modeling of conformal lattice structures using voxels as discrete V-Rep approach. They started from creating a voxel representation of both the starting object to fill with the lattice and the lattice structure itself; adopting the same voxel resolution size, a trimmed lattice structure is obtained by performing a Boolean intersection between the two sets of voxels; this operation is fast because the intersection deals with 0 (no voxel, void) or 1 (voxel, solid) data. Furthermore, to avoid the presence of incomplete lattice elements at the boundaries, a lattice skin, called "net-skin", is created and connected to the internal structure as an alternative to solid skin. Finally, the option of modeling structures with a graded size of the element is implemented.

2.2.1.2.4. Geometric modeling tools

Even though AM is rapidly increasing its user base and more and more products are produced with this technology, the geometric modeling tools offered for the modeling of complex structures such as the cellular solids still present limitations and issues [144].

Commercially, several CAD software offer dedicated packages for lattice modeling. ANSYS SpaceClaim [145] allows filling solid volumes with different types of regular and conformal beam-like and TPMSs lattice structures; it is possible to define the filling percentage and the size of the cell and the elements. The add-on module "Lattice Structure Design" in Siemens NX [146] enables the users to design components with lattice structures characterized by beams and shells controlling the dimension of the structure. Similar operations can be performed with other software such as the 3DEXPERIENCE Part Design App by Dassault Systèmes [147], Altair Inspire [148], the Lattice module inside Materialise 3-matic [149], the Structures module inside Materialise Magics [150], and PTC Creo [151] or the Volumetric Lattice extension in Autodesk Fusion 360 [152]. The users of Rhinoceros CAD software [153] and Grasshopper plugin [154] exploited the customization freedom and developed plug-ins and add-ons for the design and modeling of lattice structures. Among them, GL Software by General Lattice [155] directly works inside Rhinoceros offering a graphical user interface enabling modeling lattices based on NURBS models; Intralattice plugin [156], developed by the Additive Design & Manufacturing Laboratory (ADML) at the McGill University, and Crystallon plugin [157], developed by Aaron Porterfield, work inside Grasshopper and allow generating lattice structures taking advantage of the parametrization and the other tools available inside Grasshopper; for instance, topology and size optimization results can be used for sizing the elements of the structures. To generate the final lattice solid model, so it is required to use other plugins, such as Dendro [158] and Cocoon [159], that operate on voxel data structures and using distance based functions, to create the surface mesh models based on the marching cubes algorithm [160]. Dendro is particularly interesting since is built on top of the OpenVDB library, which uses a very efficient sparse voxel octree data structure. It provides multiple ways to wrap points, curves, and meshes as a volumetric data type, allowing to perform various operations on those volumes for instance boolean, smoothing, offsets, and morphing operations.

All the aforementioned tools are based on B-Rep parametric functions, NURBS, and meshes and often, when the number of elements increases, they become unstable, difficult to handle, and require a lot of computational time and resources. F-Rep based plugins are also available in Grasshopper environment. Jellyfish [161] is an interesting implicit modeling plugin based on the open source geometry3Sharp library, while Axolotl [162] provides a set of components for volumetric modeling, based on the principle of signed distance functions (SDF). GraMMaCAD [163] is a CAD program developed by the Computer Graphics Research of Fraunhofer Institute for multimaterial parts with locally defining material properties using trivariate nurbs. As a graphical interactive tool, it is used for augmenting 3D models stemming from commercial CAD systems with FGM information to be manufactured with corresponding AM technology.

An increasing interest in given to nTopology software [164], which is based on V-Rep implicit functions, allowing to model structures with a high number of elements without failing; the implicit modeling approach handles better operations such as blending, filleting, offsetting, and Boolean operations. Moreover, the model sizes are always smaller than the same structure modeled with a B-Rep procedure, especially when dealing with TPMSs where the model size is the same regardless the number of the cells, because the software only stores the TPMSs equations. Finally, the visualization of the model is not based on B-Reps but on the sphere tracing technique [165], a variant of the ray tracing technique; these algorithms require high computational resources but, at the same time, they are highly parallel and can take advantage of the new advancements in CPUs and GPUs parallel processing capabilities that were not available in the past. As a limitation, the implicit models obtained in nTopology are often difficult to export for reusing them for further analyses in CAE software and needs to be converted into B-Rep models, such as surface meshes. Alternatively, it is possible to adopt other software for geometric modeling TPMS graded lattice such as FLatt Pack or MS Lattice both based on implicit modeling [132,166].

According to the current state of the art, there are few strategies to design and manufacture variable density lattice structures for MEX, mainly based on pattern modification. Several tools have been developed to allow precise control of the lattice modeling and the AM process for specific applications from bioprinting to ceramics, or to translate vector graphics into toolpath and to post-process G-code [122,131,132,167]. Among all the

software tools, a similar idea to the one proposed in this work was described by Moetazedian et al. [168]. The work is based on the concept of avoiding CAD modeling, subsequent slicing, and using continuous deposition paths with varying extrusion width as opposed to fragmented ones with constant extrusion width, to improve the quality of manufactured parts by eradicating voids and defects. To demonstrate the approach in [168], the same research team developed and published a free open-source software called FullControl GCode Designer [167]. In this tool, the user defines every segment of the toolpath along with all printing parameters, which may be related to geometric and non-geometric factors, at all points along the toolpath. Similarly, Silkworm [169] is an open project released as a plugin in Grasshopper/Rhinoceros (McNeel & Associates, USA) capable to translate non-solid geometry, i.e., surfaces, curves, and points and further, into G-code for 3d printing purposes. A tool acting directly on the G-code file by post-processing operations is Velocity Painting [170]. It's a free open-source script written in perl language that, when given an image file and a G-code file, post-processes the G-code to change print speeds according to the intensity of the image pixels, projecting the image onto the skin of the physical model. This tool was used in [168] to generate graded patterns, in addition to functions.

2.2.1.2.5.   *Issues for design and fabrication*

Recently, CAD, computer-aided engineering (CAE), and AM software tools introduced functionality allowing lattice structures design [171], but do not offer the possibility of defining the thickness based on other functional requirements. Moreover, these tools are often inadequate for the more complex shapes and multi-scale geometries associated with AM [144]. The main bottlenecks are related to the significant computational resources required (e.g. in offsets, blends, Boolean operations), scalability, processing time, model coherence and robustness (elements overlapping issues and consequent Boolean operation failure), rendering and visualization troubles due to the huge number of polygons, filleting, file exchange, adaptability, and automation [131,135,172]. These limits restrict the diffusion of optimized and variable density lattice structures in the industrial field.

Design methods for topologically optimized structures and lattices should be addressed to the specific AM processes and their constraints. Detailed factors when designing for AM include requirement for support material, limitations in build angle and horizontal

overhang distance, wall and beam thickness, hole and cavities size [128]. In most design methods, the minimum element size is the only parameter taken into consideration [5]. However, other geometrical parameters such as the inclined angle and the horizontal overhang may also affect the fabrication quality and manufacturability of lattice structures, and the effects of those parameters are not completely independent [173]. Researchers have focused their efforts on developing approaches to address these issues, mostly on PBF technologies [122,171,174–185]. For instance, the selection of the cell size and minimum and maximum size of the cell elements can address some technological constraints of powder bed fusion and binder jetting technologies, such as the minimum wall/pin thickness and the minimum escape hole dimensions necessary to evacuate powders from the model. Moreover, due to the short length of the struts, the limitations in build angle and horizontal overhang distance can be disregarded when dealing with PBF, MEX, and VPP technologies. Indeed, at a mesoscale level, i.e. the typical dimension of lattice cells [186], it is possible to assume that no support is needed. In fact, in PBF, lattices are often used as support or infill, as confirmed by literature [143,175,187]. Moreover, in MEX larger overhangs and bridge may be achieved using active cooling and dedicated deposition strategies, as reported in [188,189].

Even though PBF represents the most studied category of AM process, nowadays, thanks to the possibility of using metals and advanced materials, innovative AM technologies based on MEX are attracting the attention of the academic and industrial fields. Atomic Diffusion Additive Manufacturing [190] and Bound metal deposition [191] are emerging technologies that allow producing metal parts by material extrusion, consolidated by furnace sintering. These processes have the advantage of reducing time and cost for low batch metal components, tooling, and prototypes. Unfortunately, only a few studies are available in the literature for modeling lattice structures considering the technological constraints of MEX. One example is the design and optimization method of lattice structures proposed by Tang et al. [173] that takes into consideration the manufacturability constraints of the MEX process. In this method, a concept called manufacturable element is used to link the design and the manufacturing process. To predict the quality and manufacturability of each element, an artificial neural network is established as a meta-model for the selected AM process for certain materials. Maximum and minimum beam diameters in material extrusion process constraints are also studied,

considering the diameter of the nozzle. In the work of Leonardi et al. [126], when fabricating heterogeneous lattice with MEX process, the minimum value was set to two times the nozzle diameter whereas 2.2 mm was used as the maximum, with respect to a cell size of 5 mm. The same consideration is reported by Nguyen et al. [120] where the minimum truss diameter is defined as the double of the extrusion width and set to 0.8 mm with respect to a unit cell size of 5 mm whereas the allowable range for relative densities is determined by a regression function relating the unit cell size and minimum thickness. Interesting approaches are given by Duro-Royo et al. [192] and Giachini et al. [193] both using the Direct Ink Writing (DIW) technique. The first one uses variable flow rates and material properties applied to mesh-free geometric primitives, to 3D print functional heterogeneous structures inspired by insect wing or leaf venation structures. Variable flow rates and material compositions are encoded into instructions for a robotic arm and a multi-syringe multi-nozzle system is used for the deposition of multiple viscous water-based materials. In [193] the authors deposited cellulose-based materials to realize gradient patterns by DIW technique achieving different deformation behaviours. Operating on the computer numerical control programming language (i.e., the G-code file), the deposition process is controlled in composition and cross-sectional characteristics. Another stimulating work is the 'Project Silkworm' by A. Mamou-Mani [169], an addon that translates geometry into G-code for material extrusion technologies and permits to control the extrusion parameter using geometric features. Alternatively, A. Gleadall [167] shared an interesting design approach in which the user defines every segment of the toolpath along with all the parameters, and the G-Code is directly generated without the need for any programming skills and without using computer-aided design (CAD), STL-files, or slicing software. Even if previously inconceivable 3D geometries are achieved, such as special 3D textures and lattice infill, the macroscale shape modeling still seems very difficult.

2.3. Natural Phenomena Models and Algorithms

Other than lattice structures, in order to accomplish the complexities reachable by AM it is necessary to widen the point of view taking inspiration from nature, where complexities are everywhere in terms of shape, material, behaviour and functions. Bio-inspired mathematical models and algorithms draw inspiration from natural processes and

structures observed in the biological world. They provide a framework for creating designs that mimic the efficiency, adaptability, and sustainability found in nature. For instance, algorithms based on the growth patterns of plants can be used to generate complex, branching structures. Similarly, the behavior of materials under stress or strain in biological organisms, like bones or shells, can inform the development of advanced composite materials with optimized mechanical properties. By adopting these bio-inspired modeling techniques, engineers and designers can move beyond traditional geometric considerations, opening up new possibilities for creating innovative and highly functional structures and materials. This approach not only enhances performance but also promotes sustainability by emulating the resource-efficient strategies often seen in nature. Moreover, an appreciation for natural phenomena extends beyond the realm of science, influencing art, philosophy, and our broader cultural understanding of the world.

Natural phenomena encompass a vast array of observable events and processes that occur in the world around us. These occurrences span the realms of physics, chemistry, biology, geology, and meteorology, providing a window into the complexities and intricacies of the natural world.

Pattern formation is a significant aspect among the various subjects related to natural phenomena. Pattern formation refers to the process by which ordered structures, shapes, or behaviors emerge in a system from initially disordered or random conditions. It is a fundamental concept in various scientific disciplines, including physics, chemistry, biology, and mathematics. Figure 14 gives some examples of pattern in nature.

Figure 14. Examples of patterns in nature: a) giraffe fur, b) coral branch and c) ripple marks in desert sand.

Mathematical modeling and computer simulations are commonly employed to study and predict the emergence of patterns, providing valuable insights into the underlying

mechanisms. These algorithms find applications in diverse fields such as optimization, machine learning, data analysis, robotics, and more. Here are some of the models within pattern formation:

- Reaction-Diffusion is a mathematical model that describes how the concentration of substances changes over time due to the interplay of chemical reactions and diffusion. It can lead to the formation of spatial patterns. This system is described by a set of partial differential equations (PDEs).

- Differential Growth refers to non-uniform growth rates in structures, leading to deformation or transformation. It plays a crucial role in shaping various biological organisms and is a fundamental mechanism in pattern formation. The concept of differential growth can be represented using differential equations and PDEs.

- Laplacian Growth refers to the growth of a two-dimensional interface or boundary over time, where the growth rate at a specific point is proportional to the local curvature. This leads to the formation of intricate and complex patterns. It is often described using PDEs. It follows the Laplace equation, which is a second order PDE commonly used in physics to describe diffusion processes.

- Fractals are mathematical constructs characterized by self-similarity at different scales. They manifest as intricate and detailed patterns, making them a classic example of pattern formation in mathematics and nature. They are generated using recursive mathematical functions. One of the most famous fractals is the Mandelbrot Set.

- Agent-Based Modeling simulates the behavior of individual agents following predefined rules. Through their collective interactions, emergent patterns and behaviors can arise. The mathematical representation of an agent-based model can vary widely depending on the specific application and the characteristics of the agents and their environment.

- Cellular Automata is a discrete computational model consisting of a grid of cells, each with a finite set of states. The rules for how cells change states over discrete time steps can lead to the emergence of intricate patterns.

A recent trend is to use evolutionary algorithms such as genetic algorithm (GA), and swarm intelligence (SI) based algorithms in optimization processes or decision-making problems. In fact, a wide field of SI-based algorithms have emerged in the last decades,

including ant colony optimization (ACO), particle swarm optimization (PSO), bat algorithm (BA), cuckoo search (CS) and others [173].

2.3.1. Reaction and Diffusion systems

Among the various pattern formation models, Reaction and Diffusion model is the one of the most powerful, because it can generate a huge variety of patterns commonly found in nature. Reaction-diffusion processes form the foundation of many complex systems in nature, providing a mathematical framework to explain the emergence of intricate patterns and structures. In these systems, substances interact chemically and move through space, leading to dynamic spatial configurations. One of the most intriguing aspects of reaction-diffusion is the concept of Turing patterns, named after the pioneering mathematician Alan Turing. These patterns arise from the interplay between activators and inhibitors, resulting in the spontaneous formation of stripes, spots, or other fascinating motifs. One prominent mathematical model in reaction-diffusion studies is the Gray-Scott model [194]. Proposed by mathematicians Philip Gray and Scott Scott in the 1980s, this model specifically addresses the dynamics of two reacting and diffusing substances. It is widely used in various fields, including biology, chemistry, and physics, to simulate and understand pattern formation. Applications of reaction-diffusion, including the Gray-Scott model, span various scientific disciplines. In biology, it sheds light on phenomena like animal coat markings and the development of biological structures. In chemistry, it's essential for modeling the behavior of chemicals in complex environments.

Differential equations are employed to describe how concentrations evolve over time and space, allowing researchers to simulate and study these intricate processes. One commonly employed approach for numerical solutions of RD equations is the finite difference method. It discretizes space into a grid and approximates the differential equations governing the system. This allows for a step-by-step calculation of concentrations over time. The explicit method computes the future state directly from the current state, while implicit methods consider the future state as a function of both current and future concentrations. Alternatively, the finite element method offers high flexibility for complex geometries. It divides the space into smaller, irregular elements and approximates the concentrations within these elements. This method is particularly

valuable for simulating reaction-diffusion processes in intricate and non-uniform environments.

Mathematically, RD systems are modeled as semi-linear parabolic partial differential equations, for which there are often possibilities for an analytical or numerical treatment. The general equation for a RD system is:

$$\frac{\partial \boldsymbol{q}}{\partial t} = \overbrace{\underline{\boldsymbol{D}}\nabla^2 \boldsymbol{q}}^{Diffusion\ Term} + \overbrace{\boldsymbol{R(q)}}^{Reaction\ Term}$$

where $\boldsymbol{q} = q(\boldsymbol{X}, t)$ represents the concentration function as a vector of spatial position $\boldsymbol{X}$ and time t of a chemical component, $\underline{\boldsymbol{D}}$ is the diffusion coefficient matrix, $\nabla^2 \boldsymbol{q}$ is the Laplacian of $\boldsymbol{q}$ and $\boldsymbol{R(q)}$ accounts for all specific chemical reactions.

The Fisher-Kolmogorov equation is one of the first model of RD systems in the literature [195]; it is for a mono-component and a mono-dimensional domain and represents the simplest implementation. The chemical is reacting with no other component and is either growing or decaying. The extension of RD to a bi-dimensional domain with two components is due to Alan Turing with the well-known paper "The Chemical Basis of Morphogenics" [196]. The Turing model of RD is defined by the algebraic system given by:

$$\frac{\partial u}{\partial t} = D_u \nabla^2 u + f(u, v)$$

$$\frac{\partial v}{\partial t} = D_v \nabla^2 v + g(u, v)$$

Where $u = u(x, y, t)$ and $v = v(x, y, t)$ are the concentrations of two reactants, D_u and D_v are the diffusion matrices, f and g are two generic reaction functions. Models with higher components in a bi-dimensional domain are also reported in the literature. One of the most important is the Belousov-Zhabotinsky model which describes a three components reaction.

One of the simplest bi-component models is the Gray-Scott model [194]. Gray-Scott model of reaction diffusion system describes the following chemical reactions

$$U + 2V \rightarrow 3V$$
$$V \rightarrow P$$
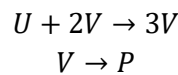
where U and V are the chemical species which interact during the reaction, while P is the inert component. The mathematical expressions are as follows:

$$\begin{cases} \dfrac{\partial u}{\partial t} = D_u \cdot \nabla^2 u - u \cdot v^2 + F \cdot (1 - u) \\ \dfrac{\partial v}{\partial t} = D_v \cdot \nabla^2 v + u \cdot v^2 - (F + k) \cdot v \end{cases}$$

where F and k are the feed rate and kill rate dimensionless parameters: F represents the rate of the process that feeds U and drains U, V and P, while k represents the rate of transformation of V to P. The system is very sensitive to the alteration of F and k. In computer simulations quantization constants are introduced for time and space (Δt and Δx) to break ∂t and ∇^2 into discrete intervals.

The evolution of the system can literally give rise to a range of patterns that can evoke reactions like mitosis, or arrangements of cells, grains within a material, or even waves in a fluid. All of this changes with the variation of f and k. The patterns of the Gray-Scott model have been classified firstly by Pearson and revised by Munafo [197,198]. This revised classification includes 17 different types of patterns plus two trivial patterns. Each type of pattern, or class, is indicated by a Greek letter from α to μ; only the two trivial patterns are indicated by the R (uniform red state) and B letters (uniform blue state). Figure 15 on the right side depicts the phase diagram of the reaction kinetics for the most interesting part of the graph on the left. In the graph on the right, replicating the blue-red color scheme used by Pearson [198], one species is highlighted in red color (generally used for areas of high u values), the other in purple (generally used for areas of low u values); different colors indicate an intermediate concentration between the two species. Outside the region bounded by the solid line, there is a single spatially uniform state (called the trivial state) (U = 1, V = 0) that is stable for all (F, k). Inside the region bounded by the solid line, there are three spatially uniform steady states. Above the dotted line and below the solid line, the system is bistable: there are two linearly stable steady states in this region. As F is decreased through the dotted line, the nontrivial stable steady state loses stability through Hopf bifurcation [199]. The bifurcating periodic orbit is stable for k < 0.035 and unstable for k > 0.035. No periodic orbits exist for parameter values outside the region bounded by the solid line.
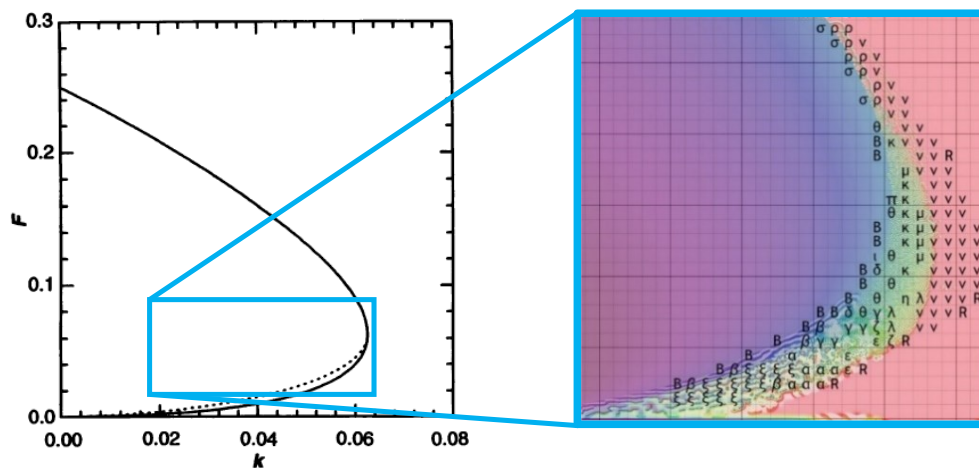
Figure 15. Phase diagram of the reaction kinetics by Pearson on the left. On the left the key to the map, where patterns are identified with greek letters and colors.

Some of the most interesting patterns are solitons, stripes, waves and cells (Figure 16) as described in [197]:

- Solitons (λ), (f = 0.034, k = 0.065), refer to circular patches that distribute themselves in space. After the space is filled, solitons rearrange into hexagonal grids. They mimic reproduction through 'mitosis', the process of cell division in which a cell divides into two identical daughter cells.

- Stripes (κ), (f = 0.058, k = 0.063), are non-straight stripes that extend from an initial point to occupy the available space, sometimes colliding and merging.

- Spirals (ξ), (f = 0.010; k = 0.041), arise from a disturbance at a point and propagate in circular waves, resembling the effect of an object thrown into a body of water, and are similar to the Belousov-Zhabotinsky reaction in a Petri dish [200].

- Cells (ρ), (f = 0.102; k = 0.055), form a branching structure that tends to simplify itself. The result resembles the division of the domain in a manner similar to cellular tissue or grains in a crystal lattice. The behaviour is like "soap bubbles" bordered by stripes exhibiting "surface tension".
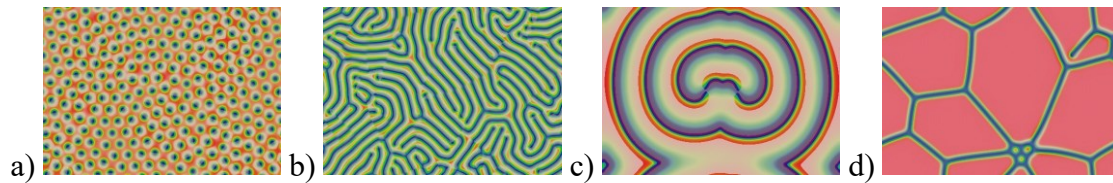
Figure 16. Gray-Scott Pattern: a) Solitons (λ), (f = 0.034, k = 0.065); b) Stripes (κ), (f = 0.058, k = 0.063); Spirals (ξ), (f = 0.010; k = 0.041); Cells (ρ), (f = 0.102; k = 0.055).

In three dimensions, there are many more types of patterns, however, they are a lot harder to simulate and display. Due to the variety of patterns the Gray-Scott model has been utilized by mathematicians and biologists, but also gain the interest of computer scientist, graphic designer and artists, for instance Karl Sims [201] which also proposed a transformed version of the phase diagram of the reaction kinetics where the more interesting areas have been expanded and warped to fall within a rectangular shape, which can be useful as a more user-friendly interface [202].
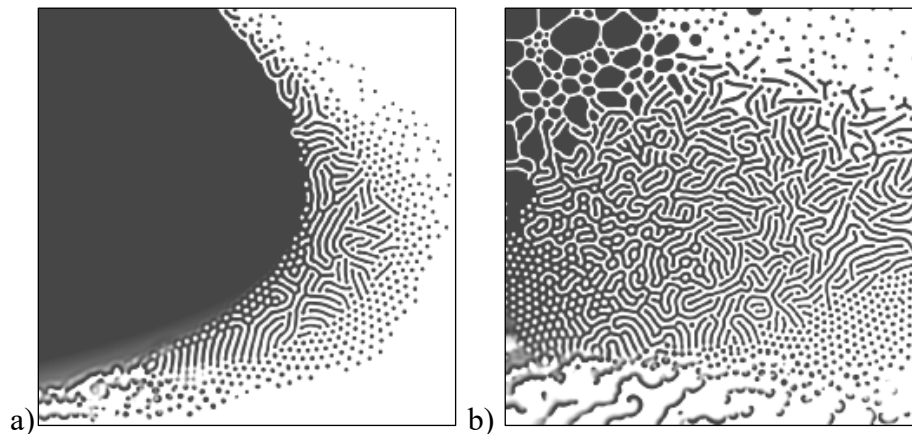
Figure 17. a) Phase diagram of the reaction kinetics (k [0.045-0.07] (X-axis); f [0.01-0.1] (Y-axis)); b) transformed version by K. Sims of the phase diagram of the reaction kinetics.

2.4. Limitations and motivation

Additive manufacturing has proven to be a promising technology enabling the production of components with unprecedented complexity. Nevertheless, AM is not mature yet. Periodically, experts and associations meet to discuss the progress made in the field and to draw AM roadmaps to drive and organize future developments [203–205]. The research community too highlights that improvements must be made in different sub-fields, as summarized in Figure 18.
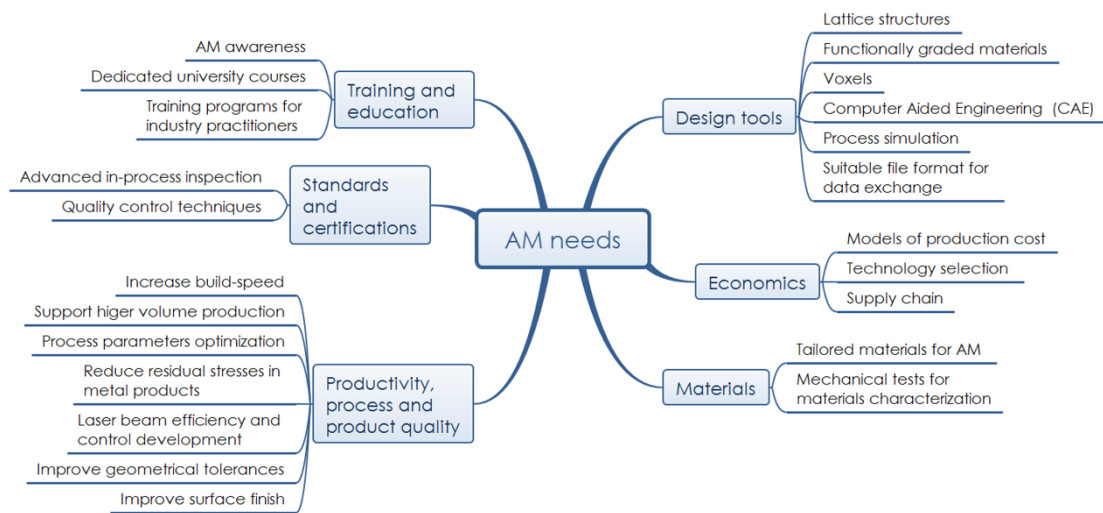
Figure 18. Additive manufacturing needs [206].

Some of the open issues underlined in Figure 18 have been exposed in the previous sections of the chapter, contextually to the recent progresses on that particular topic. So, the purpose of this section is to provide a recap of the current issues in AM.

1   Available commercial software are not suitable for designing complex parts [144].

2   The literature highlights the need for more robust and reliable approaches for geometric modeling cellular solids [131,135] and functionally graded objects [8].

3   Currently, there is a dearth of design guidelines pertaining to material compatibility and the permissible range for blending materials with variable and non-uniform properties. Additionally, a structured framework for achieving optimal property distribution, including considerations like spatial arrangement, gradient distribution, and the configuration of transition phases, remains absent [8].

4   An exhaustive workflow that covers all the design process steps is still missing, since, according to Kumke et al. [207] the current ones focus on the utilization of a single AM potential, and they are often too specific for a single case study.

5   CAD software and CAE tools should be coupled to incorporate the DfAM knowledge into the design process [208].

6   Exchanging data between different software is needed but is still an issue. Lack of a suitable and recognized standard format able to support all the required features that could be adopted in a part produced by AM technologies from design to manufacturing and more [209].

7   Mechanical characterization through experimental tests still remain a fundamental research activity to understand and predict how the parts produced by AM technologies using standard material behave with respect to the ones produced by traditional techniques [210,211].

8   New materials are developed and used to produce new shapes and features, so the static and dynamic mechanical characterization of these components is crucial [212,213].

9   The tuning of the process parameters plays a key role in improving the mechanical properties, surface finish, and geometrical tolerances, depending on the specific AM technology adopted [214,215].

More, even though ISO and ASTM organizations started collaborating to jointly develop international standards, efforts are still necessary to guarantee an adequate quality of the printed parts.

3. Bio-inspired volumetric geometric modeling for AM - Graded

In this chapter, the design and geometric modeling methods developed for graded object are described. Two different types of graded objects are investigated: graded shape and graded material.

In the area of graded shape, four geometric modeling methods, based on volumetric representations, have been implemented and enhanced to create graded lattice structures. The first method, specific for MEX AM techniques, permits the realization of lattices with relative density gradients by modifying the extrusion parameter in the CAM file, i.e., the G-code, without avoiding the creation of the lattice structure geometric model. This method is correlated with several case studies differentiated by a different volumetric data source. The second method utilizes TPMS functions to generate density, size and multi-morphology gradients, while the third one is a previously developed method by Savio et al. for modeling TPMS lattice by surface subdivision algorithm, with a small improvement which extend the possible types of data source accepted; this is mainly proposed for comparison purposes. The fourth uses a volumetric approach based on distance fields to create graded density lattices. All the methodologies share the same characteristic: different volumetric data sources, with scalar data type, can be used. Contextually, a comparison is conducted between the CAM-based approach (Graded Density Lattices via G-code editing) and one of the three CAD-based approaches (Graded Density TPMS Lattices via subdivision surface offset). Furthermore, the three CAD-based methods are subjected to a comparative evaluation amongst themselves. Finally, the strengths and weaknesses of each method are summarized.

In the area of graded materials, a methodology for achieving graded multimaterial composition has been introduced. Building upon the principles of the initial method for graded lattice structures, which hinges on G-code modification, it enables the production of components with varying compositions by adjusting the material ratio parameter in the CAM file. In this context, for material coextrusion, a deposition model and an analytical model for the Young modulus have been proposed, validated trough experimental tests.

As a secondary focus, this research investigates into the AM of advanced bioceramic porous scaffolds. This investigation examines the mechanical properties of TPMS Gyroid samples in relation to two raw materials, two AM technologies, and three different relative densities.

3.1. Shape

3.1.1. Graded Density Lattices by G-code editing

The manufacturing of complex lattice structures remains a challenge for material extrusion (MEX) technologies. The main bottlenecks for MEX technologies are related to the significant computational resources required for the modeling, visualization, file exchange, and mostly for the computer numerical control programming language (G-code) computation of complex shapes. Indeed, using standard computer-aided manufacturing (CAM) software tools for G-code computation of components with variable density lattice structures, several technological limits are highlighted, such as fragmented toolpaths, undesired porosity, long manufacturing time, and missing path especially in low dimension cell elements. On the contrary, by using standard CAM software, also known as slicing software, it is possible to obtain complex homogeneous 3D shell-based lattice structures simply working on the software infill parameters. The need for effective strategies for manufacturing variable density components is becoming of increasing interest due to the capacity of MEX technologies to process, other than polymer materials, high performing materials such as ceramics and metals.

To overcome the mentioned limitations, and tacking into account the already available tools a method to avoid CAD modeling of graded lattice structures and consider technological constraints is proposed.

3.1.1.1. Method development and implementation

Starting from a CAD model of the component without lattices,i.e, representing the boundary of a component, standard CAM software is adopted to obtain the G-code. In the CAM software, in addition to the typical process parameters, such as the layer thickness, nozzle diameter, skin thickness, and speed, it is possible to define an internal lattice by assigning a 3D infill pattern with uniform density. Finally, using a specifically developed postprocessing algorithm, the infill portion of the G-code is modified based on the density map defined in a volumetric model.

The proposed method firstly considers a CAD model. According to functional requirements, a density map can be associated with the CAD model by volumetric modeling approaches as well as by functions. To manufacture the component by MEX technologies, such as FDM, the CAD model is exported to a CAM software for the elaboration, obtaining a G-code. Based on the density map, the amount of extruded material is computed, and the G-code is consequently modified, allowing the fabrication of a variable density component.

Figure 19 shows the workflow of the proposed design method. In detail, the proposed method consists of the following steps:

1) based on functional and aesthetic requirements the component is designed in a CAD software environment. The CAD model is usually converted into a polygonal mesh and exported as an STL file or using other file formats (e.g. 3MF, AMF, STEP AP 242, ply, obj);

2) a CAM software, a so-called 'slicer', is used for the G-code generation from the STL file. The G-code contains the coordinates of the toolpath, and the amount of material extruded, which were interpolated during the manufacturing process planning. To obtain the toolpath, several manufacturing parameters considering material and hardware properties are defined, such as the printing and build plate temperature, printing speed, nozzle and filament diameter, layer thickness, and number of outer shells. Moreover, the infill pattern parameter is used to assign a 3D geometrical pattern inside the model, whereas the infill density parameter controls the pattern spacing. In this study, 3D infill patterns which create internal periodic shell-based lattice structures are of considerable interest.

3) a density map based on some functional requirements can be associated to the CAD model by volumetric modeling approaches. The density map describes the distribution of the ρ (values between 0 and 1) inside the component. The map can be obtained by different inputs such as grayscale of medical images, density map of topology optimization, or explicit function assigning a value of density to each point of the Euclidian space. In this implementation, a volumetric modeling approach based on voxels was chosen.

4) from the G-code, the infill toolpath and the amount of material extruded (length of filament fed, i.e., the "E" parameter in the G-code) are retrieved. The ρ at each point

of the toolpath is computed by a trilinear interpolation (Appendix A.3) among the voxel densities, using the coordinates of the voxels centres. Then the ρ is compared to the infill density and the amount of material extruded is recomputed and substituted in the G-code. To avoid wide density variation, when the sampling of the G-code (i.e., the space between 2 successive points of the toolpath) is too large, resampling of the path is performed.

5) the object is finally printed with a material extrusion technology using the modified G-code. In this way the extrusion width is driven by the densities, resulting in denser components in the regions with higher voxel density.
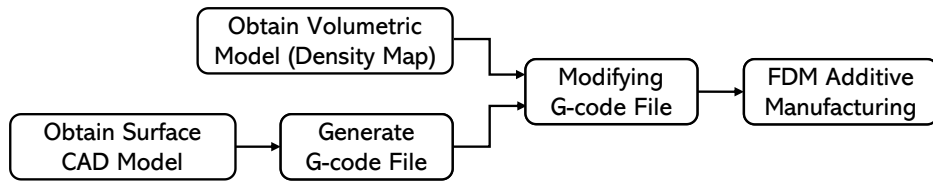
Figure 19 Workflow of the proposed method based on G-code modification

3.1.1.1.1.   *Preliminary process modeling*

A preliminary study on the process is needed to accomplish the results. The process modeling is based on the simplified assumption that the section of the material deposited on the surface is a rectangle. This simplification serves an explanatory purpose and remains inconsequential to the outcomes, as it does not exert any influence on the actual relative density. The extrusion width (E_w) denotes the breadth of the filament deposited onto the surface. (Figure 20). The layer thickness (L_{tk}) is the height of each layer, i.e., the discrete increment in the building direction. Consequently, the cross-sectional area (A_{dep}) of the material dispensed on the surface during the deposition process is equal to:
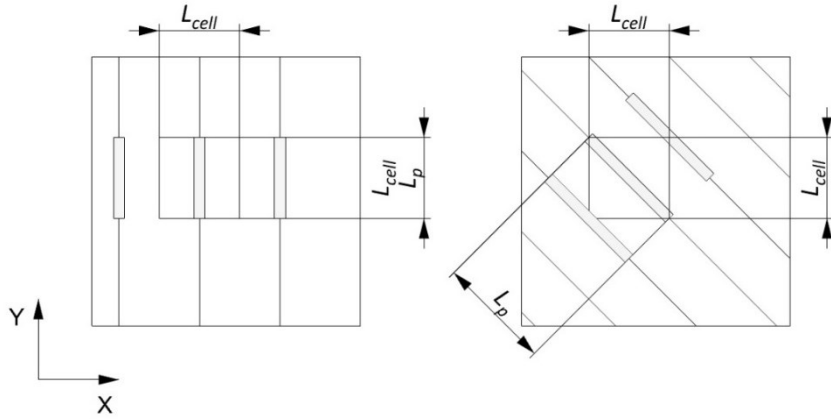
$$A_{dep} = E_w \cdot L_{tk} \tag{1}$$
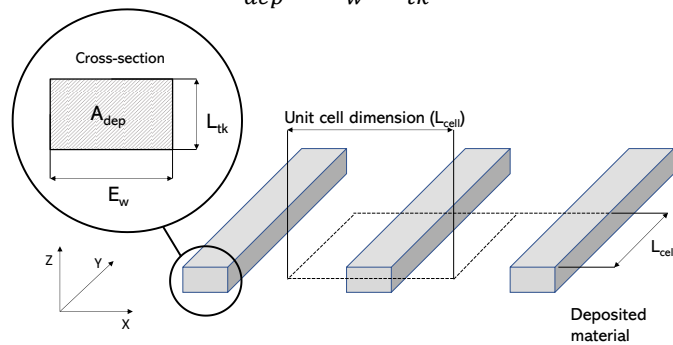
Figure 20. Main deposition parameters adopted in the process model on different infill patterns.

According to Figure 20, considering the length of dispensed filament (L_p) in the L_{cell}, ρ can be calculated as the ratio between the volume of extruded material V_m and its occupied space V_e:

$$\rho = \frac{V_m}{V_e} = \frac{E_w \cdot L_{tk} \cdot L_p}{L_{cell} \cdot L_{tk} \cdot L_{cell}} = \frac{E_w \cdot L_p}{L_{cell}^2} \tag{2}$$

Consequently, it is possible to obtain the required ρ in the component, by acting on E_w, cell pattern, and cell dimension.

3.1.1.1.2. Extrusion width limits

MEX processes work properly within a range of E_w:

$$E_{w,min} \leq E_w \leq E_{w,max} \tag{3}$$

The stability and quality of printed parts limit the maximum value for E_w ($E_{w,max}$, in yellow in Figure 21) which depends on the hardware, such as the selected MEX process, nozzle dimension and shape, and specific process parameters, such as printing speed and temperature. Moreover, from eq. 2, to obtain fully dense portions ($\rho = 1$) it is necessary to set

$$E_{w,max} \geq L_{cell}^2 / L_p \tag{4}$$

Similar considerations are also applied to the minimum E_w ($E_{w,min}$ in blue in Figure 21). Furthermore, the $E_{w,min}$ value is established considering that the extruded material should support the subsequent layers. Considering the intricate relationship among the process parameters, to identify $E_{w,min}$ and $E_{w,max}$, a specific experimental test was developed

and proposed in the following section. Alternatively, as a first approximation, it was set $E_{w,min} = L_{tk}$ and $E_{w,max} = 5\emptyset_n$, where $\emptyset_n$ is the diameter of the nozzle.
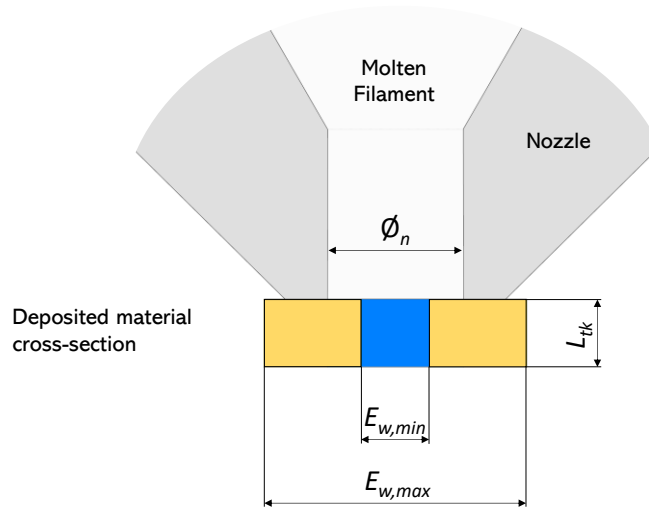

Figure 21. Deposited cross-section parameters and the nozzle shape.

3.1.1.1.3.   G-code computation

CAM software tools compute the G-code that controls the deposition process and the production of the physical component. The resulting G-code depends on a set of process parameters, which are selected according to the material and hardware characteristics.

Usually, the CAM software tools employed in MEX generate an infill pattern with constant density inside the model, to support the subsequent layers and to obtain a part using as less material as possible. The infill is controlled by the infill pattern and infill density ρ_s parameters. Depending on the selected slicer, it is possible to show that ρ_s can be related to other parameters, such as L_{cell}, L_{tk}, $\emptyset_n$. In this work, the G-code was computed using the open-source software Slic3r 1.30 [216].

3.1.1.1.4.   Infill pattern and infill density

As previously stated, $E_{w,max}$ is also related to the L_{cell}. The unit cell size gives the 'resolution' of the lattice structure. A factor, that in this work is referred to as multiplicity (m), relates to the symmetry properties of the unit cell. It defines the number of independent toolpaths for every single cell in a layer: for a linear pattern $m = 1$; for the Gyroid cell, $m = 2$ since the single cell can be subdivided in the plane in two identical geometric units, each one containing a single path. In Figure 23, the case of the Gyroid is shown. Considering m , eq. 2 becomes:

$$\rho = \frac{E_w \cdot m \cdot L_p}{L_{cell}^2} \tag{5}$$

For a generic cell, L_p can be parametrised on L_{cell},

$$L_p = k_c \cdot L_{cell} \tag{6}$$

where k_c is a coefficient depending on the infill pattern, obtained as the average length of the trajectories in the unit cell, and equal to 1.23 for a Gyroid. Consequently, eq. 5 becomes:

$$\rho = \frac{E_w \cdot m \cdot k_c}{L_{cell}} \tag{7}$$

In the slicing software adopted in this work, E_w in the infill depends on $\emptyset_n$

$$E_{ws} = k \cdot \emptyset_n \tag{8}$$

where $k = 1.25$ and E_{ws} is the width of the "rectangle with semicircular ends" of the section of the deposited material (Figure 23.a) [217].
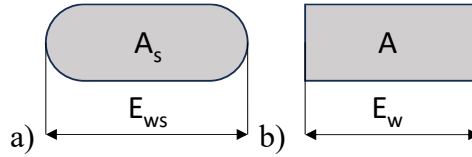
Figure 22. Sections deposited material with same area: a) rectangle with semicicular ends, b) rectangle.

Moving to the rectangular section ($A_s = A$) of the proposed model (Figure 23.b):

$$E_w = 1.25 \cdot \emptyset_n + \left(\frac{\pi}{4} - 1\right) \cdot L_{tk} \tag{9}$$

obtaining from eq. 7:

$$\rho_s = \frac{m \cdot k_c \cdot \left(1.25 \cdot \emptyset_n + \left(\frac{\pi}{4} - 1\right) \cdot L_{tk}\right)}{L_{cell}} \tag{10}$$

where ρ_s represents the ρ adopted in the slicing process.
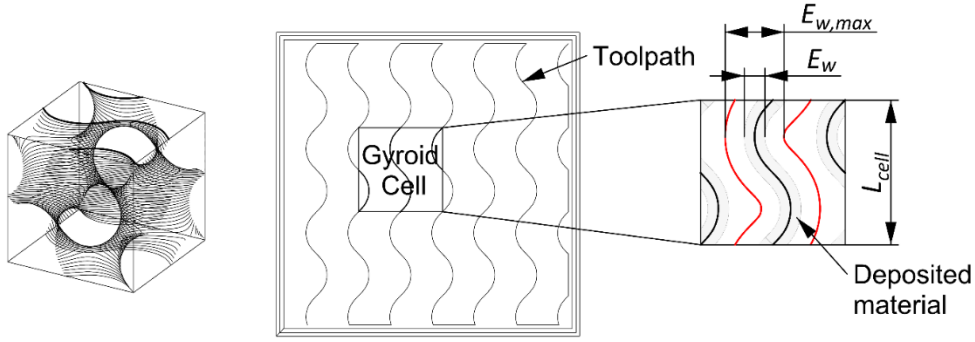
Figure 23. Top view of a single layer with Gyroid infill and deposition parameters for the Gyroid cell.

Based on the infill pattern, considering eq. 7, it is possible to compute the L_{cell} required to achieve a 100% relative density ($\rho = 1$):

$$L_{cell} = E_{w,max} \cdot m \cdot k_c \tag{11}$$

The correlation between the Gyroid L_{cell} and ρ_s is reported in Figure 24 for $\emptyset_n = 0.40$ mm and $L_{tk} = 0.20$ mm.

It is observed that knowing that the maximum extrusion width for the printer configuration is $E_{w,max} = 1.22$ mm, it is possible to obtain a fully dense cell with $L_{cell} = 3$ mm, and the infill density is $\rho_s = 0.37$ (blue solid dot in Figure 24). As previously discussed, all the combinations with lower cell dimension are suitable solutions (the red area in Figure 24) but increase the model complexity; on the other hand, the blue area in Figure 24 identifies feasible solutions in which it is not possible to obtain a fully dense part, after editing the G-code. So $E_{w,max}$ establishes the ideal value of L_{cell}, and, consequently, the ρ_s. The trend in Figure 24 is obtained by regression approaches: the actual dimension of the unit cell size (Gyroid) generated at different infill density was measured from the reconstructed toolpath (polyline). This approach can be done for every type of infill (and $\emptyset_n$, L_{tk}), once identified the unit cell in the pattern (see section 3.1.1.2.1).
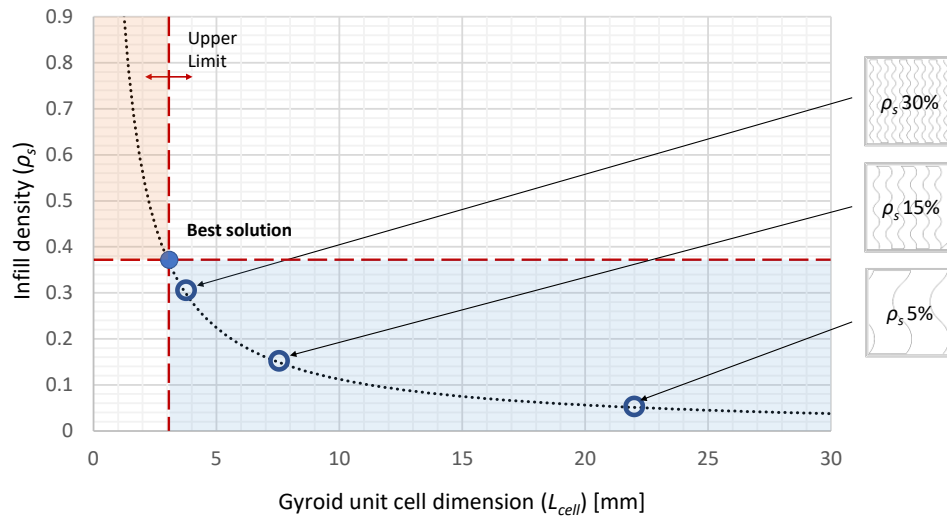
Figure 24. The correlation between Gyroid unit cell dimension (L_{cell}) and infill density (ρ_s) for $\emptyset_n$ = 0.40 mm and L_{tk} = 0.2 mm.

3.1.1.1.5. G-code editing

The method has been implemented in IronPython language in Grasshopper, a visual programming environment that runs within the Rhinoceros 7 CAD Software (McNeel & Associates, USA).

A G-code file serves as a sequential set of instructions read by either a computer numerical control or an FDM machine. Typically, this file is compartmentalized into distinct sections: a header, body, and footer. The body segment, constituting the crux of the G-code, encompasses specific lines housing essential commands for materializing the component. This portion typically adheres to a recognizable structure characterized by a repetitive pattern. For instance, a simplified operational sequence for each layer involves: transitioning to the next layer, constructing perimeters, and executing infill. In the proposed method, the initiation of each infill section is first pinpointed by detecting the line denoting the printing speed, and subsequently, it is subject to modification.

In the body section of a G-code for a 3D printer, most lines consist of motion instructions, typically expressed in the following syntax: G# X# Y# Z# E# F#.

In this context, "G" serves as the command denoting linear motion (e.g., G0, G1), while "X, Y, and Z" specify the absolute or relative Cartesian coordinates of the subsequent point. The parameter "E" pertains to extrusion and dictates the quantity of filament to be supplied to the extruder. This value is represented in either absolute or relative

63

coordinates, measured in millimeters (indicating filament length) or in mm³/s (reflecting flow rate). The exact syntax depends on the firmware for FDM and its specific configuration. For example, if the FDM system is operating with Marlin firmware, the volumetric extrusion mode is activated using the command "M200 S1" and deactivated with "M200 S0". [218]. For the following considerations, the parameter "E" is employed to represent the length of the filament. Additionally, "F" specifies the printing speed, measured in millimeters per minute (mm/min). With a comprehensive understanding of the G-code's structure, syntax, and commands generated by a particular slicer, one can manipulate the "E" parameter to generate a specified density map within the infill portion of the component.

Indeed, the G-code lines pertaining to the infill are discerned by the chosen speed during the slicing process, denoted by a distinct value of "F". These lines allocate the coordinates defining the relative position of the constructed part in relation to the nozzle's position, in addition to the "E" parameter (Figure 25).
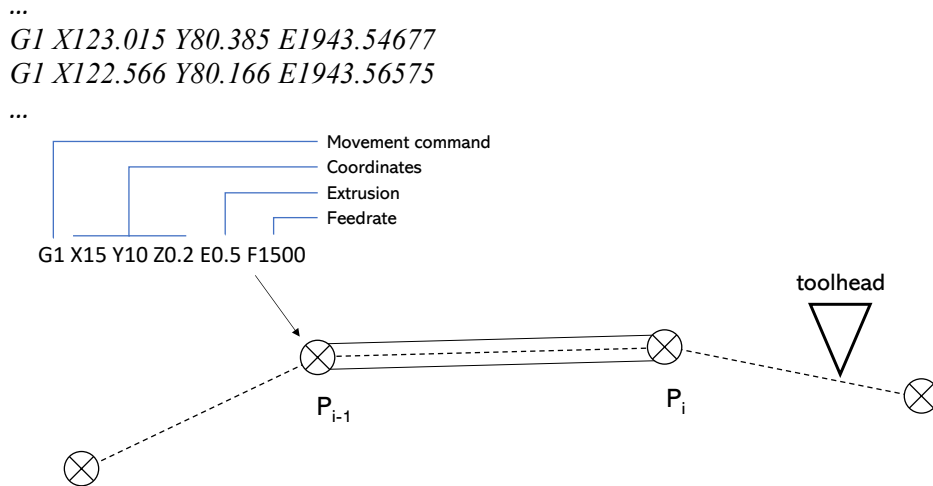
Figure 25. Illustration of G-code meaning.

Considering two consecutive G-code lines it is possible to identify the nozzle-part shift Δs_i and the filament shift $\Delta E_{s,i}$ obtained by the slicing process:

$$\Delta s_i = \sqrt{(X_i - X_{i-1})^2 + (Y_i - Y_{i-1})^2} \qquad (12)$$

$$\Delta E_{s,i} = E_{s,i} - E_{s,i-1} \qquad (13)$$

where i represent the i-th line.

In the Δs_i, the extruded material volume $\Delta V_{ms,i}$ is given by:

$$\Delta V_{ms,i} = \Delta s_i \cdot E_w \cdot L_{tk} \tag{14}$$

Considering the cross-sectional filament area A_f and the filament diameter $\emptyset_f$, the $\Delta E_{s,i}$ is given by:

$$\Delta E_{s,i} = \frac{\Delta V_{ms,i}}{A_f} = \frac{\Delta V_{ms,i}}{\pi \frac{\emptyset_f^2}{4}} \tag{15}$$

By the X_i, Y_i, Z_i coordinates and the density map of the volumetric model, adopting a trilinear interpolation method [122], it is possible to establish the required ρ after the G-code editing at the i-th point ($\rho_{e,i}$). Consequently, considering eq. 2,

$$\rho_s = \frac{V_{ms}}{V_e}, \quad \rho_{e,i} = \frac{V_{me}}{V_e} \tag{16}$$

where V_{ms} is the extruded material volume in the slicing process and V_{me} is the extruded material volume in the G-code editing. Dividing the eq. 17, we obtain:

$$\frac{\rho_{e,i}}{\rho_s} = \frac{V_{me}}{V_{ms}} \tag{17}$$

Moving eq. 18 from V to ΔV and considering eq. 16:

$$\frac{\rho_{e,i}}{\rho_s} = \frac{\Delta V_{me,i}}{\Delta V_{ms,i}} = \frac{\Delta E_{e,i} \cdot A_f}{\Delta E_{s,i} \cdot A_f} \tag{18}$$

Consequently, from eq. 19, the $\Delta E_{e,i}$ for editing the G-code is given by:

$$\Delta E_{e,i} = \Delta E_{s,i} \cdot \frac{\rho_{e,i}}{\rho_s} \tag{19}$$

Editing the G-code it should also be considered that $E_{w,min}$ limits the minimum ρ_e ($\rho_{e,min}$), that can be computed by eq. 7. Moreover, considering that the shape of the section of material deposited is not a perfect rectangle, E_w can be better derived from the cross-sectional area, using eq. 1.

Within the Rhinoceros software, both the CAD model and the volumetric model are accessible. To manipulate the G-code, the subsequent pseudocode was developed in Python:

```
-   Read G-code lines
-   initialize the edited_G-code
-   set X0, Y0, Z0, E0, new_E to 0
-   for each line:
```

```
        -  if available, extract X, Y, Z, E
        -  compute ΔE = E - E0
        -  if line is infill:
                -  compute ΔX, ΔY and Δs
                -  if Δs is too large:
                        -  divide ΔX, ΔY and ΔE in n-portion
                -  for each portion:
                        -  calculate $\rho_{e,i}$
                        -  if $\rho_{e,i} < \rho_{e,min}$:
                                -  $\rho_{e,i} = \rho_{e,min}$
                        -  compute new_ΔE, new_X, new_Y
                        -  new_E = new_E + new_ΔE
                        -  create a new_line string with new_X, new_Y and
                           new_E
                        -  add new_line to the edited_G-code
        -  else:
                -  if E in line:
                        -  new_E = new_E + ΔE
                        -  in line, substitute E with new_E
                        -  add line to the edited_G-code
                -  else:
                        -  add line to the edited_G-code
        -  set X0, Y0, Z0, E0 variables with X, Y, Z, E
    -  write edited_G-code
```

For streamlining G-code editing, the slicer software has the "Verbose" option and the "Relative extrusion" mode enabled. The "Verbose" option appends a distinct string to each section of the G-code. Meanwhile, the "Relative extrusion" mode employs relative "E" coordinates in the G-code, as opposed to absolute coordinates. In this scenario, the pseudocode transforms as follows:

```
    -  Read G-code lines
    -  initialize the edited_G-code
    -  for each line:
        -  if available, extract X, Y, Z, E
        -  if line is infill:
                -  compute ΔX, ΔY and Δs
                -  if Δs is too large:
                        -  divide ΔX, ΔY and E in n-portion
                -  for each portion:
                        -  calculate $\rho_{e,i}$
                        -  if $\rho_{e,i} < \rho_{e,min}$:
                                -  $\rho_{e,i} = \rho_{e,min}$
                        -  compute new_E, new_X, new_Y
                        -  create a new_line string with new_X, new_Y and
                           new_E
                        -  add new_line to the edited_G-code
        -  else:
                -  add line to the edited_G-code
    -  write edited_G-code
```

3.1.1.1.6. Experimental E_w limits

To establish the feasible range for E_w, an experimental test is proposed in which a single perimeter pipe is printed, obtaining a circular path. The geometry is repeated in several layers to better identify any issue in the deposited material profile and avoid boundary effects related to the first layer. In this sample, E_w is gradually varied from a lower value to an upper value: $E_{w,min} = L_{tk} = 0.2$ mm and $E_{w,max} = 5\emptyset_n = 2.0$ mm are assumed as initial empirical limits. A G-code is generated using a script in Grasshopper with the process parameters previously reported in Table 1, assigning the required ΔE parameter to the toolpath (150 segments, diameter 80 mm):

$$\Delta E_i = \frac{4 \cdot \Delta s_i \cdot L_{tk} \cdot E_{w,i}}{\pi \, \emptyset_f^2} \tag{20}$$

The G-code is executed, and the produced sample is scrutinized for any signs of interruptions, irregularities in flow, or other anomalies that might affect the deposition quality. These concerns primarily stem from variations in viscosity and pressure within the heating chamber of the nozzle, a consequence of the amplified flow rate associated with higher extrusion widths E_w [219]. An elevated flow rate implies that the polymer spends less time in the melting zone, leading to a slightly cooler extrusion. This lower temperature, combined with increased filament shear stress within the nozzle, results in higher pressure. Consequently, this exerts greater stress on both the filament and the extruder [219,220]. As the flow rate is elevated, there reaches a threshold where either the motor skips steps or the filament undergoes grinding, resulting in a loss of control over the extrusion process. Consequently, the volume of extruded material and the E_w is lower than planned. This limit can be detected by clicking and grinding noises [221]. To verify the results and compensate possible under extrusion, the designed and the printed sample are compared on two cross-sections area of the sample measured by a stereomicroscope (Leica MZ 7.5 equipped with an IC 90 E camera). Knowing the designed cross-section area A_n and the measured one for n layers A_a, it is possible to calculate the E_w as the ratio:

$$E_w = \frac{A_a}{n \cdot L_{tk}} \tag{21}$$

Under the tested conditions, no issues were observed. Therefore, it is viable to reprint the sample by either further increasing the limits or affirming the results to prevent significant

under extrusion, as was decided in this instance. Figure 26 shows the sample sections used to evaluate the actual printable E_w range. The area $A_{a,min}$ is 0.2245 mm^2 and $A_{a,max}$ is 1.06 mm^2, calculated considering 3 layers. Consequently, E_w range is 0.374 – 1.76 mm. The higher value for $E_{w,min}$ with respect to the designed one is supposed to be influenced by the delay in the extrusion response and the elasticity of the melted material in the nozzle, thus the minimum value has not been achieved, but it can be assumed as an effective value considering the continuous flow variation in real conditions. Therefore, for a Gyroid infill pattern, by eq. 11 L_{cell} = 4.33 mm, by eq. 10 ρ_s = 0.26 and by eq. 7 $\rho_{e,min}$ = 0.21 were computed.
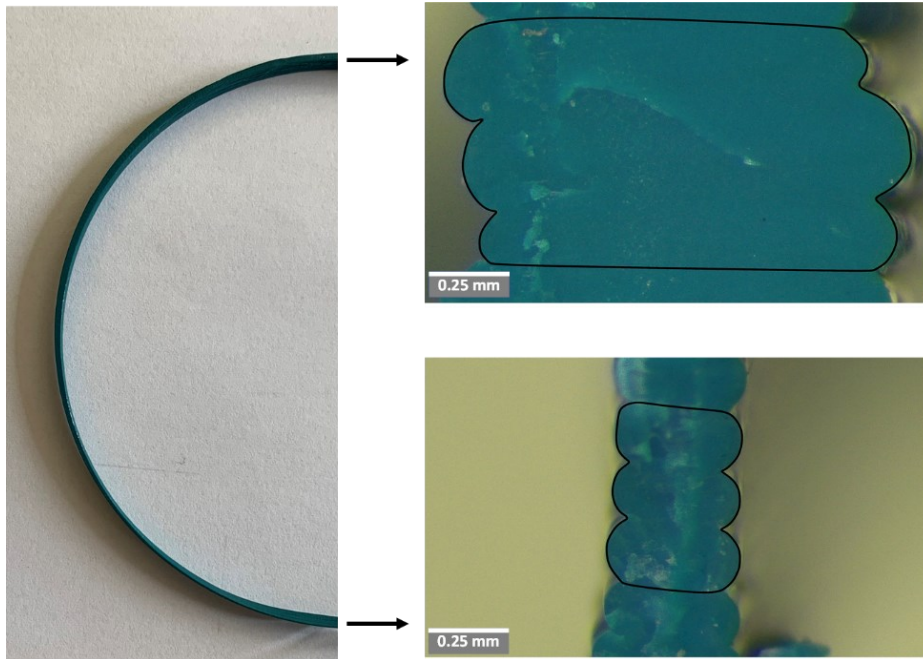
Figure 26. Sample for $\mathbf{E}_w$ limits evaluation. On the left, the half of the printed circular sample (top view). On the right, the two cross-sections of the maximum (top) and minimum (bottom) $\mathbf{A}_a$ (the actual area are highlighted by the black curves).

3.1.1.1.7. Process configuration

A Geeetech i3 Pro B desktop FDM 3D printer (Shenzhen Geeetech Technology Co.,Ltd, China), equipped with a Titan extruder (E3D-Online Ltd, Great Britain), and configured in a pre-calibrated direct drive arrangement, was utilized. This setup included a V6 hotend and a brass nozzle (E3D-Online Ltd, Great Britain), and it operated using generic PLA filament.

The process parameters are reported in Table 1. Among these, v_p, T_n, and L_{tk} are those mainly influencing the infill density selection. By the following experimental procedure $E_{w,max}$ and $E_{w,min}$ are assessed, allowing for ρ_s and $\rho_{e,min}$ computation.
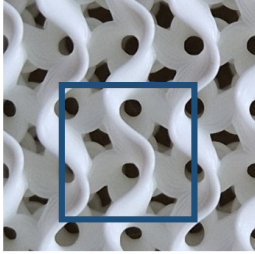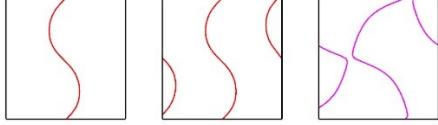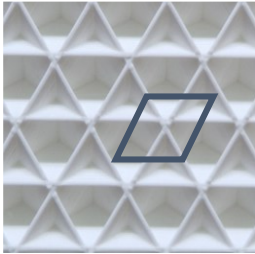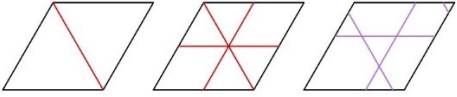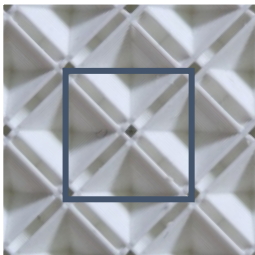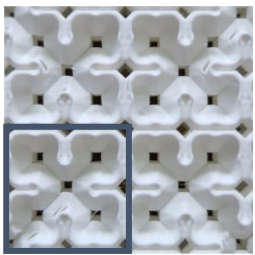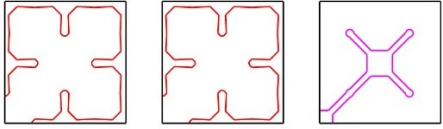
Table 1. Main process parameters.

Infill pattern	Gyroid	L_{tk}	0.2 mm
Infill speed v_p	25 mm/s	Perimeter speed v_s	30 mm/s
Nozzle temperature T_n	215 °C	Bed temperature T_b	55 °C
Nozzle diameter $\emptyset_n$	0.4 mm	Filament diameter $\emptyset_f$	1.75 mm
Number of perimeters	3		

3.1.1.1.8.   Method configuration for other infill patterns

The method can be extended to other cell topology by defining the m and k_c parameters. Aside from the Gyroid pattern, other infill patterns like Octet, Cubic, and Cross3D are excellent choices for creating functional 3D printed parts. Octet infill, also referred to as tetrahedral infill, consists of stacked pyramid shapes. Cubic infill forms a 3D pattern with stacked and tilted cubes. Cross 3D, on the other hand, is a 3D recursive pattern akin to the Sierpinski curve fractal [222]. It's important to note that the density variation in this last pattern is attributed to its recursive nature, making it challenging to identify a distinct unit cell. In this case, starting from the average length of the toolpath in the unit cell it is possible to establish k_c. Table 2 shows the infill patterns, highlighting the unit cell, the single path, the multiplicity, and the path in another layer, summarizing for each pattern the value of m and k_c. By these coefficients and eq. 10, graphs similar to Figure 24 can be obtained. Nevertheless, actual relation between unit cell dimension and infill density can be slightly different due to the specific slicer implementation. In this work, Slic3r for Gyroid and Cubic, and Cura for Octet and Cross3d were adopted.

Table 2. Parameters needed for the extension of the method to other infill patterns.

Infill Pattern	Unit Cell	Unit Cell Path	m	k_c
Gyroid			2	1.23
Cubic			3	1
Octet			4	1.42
Cross3D			1	5.63 (ρ_s=15%)

3.1.1.2. Method validation and applications

As an initial test, constant density infills were considered to verify if a full density component and the minimum infill density can be obtained. Figure 27 shows the printed samples for a 2.7 mm Gyroid unit cell obtained with different values of E_w: $E_w = 1.35$ mm ($\rho_e = 1$) (Figure 27a), $E_w = 0.75$ mm ($\rho_e = 0.76$) (Figure 27.b) and $E_w = 0.3$ mm ($\rho_e = 0.27$) (Figure 27c). It possible to observe that in the higher density part (Figure 27a), few void areas close to the perimeter appear, whereas, in the lower density case (Figure

27c), there is a non-ideal connection between the infill and the perimeter. These shortcomings can be avoided by increasing the E_w of the internal perimeter.
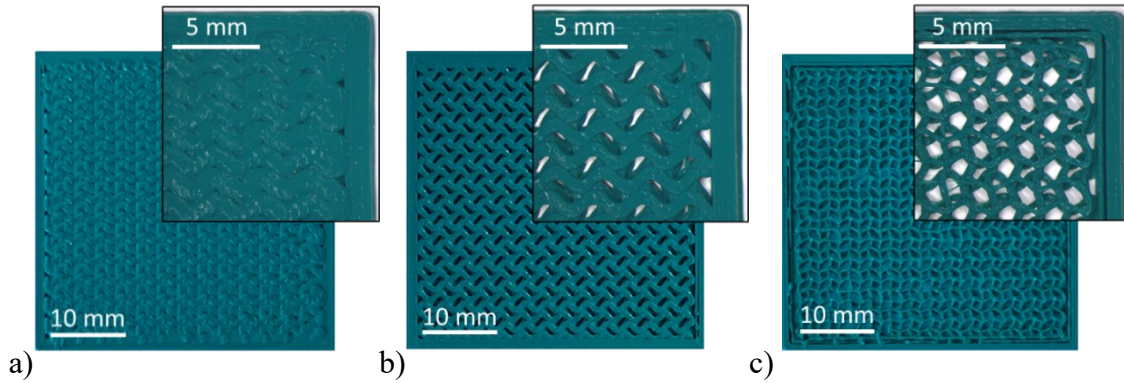

Figure 27. Printed samples for (a) $E_w = 1.35$ mm ($\rho_e=1$), (b) $E_w = 0.75$ mm ($\rho_e=0.76$) and (c) $E_w = 0.3$ mm ($\rho_e=0.27$), for a 2.7 mm Gyroid cell.

3.1.1.2.1. Infill test cases

To show the generalization of the method to different infill patterns, a sample with linear gradient in the Y direction from 80% to 20% density, based on the cellular structures presented in section 3.5, was manufactured. The sample is a 40 mm square with a 20 mm fillet in XY-plane and 5 mm high (Figure 28). The fillet was introduced to show the behavior of the infill on a curved surface.

As a preliminary confirmation of the reliability of the method the samples were weighed (Table 3). The theoretical mass was determined by summing the E values from the G-code, each multiplied by the cross-sectional area of the filament. The material density (1.15 g/cm³) was derived from a series of samples without any G-code modifications. The variation between actual and theoretical mass is minimal, less than 4%. This slight difference could be attributed to factors like filament diameter accuracy, a minor deviation between the intended and actual infill density prior to G-code adjustments, and other factors discussed earlier.
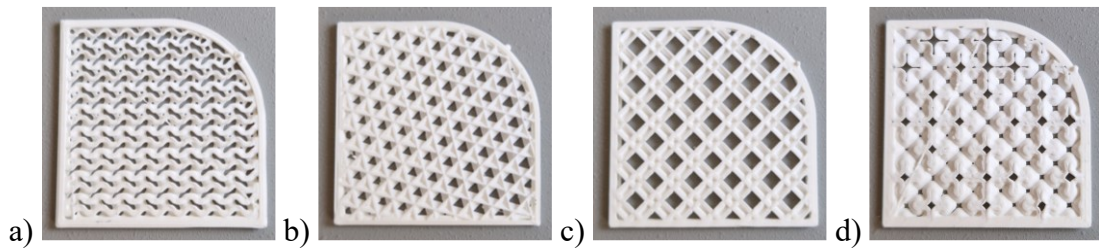
Table 3. Sample weights

Sample	Theoretical Mass [g]	Actual Mass [g]
Gyroid Y Gradient	5.19	5.10
Cubic Y Gradient	5.17	5.29
Octet Y Gradient	4.95	5.14
Cross 3D Y Gradient	4.97	4.88

The applicability of this method to diverse functional requirements is contingent upon the availability of a volumetric model. In the subsequent sections, various case studies are outlined to underscore the adaptability of the method, employing different types of volumetric models as input. The initial steps of the workflow are slightly tailored for each specific volumetric model used, while the core process, involving the modification of the g-code, remains unchanged. In the initial case study, images are utilized to construct the volumetric model. The second case incorporates a volumetric model derived from a CT scan as input. Finally, the third case integrates a volumetric model generated from the density map of a Topology Optimization performed on the geometric model of a jet engine bracket.

3.1.1.2.2.   Case Study 1 – Images

In this case study, the volumetric model is constructed from a 2D image. The general workflow is depicted in Figure 29.
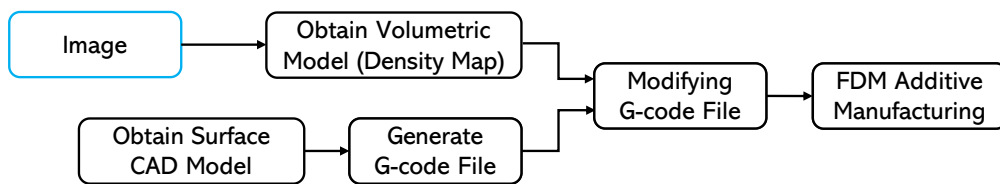

Figure 29 Reworked workflow for image input for volumetric model

An RGB image is converted into a vector of normalized grayscale values in the range 0-1, that can be interpreted as a relative density map. This vector is obtained by sampling the image with a regular 2D grid of points (sampling array). The number of sampling points nX and nY in the 2D grid can correspond to the image resolution, so in the x

direction, nX is the image resolution width and in the y direction, nY is the image resolution height. nX and nY are also the number of voxels in x and y directions. The voxel size (vS) is then set, for instance, based on the bounding box of the B-rep CAD model (Figure 30). The number of voxels in the z direction, nZ, is calculated according to the volumetric model height. The full volumetric representation is obtained by repeating the normalized grayscale vector nZ times. Otherwise, it is possible to project the grayscale values only on a single or on multiple layers, showed in Figure 31. Finally, the volumetric model is aligned with the B-rep CAD model.
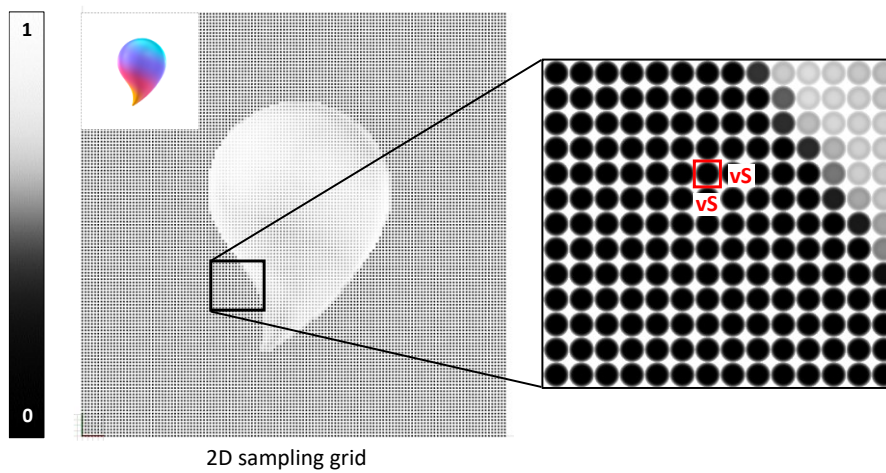

Figure 30. The grayscale values visualized as points sampled from the color image in the top left, and a particular of the grid with voxel parameter reported (vS).
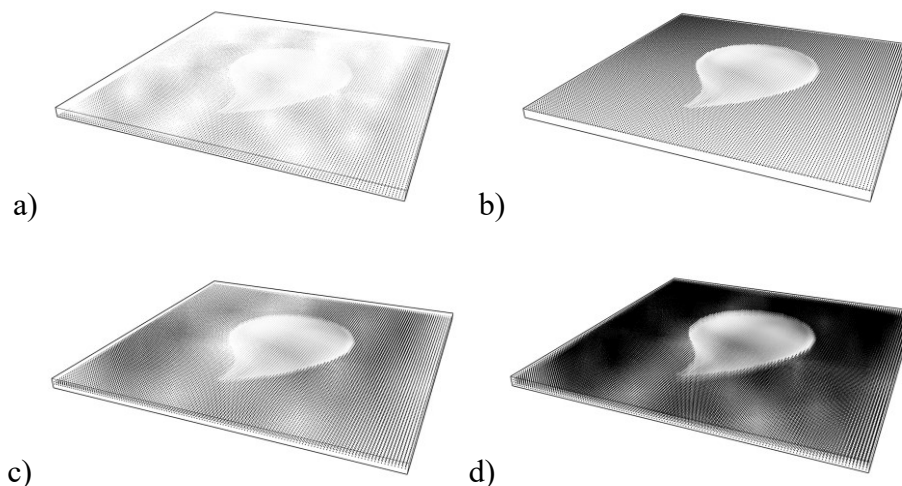

Figure 31. 3D array visualization with nZ = 4. Single projection a) on first layer and b) on last layer; multiple projections c) 2 mid-layers and d) completely filled array (repeated nZ times).

The method is firstly applied in the case of single image. The image employed possesses a resolution of 142x142 pixels. The overall object takes the form of a box measuring 80x80x2.4 mm. The voxel size remains consistent at 0.56 mm (isotropic). This translates to nX = 142, nY = 142, and nZ = 4. Each individual layer is characterized by 20164 grayscale values, necessitating a total of 80656 values to completely fill the array. These values are projected across all four layers of the array (refer to Figure 31.d). The chosen infill pattern, representing the lattice structure, is a Gyroid with a cell size of 3.25 mm (ρ_s = 0.35), covering an E_w range of 0.3 – 1.6 mm (Figure 32.a, where $E_{w,min}$ corresponds to the black color, and $E_{w,max}$ to the white color). Additional process parameters encompass a printing temperature of 215°C, an infill speed of 25 mm/s, three external perimeters, and the absence of both top and bottom layers. The finished printed object is depicted in Figure 4b, fabricated using white PLA material.
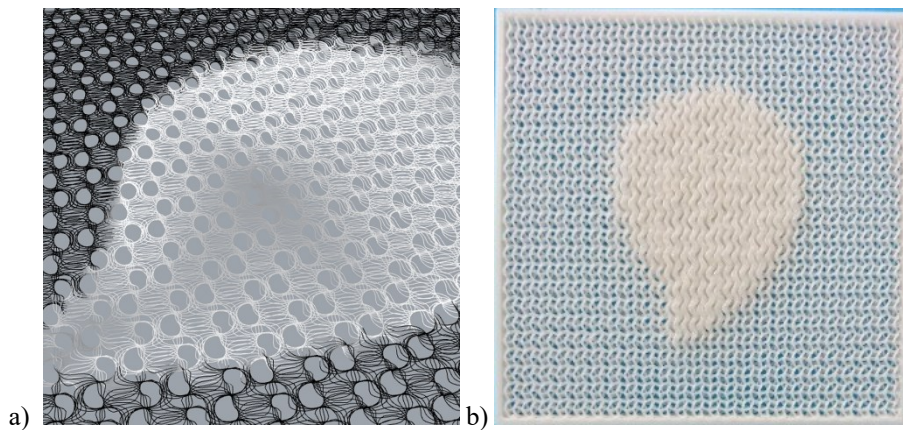

Figure 32. Main process phases visualization: a) particular of the infill pattern lines with extrusion width values visualized (Ew,min = black color, Ew,max = white color); b) printed component.

In this case multiple images are used to construct the volumetric model. The two images (Figure 33.a) used have different resolutions. The "drop" image of the previous example is 142x142 pixels, whereas the "symbol" image (known as "Triskelion") is 232x232 pixels. The sampling array is obtained using the lower resolution image, nX = 142, nY = 142. The bulk object is a box 80x80x2.4 mm. By using the resolution of the first image, the voxel size vS is 0.56 mm. nZ is consequently equal to 4. The grayscale values of the drop image are projected in the 4th layer of the array, while the Triskelion values are projected on the 2nd layer, while the remaining layers are filled with 0 values. The grayscale values are inverted from the previous example. The other parameters remain

unchanged from the previous case study. The printed object is shown in Figure 33.b,c in which it is possible to appreciate both images, one on the top side and the other one on the bottom.
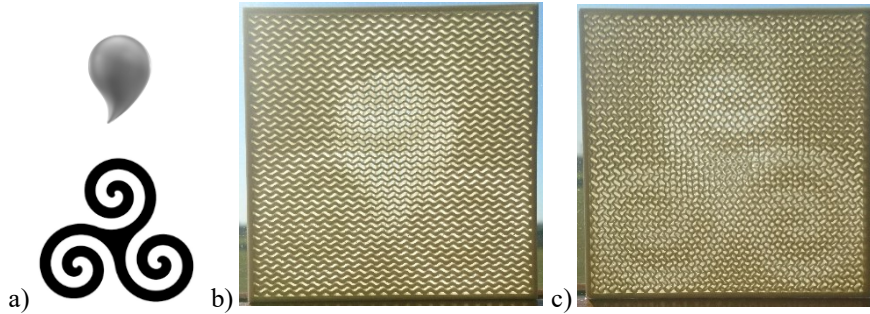

Figure 33 a) Images used in this case study; b) printed component top side and c) bottom side.

3.1.1.2.3.　　Case Study 2 – Topology Optimization

In this case study, the volumetric model is obtained from a topology optimization algorithm. The methodology is implemented in Rhinoceros 7 (McNeel & Associates, USA) and its plugin Grasshopper using existing addons and custom Python scripts.
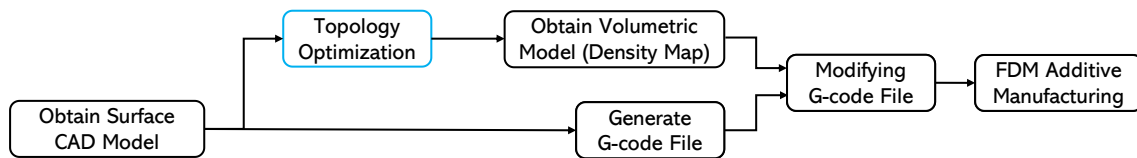

Figure 34 Modified workflow for topology optimization input for volumetric model.

A jet engine bracket is used as a case study to illustrate the proposed design and manufacturing method. The CAD model is the well-known jet engine bracket used by General Electric and GrabCAD during a 3D printing design challenge in 2013 [223], that was scaled to an overall size of 90x55x31 mm (Figure 35.a).

At first, the G-code file is generated by Slic3r. The Gyroid infill is chosen as the infill type, due to its low anisotropic behaviour [224], and to have a L_{cell}= 4 mm, the infill density is set to 28%. The other process parameters are summarized in Table 1.

The volumetric model results from a TO density map. In this work, Millipede [225], a Grasshopper addon based on SIMP and inspired to the Bendsøe and Sigmund's studies [226], was used for computing the TO. The penalization coefficient is set to 1 to obtain intermediate densities values. The mass minimization objective is set to 20%, using a

75

resolution of 30 (number of voxels along the X direction), 20 iterations, and a unitary smoothing factor. A static load of 1000N in the Z direction on the horizontal holes and fixed constraint on the four holes of the basement were applied (Figure 35.a). In Figure 35.b, the relative densities resulting from the TO are visualized by 3D grayscale cubes: light small cubes indicate lower density areas, and dark large cubes indicate higher density areas. Figure 35.c shows the component during the fabrication process, in which it is possible to see the different infill density.

The proposed approach automatically handles the cases where the layer perimeter is curved or inclined, indeed, the initial G-code is computed by standard slicer that provide a solution for this issue. When the G-code is edited, no modification in path is performed, but only the deposited material is varied to follow the desired density. As an example, Figure 35d show the tool path at curved and inclined surfaces.

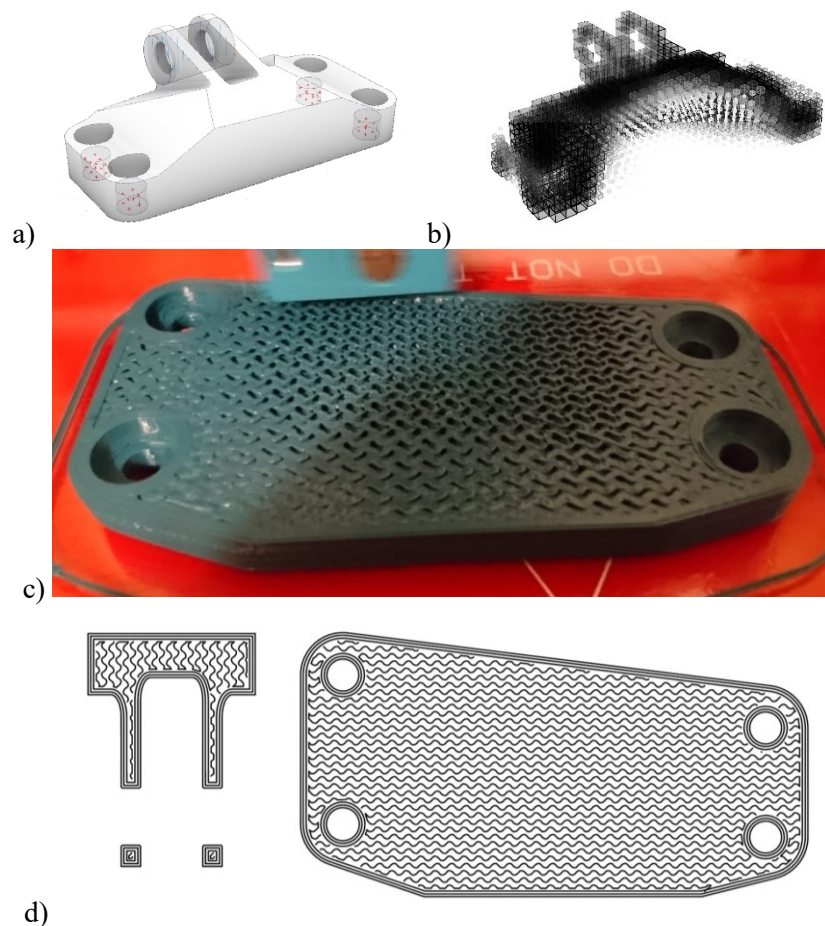a)   b)

c)

d)

Figure 35. The Jet Engine Bracket case study: a) shape and boundary conditions, b) 3D density map visualization, c) image of the fabrication process, d) toolpath closed to curved or inclined surfaces (Layer 155 and layer 11).

This example also explains that the method has a general implementation and can be adopted in any shape in which a graded density is needed. The generalization of the method to other functional requirements is limited only to the possibility to obtain a volumetric model. For instance, in biomedical field the grayscale of a medical image can be associated to density of the bone, as it is described in the following example.

3.1.1.2.4. Case Study 3 – Medical Imaging

In the case of bone diseases necessitating partial bone replacement, it is feasible to substitute cancellous bone with a graded density scaffold possessing comparable porosity to that of healthy bone. This study presents a case example addressing this issue, underscoring the adaptability of the proposed approach. Both the volumetric model, representing internal tissue density through grayscale images, and the surface model (B-Rep), derived from the V-Rep, are constructed using a CT scan. Figure 36 outlines the adjusted workflow. While the described workflow pertains to CT scans, it can be extended to various types of volumetric medical imaging diagnostics such as MRI, PET, fMRI, and echography. The methodology is implemented in Rhinoceros 7 (McNeel & Associates, USA) and its plugin Grasshopper using existing addons, such as Monolith, and custom Python scripts.
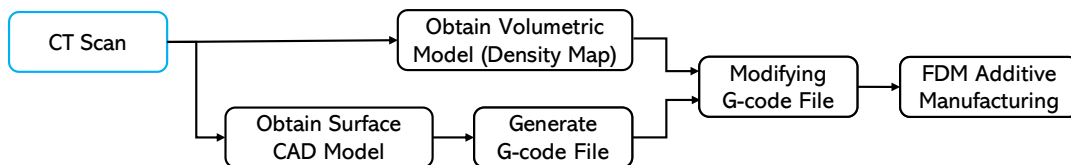

Figure 36. Modified workflow for CT scan input for volumetric model.

Prior to applying the method, some preparatory steps are required for file handling. CT scans, typically stored in .dicom or .nrrd format, can be accessed using a 3D medical imaging software viewer to assess the volume and voxel dimensions of the volumetric dataset. It's important to note that in CT scans, the voxel is often anisotropic in the Z-direction, implying that it is elongated in that axis due to factors associated with acquisition and machine operation [227]. CT scans comprise a series of 2D images, which are computationally reconstructed to obtain volumetric data. These images are represented in grayscale, denoting the density or attenuation values displayed in units known as Hounsfield units (HU). Technicians adjust the 'window level' (WL) and

'window width' (WW) to establish a diagnostically relevant grayscale, depending on the tissue under examination. The WL corresponds to the central Hounsfield value within the WW range. To emphasize specific tissues for easier segmentation, a lookup table can be employed to remap the existing grayscale to colors, or alternatively, WW and WL values can be adjusted accordingly [228].

A 3D grid is established based on the dimensions and spacing of the initial CT scan images. In the X direction, nX represents the width corresponding to the image resolution, while nY represents the height. The number of images determines the voxel count in the Z direction, denoted as nZ. The anisotropic voxel dimensions are defined by the image spacings, which involve the pixel size in the XY-plane and the pitch in Z. The pitch refers to the distance, in millimeters, that the table moves during a complete rotation of the X-ray tube, divided by the slice thickness. The grayscale values, ranging from 0 to 1, of each pixel are utilized to populate the property variable within the voxel structure.

The surface is created from the scalar values stored in the voxel structure using a polygonization algorithm, such as Marching Cubes (Appendix A.4), imposing a specific value (called isovalue) in the greyscale domain, which acts as a threshold for the surface determination (Figure 37). It is crucial to generate geometric model that includes only the desired bodies, then Boolean operations can be done to isolate the specific part of interest.
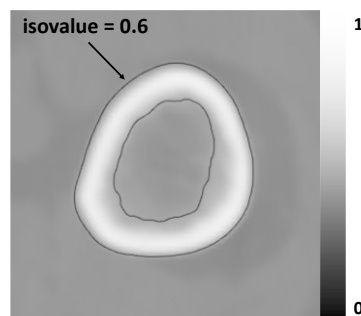

Figure 37. Isocurves visualization for the isovalue = 0.6 on top of the corresponding CT slice.

The CAM file preparation and modification remains the same of the standard method previously described.

Most of the time, the volumetric model and the G-code aren't mutually aligned in the 3D space. To transfer the attributes of the volumetric model to the CAM model, these two models need to be aligned in the 3D space. Adjustments need to be made because the G-

code toolpath is centered relative to the printer's bed, while the volumetric model is usually constructed starting at the reference system origin. This can be achieved by either moving the volumetric model or the CAM model. In this case, the individual points that describe the toolpath are moved rigidly to align with the volumetric model using a vector. As a first approximation $E_{w,min} = \varphi/2$ and $E_{w,max} = 3*\varphi$, where φ is the nozzle diameter, for a 0.2 mm layer thickness.

When the values are not optimal, like when a specific gradient is absent or the extrusion range from grayscale colours needs expansion, there are several adjustments that can be made. Possible approaches include applying filtering functions to refine the data or using functions to set minimum and maximum limits. These modifications can assist in fine-tuning the scaffold design to attain the desired properties and characteristics.

The methodology has been applied in the realization of a femur section replicating the relative density of the same bones. The algorithm is developed in Rhinoceros 7 (McNeel & Associates, USA) and Grasshopper using the original custom Iron Python script. Monolith, a Grasshopper add-on based on voxel data structure was used for geometric modeling and for computing the volumetric model and the isosurface respectively.

The dataset is a CT scan of the bones of a knee (Figure 38.a) [229], obtained from a free online community of medical 3D printable models. The properties of the CT scan have been examined using 3D Slicer 4.11 (Harvard University, NIH), a free and open-source software:

- Input File Format: .nrrd.
- Dimensions: 182, 197, 107 mm in XYZ
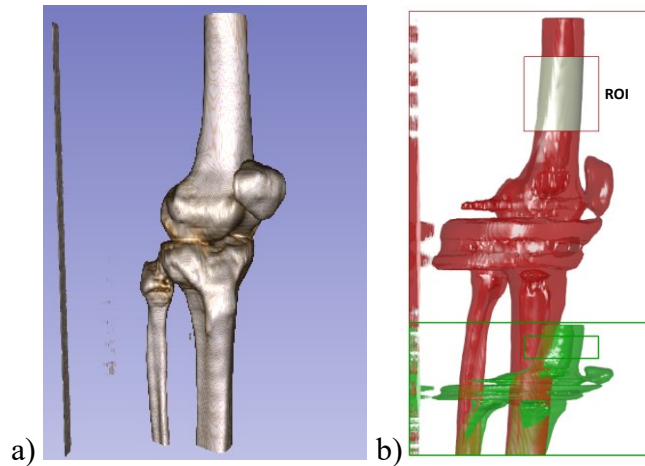- Voxel size: 0.976562, 0.976562, 3.269997 mm in XYZ

Figure 38. a) Volume Rendering of bones structures (in 3D Slicer), b) isosurface (mesh), in red the femur section reproduced.

In the CT scan WW = 2413 and WL = 206.5 are the preset values adopted (Figure 39.a). In this study a grayscale lookup table was used without changing the predefined values of WW e WL to maintain a certain gradient inside the bones structure. In addition, interpolation option is enabled (Figure 39.b).
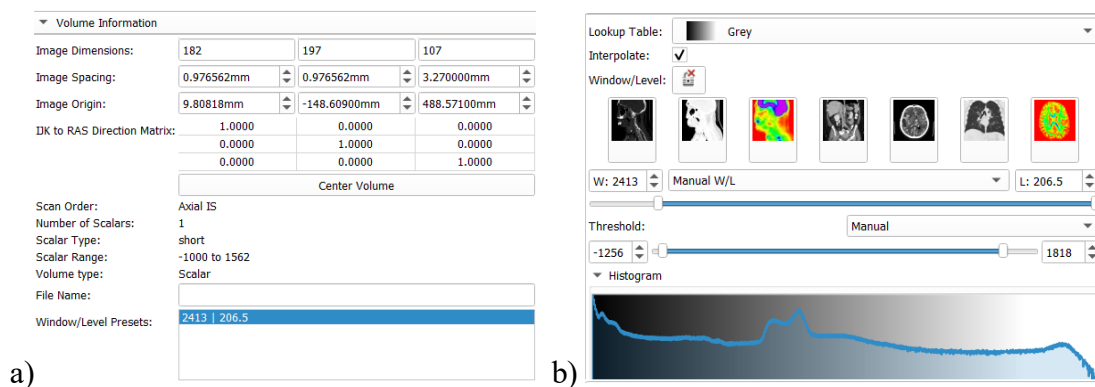

Figure 39. CT scan a) volumetric properties and b) look-up table in 3D slicer software.

The isosurface is created by marching cubes algorithm using an isovalue = 0.6, then scaling operations are used to obtain the correct dimensions in X, Y and Z direction, because it is not possible to work with anisotropic voxels in Monolith. The femur section geometric model is then achieved by a Boolean intersection operation between the entire surface model and a box, then the medullary canal cavity is closed. The mesh is then reconstructed using a quad remesh command to obtain a better mesh quality. The cropped section of the femur bone is highlighted in white (the ROI region) in Figure 38.b.
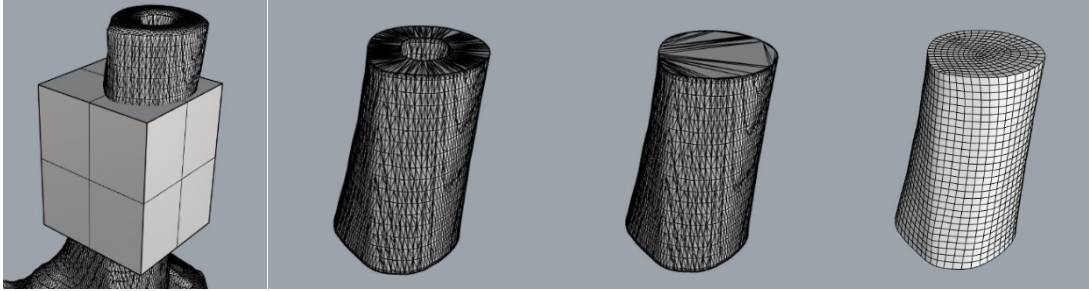
Figure 40 Successive operations to obtain the B-Rep of the femur section (ROI).

The G-code file for the printer is realized using Slic3r [216], visualized in Figure 41.c. Table 4 summaries the fundamental process parameters used. By using the graph in Figure 24 and knowing the maximum extrusion width that can be reached by the printer configuration, it is possible to choose the infill density value. The exact maximum extrusion width for the printer configuration is $E_{w,max}$ = 1.1 mm, obtained using the test described in section 3.1.1.1.6, then it is possible to obtain a fully dense gyroid cell with L_{cell} = 2.33 mm, and the infill density is ρ_s = 0.48 ~ 0.5. Minimum extrusion width (= 0.33 mm) describes the minimum relative density in the CT scan. The modification of the extrusion width only affects the infill pattern and not the perimeters.

Table 4. Process parametes adopted in the process.

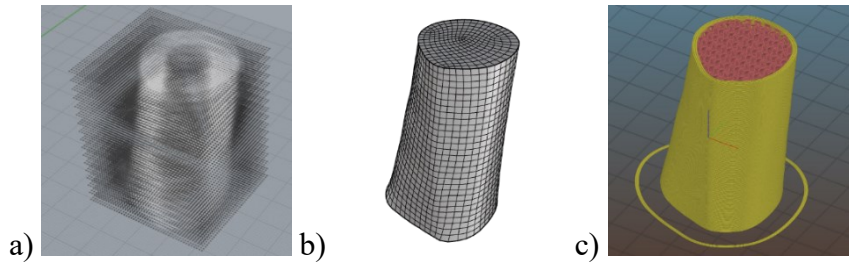| Process Parameter	
infill density	50%
infill type	Gyroid
infill speed	1500 mm/min
Extrusion width	0.4 mm
Layer thickness	0.2 mm
N. of perimeters	3
Bed temperature	55°C
Extrusion temperature	215°C
Filament diameter	1.75 mm

Figure 41. Visualization of the a) density map for the ROI region used to drive the extrusion parameter, b) Surface model, c) G-code,

Table 5. Property and domains used in the proposed method.

	Hounsfield Scale	Gray Scale	Relative Density	Extrusion Width [mm]
Domain	-2206.5 - 2619.5	0 - 1	0 - 1	0.15 – 1.10

A Creality CR-10 Smart Pro was used to manufacture the object in white PLA material (3DJake ecoPLA) (Figure 42.a, b). The printer is equipped with a Creality Sprite Pro extruder (direct-drive) using a 0.4 mm MK8 steel nozzle.
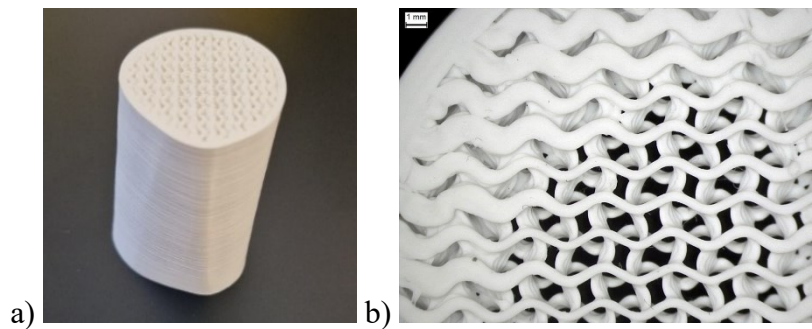
Figure 42. a) The printed graded component and b) the top view of the first 10 layers

3.1.2. Graded Size, Density and Topology Lattices by implicit TPMS functions

TPMS lattices structures are usually modeled using implicit functions [132,133,166]. By directly modifying the parameters in the functions it is possible to move the origin of the functions or to obtain different cell sizes and different deviations of the values. TPMS graded lattices can be achieved by using variable parameters instead of constant parameters in the function. A variable parameter is usually described by functions too. In this way it possible to obtain heterogeneities and, if the function used to describe the

parameter behaviour, is not discontinuous, graded structure can be achieved. In addition to cell size and deviation, multi morphology structures can be described by using a weighted sum of two or more TPMS functions [133]. Then it is possible to obtain the B-Rep (usually a surface mesh) by evaluating the $\phi(x,y,z)$ at a specific value C (called isovalue) using level-set method and polygonization algorithms. Level-set approach is commonly adopted for the TPMS surface construction. In this approach a level-set equation $\phi(x,y,z)$ is run through a polygonization algorithm, for instance a Marching Cubes algorithm. This procedure has been previously considered as an effective method to extract iso-surfaces in 3D data fields, and is a common tool used for implicit surface modelling or scalar fields polygonization. The marching cubes algorithm generates the surface by evaluating the implicit function in a cubic voxel data structure. The results are then used to create a triangular facet pattern depending on each voxel corners' values. Further details on this polygonization procedure can be consulted on Appendix A.4.

Albeit graded density TPMS based on implicit functions can be modeled by several software, they are limited to linear density gradients, or at least gradients described by trivariate functions, thus not being able to handle spatial density distributions from 3D data sources, such as CT scan. To extend the possibilities of such approach, a method has been developed to design and generate graded TPMS lattices with implicit function approach and 3D scalar fields, or volumetric map, by locally modify cell size, deviation function and topology.

3.1.2.1. *Method development and implementation*

By composing a function with a combination (weighted sum) of several parametrized TPMS functions, it is possible to locally modify the, the cell sizes, deviation functions (i.e. relative density) and the topologies by means of 3D scalar fields, accordingly to the design requirements. The TPMS lattice is described in purely mathematical terms by implicit function. Finally, the combined function (called Field Function) is evaluated, and the B-Rep can be extracted by means of marching cubes algorithm. Figure 43 shows the workflow of the method that is explained in the following paragraph.
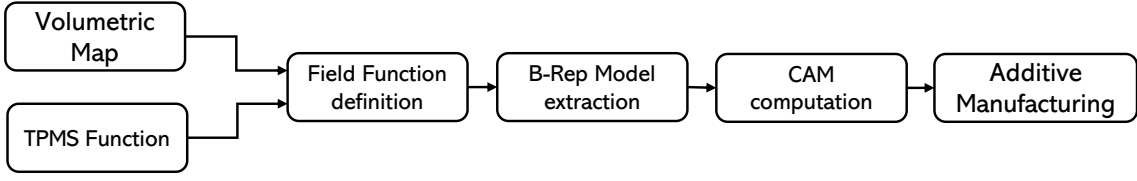
Figure 43. The workflow of the developed method based on implicit TPMS functions.

The method starts by choosing one or more TPMS implicit functions, such as:

$$g(x, y, z) = sin(x)cos(y) + sin(y)cos(z) + sin(z)cos(x) = 0 \qquad (22)$$

$$p(x, y, z) = cos(x) + cos(y) + cos(z) = 0 \qquad (23)$$

$$d(x, y, z) = sin(x)sin(y)sin(z) + sin(x)cos(y)cos(z) + cos(x)sin(y)cos(z) + cos(x)cos(y)sin(z) = 0 \qquad (24)$$

which represents respectively the Gyroid, the P-Surface and Diamond implicit functions. Figure 44 shows the unit cell of the three TPMS implicit functions.

a)   b)   c)
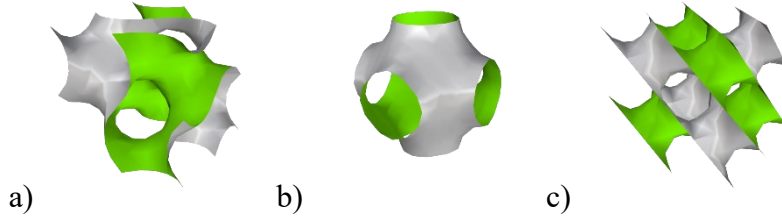
Figure 44. Visualization of the unit cell of a) Gyroid, b) P-Surface, and c) Diamond.

These TPMS functions are then modified by introducing two parameters: one to modify the unit cell size by changing the period of the trigonometric functions and the second to change the deviation of the function, so the values that the function assumes are shifted from the values of the unmodified function by a certain amount. When this deviation is defined as a spatial gradient, it permits control the relative density of the lattice once the B-Rep is extracted. The parametrized version of Gyroid, P-Surface and Diamond implicit functions become:

Gyroid: $F_1(x, y, z) = sin(k_1 x)cos(k_1 y) + sin(k_1 y)cos(k_1 z) + sin(k_1 z)cos(k_1 x) + h_1 = 0$ \qquad (25)

P-Surface: $F_2(x, y, z) = cos(k_2 x) + cos(k_2 y) + cos(k_2 z) + h_2 = 0$ \qquad (26)

Diamond: $F_3(x, y, z) = sin(k_3 x)sin(k_3 y)sin(k_3 z) + sin(k_3 x)cos(k_3 y)cos(k_3 z) + cos(k_3 x)sin(k_3 y)cos(k_3 z) + cos(k_3 x)cos(k_3 y)sin(k_3 z) + h_3 = 0$ (27)

where $k_i = k_i(x,y,z)$ is the parameter for cell size modification and $h_i = h_i(x,y,z)$ is the parameter for the deviation function. k_i and h_i can be eventually differentiated in the three Cartesian directions to generate anisotropic cells (for instance $k_{i,x}$, $k_{i,y}$, $k_{i,z}$).

All the parameters operate in a specific domain related to each TPMS function. Gyroid, P-Surface and Diamond functions have three different codomains, independent on the cell size (k): Gyroid [-1.5 - 1.5], P-Surface [-3 - 3] and Diamond [-1.42 - 1.42].

After the parametrization of each selected TPMS function, it is possible to combine several functions together in a specific order by a weighed sum obtaining a parametrized TPMS implicit function:

$$F(x, y, z) = \sum_{i=1}^{n} w_i * F_i(x, y, z) = 0$$ (28)

where $w_i = w_i(x,y,z)$ and it can be normalized in the range [0-1]. The weights can be determined using different approaches. The values of w_i are usually correlated, to obtain a gradient of multiple morphologies. In the case of the two functions F_1 and F_2 the TPMS implicit function becomes:

$F(x, y, z) = w_1 * F_1 + w_2 * F_2 = w_1(sin(k_1 x)cos(k_1 y) + sin(k_1 y)cos(k_1 z) + sin(k_1 z)cos(k_1 x) + h_1) + w_2(cos(k_2 x) + cos(k_2 y) + cos(k_2 z) + h_2) = 0$ (29)

Concurrently one or more volumetric maps, based on some functional requirements, are constructed or obtained from 3D scalar fields, such as a CT scan, or a function. The number of 3D scalar fields required depends on the number of parameters that the designer wants to modify spatially in the implicit function. If no volumetric map is used, it is possible to set a single value, but this operation results in a model without gradients. The values of the volumetric map are then interpolated into a structured 3D grid of points (evaluation grid), which is used for the evaluation of the implicit function. Interpolation method is developed as a Python Script reported in Appendix A.1. In case the volumetric map is sampled with an unstructured 3D grid (Figure 46.b), a radial basis function (RBF) interpolation method can be used and in Appendix A.1 is reported the Python script for the RBF interpolation, that have been used in those cases. For structured grids, the resolution of the evaluation grid is defined by the number of points in x, y and z direction

(nx, xy, nz) and the spacing between points (vS). The evaluation grid and the volumetric map must be aligned properly in the 3D space to perform the trilinear interpolation correctly. After this step, each grid point P(x,y,z) is associated with a specific set of values (interpolated) for the parameters (k, h, w). Each function is then evaluated for each point, giving a single value v_i as result. Finally, if the B-rep is needed, those values are used to fill a voxel data structure with the same resolution nx, ny, nz and spacing vS (voxel size) of the evaluation 3D grid. A surface mesh is extracted by means of a marching cubes algorithm using Monolith components in Grasshopper, a Rhinoceros 7 (McNeel & Associates) plugin.

3.1.2.2. Method validation and applications

Beneath the three parameters defined, the weights w_i needs more attention. To estimate w_i it is necessary to split the interpolated value in n values. There are various possibilities and functions that can be used to perform this operation. In this implementation, gaussian functions are used to smoothly mix the n functions. Each gaussian function is associated to a specific range of w domain, by shifting the function along the X-axis. Considering the TPMS implicit function for n = 3, (Gyroid, P-surface and Diamond in this order):

$$F(x, y, z) = w_1(sin(k_1 x)cos(k_1 y) + sin(k_1 y)cos(k_1 z) + sin(k_1 z)cos(k_1 x) + h_1) + w_2(cos(k_2 x) + cos(k_2 y) + cos(k_2 z) + h_2) + w_3(sin(k_3 x)sin(k_3 y)sin(k_3 z) + sin(k_3 x)cos(k_3 y)cos(k_3 z) + cos(k_3 x)sin(k_3 y)cos(k_3 z) + cos(k_3 x)cos(k_3 y)sin(k_3 z) + h_3) = 0 \qquad (30)$$

Three parametric gaussian functions are used for the definition of w_1, w_2, w_3. The general formula is:

$$g(x) = a * \exp\left(\frac{-(x-b)^2}{2c^2}\right) \qquad (31)$$

where the parameter a is the height of the curve's peak, b is the position of the center of the curve, and c controls the width of the "bell" (the standard deviation). Then the gaussian functions used are defined by:

$$g_1 = exp\left(\frac{-(x)^2}{2*0.15^2}\right), g_2 = exp\left(\frac{-(x-0.5)^2}{2*0.15^2}\right), g_3 = exp\left(\frac{-(x-1)^2}{2*0.15^2}\right) \qquad (32)$$
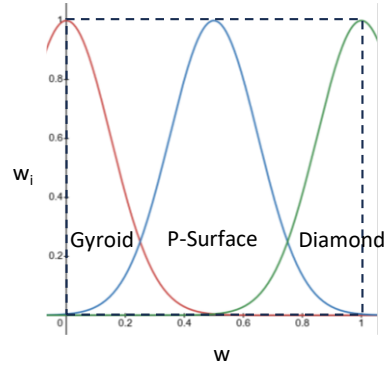
Figure 45 Visualization of the Gaussian functions and the evaluation domain.

where 0.15 is defined arbitrarily. The functinos are evaluated in the range [0-1] for X domain and Y codomain. When w is equal to 0, the weights of the field function become $w_1=1$, $w_2=0$, $w_3=0$ and the function associated with the first gaussian is active, for w = 0.5, $w_1=0$, $w_2=1$ and $w_3=0$, and the second function is activated, and for w = 1, $w_1=0$, $w_2=0$ and $w_3=1$, the third function become active. In all the other cases, a mixed topology with two functions is obtained. With the Gaussian functions defined previously it is possible to mix n-1 TPMS functions. Since the parametrized TPMS functions are written following an order, i.e., F_1 = Gyroid, F_2 = P-Surface and F_3 = Diamond, the "active" function is the Gyroid when w = 0, the P-surface when w = 0.5 and the Diamond when w = 1.

In the following several examples are presented, showing the capabilities of the method. The independent variation of k, h and w are showed. Figure 46.a shows the effect of a linear variation of k only for the P-surface (F_2), that means w = 0.5 so $w_2=1$. k_2 is defined as

$$k_2(x, y, z) = 0.02x + 0.02y + 0.02z \tag{33}$$

Then is substitute in equation 30. The implicit function is evaluated on a grid size nx = ny = nz = 21, spacing 0.1 mm. The surface is extracted using the same resolution. Figure 46.b shows the effect of a linear variation of h along x always for the P-surface (F_2). h_2 is defined as

$$h_2(x, y, z) = x. \tag{34}$$

The implicit function defined by equation 30 is evaluated on a grid size nx = 21, ny = nz = 11, spacing 0.1 mm. Differently from the previous result, the cell dimension doesn't change, L = 1 mm, but it changes the isosurface defined at the 0 value by the implicit function. This could be used to generate gradient in relative density. Finally, Figure 46.c shows the effect of a variation of w for the complete implicit function (equation 30). k_i are defined to obtain a unit cell size L = 1 mm, h_i are set equal to 0. w is defined as a linear variation in the range [0 – 1] to span all the three types of cells using the Gaussian functions previously defined. The implicit function is evaluated on a grid size nx =51, ny = nz = 21, spacing 0.1 mm. The surface is extracted using the same resolution. The resulting surface depicts how gradually the Gyroid cell, on the left side, smoothly turns into a P-Surface and then to Diamond cell. Since is a linear gradient, and the Gaussian are defined as in equations 32, the perfect cell type is never present in the final model. One solution could be changing the smoothing functions, using for instance piece-wise functions made up of trigonometric or sigmoid functions, or using blending functions such as Bezier functions.

a)   b)

c)
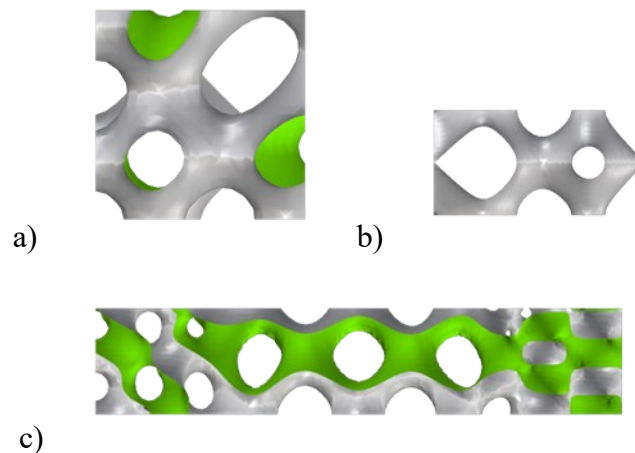
Figure 46. Side view of the surfaces obtained varying k,h and w a) cell size k gradient for the P-Surface, nx = ny = nz = 41. b) deviation function h gradient (Relative density) for the P-surface, nx = 41, ny = nz =21. c) Morphology gradient (order Gyroid, P-Surface, Diamond), nx = 101, ny = nz =21.

The method can be applied to generate a multiple gradients TPMS structure with a thickness. In the lattice structure in Figure 47, two TPMS cell are used (P-Surface and Gyroid). A linear gradient in X direction control the topology (w_i) between P-surface and the Gyroid. Cell sizes is also controlled by the same linear gradient but remapped for

different codomains: Gyroid k_1 = [0.10-0.06] mm, P-Surface k_2 = [0.12-0.08] mm. It is possible to observe how the cell sizes for both P-Surface and Gyroid decreases from left to right, and similarly the topology smoothly turns from a complete P-Surface to Gyroid structure. Furthermore, the same approach, if extended to R^4 space, can be used to explicitly model scalar fields, based on TPMS functions. These scalar fields can be useful for the definition of material ratios in a component or to drive other volumetric properties.
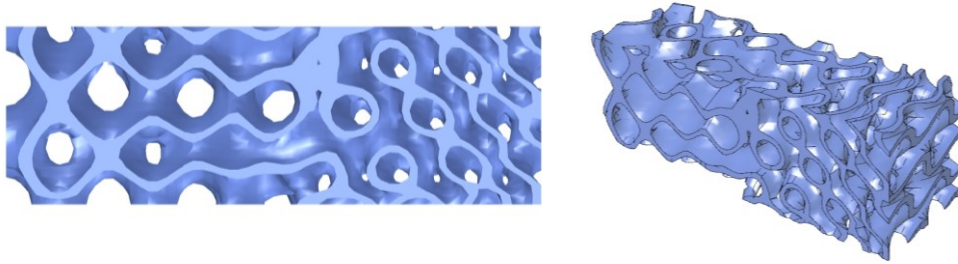

Figure 47. Isosurfaces, front and perspective view (isovalue range [0- -0.62]).

3.1.3. Graded Density TPMS Lattices by subdivision surface offset

There are different geometric modeling approaches for TPMS as already discussed in previous sections. The main bottlenecks are related to the significant computational resources required (e.g. in offsets, blends, Boolean operations), scalability, processing time, model coherence and robustness (elements overlapping issues and consequent Boolean operation failure), rendering and visualization troubles due to the huge number of polygons, filleting, file exchange, adaptability and automation.

In this work, a method, implementable in a CAD environment, for geometric modeling TPMSs is proposed, aimed at reducing the computational time and increasing the shape complexity in geometric modeling, data exchange and visualization, compared to standard CAD software tools. This method is based on the work by Savio [122], was improved to accept various type of volumetric model to drive the thickness of the mesh in the thickness assignment step. Furthermore, it will be used in the method comparison section (3.1.5).

After the definition of a simple initial mesh representing a unit cell, on which a subdivision surface algorithm is applied, a differential offset is computed to obtain the desired relative density. Adopting the proposed method, gradient density minimal surface could be easily obtained, which could be useful in the design of biomimetic scaffolds

having a planned relative density point by point. Likewise, relative density computed by topology optimization could be adopted in the proposed design procedure.

The proposed approach allows enhancing automation and shape complexity of CAD tools compared to other mesh and NURBS approaches for modeling shell-like periodic surfaces, obtaining consistent polygon meshes. These opportunities will increase the potential of the proposed approach, reducing computational time and, with minor modifications of file format, the file size.

3.1.3.1.   Method development and implementation

The main steps of the proposed geometric modeling procedure include (Figure):

- the design of a simple initial mesh representing the unit cell which can be for instance a simplified representation of a triply periodic minimal surface (TPMS),
- scaling and repeating side by side a regular unit cell, to fill the design space,
- possibly deforming the model obtaining a pseudorandom structure shape, consisting of a conformal or in a warped mesh,
- using subdivision surface algorithms to achieve a smooth geometric model,
- assigning thickness to the mesh adopting a differential offset algorithm, aimed at obtaining point by point thickness and density satisfying functional requirements,
- optionally cropping the geometric model to the desired shape.

The proposed timeline is not mandatory, for instance, the step order "subdivision, warping and thickening" can be modified depending on specific requirements: to simplify the computation, warping, and thickening could be done before the subdivision.

In this study, a TPMS Gyroid is considered. The unit cells were obtained rotating and/or mirroring an elementary portion made up of six faces and 13 vertices matching the Gyroid and equations: $\sin 2x \cos 2y + \sin 2y \cos 2z + \sin 2z \cos 2x = 0$. Figure 48 summarizes the vertex coordinates, the shape of the elementary portion, the initial mesh representing the unit cell and the mesh resulting after two iterations of the Catmull–Clark subdivision scheme [230]. In the same way, other subdivision algorithms can be adopted. The Catmull–Clark subdivision surface is an algorithm for recursively generating smooth surfaces, widely used in computer graphics, which approximates points preferably lying on a quadrilateral mesh. According to the initial mesh vertices, iteratively averaging their

coordinates, new vertices are computed following a subdivision rule, splitting each quad into four faces. Considering functional and manufacturing constraints, a cell dimension is defined.
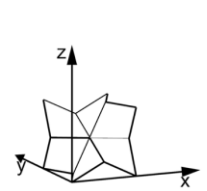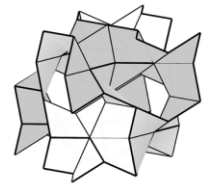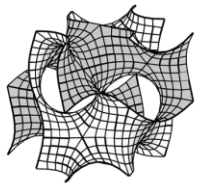
Minimal surface	Vertex coordinates	Elementary portion	Unit cell	Subdivided cell
Gyroid	P1=(0,0,0) P2=(0.5,0,0) P3=(0.125,0.250,0) P4=(0,0.5,0) P5=(0.25,0,0.125) P6=(0.5,0.125,0.25) P7=(0.25,0.25,0.25) P8=(0,0.375,0.25) P9=(0.25,0.5,0.375) P10=(0.5,0,0.5) P11=(0.375,0.25,0.5) P12=(0,0.5,0.5) P13=(0.5,0.5,0.5)			

Figure 48. Modeling minimal surfaces by subdivision schemes.

Then, the unit cell is scaled to fit the desired dimension and repeated along the x, y, and z-axes until the design space is filled. All the built cells are joined in a single-mesh model, removing the duplicate vertices. If necessary, using standard CAD tools it is possible to warp or bend the mesh and subdivide the model. Afterward, a thickness at each mesh vertex is assigned, which value can be computed by varying linearly along a direction, by other equations as a function of the vertex coordinates, or adopting values derived from functional requirements, such as fluid dynamics, thermal, biomimetic or structural studies. Volumetric models are used to drive the thickness values in this improved version of the method. To assign the values of thickness at each vertex of the mesh model, a trilinear interpolation of the density and the relation between the thickness and relative density are adopted.

The relative density (ρ) values obtained at various normalized thickness levels (defined as the ratio of thickness 't' to cell dimension 'L') for both P-Surface and Gyroid structures are presented in Figure 49. The results are accurately fitted by a quadratic function. Notably, at equivalent levels of normalized thickness, the Gyroid exhibits a higher density compared to the P-Surface. This disparity arises from the greater surface area of the Gyroid (specifically, the P-Surface area measures 2.35 mm², whereas the Gyroid area spans 3.10 mm² for a 1 mm cell side). It's crucial to recognize that when scaling a model, the area expands proportionally to the square of the scale factor, while the volume augments in relation to the third power of the scale factor.
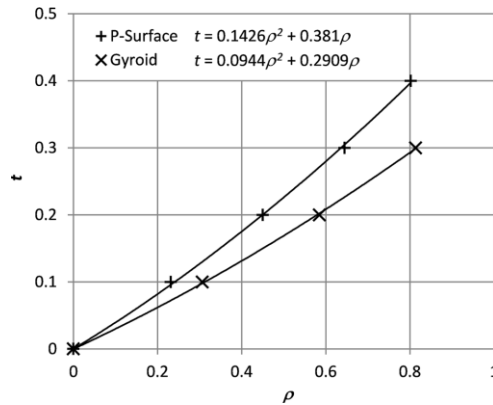
Figure 49. Relation between relative thickness t and relative density ρ.

The desired thickness is obtained implementing a differential offset (Figure 50): the process begins with the computation of the mesh normal at every vertex. Subsequently, two fresh meshes are created, maintaining the same data structure as the original mesh. In this step, each vertex is displaced along the normal, one by half of the thickness in a positive direction and the other by half the thickness in a negative direction. At the boundaries, where corresponding edges of the two new meshes meet, a new mesh face is constructed. This procedure results in the generation of a watertight model, a crucial prerequisite for a geometric model in AM.
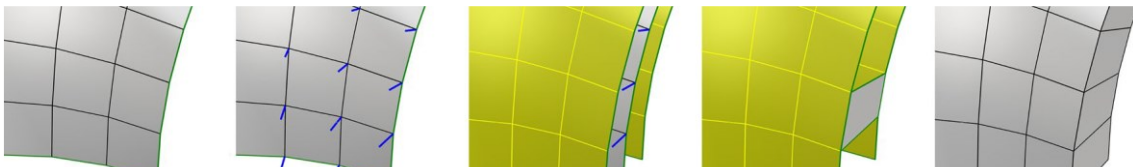
Figure 50 The proposed offset approach.

3.1.3.2. *Method validation and applications*

Figure 51 shows a simple example of gradient thickness Gyroid (cell side 40 mm, design space 120 × 120 × 120 mm3, thickness ranging between 2 and 6 mm), obtained adopting three iterations of the Catmull–Clark subdivision surface scheme and cropped along the diagonal, fabricated using BJ AM technologies (ZPrinter® 450, 3D System, USA).
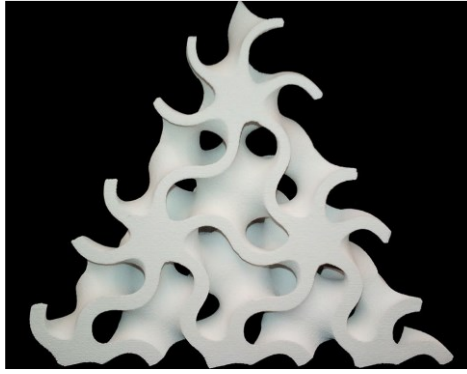
Figure 51. Diagonal section of gradient thickness Gyroid.

Furthermore, the method has been applied in the realization of a graded density TPMS lattice from the CT-Scan file reported in Section 3.1.1.2.4, for the same portion of the femur bone. The offset gradient of the lattice is derived from the measured density in CT-Scan, similarly to the previous case study. The B-Rep of the bone is the same obtained previously and it is used to crop the exact shape of the bone out of the lattice structure using Boolean operations. A Gyroid unit cell with a cell size = 5 mm is used. The voxel data structure for the interpolation is constructed in the same way described in Section 3.1.1.2.4. The density values were remapped and limited to 0.7 vol %, this means no fully dense structure are achieved; minimum thickness was set at 0.25 mm, related to manufacturing constraints. Two levels of Catmull-Clark subdivision algorithm were adopted. In this case, there is no need to correct the alignment of the B-Rep with the density map, because they are in the same position. The resulting graded lattice structure model is showed in Figure 52.

Figure 52. Femur Bone section with Graded Density Lattice Structure (Gyroid) driven by CT-Scan data.

3.1.4. Graded Density Lattices by distance fields

Another method to design and model graded lattice structures is proposed in the following. The method exploits the advantages of volumetric approaches to extend the possibility to generate graded and not graded structures. As a key step a distance field, build upon B-Rep geometric entities, is used to define a continuous volumetric model, then evaluated on a voxel grid to generate the B-Rep. The distance field is defined over B-Rep entities, s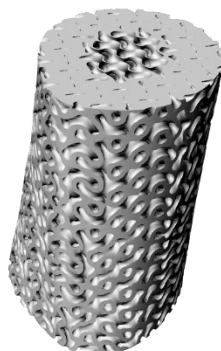uch as points, lines/curves and surfaces. The B-Rep geometric entities belong to a basic lattice structure model, i.e., a sort of skeletal geometric model without any thickness. In the case of beam-based lattices the basic lattice structure model represents a wireframe model, i.e., a model made up of lines or curves, and in the case of shell-based lattices, like TPMS, is a surface mesh model. Points can be extracted from the basic lattice structure model and used for the definition of the distance field in both cases. The contemporary use of both B-Rep and V-Rep approaches simplify the definition of the lattice structure shape, cause geometric entities are easy manageable and the distance-based volumetric model improves the realization of complex density gradients. A similar approach is used by nTopology software, which adopts implicit functions and fields to model shapes. The proposed method differs from this last one because it is more flexible in terms of sources to describe the gradient, accepts B-Rep geometric entities and the isosurface mesh extraction is more efficient due to the voxel data structure used. In addition, it overtakes some limitations of lattice structures based on mesh modeling approaches, referred to the errors in the vertices alignment for coherent and watertight geometries and self-intersections for high density lattice structures.

3.1.4.1. Method development and implementation

The method is generally valid for every type of structure, but it is described for the realization of graded lattice structures. The workflow of the method is depicted in Figure 53.
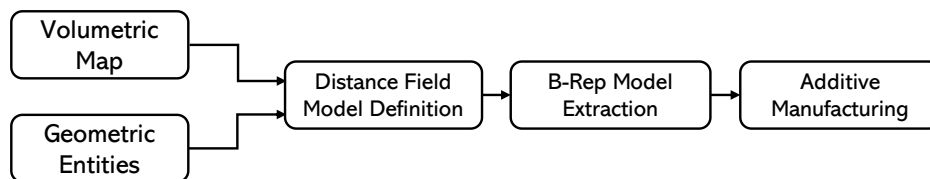

Figure 53. Workflow of the proposed method based on distance fields

A volumetric model is imported or constructed, involving some functional requirements. Several type of sources can be used, such as functions, CT scans etc. as already mentioned. The volumetric map values, for instance relative densities (ρ) in the range [0-1], are then remapped into distances (r) using a suitable function (Figure 54). This distance values r_i constitute a distance map, and they are used to drive the local thicknesses used in the definition of the lattice structure. Given that the distance function is defined in the [0 - $+\infty$] range, it is necessary to confine it within a specified domain [r_{min} - r_{max}], representing the minimum and maximum values. Distances are quantified in the same unit of measure specified in the CAD environment, typically expressed in millimeters (mm). Furthermore, it is possible to impose constraints on the maximum and minimum relative density, rather than on the distance.
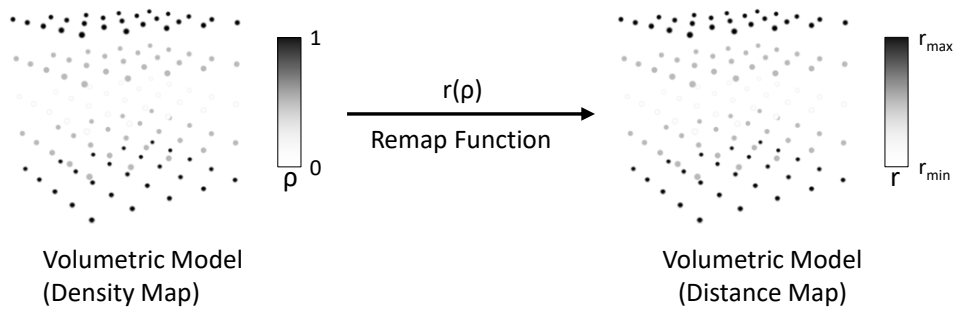
Figure 54. Density-Distance remap.

Volumetric model data can be various, but usually they are often defined in terms of relative density. The relative density drives the thickness of the lattice structure. Regression method can be adopted to estimate the function $r(\rho)$ which establishes the mapping between density (ρ) and distance (r), or equivalently, thickness (t ~ 2r). This is accomplished by assessing the relative density (ρ) obtained at different distances (r) for a specific unit cell type and size. To decouple the distance (r) from the cell size dimension, it can be normalized in relation to the cell size (L), yielding $r/L(\rho)$. In Figure 55.a are showed the trends for two beam-based unit cells, with a cubic polynomial regression function: BCC and Octet-truss. It is possible to see that at the same level of r/L, Octet is denser than BCC cell, due to the higher number of beams. The same can be done for shell-based lattices, like TPMS. Figure 55.b shows the quadratic polynomial regression functions for three type of shell-based TPMS: Gyroid, P-Surface and Diamond.
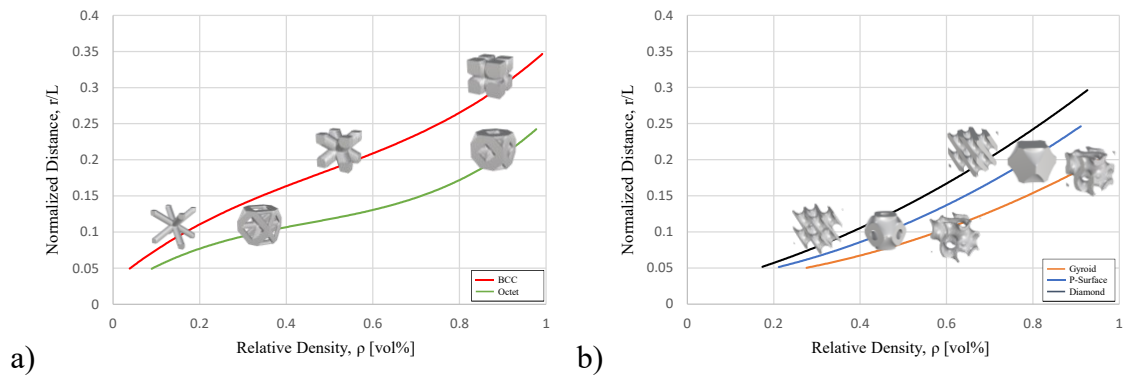
Figure 55 Normalized Distance/Relative density functions for: a) BCC and Octet unit cell, b) Gyroid, P-Surface and Diamond TPMS unit cells.

In parallel, geometric entities are defined. In the context of lattice structures, there are two distinct methods of definition dependent on the cell type. For beam-based lattices, the elemental structure of the unit cell is represented using lines or curves, which serve as the geometric entities. Conversely, shell-based lattices employ surfaces. Subsequent to establishing the unit cell type (and size 'L'), the relevant geometric entities are extracted to accommodate the designer's specifications. Points can be derived in both scenarios: when working with lines/curves, the geometry can be subdivided to yield smaller segments, from which the endpoints of each section are obtained. Regarding parametric surfaces, points can be constructed directly on the surface. In the case of discrete surfaces, the mesh vertices are employed (Figure 56.a).

a) B-Rep Geometry

b) Extracted Geometric Entities (Points)

c) Distance Field Model

d) Distance Field Evaluation

Figure 56. Method esemplification for a 2D case. a) A B-Rep geometry is modeled (mesh face), b) the geometric entities are extracted (mesh vertices=points) and the distance fields for each entity is modeled; c) the distance fields are merged to obtain the complete distance field that can is then d) evaluated at the corresponding distance r_i for each entity. In this case $r_i = cost = 1$.

96

The chosen geometric entities, belonging to the unit cell, are repeated in the Cartesian space along X-, Y- and Z-axis nx, ny, nz times (with spacing = L) to construct the overall lattice. It is also possible to firstly repeat the unit cell in the space and then extract the geometric entities. Then geometric entities of the overall lattice are used to generate the distance field. The distance field is a combination of multiple distance fields, one for each geometric entity; so, if three geometric entities are used, then three distance fields are constructed and merged using smooth Boolean operators (Figure 56.c). Each distance field is defined by the Euclidean distance equation:
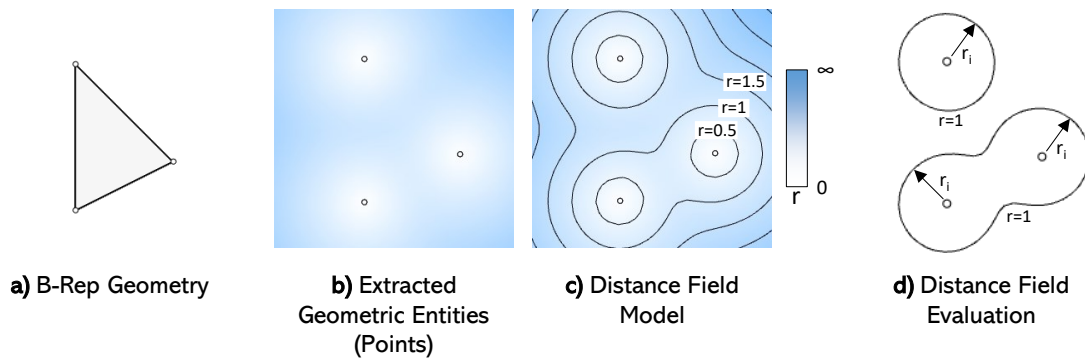
$$r\,(x, y, z) = (x^2 + y^2 + z^2)^{\frac{1}{2}} \tag{35}$$

The distance field is subsequently assessed through a voxel data structure characterized by a designated voxel size (vS). This data structure enables the extraction of the lattice's isosurface using a polygonization algorithm, with the distances r_i serving as isovalues. This operation yields a surface mesh. The lattice configuration generated possesses a distinct thickness at each specified geometric entity. In Figure 56.d, this procedure is depicted in a 2D context, where the outcome is not a mesh, but rather a curve (isocurve).

The method is implemented in Rhinoceros 7 (Robert McNeel & Associates, USA) and its plugin Grasshopper. Dendro add-on [158] is used to define and evaluate the distance field on a Sparse Voxel Octree data structure (Appendix A - Dendro).

3.1.4.2. Method validation and applications

The definition of the r domain [r_{min} - r_{max}] is related to computational and AM process observations. For instance, r_{min} must be > 0, and the minimum value is constrained by the voxel size used for the evaluation of the field, which is limited by the computational power. On the other hand, r_{min} must take into account technological limits of the specific AM process, such as the resolution of the printer and the minimum escape holes dimension necessary to evacuate powder or resin from the model. Maximum thickness r_{max} as no limitations if the B-Rep model is then cropped.

The method is applied in the realization of a graded density Diamond TPMS using points as geometric entities, because of their flexibility. B-Rep model of the unit cell is obtained using Axolotl [162,231], see Appendix A. The Diamond TPMS is defined by the function:

$$cos(x * 2\pi/L)cos(y * 2\pi/L)cos(z * 2\pi/L) - sin(x * 2\pi/L)sin(y * 2\pi/L)sin(z * 2\pi/L) = 0, \qquad (36)$$

with a unit cell size L = 3 mm. The function is evaluated in using a voxel data structure and the surface mesh of the unit cell is obtained with a marching cubes algorithm. A resolution of 20 voxel for axis is used, since is a good compromise between accuracy and computational efforts. The resolution of the voxel grid influences the mesh surface quality and the number of faces/vertices, thus the number of entities that can be extracted; more entities (less distance between entities), better distance fields and better final mesh. Generally, the selection of a correct initial B-Rep model, associated to the voxel size for the distance field evaluation, is crucial for the final mesh result. Two issues are possible (Figure 57.b,c): final result with disjoint mesh, or low surface mesh quality. The first one is related to the incorrect choice of the distance between the geometric entities and the voxel size. The second one to the excessive dimension of the voxel size. As first approximation, the minimum radius (half of the thickness) must be at least 2 times the average distance between entities to have a coherent and accurate surface mesh. In the case showed in Figure 57, the vertices of the mesh has an average distance equal to 0.214 mm, obtained from the edges length, while the radius used in Figure 57.a is 0.05 mm with a voxel size for the evaluation voxel data structure equal to 0.015 mm. To obtain a joint mesh the solution is to decrease the distances between entities by increasing the number of faces/vertices of the initial surface mesh. On the other hand, Figure 57.b highlights the second issues. The radius is increase to 0.450 mm to match the average distance, and the voxel size is increased to half of the radius value. The result is a low-quality surface mesh that didn't match to the expected result.
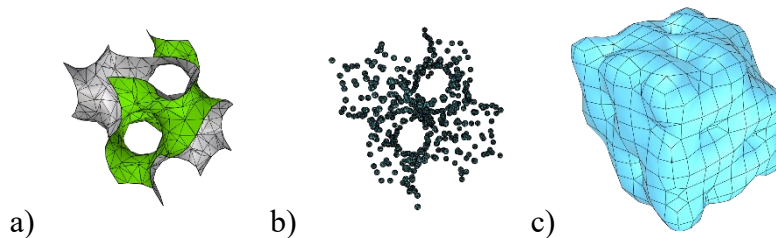

a)   b)   c)

Figure 57 a) Initial B-Rep, TPMS Surface Mesh, b) Disjoint mesh c) Low mesh quality.

Anyway, is not possible to increase the number of entities and to reduce the voxel size excessively, due to computational limits. In addition, when generating gradients with low

relative densities, the number of entities must be increased, and the voxel size must be decreased (at least 2 times smaller than the minimum radius) to effectively evaluate distances and to obtain a consistent mesh. A trade-off must be found between the number of entities and voxel size. Finally, it is possible to mitigate both the errors (and avoid excessive computational efforts) by applying volumetric filters on the volumetric fields to smooth the data and obtain a better isosurface, or smooth the isosurface mesh, but in these cases the designed thicknesses or relative densities must be verified lately. Appendix A - Dendro elucidates the Point Cloud to Volume component used for this implementation.

The vertices are extracted from the unit cell and repeated in the 3D space 3 times in each direction (nx=ny=nz) to obtain the lattice structure made up of geometric entities. The volumetric model is a 3D grid of points, and the density map is described by the gradient visualized in Figure 54. These values are trilinearly interpolated at the vertices locations. A 4th-grade polynomial is used to calculate the normalized values r/L as a function of ρ. The function for the TPMS Diamond is:

$$r/L(\rho) = 0.7245\rho^4 - 1.1722\rho^3 + 0.6977\rho^2 + 0.1004\rho + 0.0136 \qquad (37)$$

The resulting values of r/L are in the range 0.041 - 1.092 and are then remapped to 0.205-0.971 to satisfy computational limits for the lower value and a predefined maximum relative density of 95%. The distance field is then costructed by the vertices using Dendro PointsToVolume command. The isosurface, locally defined by the r/L values, is extracted using a dual contouring algorithm (Appendix A.4) on the sparse voxel octree data structure of Dendro (CreateSetting command) with a voxel size of 0.10 mm. Figure 50 shows the final isosurface mesh and the cropped version, using a cube of 30x30x30 mm.

a)   b)
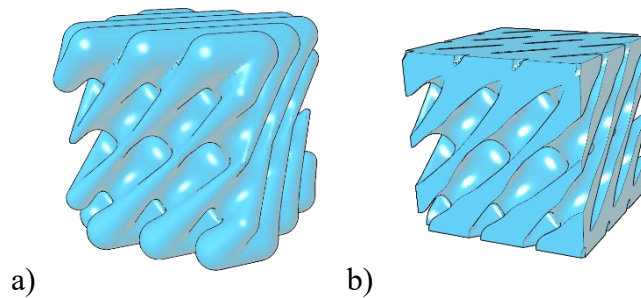
Figure 58 Graded Density Lattice Stucture. a) Final Mesh model, b) Cropped model.

Moreover, a lattice based on Gyroid TPMS surface was used to create a graded density lattice from the CT-Scan data detailed in Section 3.1.1.2.4, covering the same segment of the femur bone. The gradient is determined by the measured density from the CT-Scan data. The B-Rep of the bone segment remains consistent with the one obtained earlier and is employed to precisely extract the bone's shape from the lattice structure through Boolean operations. Volumetric Boolean operations are performed for lower computation time with respect to Boolean operation on mesh. A Gyroid unit cell with a cell size = 5 mm is used. The voxel data structure for the interpolation is constructed in the same way described in Section 3.1.1.2.4. Voxel size for surface mesh was set a 0.02 mm. The interpolated density values are remapped to r values in the range [0.3-1.2] mm. There is no need to correct the alignment of the B-Rep with the density map because they are in the same position. The resulting graded lattice structure model is showed in Figure 59.

Figure 59. Femur bone section with graded density lattice structure (Gyroid) driven by CT-Scan data.

In addition, the methodology developed is employed to design and mechanically test two different type of unit cells with relative density gradients, to mimic the porosity of bone structures. Compression and Flexure specimens were prepared using Diamon beam-based and Diamond TPMS (shell-based) and manufactured using SLA AM technology. This work aims a proposing a possible general approach for modeling advanced graded structures and evaluate them on the basis of tensile, compression and bending tests mimicking all the possible situations a bone scaffold can undergo when applied in situ.

3.1.4.2.1. Modeling

The modeling method adopted is the one described in Section 3.1.4. Two different cells, Diamond beam-based and Diamond TPMS (shell-based), showed in Figure 60, are used as the initial B-rep. A unit cell size of L = 3 mm is used for both cells.

For the Diamond beam-based initial shape, as it modeled manually by lines, points are generated subdividing each line in 30 segments and considering the endpoints of each segment. For the Diamond TPMS, the unit cell is extracted performing a marching cube algorithm on a voxel data structure. The Diamond TPMS is defined as

$$D(x, y, x) = sin(x)sin(y)sin(z) + sin(x)cos(y)cos(z) + cos(x)sin(y)cos(z) + cos(x)cos(y)sin(z) = 0. \tag{38}$$

The voxel grid as a resolution of 20 within a cubic volume of 3 mm. Vertices of the isosurface mesh are considered the geometric entities for the following steps. The geometric entities are then repeated in the Cartesian space for both cells.
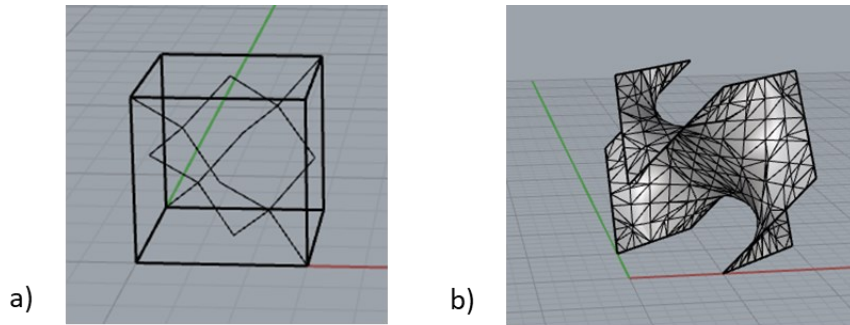
Figure 60. a) Diamond (beam-based) unit cell and Diamond TPMS (shell-based) unit cell.

To mimic the porosity of the bone, a radial gradient on porosity is designed for the compressive specimens using the following function:

$$Gr_{radial} = \rho min + ((\rho max - \rho min)/r) * ((x^2 + y^2)^{0.5}) \tag{39}$$

where ρmin and ρmax are the relative densities limits and r represent the distance from the center. While for the bending specimen the following linear function is used to describe a gradient symmetric respect to the XY-plane:

$$Gr_{lsymm} = \rho min + ((\rho max - \rho min)/\Delta z) * |z| \tag{40}$$

101

where ρmin and ρmax are the relative densities limits and Δz represents the difference between the maximum and minimum z values, so the spreading of the gradient in z direction.

Then in order to relate the relative density distributions to the r/L parameter for the two cells, two different regression functions are used:

$$Diamond: r/L = -0.1822 \, \rho_r^4 + 0.7337 \, \rho_r^3 - 0.8011 \, \rho_r^2 + 0.5706 \, \rho_r + 0.0208 \quad (41)$$

$$TPMS \, Diamond: r/L = 0.7245 \, \rho_r^4 + 00.6977 \, \rho_r^3 - 0,1004 \, \rho_r^2 + 0,5706 \, \rho_r + 0,0136$$
$$(42)$$

For the generation of the isosurface from the distance field (dual contouring algorithm), a voxel size of 0.1 mm was used for all the models. The graded lattice structures were modeled and finally trimmed for the specific specimen dimensions. The domains for the relative density were set to [0.15 – 0.95] vol% (average = 0.55 vol%) for the Diamond beam-based and [0.25 – 0.95] vol% (average = 0.6 vol%) for the TPMS Diamond. The higher value for lower limit of the TPMS Diamond is due to computational limitations, i.e., higher resolution of the initial grid is needed if maintaining constant the voxel size (0.1 mm) for the isosurface extraction. The radii domain for the two lattices is in the range [0.27-0.96] mm for the Diamond and [0.20-0.97] mm for the TPMS Diamond. The models differ in terms of volume, due to the differences in relative densities (Table 6).

Table 6. Specimen models (mesh) properties.

Specimen Models	Mesh Faces	Volume (mm³)
Diamond Compression	1910846	3638.07
TPMS Diamond Compression	632146	3842.57
Diamond Flexure	2419130	5960.30
TPMS Diamond Flexure	1414679	6739.08

3.1.4.2.2. Mechanical Properties

White Resin (Formlabs, USA) is chosen as material for manufacturing the samples. It is not biocompatible. From a mechanical perspective, data sheets show that post-cured White Resin has an ultimate tensile stress (UTS) of 65 MPa, elastic modulus E = 2.8 GPa and presents lower deformation. Flexural Modulus is 2.2 GPa, see Appendix C. In order

to assess the mechanical properties of the printed material, tensile tests were conducted on dog bone specimens. The ISO 527 standard [232] was employed for these tensile tests, using type 1BA specimens. The density of the material is 1.15 - 1.20 g/cm^3 after curing [233]. The porosity of the lattice is estimated in the printed samples from the geometric density using 1.15 g/cm^3 for the material density.

In addition to the material characterization tests, compression and flexural tests were performed to evaluate the designed graded lattice structures. Compression tests followed the ASTM D695 standard [65], utilizing type B specimens that were cylindrical with a height-to-diameter ratio of 2:1. The overall dimension of the cylindrical specimen are showed in Figure 61. The cross-head speed was set at 1 mm/min. The compression stresses were calculated as the ratio between the load and the initial circular cross-sectional area measured for each printed specimen, including the designed pores (nominal area $A_{c,nom}$ = 176.7 mm^2). The gradient in this case is radial, while longitudinal gradients will be considered in subsequent studies to examine local deformations.For flexural testing (3-pt bending), the ISO 178 standard [66] was employed. The samples dimensions are depicted in Figure c Length span used for the test, L = 96 mm and 2 mm/min has cross-head speed. The flexural stresses were calculated as the ratio between the load and the initial rectangular midspan cross-sectional area measured for each printed specimen, including the designed graded porosity (nominal area $A_{f,nom}$ = 90 mm^2). All the tests were performed using an MTS Acumen 3 Electrodynamic Test System (MTS Systems Corporation, USA).

Specimens shape and dimensions are depicted in Figure 61.
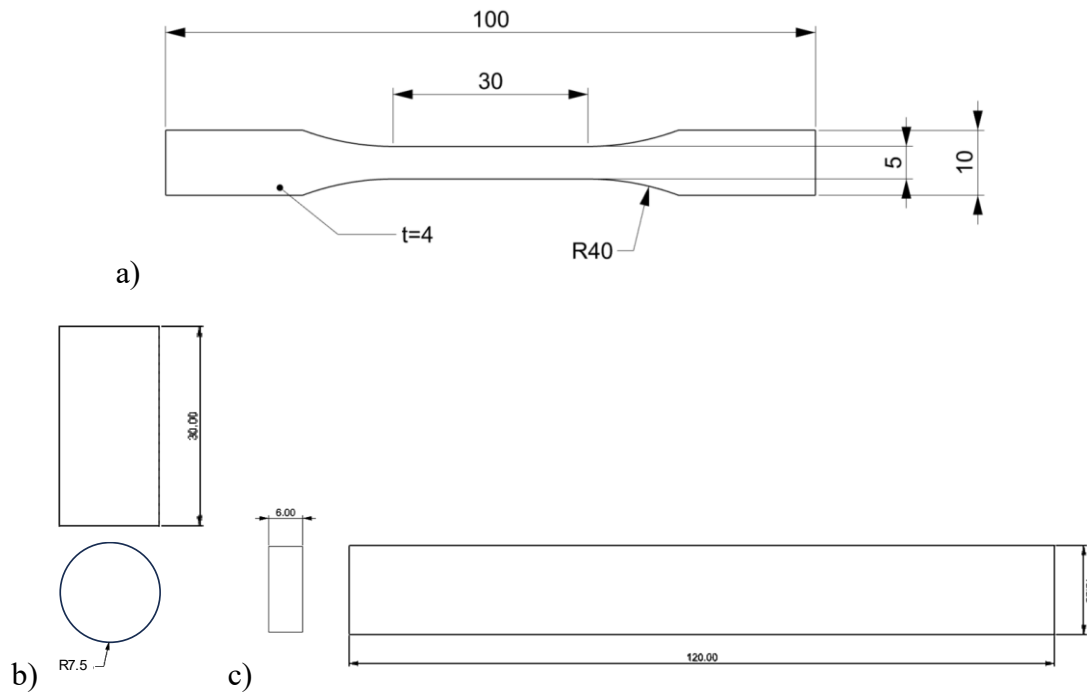
Figure 61. Specimens overall dimensions. a) traction specimen ISO527 1BA; b) compression specimen ASTM D695 type B; c) flexure specimen ISO 178.

Three specimens for each typology were printed using a Form 3 (Formlabs, USA), which is a semi-industrial SLA 3D printer. The files for the 3D printer were prepared within the proprietary software Pre-Form (Formlabs, USA) importing the stl files for the models. A layer thickness of 0.1 mm was set for all the specimens, which were printed in a vertical position (relative to the main dimension of the specimens) to minimize the need for support structures; compression specimens were printed with supports on the base, whereas flexural specimens were positioned directly on the platform. Other printing parameters cannot be controlled directly but they are defined by the printer company based on the specific material used. After printing, the specimens were cleaned by compressed air and isopropyl alcohol, then they were cured for 10 min at 30°C using a Form Cure machine (Formlabs, USA). A total of 12 specimens were prepared and tested in addition to three dog bone specimens.

3.1.4.2.3. Results

The trend highlighted in Table 6 is maintained for weights and geometric densities (Table 7) in the printed specimens (Figure 62). The obtained values for the porosity show how the flexure specimens present lower average porosities with respect to the designed. This

may be due to trapped resin that cannot be cleaned properly due to the tortuosity of the shape and remained stuck to the surface. Common issues for SLA process, such as "suction cups" (i.e. hollow volumes or concave geometries in a 3D model), were not detected in the Pre-form software. Additionally, during the printing process were not observed any problem related to "suction cups" due to the interconnected porosity. . Only the compression specimen with the Diamond beam-based unit cell respects the average designed porosity. On printed samples cross-sectional areas slightly differ from the nominal areas of the geometric models: the average cross-sectional areas for the compression specimens are 178.9 ± 1.2 mm^2 and 178.1 ± 0.6 mm^2, for the Diamond beam-based and the TPMS Diamond shell-based respectively; the average cross-sectional areas for the flexure specimens are 93.5 ± 1.1 mm^2 and 93.1 ± 0.1 mm^2, for the Diamond beam-based and the TPMS Diamond shell-based respectively.
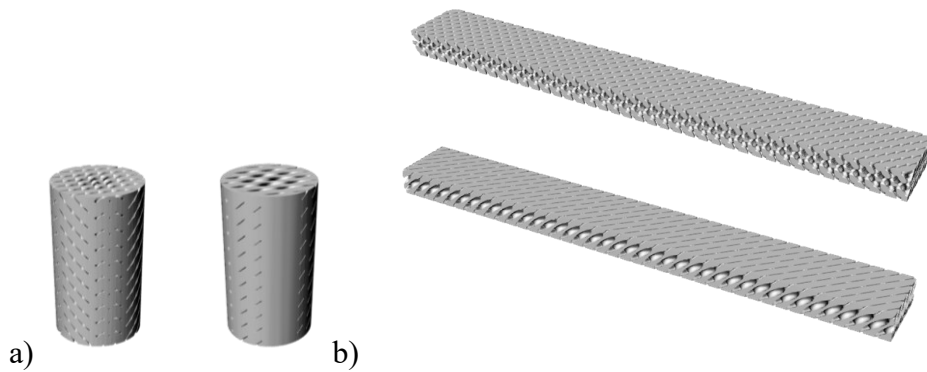
Figure 62. Geometric Models of the Graded Lattice Specimens, a) Compression Specimens, b) Flexure Specimens.

Table 7. Printed specimens physical properties.

Specimen Models	Weight (g)	Geometric Density (g/cm^3)	Porosity
Diamond Compression	4.90 ± 0.18	0.69 ± 0.01	0.40 ± 0.01
TPMS Diamond Compression	5.20 ± 0.10	0.80 ± 0.01	0.31 ± 0.01
Diamond Flexure	7.79 ± 0.08	0.92 ± 0.03	0.20 ± 0.02
TPMS Diamond Flexure	8.87 ± 0.09	0.98 ± 0.02	0.15 ± 0.03

Figure 63 highlights the graded lattice structure obtained for the two types of specimens and unit cell. The two types of unit cells are visibly distinguishable, i.e., a, c refers to the

Diamond beam-based and b, d to the TPMS Diamond. Layers are clearly visible in Figure 63.c,d.
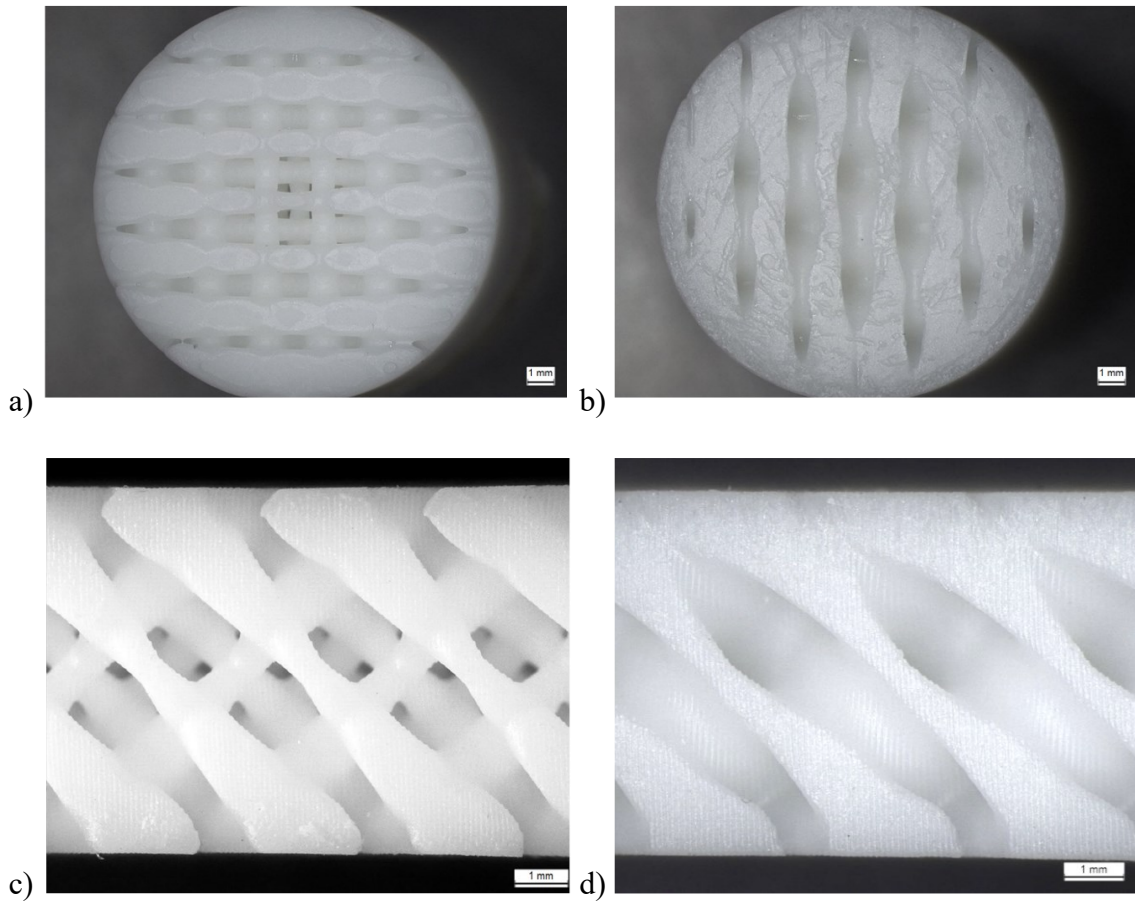
Figure 63. Magnification of the printed samples, highlighting the graded structure. a) Diamond Compression and b) TPMS Diamond Compression (Top View); c) Diamond Flexure and d) TPMS Diamond Flexure (Side View).

Tensile tests show a comparable value for the Young Modulus (E = 2.25 ± 0.23 GPa) with the one in the datasheet (E = 2.8 GPa) but a lower ultimate tensile strength (UTS), UTS = 38.42 ± 2.36 MPa (Datasheet UTS = 65 MPa). This deviation may be due to printing errors or trapped air, as visible in Figure 64 on the left side.
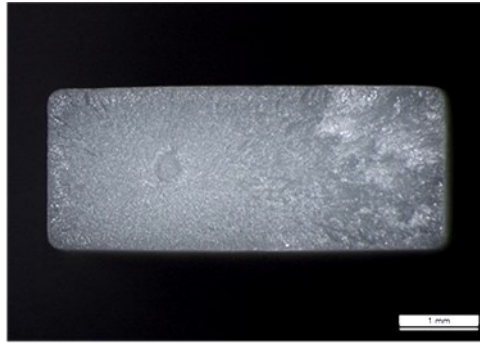
Figure 64. Fracture surface of a tensile dog-bone specimen.

For the compression tests, in the graphs in Figure 65, both Diamond beam-based (DC) and TPMS Diamond (SD) unit cell specimens show some samples with a final descending curve. The specimens showing this behaviour are the ones collapsed with cracks (Figure 66, on the right), while the other specimens with upward-sloping final curves are the ones that experienced the phenomenon of barreling [234] and are also the most stable specimens (Figure 66, on the left). The ideal compression curve tends to rise at the beginning of the test as the specimen is resisting the compressive force. Once the plateau is reached, the specimen is no longer working, but the internal structures are collapsing on top of each other, causing failure. The second part of the graph, showing an upward trend, is a result of the specimen resisting the applied compressive load after reaching failure and decreasing in size.
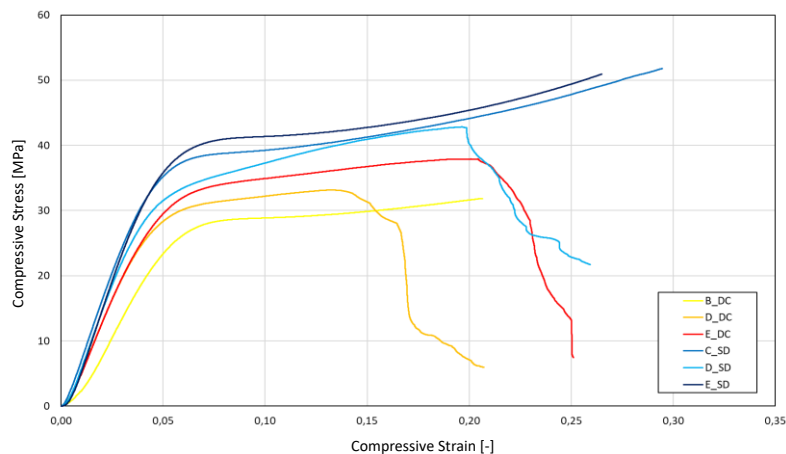
Figure 65. Stress-Strain Graph for the Compressive Test.
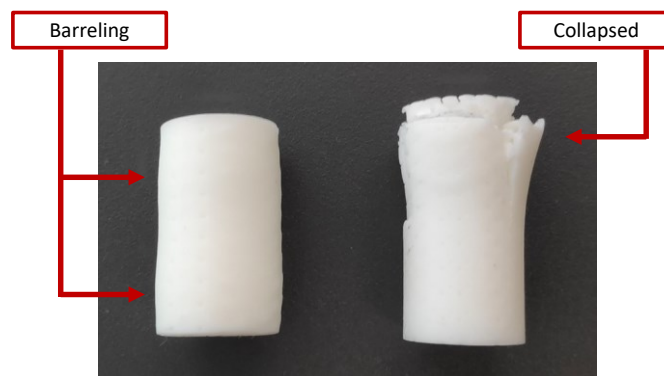
Figure 66. Differences between stable specimens and specimens with internal inhomogeneity after the compression test.

From the graph in Figure 67, specimens with Diamond beam-based unit cell (DC) are less resistant compared to those with TPMS Diamond unit cell (SD). As for the maximum deformations, the specimens with DC unit cell reach values almost twice as high as the maximum deformations of the specimens with SD unit cell.

The DC specimen shows an elastic modulus (E) of 0.76 GPa, whereas the SD exhibits a higher modulus at 0.89 GPa. This indicates that the SD specimen is more rigid. When subjected to compression, the DC specimen has a yield stress (σ_y) of 25.53 MPa, while the SD displays a higher yield stress of 31.87 MPa. This implies that the SD specimen can withstand greater compressive forces before deformation occurs. In terms of compression rupture stress (σ_r), the DC specimen unit cell experiences a stress of 34.55 MPa, while the SD sustains a higher stress of 38.93 MPa. Regarding rupture strain (ε_r), the DC unit cell exhibits a strain of 0.08, while the SD displays a slightly higher strain of 0.09. This suggests that the SD has a marginally greater ability to deform prior to fracture. The SD specimens outperforms the DC specimens in terms of compression-related mechanical properties, displaying higher stiffness, yield stress, rupture stress, and rupture strain. Table 8 reports the most important properties discussed.

For the 3-pt bending test, the trends in the graphs (Figure 67) align with the two types of specimens, as the minimum density of the SD specimens, being 25%, conveys greater resistance to the specimens with SD unit cell, compared to the DC specimens which have a minimum density of 15%. Therefore, the observed differences can be attributed to two factors: the different minimum densities and the different types of unit cell.
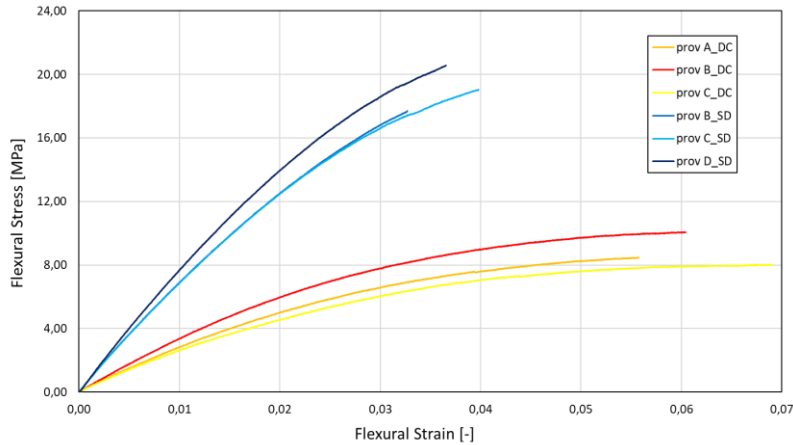
Figure 67. Stress-Strain Graph for the 3-pt Bending Test.

From the tests, mechanical properties were calculated. For the DC lattice, the maximum force F_{max} was 52.57 N, maximum deflection was 15.71 mm, flexural stress at rupture σ_r was 8.84 MPa, and rupture strain (ε_r) was 0.06. In contrast, for the SD lattice, these values were higher: F_{max} was 113.91 N, maximum deflection was 9.70 mm, σ_r was 19.10 MPa, and ε_r was 0.04. This indicates that the DS lattice exhibited superior flexural strength compared to the DC lattice, while DC specimens are more flexible due to the lower relative density and the cell topology. Table 8 reports the most important properties discussed.

Table 8. Main mechanical properties for the two type of specimens tested.

Specimen Models	Compression		Flexure	
	E (GPa)	σ_y (MPa)	F_{max}	σ_r
Diamond	0.76 ± 0.03	25.53 ± 2.03	15.71 ± 1.46	8.84 ± 1.08
TPMS Diamond	0.89 ± 0.08	31.87 ± 2.91	113.91 ± 8.36	19.10 ± 1.43

Further investigation will involve comparing these lattice structures with other type of unit cells and bulk specimens of the same volume. Additionally, exploring the potential use of biocompatible and bioresorbable materials for biomedical applications represents a significant advancement in this area of research.

3.1.5. Methods Comparison

In this section, the design and modeling methods for graded lattices previously proposed are briefly compared with each other with respect to modeling and fabrication aspects.

To understanding the differences the four methodologies two comparisons are proposed. At first the comparison between the G-code modification method and the subdivisions surface offset method is provided. The subdivisions surface offset method is chosen as representative of the CAD modeling methods. In the first method the lattice geometric modeling operations are not performed while in the subdivisions surface offset method the operations are done in a CAD software and a 3D model is realized. Secondly the three methodologies concerning a fundamental CAD modeling step are compared with each other.

Both the comparisons are discussed and evaluated on the base of quantitative criteria. Then a comprehensive evaluation based on qualitative criteria is given for all the four methods. Quantitative criteria include computation time, file size, and printing time (only for the CAD-CAM comparison), while qualitative criteria embrace min-max density reachability, modeling flexibility, AM technology suitability and modeling efforts.

All the methods for this comparison are implemented in Rhinoceros 7 (McNeel & Associates) using the same hardware and without parallel computing.

3.1.5.1.   CAD vs CAM method comparison (Quantitative)

A CAD-based method, among the three proposed, and the CAM-based method are compared. It is possible to choose between the three methods because the 3D models obtained from them suffer of the same weaknesses when adopted in FDM printing.

The CAD method based on subdivisions surface offset (section 3.1.3) is chosen. The two methods are compared based on the printing of a cube of 40x40x40 mm with a perimeter thickness of 1.35 mm and filled with Gyroid TPMS surface a gradient density ranging between 15% to 70% in the Y direction (Figure 68).

The subdivisions surface offset method, described in Section 3.1.3 can be used to model a graded lattice by a volumetric density map. As already explained, starting from a coarse polygonal quad mesh, the Catmull-Clark subdivision algorithm is used to model TPMS surfaces [122]. The relative density gradient is modeled calculating the thickness from a density map. Then, a thickened shell is possibly created, and the final model is obtained by a boolean union (Figure 68.b). It should be noted that adopting a CAD model with variable density lattices, it is necessary to set $\rho_s = 1$ (max) as infill density in the CAM software for MEX technologies to obtain a solid object.

Figure 68 shows the result obtained by the main steps of the two methods in a single layer (on the top, Figure 68.a,b,c), the CAM-based, on the bottom (Figure 68.d,e,f) the subd-based approach in [122]).

In the graded density by G-code editing method (section 3.1.1), the initial model is a cube (Figure 68.a) and by setting the process parameters (infill pattern = Gyroid, $\rho_s = 0.35$, $L_{cell} = 4.8$ mm, calculated using $E_{w,max} = 1.95$ mm and $L_{tk} = 0.2$ mm, perimeter thickness 1.35 mm), the slicing process produces the toolpath in Figure 68.b. The G-Code is edited based on the volumetric model, and then the part is manufactured obtaining the physical model in Figure 68.c.

Looking carefully, it is possible to observe that two adjacent paths show a small difference due to the previously mentioned delay in section 3.1.1.1.6. On the contrary, considering that the gradient is similar in two closed paths, and the path direction is opposite, if in one direction the material is under extruded (i.e., when E_w increases), in the opposite direction it is over extruded (i.e., when E_w decrease). Then, on average, there is an error compensation. Moreover, decreasing the speed or increasing the nozzle temperature allows for a reduction of this shortcoming [168,221,235]. Indeed, as shown by Moetazedian et al. [168], process parameters such as print speed, acceleration, retraction and temperature can be used to control the deposited material shape among the extrusion rate. They argued that a change in extrusion width can be achieved relatively rapidly by changing print speed. Retraction and acceleration can be adjusted concurrently to smooth the transition from one extrusion width to another. Temperature is shown to play a role in controlling the delay too, reporting that for three different print speeds (1000 mm/min; 3000 mm/min; 6000 mm/min) at three different temperatures (195°C; 205 °C; 215°C), a change in extrusion width from a target dimension to half of the dimension, is reached more rapidly by the highest temperature profile.

To fully exploit the potential of the proposed method, the maximum admissible density variation in the unit length (i.e., the gradient of density variation) should be established in both the plane and the Z directions. In the proposed approach, the density variation is continuous due to the trilinear interpolation and the volumetric model cell dimension is independent from the slicing unit cell. Consequently, in the XY-plane, only a continuous density variation is achievable. To obtain abrupt variations of density among adjacent cells, it is possible to use standard slicing software such as Slic3r, adopting discrete

pattern definition using "Modifier Meshes" [236]. On the other hand, in Z direction, discontinuous density is achievable implementing specific strategies, and the maximum density variation is mainly related to the support provided by the layers below and by active cooling. Also in this case, the maximum admissible variation is strictly related to the set of hardware and process parameters.

Figure 68.e shows the toolpath resulting from the slicing process applied to the lattice model. It is possible to observe that a fragmented toolpath appears, inducing discontinuities in the physical model due to missing zones in the toolpath (Figure 68.f).

The two methods seem very similar in terms of operations. The main differences are related to the modeling operations and the order of the operations.

Creating lattice structures can pose challenges, even for experienced designers. Operations like Boolean unions between shells and lattice may not always yield the desired outcome, but it is extremely related to the CAD software implementation. Subsequently, slicing the model can be particularly intricate for a lattice CAD model, potentially resulting in no viable path depending on the slicer software used (see Figure 68.d). It might take multiple attempts to achieve satisfactory results. The perimeters of the printed objects have not been altered, so significant dimensional variations are not expected in the overall shape. The effect of graded infill can create different shrinkage, particularly where the relative density is higher. Depending on the material used, the actual extrusion width, also linked to response delay, will be the subject of future developments.

Due to the constant extrusion width of the infill in CAM process, the CAD-based only allows discrete density variations in material extrusion (MEX). This is why, in the proposed method, slicing is executed as an initial step, and all modifications are made directly in the CAM file (G-code). However, it's worth noting that achieving conformal lattice structures, as well as variable size and topology lattices, would require additional complex implementations.
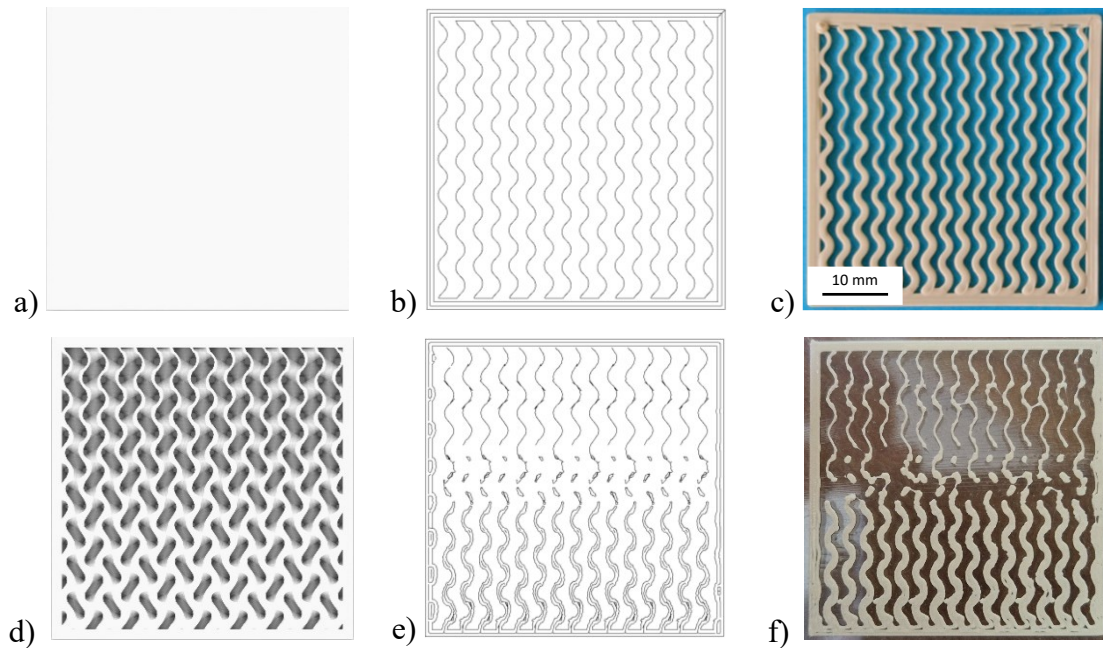
Figure 68. Comparison between the G-code modification method (left side) and the based on subdivisions surfaces (right side): a),b) CAD models sections (Top view); c),d) Toolpath preview of a single layer; e) f) Printed results of the correspondent layer.
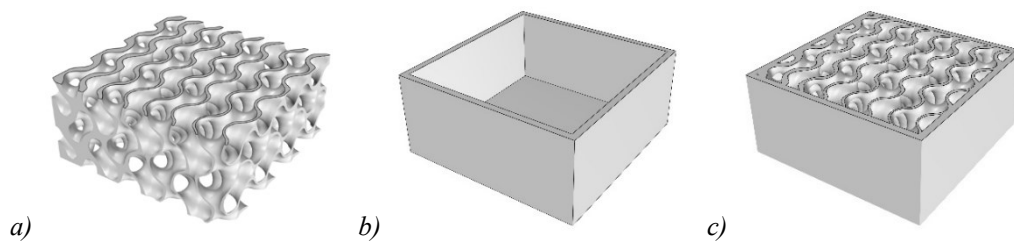
Figure 69. Modeling results of the manual operations (cropping, shelling, union) needed to obtain the desired printable object. Sections of a) the cropped TPMS Gyroid lattice, b) the external shell, and c) the final joined model.

For the CAM-based method, the computational time is represented by the sum of the slicing time and post processing operations, whereas for the CAD-based method the value is representative of the lattice thickening, mesh subdivision, Boolean operations, and slicing time. As shown in Table 9, more than 3 minutes are necessary to correctly obtain a printable model by the previously proposed method, whereas the new one required only 11 s.

The file size for the method is the sum of the main files used in the workflow. In the CAM-based method, there are one CAD model and two G-code files: one comprising the

unmodified G-code and the other containing the modified G-code. On the other hand, for the Mesh Offset method, there are the mesh model and the G-code file. In the first case, the total file size is 13.640 MB (refer to Table 9): 6.082 MB for the initial G-code and 7.558 MB for the edited one. Additionally, the stl binary file of the mesh model is approximately 1 KB (12 faces, 8 vertices). Conversely, in the second case, the mesh model in stl binary format is about 20.298 MB (with 865183 vertices), and the G-code is 48.510 MB, resulting in a total of 68.808 MB. As illustrated in Figure 68.b and d, it's evident that the toolpath of the CAD-based method is longer and more complex than the CAM-based, particularly in areas of higher densities. This is attributed to the constant value of extrusion width used by the CAM software when processing a CAD model with variable density lattices. Consequently, the number of lines and commands, or in other words, the character count in the file, is greater in the CAD method. This is reflected in the complexity and size of the G-code file.

Printing time refers to the needed time in minutes to print the model using an FDM printer. The model prepared with the G-code modification method is significantly faster than the method based on Surface subdivision as reported in Table 9. The main reason is related to the difference in the toolpath length required to build the geometry at the same speed, as shown in Figure 68.c,d, and the number of non-extrusion movements required, although, at constant E_w the speed could be increased. This result can be extended to the other CAD methods, supposing that the 3D graded models are similar.

Table 9. Comparisons between the CAD-CAM methods.

	Computational time [s]	File size [MB]	Printing Time for FDM technology [min]
G-code modification	~11	13.640	144
Surface Mesh Subd	~220	68.808	438

3.1.5.2. CAD methods comparison (Quantitative)

The three methods based on CAD modeling are compared based on the printing of a cubic Gyroid lattice of 2 x 2 x 2 mm, unit cell size = 1 mm and a graded relative density ρ from 70% to 30% along Z direction, where 70% is the maximum density reachable by the Subdivision surface offset method without self-intersections in the mesh.

For the implicit function-based method, the gradient can be modeled by a function $h(z) = 0.4 * (z + 1.6)$ that modify the codomain (enlarge the limit values) of the TPMS equation; the implicit function for the TPMS structure becomes:

$$F(x, y, z) = \big(cos(kx)sin(ky) + cos(ky)sin(kz) + cos(kz)sin(kx)\big) + 0.4 * (z + 1.6) = 0.$$

$$(43)$$

The function is evaluated using a marching cube algorithm, with a voxel size of 0.025 mm. Notably, no Boolean operations are required in this process. The solid mesh model is derived by applying isovalues within the domain range of [-0.75 to 0.75]. In the Subdivision surface offset method, the lattice is designed utilizing four repetitions of the unit cell for each Cartesian axis. Subsequently, two levels of the Catmull-Clark subdivision algorithm are applied. Finally, the effective dimension is cropped using a Boolean intersection. By doing so, a perfect cubic shape is obtained, avoiding boundary effects. The density gradient is defined by a linear function along z,

$$\rho(z) = \rho_{min} + (z - z_{min}) * (\rho_{max} - \rho_{min})/(z_{max} - z_{min}) \qquad (44)$$

where ρ_{min}, ρ_{max} are respectively the minimum and maximum relative density, and z_{min}, z_{max} are the z limits in which the gradient is described. The correlation between relative density and the normalized thickness t/L for Gyroid is given by:

$$t/L(\rho) = 0.0944\rho^2 + 0.2909\rho \qquad (45)$$

t/L domain is [0.095 - 0.250].

In the Distance Field approach, the lattice is modeled using the same approach adopted for Subdivision surface offset, i.e., using Boolean intersection on a lattice with more repetitions. The initial B-Rep surface is a TPMS Gyroid unit cell mesh with 1914 vertices used for the implementation of the method, extracted by a marching cubes algorithm on a grid 30x30x30 in a 1 mm^3 volume. The gradient is defined by the same linear function (eq. 44) and the correlation between relative density and the r/L parameter for the Gyroid is given by the quadratic equation:

$$r/L(\rho) = 0.0777\rho^2 + 0.1303\rho + 0.0024 \qquad (46)$$

r/L domain is [0.048 - 0.132]. The voxel size is 0.025 mm, which is 1.92 times higher than the r/L lower limit.

Computational time is an estimation of the computational efforts of the methods. Computation time value for the three methods is representative of the time for computing the solution and the Boolean operation to crop the mesh lattice. The TPMS field function has the longest computational time (~ 100 s), even if no Boolean operations are performed. A big amount of time is absorbed by the evaluation of the function and the alignment of the vertices in the final mesh, to have a solid closed surface model; both are related to the resolution of the voxel grid. Distance fields has the second highest computational time due to the evaluation of the gradient function and to the intersection Boolean operation (~ 80 s); in this case are dependent on the amount of the initial geometric entities and on the voxel grid resolution. The grid resolution also influences the amount of time needed to perform the Boolean operations, because the resulting mesh model has smaller faces. The quickest method is subdivision surface offset with ~ 15 s. The main reason is related to the fact that no polygonization algorithms are needed, differently from the other methods. The Boolean operations are still the longest process in this case.

The file size for the methods is the size of the 3D mesh model saved as binary stl. The Subdivision surface offset method achieves the smallest file size, containing 17335 vertices, and this number is solely contingent on the Catmull-Clark subdivision level utilized. Additionally, the TPMS surface mesh obtained through this method is always coherent. In contrast, the other two methods heavily rely on the polygonization algorithm and its resolution to ensure a coherent surface that accurately represents the scalar field from which it is derived. Consequently, a greater number of vertices are required, resulting in larger file sizes.

a)   b)   c)
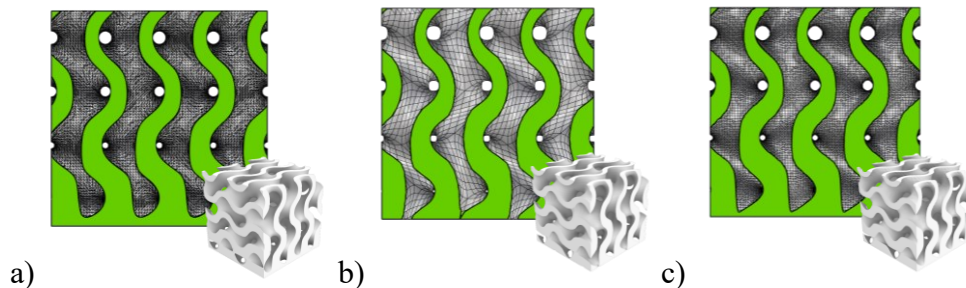
Figure 70. The three geometric model used for the comparison. a) Implicit function, b) subdivision surface offset, c) distance fields.

For models generated by Subdivision surface offset methods, cropping processes performed with Boolean operations may take several minutes to compute or may fail, depending on the CAD software implementaion. On the other hand, the mesh models created with TPMS implicit function method and distance field method can be cropped using Boolean operations on the final mesh, with the same issues, but Boolean operations can also be performed before the isosurface generation while working with volumetric models. The Boolean operations performed on volumetric model never fail and take less computational time [80].

Table 10. Comparisons between the three CAD methods.

	Computational time [s]	File size [kB]
TPMS Fields Function	~ 100	8.858
Subd Surface Offset	~ 15	1.452
Distance Field	~ 80	11.289

Mesh surface quality for the three methods is different. Using the same average edge length and the same relative density 20% for comparison purposes, as shown in Figure 71, the method based on Subdivision surface offset presents a better mesh in terms of quality, smoothness, and curvature [237]. The other two methods rely on polygonization algorithms and present bad meshes, since the surface quality increase accordingly to the voxel grid resolution. In particular the Function-based method implements a marching cubes algorithm while the distance field method implemented a dual contouring algorithm [238] (Appendix A)

a) b) c)

Figure 71. The three lattice models obtained using the three CAD approaches developed: a) implicit Function-based method, b) Subdivisions surface offset, c) Distance field approach. Average edge length 0.0324 ± 0.0001.

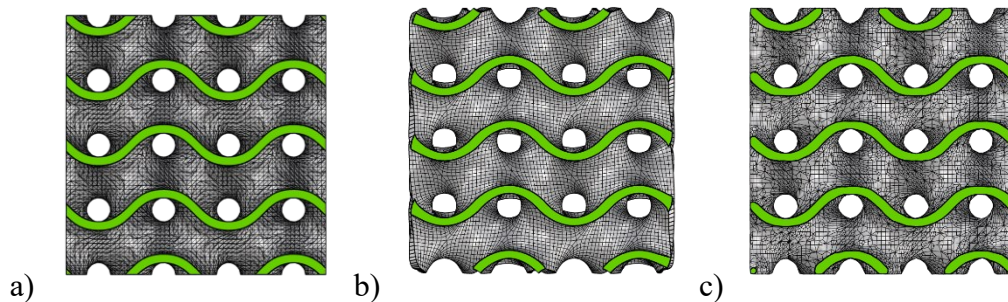Slightly different TPMS 3D models are obtained when using the TPMS implicit functions description and the methods based on offset/distances from a initial surface as observed in [134]. The TPMS implicit function gives the exact representation of the TPMS structure in the space, within a symmetric codomain, for instance in the case of a Gyroid function the codomain is v = [-1.41 – 1.41] and it is not related to the any geometrical dimension (Figure 72.a). Conversely, distance based function has a different trend, with a positive domain in this case, and for a unit cell dimension of 1 mm is v = [0 - 0.45] mm (Figure 72.b). The deviation between the exact and the distance-based representation increased accordingly to the relative density considered, as visible in Figure 72.c, highlighted by the isocurves in the 2D section of the two TPMS gyroid scalar fields. This distinction is evident in the trends of the approximation functions depicting the relationship between relative density (ρ) and isovalue (k) for TPMS functions, as opposed to the relationship between relative density (ρ) and r/L for distance-based approaches. Here, k represents the isovalue normalized within the range of [-0.5 – 0.5], allowing for a comparison across various TPMS functions defined within different domains. Figure 73 depicts the trends for three different TPMS cells: Gyroid, P-Surface and Diamond.
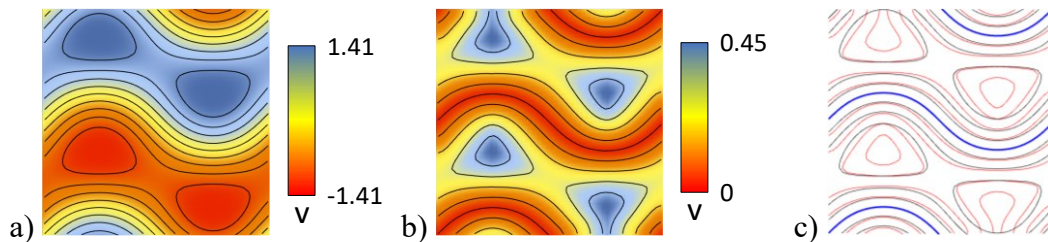

Figure 72. 2D sections visualization of the fields and isocurves generated by the two methods for a Gyroid cell: a) Functions based method; b) Distance based method c) Superimposition of the equivalent isocurves, distance based in red, function based in black, blu curve visualize the isocurve = 0.
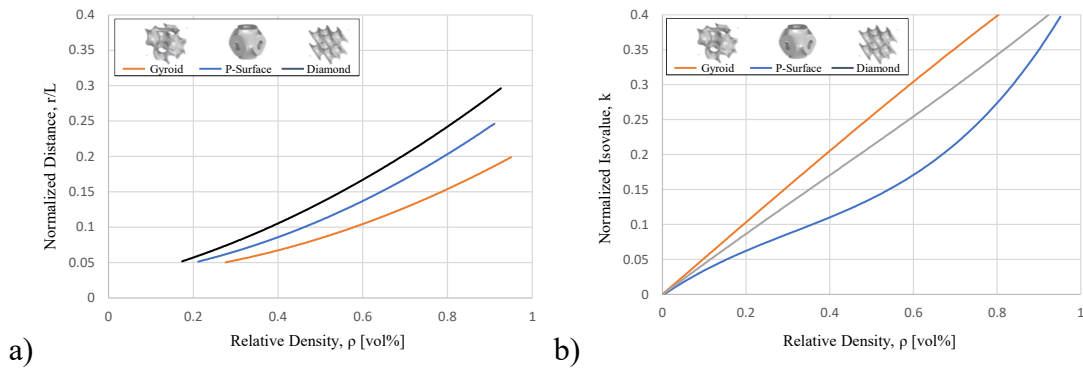
Figure 73. Trends for r/L and k parameters vs relative density for three different TPMS Gyroid, P-Surface and Diamond.

3.1.5.3. Qualitative Comparison

Min-max density reachability refers to the limits of the method in the creation low density and full density structures, thus is a quite important criterion. The method based on G-code modification permits the creation of full density structures, with some limitations related to the type of infill/lattice chosen and the cell size. Those limitations are related to the diameter of nozzle because the maximum extruded material amount is limited by the actual quality of the deposition as described in Section 3.1.1.1.6. On the other hand, the nozzle size and the layer thickness limit the minimum density since the minimum extrusion width possible corresponds to the layer thickness. Anyway, the exact limits can be understood by experimentally test the machine configuration. The method based on functions can reach full density in the 3D model since the B-Rep is extracted by polygonization algorithm; the resolution used for the polygonization algorithm fix the lower limit for the lattice structure thickness to have a coherent surface mesh. The method based on Subdivisions surface offset cannot reach the full density of a lattice structure, but it is usually limited to 70-75%. This limit is due to the self-intersections of the surface mesh to the increasing thickness of the walls. On the other hand, this method does not possess a lower limit for the relative density, which is only set by technology resolution on the minimum thickness. The fourth method based on volumetric approach has the same limits of the method based on functions. Anyway, lower limits are set by technological constraints related to the specific AM technology, for instance the minimum escape hole size and minimum thickness, which is mainly related to the resolution of the machine. Modeling flexibility refers to the representational capacities, so the range of models that can be prepared, and reflects the practical usefulness. The method based on the G-code

119

modification can be adapted to other type of models and not only to the realization of graded lattices, since it not specifically based on a graded CAD model. For this reason, the modeling flexibility is related to the possible patterns that can be adopted while generating the CAM file, and the printer configuration. The pattern available in a CAM software are usually not in a big a number, and only a smaller part of them represents complex lattice structures. The method based on functions, as it is, is only suitable for TPMS modeling of various gradients that are not possible with the other methods; it could be extended to other type of functions as well, for lattice and non-lattice models. The method based on subdivision surface offset has been used to model two types of TPMS surfaces (Gyroid and P-surface). It can be extended to other TPMS surfaces, but the limitation is the necessity of the simple quad mesh model for each basic unit cell type. The last method has no highlighted limitations for graded lattices since it relies on an initial B-Rep model that can be obtained in several ways. For this reason, it can be adopted in the realization of different lattice and non-lattice graded structures. All the methods accept volumetric maps as input to describe the gradient of relative density, so they can ideally realize very complex graded structures.

Modeling efforts refers to easiness to realize the 3D model. The CAM-based method has no modeling efforts since graded structure is directly generated in the CAM phase. The implicit function method requires high mathematical skills since the correct model is obtained from an appropriate function definition. The subdivision surface offset method doesn't need specific modeling efforts. While the distance field method request modeling skills for the initial B-Rep shape definition. All these last three methods have a common drawback when modifying the lattice mesh model and this step can be tricky even for an expert designer: boolean operations are not always performed successfully.

AM technologies suitability refers to which AM technologies the methods can be applied to. The proposed methods based on functions, on surface subdivision offset and on volumetric approaches are suitable for all the AM technologies, since the output of the method is a 3D model. On the other hand, method based on G-code modification is only suitable for MEX technologies such as FDM or DIW. This method could also be applied to other AM technologies that use pathways or material deposition, such as DED, with appropriate modifications of equivalent parameters. Limitations are identifiable when

printing graded lattices using MEX processes, as already highlighted in the CAD-CAM comparison.

Table 11. Comparisons between the four methods, qualitative.

Method	Min-Max Density Reachability	Modeling Flexibility	Modeling Efforts	AM Technology Suitability
G-code modification	> 0, 100 with limitations	Low	Low	MEX, DED
TPMS Implicit Functions	0, 100	Medium	High	All
Subd Surface Offset	0, <100 depends on the unit cell type	Medium	Medium	All
Distance Fields	0, 100	High	Medium	All

3.1.6. Remarks and discussions

Table 12. Overall summary of the benefits and drawbacks

Method	Benefits	Drawbacks
G-code modification	The lattice structure is not geometrically modeled. No extreme CAD modeling skills are needed. Avoid CAD complexities related to lattice The file size is extremely small. Relatively low time for modeling. The toolpath is always consistent.	Delay in the deposition. Lattices are limited to infill patterns in the slicer and not all the infill patterns work properly. Conformal lattice structures and lattices with variable size and topology cannot be obtained. No analyses and simulations can be performed. Mainly MEX technologies.
TPMS implicit functions	All type of gradients can be modeled. Full dense structure can be obtained. Simple conformal lattice structures could be obtained using the B-Rep. Exact TPMS shape from isovalues.	Boolean Operations on the isosurface. Large file size. High mathematical skills required. No conformal lattice structure. Not easily to implement and to handle. B-Rep (mesh) quality depends on the polygonization algorithm and resolution used. Possible errors on mesh model.
Subd surface offset	Low file size. Coherent/watertight and closed mesh. Easily implementable. Simple conformal lattice structures and	Boolean Operations. For TPMS lattices, it needs the coarse unit cell model. Gradient topology cannot be obtained. No full dense structure can be obtained.

	lattices with variable size could be obtained.	
Distance fields	Both B-rep and V-Rep. Easy implementable. Relatively low time for modeling. B-Rep make the geometry modification easy. Shape flexibility. Full dense structure can be obtained. Simple conformal lattice structures could be obtained using the B-Rep.	Boolean operations on the isosurface (B-Rep). Usually large file size. Gradient topology cannot be obtained easily. B-Rep (mesh) quality depends on the polygonization algorithm and resolution used. Possible errors on mesh model.

In summary, the choice of method depends on the specific needs:

1. G-code Modification Method: to create graded density lattices using FDM technologies, consider this approach.

2. TPMS Implicit Functions Method: select this method for TPMS lattices with advanced gradients.

3. Subdivision Surface Offset Method: this is the best choice when it is needed TPMS graded lattices for fast applications and smaller file sizes.

4. Distance Fields Method: opt for this method if it is required flexibility and intuitiveness for creating graded lattices.

3.2. Material

3.2.1. Graded Materials

The methodology proposed in this section, derives from the first method which was used for designing and modeling graded lattice structures for FDM technologies by modifying the extrusion parameter E in the G-code file. Following a CAM file modification approach, another process parameter was modified to control material composition and distribution by using a FDM machine configured for multimaterial 3D printing. Furthermore, a model of the deposition behaviour for a bi-material extrusion is proposed.

3.2.1.1. Method development and implementation

In this method another process parameter, i.e., the material ratio parameter, is considered. The material ratio parameter is controlled by using a volumetric map as in the previous method describe in Section 3.1.1. In this way it is possible to drive the material composition and distribution in a printed component using a FDM printer configured for

multimaterial co-extrusion printing. Differently to that method, it is not necessary to wisely control the infill pattern and infill density parameters to create a lattice, but every type of infill and density can be used.
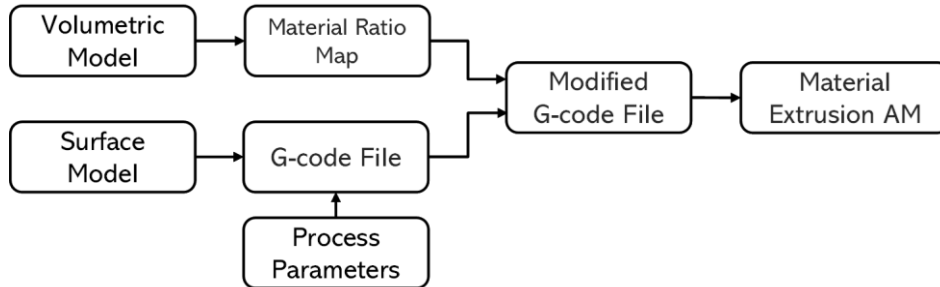
Figure 74. Proposed workflow for the graded material realization.

The method has been implemented as a script in IronPython language in Grasshopper, a visual programming environment that runs within the Rhinoceros 7 CAD Software (McNeel & Associates, USA).

As mentioned, the surface model is obtained in the design from functional and aesthetical requirements. Usually, in mechanical design, the parts are made of homogeneous materials, and it is sufficient to represent only the surface of the components, which can be achieved by different representation schemes, such as boundary representation or constructive solid geometry in a CAD environment. Analogously, in the proposed approach it is possible to define the surface model by standard approaches. This model is exported in a STL file format, that is the de facto standard for AM data exchange [78,239]. The model is imported into the CAM software, positioned, and oriented with respect to the manufacturing platform. Then the process parameters, such as layer thickness, speed, temperature, slicing strategies, and infill density are set, and then, the G-code is computed as in a standard FDM workflow. The G-code is the language used by the computer numerical control (CNC) to drive the machine tools during the manufacturing process. This language holds the manufacturing instructions, such as the tools movements and speeds.

3.2.1.1.1. *Material Ratio Map*

The functional requirements were also used to establish the distribution of the materials in the part, which is considered to define the volumetric model. A voxel-based volumetric

model is selected. Scalar data type representing some properties in the three-dimensional space (e.g. density, materials fractions, and color) can be assigned to the voxel data structure according to the position of the unit volume (voxel) in the space [240–243]. The properties of the voxels can be assigned to the voxel centroids.

When working with 2 materials it is possible to use color maps adopting the grayscale format that carries only intensity information (one scalar value). The intensity is expressed within a given range between a minimum and a maximum, inclusive. This range is represented in an abstract way as a range from 0 (or 0%) (total absence, black) and 1 (or 100%) (total presence, white), with any fractional values in between. Sometimes the scale is reversed. It follows that it is possible to associate the desired material information by the attribution of the material property to a chosen color. Specifically, the color information P, e.g., the white color, can be associated to the material fraction (MF) of material X and the MF of Y is 1 - P. For example, P = 0 (white color) means 100% of X and 0% of Y, while P = 1 (black) means 0% of X and 100% of Y and P=0.5 means 50% of X and 50% of Y. When working with 3 materials are used, the RGB color model (red, green, blue) can be adopted, and the MF of a single material can be assigned to each channel. Analogously RGBA color model (red, green, blue, and alpha channels) can be used in the case of 4 materials; alternatively it is possible to assign the density to the alpha channel (transparency) that can be used to establish the extrusion amount, as previously proposed in literature for manufacturing graded lattice structures [244]. If more than 4 materials are used is possible to use convenient remapping functions to weight the channels values.

3.2.1.1.2. *Modified G-Code file*

According to the G-code, the required fraction of each material is obtained by simultaneously controlling the amount of material pushed by each extruder. Adopting the Marlin firmware, the material percentage is coded into the G-code using two possible approaches. The first record a specific material ratio combination and assigns this record to a virtual tool. This is obtained by the commands M163 and M164 [245], such as:

M163 S0 P0.65
M163 S1 P0.35
M164 S5

that means that the tool number 5 (S5) is set to be 65% of material in the extruder 0 and 35% of material in the extruder 1. To call the n-virtual tool it is necessary introducing the line T*n* in the right position of the G-code listing, where *n* is the number of the tool (5 in the example, i.e. T5) [246]. One limitation is the possibility to define only a finite number of tools. This approach is usually adopted for small amounts of material combinations/tools, to prepare a palette of tools at the beginning of the G-code to recall at specific position. When working with a huge number of combinations/virtual tools, the solutions is to redefine the material amount of a tool during the process. The alternative solution is to adopt the M165 command [247] assigning the mixing ratio using a single line of code such as:

M165 A0.2 B0.4 C0.3 D0.1.

This means that four materials (i.e., extruders), identified by the letters A, B, C, D are used, and the ratios are 0.2, 0.4, 0.3 and 0.1 respectively. The sum of these values must be 1. The values represent the weights of each extruder utilization ratio. A maximum of 6 materials are achievable, but infinite number of mixes can be defined. The command is usually written in the G-code before the movement that needs the specific material mix. To allow a graded variation of composition in the XY-plane, the previously obtained G-code is manipulated by a Python script that divides the initial toolpath into shorter segments. To edit the G-code, the following pseudocode was implemented:

```
-   Read G-code lines
-   initialize the edited_G-code
-   for each line:
    -   if available, extract X, Y, Z, E
    -   if line is infill:
        -   compute ΔX, ΔY and Δs
        -   if Δs is too large:
            -   divide ΔX, ΔY and E in n-portions
            -   create a new_line string with M165 and material
                ratios (A,B,C…)
            -   add new_line to the edited_G-code
    -   else:
        -   add line to the edited_G-code
-   write edited_G-code
```

3.2.1.2. Method validation and applications

3.2.1.2.1. Case study

The proposed modeling approach was tested on an earphone component. The model was geometrically shaped in Rhinoceros 7 using NURBS surfaces. The parts, i.e., the hard case and the soft earpad, were consolidated into a single component. The surface model was meshed and exported as an STL file. Figure 75 shows the model with the main dimensions and a longitudinal section to show the internal detail.
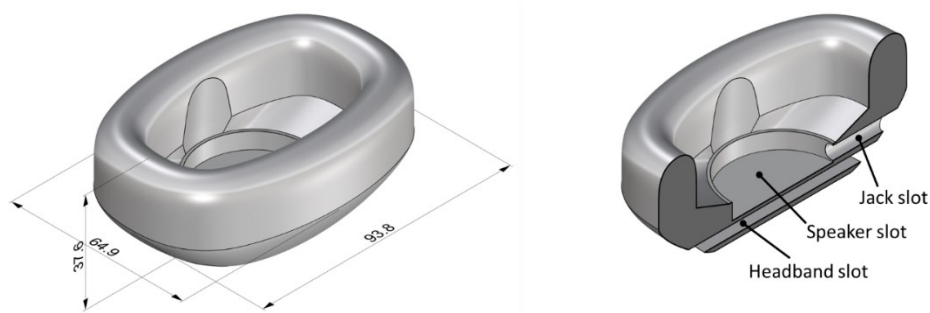
Figure 75 Surface model: main dimensions and internal detail.

Two materials were selected: PLA Extrafill (polylactic acid) for the rigid portions, and FlexFill TPU 98A (thermoplastic polyurethane) for the compliant areas, both supplied by Fillamentum [35]. Table 13shows the main properties of the material selected in this work. The choice of this couple of materials is due to the wide range of properties that can be reached by varying the material fraction and the compatibility between them while maintaining rather similar process conditions that are easy to achieve with standard equipment, as confirmed by the literature [248–251].

Table 13. Main properties of the chosen materials.

Properties	PLA Extrafill	Flexfill TPU 98A
Density [g/cm^3]	1.24	1.23
Ultimate tensile strength [MPa]	60	53.7
Elongation at break (%)	6	318
Elastic modulus [MPa]	3600	160*
Print temperature range [°C]	190-210	220-240
Bed temperature range [°C]	55-60	50-60

* measured by mechanical tests.

The material distribution and CAM parameters (e.g., infill density and number of perimeters) are closely related to the local stiffness of the part, and they can be defined by functional requirements in the design process. Linear variations of material fraction along the Z-axis are assumed, as shown in Figure 76, where the material distribution is visualized by the color of the model. To prevent clogging issues during manufacturing, it could be useful to avoid material fractions (MF) less than 5% and over 95%. Theoretical MF variation can be introduced in every direction, but at this first stage, the study was limited to the Z-direction, to neglect the delay effects due to the volume of material in the melting chamber, which will be studied in future works.
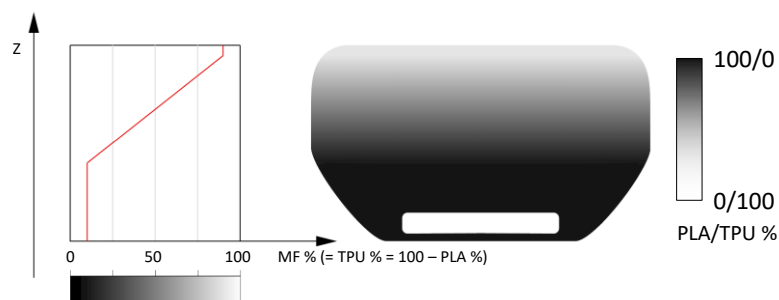
Figure 76. The red curve represents the MF according to Z coordinate. On the right, the visualization of the model in which the black color represents the PLA, whereas the white represents TPU.

The shape is described by a mesh as input for the CAM processing. The G-code is generated by the open-source software Slic3r [216] starting from the geometry following a conventional workflow. Table 14 summarizes the selected manufacturing process parameters which consider the range of manufacturing parameters suitable for both PLA and TPU. The nozzle temperature and print speed were selected based on the characteristics of the two materials: the nozzle temperature represents the lower limit within the temperature range of the higher temperature filament and the print speed value is adjusted in consideration of the material with lower viscosity and the hotend configuration [219]. A systematic study on the rheological properties of the combined materials will be the focus of future investigations.

Table 14. Process parameters.

Nozzle Temperature	220 °C	Line width and nozzle diameter	0.8 mm
Bed Temperature	60 °C	Number of perimeters	2
Infill	Cubic, 30%	Retraction enabled	False
Infill/perimeters overlap	15%	Supports enabled	True
Initial/top/bottom print speed	15 mm/s	Support angle	70°
Travel speed	80 mm/s	Flow	100%
Print speed	30 mm/s	Top/bottom thickness	1.6 mm
Layer height	0.4 mm	Fan speed	Enabled 100%

The MF can be described with an equation via arithmetic operators, mathematical functions, and logical operators. The cartesian coordinates are denoted by x, y, z if absolute or u, v, w if relative. More, u, v, w are normalized within the voxelization volume. The MF for the headphone is described by a mathematical function as follows:

$if\ w < f_{z1}$:

$$MF = f_{p1}$$

$elif\ f_{z1} < w < f_{z2}$:

$$MF = f_{p1} + \left(\frac{w - f_{z1}}{f_{z2} - f_{z1}}\right) \cdot \left(1 - 2 \cdot f_{p1}\right)$$

$else$:

$$MF = 1 - f_{p1}$$

where f_{z1} and f_{z2} define the upper and lower bounds of the gradient along the z-direction. Outside this height, a constant MF is maintained, respectively f_{p1} and $f_{p2} = 1 - f_{p1}$; w is the normalized height and ranges between 0 and 1. The information regarding the MF and the shape is used as input for generating the voxel data structure: a voxel 3D grid is created according to the overall dimensions of the headphone (bounding box) and the resolution; the properties of each voxel are assigned according to the voxel centroid and the MF computed in the same position. Assuming f_{p1} = 0.1, f_{z1} = 15/37.6, f_{z2} = 35.6/37.6 (37.6 mm is the high of the model, 15 mm is the beginning of the MF linear variation, and 35.6 mm is the end, and resolution = 40), the resulting volumetric map for the model is visualized in Figure 77 as a colored point clouds representing the voxel centroids.
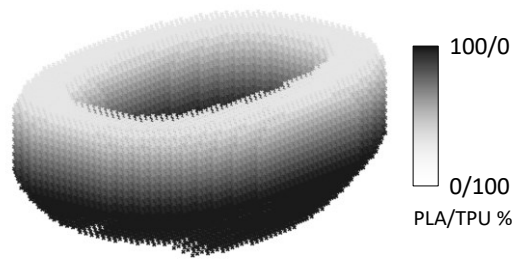
Figure 77. Visualization of the volumetric information as point cloud (voxel centroids) with different colors according to the material fraction.

The volumetric information is then associated to toolpath points adopting the same routine and trilinear interpolation algorithm used in Section 3.1.1.1.5. The modified G-code is finally printed using a Geeetech A20M Dual Extruder (Shenzhen Geeetech Co. Ltd, Shenzen, China) (Figure 78.a), equipped with a Marlin firmware modified conveniently for multimaterial (Appendix A.5) and a Cyclops hotend with a steel nozzle with a diameter of 0.8 mm. The materials reach the hotend through two bowden tubes and the combined materials simultaneously flow through the same nozzle without mixing as shown in Figure 78.b.
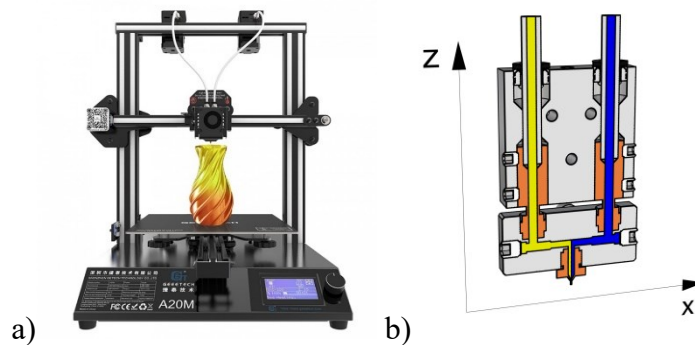
Figure 78. a) The Geeetech A20M Dual Extruder; b) CAD model adapted from GrabCAD of the Cyclops hotend representation.

Figure 79 shows the headphones produced following the workflow described above. It is possible to observe that a graduation in color appears along the Z-axis. Moreover, at the same Z-level, due to the hotend movement and the absence of mixing, a graduation in color appears at the same MF, confirming other results dealing with coextrusion in literature [73].
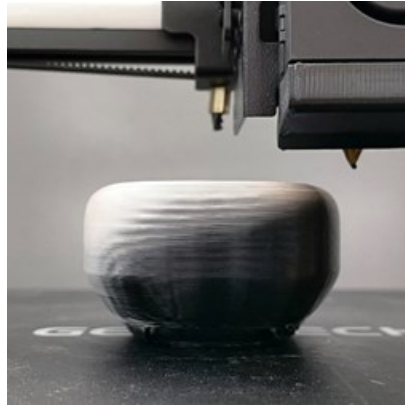
Figure 79. Manufactured part with functionally graded material

The graded composition allows to meet graded properties and consequently multiple functions can be reached in a single part thus enabling parts consolidation and reducing assembly costs. The proposed method can be easily integrated between the design and the manufacturing workflows recently proposed for FGM/FGAM [8,206,244,252,253], overcoming the limits of the current CAM and postprocessing software. For instance, Geeetech provide the Color Mixer Software [254] that allows for linear variations of MF along the Z-axis. As in our approach, Color Mixer, relies on G-code editing and achieves consistent results in linear gradients along the Z-axis. In contrast, our proposed method calculates the material fraction directly from a volumetric model, enabling a gradual transition in all directions, not limited to just the Z-axis. It's worth noting that there's room for technical enhancements to further improve product quality. For instance, addressing the delay between material deposition and extruder control can be achieved by anticipating the extrusion amount and material fraction equivalent to the volume of the melting chamber between the mixing zone and the nozzle exit. Other aspects are related to the rheological properties according to the temperature, such as surface tension, viscosity, and the hotend dynamics, to the deposition pattern that influence the distribution of the coextruded materials [73,255] and to the adhesion among materials.

3.2.1.2.2.   *Multimaterial coextrusion characterization*

In the following section, coextrusion process in MEX technologies are investigated as a consequence of the results obtained by the modeling method for graded materials, described in Section 3.2. This works aims to lay the foundations to understand the FDM coextrusion process, identifying models of material distribution from a geometrical point of view which is the base to describe mechanical properties. Based on a simplified

deposition model, the couples of PLA-TPU and ASA-TPU were analytically and experimentally studied.

3.2.1.2.3.   *Materials*

The PLA- PLA, PLA-TPU and ASA-TPU couples of materials were studied. The choice of these pairs allows a wide range of properties while maintaining rather similar process parameters. In detail, the materials used in this research are PLA Extrafill, ASA Extrafill, and Flexfill TPU 98A (hardness 98 Shore A), which are 3 thermoplastic filaments by Fillamentum [256]. All the filaments are supplied in spools in standard 1.75 mm diameter. PLA is the most widely used thermoplastic filament for FDM. PLA is a rigid and brittle filament that is easy to use, and biodegradable in industrial composting systems. While ASA has similar properties to ABS, however, it is more eco-friendly and has better UV resistance. TPU is a semi-flexible material that offers high tensile strength and high elongation at break.

Table 15. Main properties of the chosen materials [256].

Properties	PLA Extrafill	ASA Extrafill	Flexfill TPU 98A
Density [g/cm^3]	1.24	1.07	1.23
Ultimate tensile strength [MPa]	60	40	53.7
Elongation at break (%)	6	35	318
Tensile modulus [MPa]	3600	1726	-
Poisson ratio	0.33 [257,258]	0.38 [259,260]	0.45 [261,262]
Heat distortion temperature (at 0.45 [MPa]) [°C]	55	96	-
Print temperature (range) [°C]	190-210	240-255	220-240
Bed temperature (range) [°C]	55-60	90-105	50-60

The other process parameters used in the specimens manufacturing are:

- nozzle diameter: 0.4 mm
- nozzle temperature: 220 °C PLA-TPU98A; 240 °C ASA-TPU98A
- bed temperature: 60 °C PLA-TPU98A; 80 °C ASA-TPU98A
- printing speed: 30 mm/s
- layer thickness: 0.2 mm
- hatching space: 0.4 mm
- n. of perimeters: 3
- infill density: 100%

The printing speed assumes the same value for both infill and perimeters to avoid material flow variations that can compromise the actual percentage of material extruded.

3.2.1.2.4. Modeling material deposition

According to the G-code, the required fraction of each material is obtained by simultaneously controlling the amount of material pushed by each extruder. Adopting the Marlin firmware, the material percentage is coded into the G-code by the commands M163 and M164. The former sets the mutual amount of each material, whereas the second latter assigns the mixing to a virtual extruder [245]. Table 16 reports the G-code command lines set for the 3 different tool combinations, that are going to be used in the following investigation.

Table 16. G-code lines for tool configuration for two materials.

Combination 1	Combination 2	Combination 3
M163 S0 P0.75	*M163 S0 P0.50*	*M163 S0 P0.25*
M163 S1 P0.25	*M163 S1 P0.50*	*M163 S1 P0.75*
M164 S1	*M164 S2*	*M164 S3*

Combinations 1 set 75% for material pushed by extruder 0 and 25% for material pushed by extruder 1 for tool 1. To call the needed tool it is necessary introducing the line T*n* in the right position of the G-code listing, where *n* is the number of the tool (3 in the example, i.e. T3) [246].

Using the configuration of the printer discussed in Section 3.2.1.1, materials do not mix, instead, they stand side by side with a reciprocal position that depends on the nozzle path. Considering the extruder mounted as shown in Figure 78.b, due to the hotend configuration, the coextruded materials flow in the nozzle sharing an interface at a plane parallel to the YZ-plane. Consequently, when the nozzle moves along the Y-axis, the material in the left channel is deposited on the left, while the material flowing in the right channel is deposited on the right (Figure 80.a and b). Otherwise, when the nozzle moves along the X positive direction, the material on the right is deposited below the material on the left, whereas, when the nozzle moves along the X negative direction, the material flowing on the left is deposited under the material on the right.
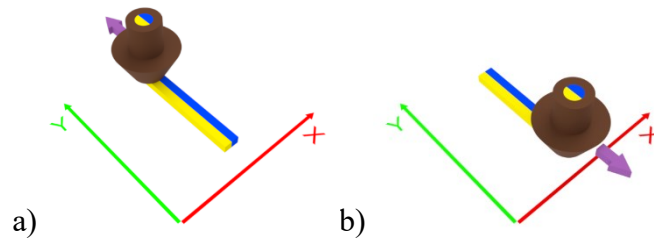
Figure 80. Distribution of the materials deposited depending on the nozzle path.

In a generic nozzle path, moving from the vertical axis (nozzle axis, Z-axis) to the deposition plane (XY-plane), the coextruded materials rotate by 90° around an axis perpendicular to the deposition direction in the deposition plane ($\perp$ dep. dir. in the XY-plane) as shown in Figure 81. Consequently, denoting γ as the angle between the x-axis and the deposition direction, the line that separates the deposited coextruded materials also maintains the same angle γ.
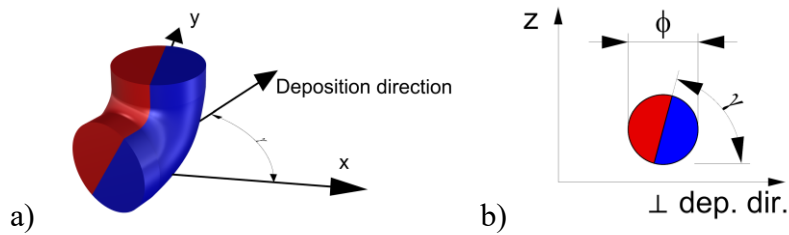
Figure 81. Distribution of the coextruded materials from the nozzle to the deposition plane, considering the deposition direction (a), and initial section of the deposited material in a plane perpendicular to the deposition direction (b).

During the deposition, the shape of the extruded material changes from a circle with a diameter ϕ at the nozzle to a new shape, which can be approximated by a rectangle or a rounded rectangle once the material solidifies [246]. This rectangle has a base equal to the hatching space (hs, distance between two adjacent nozzle paths), and the height equal to the layer thickness (lth).

As a first approximation, to adapt the extruded circle (Figure 81.b) to the rectangle, the circle and the materials separation line are scaled in an ellipse inscribed in the rectangle, with the axes proportional to the sides of the rectangle (Figure 82). Therefore, the scaling factor along the vertical axis will be assumed to be equal to lth/ϕ, while the scaling factor in the horizontal direction will be assumed to be equal to hs/ϕ. As a result, the horizontal

(perpendicular to deposition direction) and vertical (Z-axis) components of the separation line can be calculated as follows:

$$h = (lth/\phi) \cdot (\phi \cdot sin(\gamma)), b = (hs/\phi) \cdot (\phi \cdot cos(\gamma)), \qquad (47)$$

and the new inclination of the interface between the materials γ1 is defined by the equation:

$$\gamma 1 = arctan(tan(\gamma) \cdot lth/hs) \qquad (48)$$
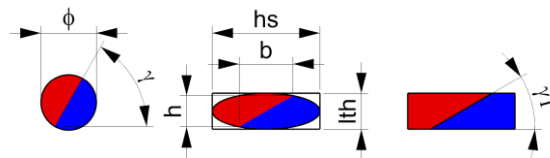
Figure 82. Adaptation of the extruded material to a rectangle.

Different fractions of materials flowing from the nozzle can be modeled by simply moving the separation line to the right or left to reflect the materials fraction on the area of each material.

A more realistic model should consider the presence of an adjacent deposited line. As mentioned, the deposited material can be modeled as a rounded rectangle if there is no other adjacent deposited material in the same layer (Figure 83a). In the case of previously deposited material on the right, the new stripe assumes a shape similar to Figure 83.b, whereas if there is material on the left, the stripe assumes the shape of Figure 83.c.
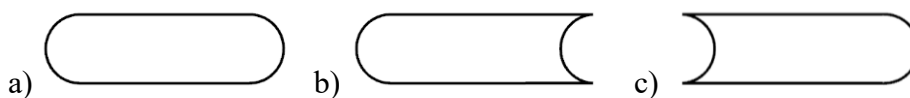
Figure 83. Sections of the deposited material: a) without any adjacent material, b) with previous material deposited on the right, c) with previous materials deposited on the left.

Introducing the shape modification of Figure 83 in the model of Figure 82, the separation line can be warped as in Figure 84, by translating the separation line point by point.
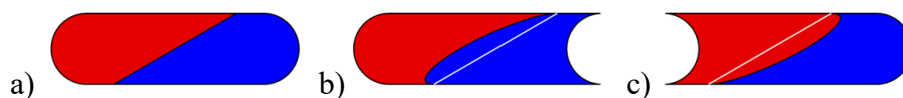
Figure 84. Model of the coextruded material considering a rounded rectangle shape and the previously deposed material for g =60°.

To assess the precise interface between the deposited materials, a specific G-code was generated. This G-code was derived from a path followed by the nozzle, wherein a regular dodecagon with a side length of 150 mm is iterated five times within the same layer, each time with an offset distance of hs = 0.4 mm. This process is then repeated for five layers (lth= 0.2 mm). The movement of the nozzle proceeds in a counterclockwise direction, starting from the outer edge and progressing towards the center. (Figure 85). Each side of the dodecagon was cut in half and the section was analyzed by an optical microscope (Leica MZ 7.5 equipped with an IC 90 E camera). To avoid boundary effects, only the central element of each section was studied. Unlike other shapes, the polygon allows for better identification of the actual deposition direction angle γ.

Furthermore, images were captured using scanning electron microscopy (SEM, FEI Quanta 200 ESEM, Eindhoven, Netherlands) to investigate the interface between distinct materials and within the layers.
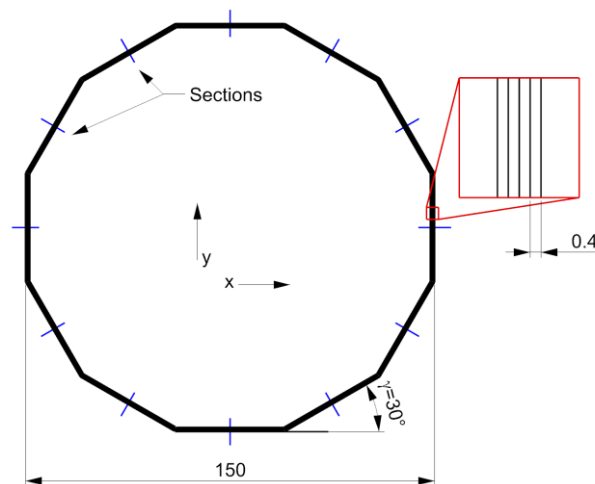
Figure 85. Deposited section studied.

Figure 86 shows one of the manufactured dodecagon to evaluate the interface between the deposited materials.

Figure 86. Deposition test (dodecagon shape) ASA-TPU additively manufactured.

Figure 87 shows the SEM images of a section of the dodecagon with 0.5 material fraction. In both mixes, i.e., PLA – TPU and ASA – TPU, the coextruded stripes show a clear separation between materials, i.e., the materials do not mix, and consolidate with an appropriate strong adhesion. Moving to the interface between stripes, in the same or in different layers, a good adhesion between the materials is observed, even if few pores appear, which are typical of the FDM process [219,263]. These defects can be mitigated by tuning process parameters such as raster angle, build orientation, flow, and temperature [264–266]. Moreover, the different melting temperature of the materials leads to a different viscosity and the more fluid material allows for a better flow in the nozzle and leads to a better coverage of the pores. Other aspects that influence material adhesion are related to adsorption, diffusion, and electrostatic phenomena [267]. In the coextrusion process, the more compliant material reduces the product defects and increases the manufacturability; indeed, the TPU compliance and adhesion allow to compensate for the solidification shrinkage of the other material, especially in the case of ASA, reducing the delamination among layers, and increasing the adhesion to the printer bed surface.
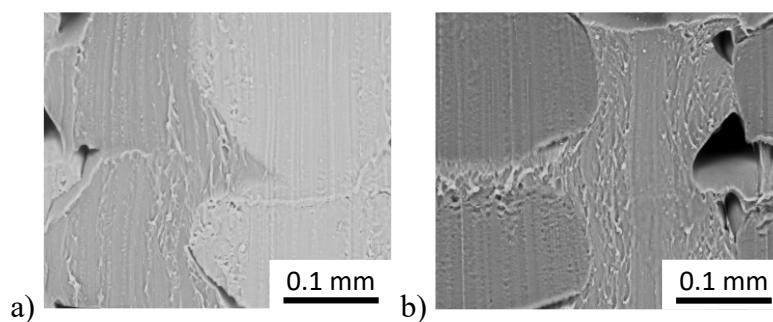
Using the adopted process parameters, i.e., lth=0.2 mm and hs=0.4 mm, the inclination of the interface between the materials γ1 (Figure 82) is represented in Figure 88, according to the deposition direction γ and equation (48). The trend is not linear, and the inclination of the interface always results lower than the deposition angle.
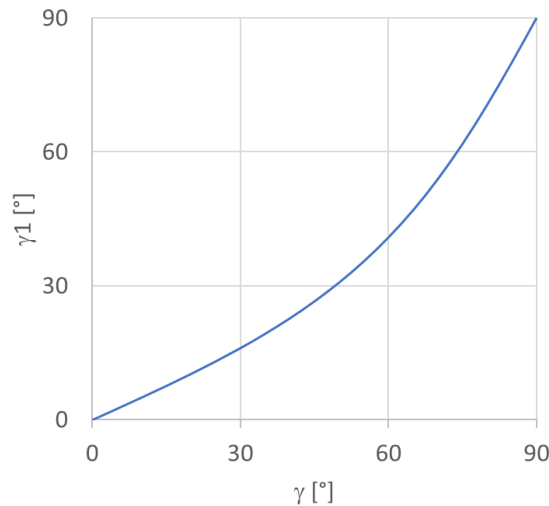
Figure 88. γ1 vs γ for lth=0.2 mm and hs=0.4 mm.

To evaluate the actual interface between the coextruded materials and avoid boundary effects, the central stripe of each dodecagon section, representing the 3rd stripe of the 3rd layer, was extracted and superimposed to the rectangular deposition model presented in Figure 82 together with the angles of γ1 (equation 43), as shown in Figure 88. The rectangular deposition model was selected to reflect the condition of the analytical model.
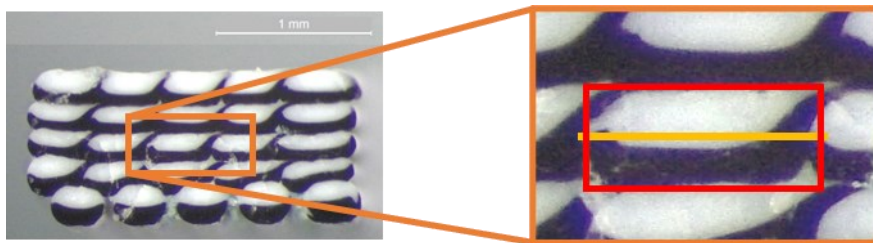
Figure 89. Analysis of the dodecagon section and deposition model superimposition.

Figure 90 shows the actual cross section of the material deposited in the dodecagon, superimposed to the rectangular model for the 3 couples of materials, PLA-PLA,

PLA-TPU, and ASA-TPU, at 50% of material fraction. Due to the periodic behavior, only the results in the range 0°-90° are presented. The yellow lines represent the inclination of the interface between the materials γ1, according to equation 48 and , while the red rectangle represents the rectangular deposition model (Figure 82). As observed in the SEM images, a clear interface between the coextruded materials appears both inside each stripe and between stripes. It can be observed that the proposed model well represents the actual angle formed between the two coextruded materials especially in the couples PLA-PLA and PLA-TPU. ASA-TPU slightly differs from the model; in this case, there are bigger deviations such as non-linear "shapes" in the material interfaces, like squeezing or warping in the center or alterations towards the corners. The deviations from the model can be due to the differences in the materials rheological properties according to the temperature, such as surface tension, viscosity, diffusion, the hotend dynamics [219], the deposition order of the pattern, and the polymers density. For example, the upper right corner of every section forms a hook-like shape, involving the downer material, due to the deposition order, so that the deposited material "anchors" to the previous deposited one. Moreover, porosities can be appreciated at the four corners among the stripes that are typical of the FDM process and can be reduced, as previously discussed, by tuning the process parameters.

Figure 91 shows the actual cross section of the material deposited, superimposed to the rectangular model for the couple PLA-TPU for three material fractions: 75%-25%, 50%-50%, 25%-75%. The yellow lines are translated to reflect the material fraction in the rectangular model (red line). Considerations like the previous case can be made and it is possible to observe that the translation related to the material fraction is effective. Moreover, the interface between the coextruded material is not perfectly straight and it is more similar to the model based on rounded rectangle as shown in Figure 84. On the other hand, this first approximation can be considered adequate for the analytical model.
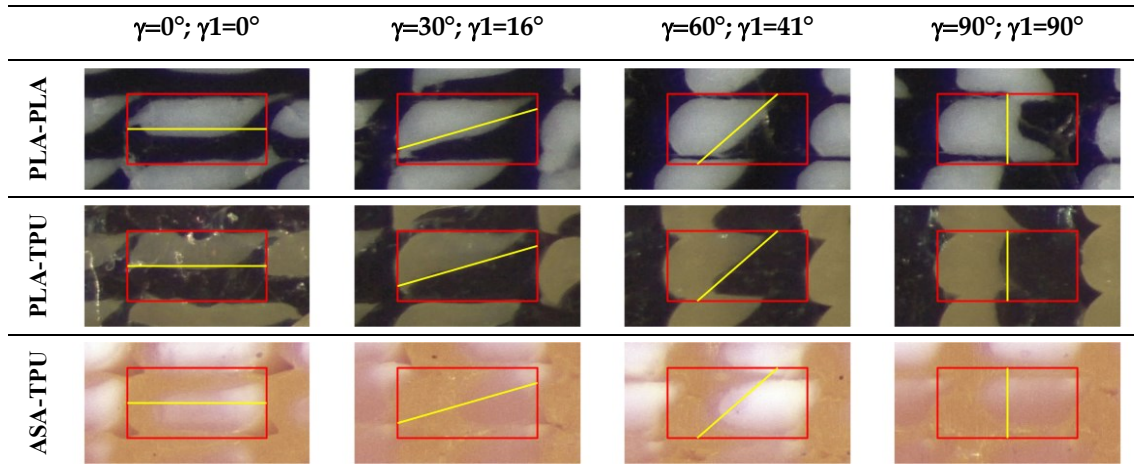
Figure 90. Actual cross section of the material deposited and rectangular model superimposition for the couples of materials PLA-PLA 50%-50%, PLA-TPU 50%-50%, ASA-TPU 50%-50%. The rectangular model is highlighted in red, whereas the inclination of the interface is highlighted in yellow.
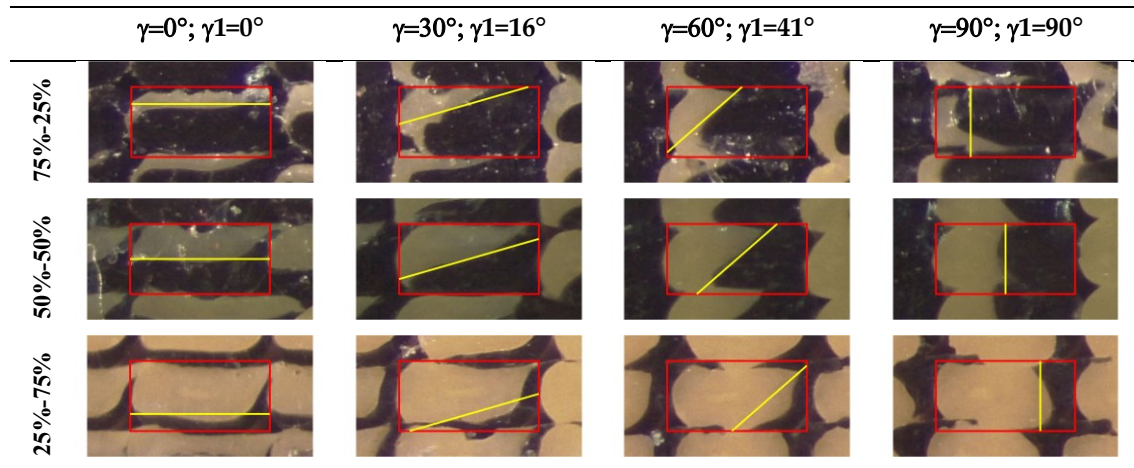
Figure 91. Actual cross section of the material deposited and rectangular model superimposition for the couple PLA-TPU for different material fraction. The rectangular model is highlighted in red, whereas the inclination of the interface is highlighted in yellow.

3.2.1.2.5.   *Analytical model for the elastic modulus*

Under the initial assumption that the nozzle moves along the X-axis in a layer and along the Y-axis in the next one, and that the deposited material has a rectangular section, a unitary volume element can be described as in Figure 92 for different materials fractions. The material behaves as a composite which shows different mechanical properties along the X, Y, and Z-axes. To establish the range of the elastic properties as a function of the material fraction, each portion of the volume element is initially modeled as a spring.
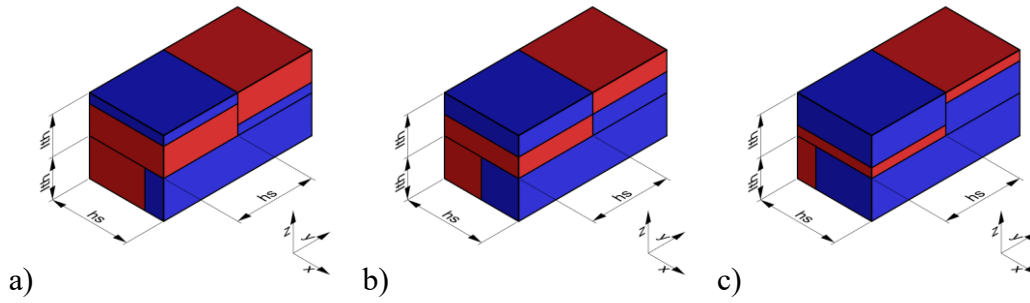
Figure 92. Volume element of deposited material: the first layer is deposited along the y-direction, whereas the second along the x-direction. Blue represents a generic "A material", and red a generic "B material". In a) the volume element is made of 25% of "A material" and 75% of "B material", in b) 50% of "A" and 50% of "B", and in c) 75% of "A" and 25% of "B".

To simplify the model, the layer deposited along the X positive direction is flipped as shown in Figure 93 and the interaction among layers and between adjacent stripes is neglected.
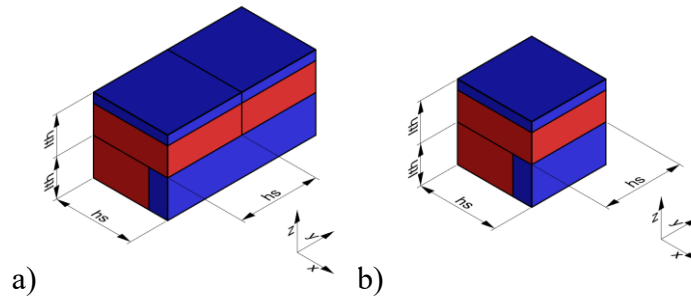
Figure 93. Simplified model for elastic modulus estimation: (a) flipped material extruded along the X positive direction, (b) reduced length.

For a rod of length L, width b, and thickness t, the stiffness k is defined as

$$k = E \cdot b \cdot t/L, \tag{49}$$

where E is the elastic modulus of the material. The stiffness of each element in the proposed models is contingent on parameters including the fraction of "material A" f, the fraction of "material B" 1-f, hs, lth, the elastic modulus of "A" E_A, and the elastic modulus of "B" E_B. To combine 2 or more springs and obtain the resultant stiffness, it is sufficient to apply the relations for parallel and series combination which are respectively:

$$Kp = k1 + k2 + \cdots + kn, \tag{50}$$

140

$$1/ks = 1/k1 + 1/k2 + \cdots + 1/kn \tag{51}$$

Based on the above-mentioned assumptions, Table 17 shows the resultant spring models along the X-, Y-, and Z-axis, where the deposition direction is identified by the numbers 1 (Y direction) and 2 (X direction).

Table 17. Spring models and resultant elastic modulus along the x, y, and z directions.

Spring model	Spring stiffness	Elastic modulus
	$kx2A = \dfrac{E_A \cdot hs \cdot (lth \cdot f)}{hs}$ $kx2B = \dfrac{E_B \cdot hs \cdot (lth \cdot (1-f))}{hs}$ $kx1B = \dfrac{E_B \cdot hs \cdot lth}{hs \cdot (1-f)}$ $kx1A = \dfrac{E_A \cdot hs \cdot lth}{hs \cdot f}$	$kx = lth \cdot \left(\dfrac{E_A \cdot E_B}{(1-f) \cdot E_A + f \cdot E_B} + f \cdot E_A + (1-f) \cdot E_B \right)$ $E_x = \dfrac{1}{2} \left(\dfrac{E_A \cdot E_B}{(1-f) \cdot E_A + f \cdot E_B} + f \cdot E_A + (1-f) \cdot E_B \right)$
	$ky2A = \dfrac{E_A \cdot hs \cdot (lth \cdot f)}{hs}$ $ky2B = \dfrac{E_B \cdot hs \cdot (lth \cdot (1-f))}{hs}$ $ky1A = \dfrac{E_A \cdot (hs \cdot f) \cdot lth}{hs}$ $ky1B = \dfrac{E_B \cdot (hs \cdot (1-f)) \cdot lth}{hs}$	$ky = 2 \cdot lth \cdot (f \cdot E_A + (1-f) \cdot E_B)$ $E_y = f \cdot E_A + (1-f) \cdot E_B$
	$kz2A = \dfrac{E_A \cdot hs \cdot hs}{lth \cdot f}$ $kz2B = \dfrac{E_B \cdot hs \cdot hs}{lth \cdot (1-f)}$ $kz1B = \dfrac{E_B \cdot (hs \cdot (1-f)) \cdot hs}{lth}$ $kz1A = \dfrac{E_A \cdot (hs \cdot f) \cdot hs}{lth}$	$\dfrac{1}{kz} = \dfrac{lth}{hs^2} \cdot \left(\dfrac{f}{E_A} + \dfrac{(1-f)}{E_B} + \dfrac{1}{f \cdot E_A + (1-f) \cdot E_B} \right)$ $E_z = \dfrac{2}{\dfrac{f}{E_A} + \dfrac{(1-f)}{E_B} + \dfrac{1}{f \cdot E_A + (1-f) \cdot E_B}}$

Figure 94 shows the trend of the elastic modulus according to the analytical model described previously. The E_x, E_y, and E_z curves were obtained by applying the equations in Table 17 and using the elastic moduli of the pure materials, i.e., PLA, ASA, and TPU, from the results of the mechanical tests presented in the previous section.
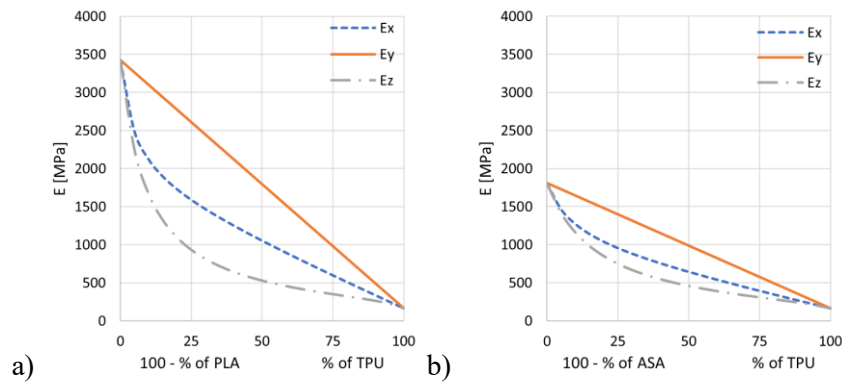
Figure 94. Elastic modulus according to the analytical model: a) PLA – TPU mixes; b) ASA – TPU mixes.

3.2.1.2.6.   *Experimental mechanical properties*

According to the ISO/ASTM DIS 52927 international standard (under development at the time of writing) [268], the tensile strength of additively manufactured polymer parts can be tested following the ISO 527 standard [232]. Figure 95.a shows the dimensions of the type 1BA test specimens and the manufacturing orientation with respect to the building plate. More, according to the ISO/ASTM 52903 international standard [269], three samples for each couple of materials (PLA-TPU and ASA-TPU) and constant material fraction (0, 0.25, 0.5, 0.75, and 1) were produced, for a total of 27 specimens.

The mechanical tensile properties of FDM printed specimens are contingent on the filament deposition direction. Therefore, it's essential to assess mechanical properties in both the direction parallel to the deposition path and the perpendicular direction to measure intra-layer adhesion. In this preliminary investigation, to streamline testing and obtain an initial overview, the coextruded samples were aligned along the diagonal of the build plate (Figure 95.b), employing a deposition direction perpendicular to the edges of the samples (i.e., $\gamma = \pm 45°$ and $\gamma = \pm 135°$).

Since very high elongations are expected, especially for TPU specimens, two types of test apparatus were adopted. The first focuses on the linear zone to obtain the elastic modulus, whereas the second aims to obtain the complete Stress-Strain curve of the specimens, up to failure. The tests were executed as follows:

- For the determination of the elastic modulus, the tests were performed on a MTS Electrodynamic Test Systems Acumen 3 (MTS Systems Corporation, USA) equipped

142

with a 3 kN load cell and a MTS 634.31 F extensometer. A 25 mm gauge length was used, and the test rate was 0.25 mm/min.

- For the characterization of the specimens up to failure, a Galdabini SUN 2500 equipped with a 25 kN load cell and a Galdabini PLAST extensometer was used. The test rate was 10 mm/min.

The samples were tested for the elastic modulus (E), also referred to as Young's modulus, the ultimate tensile strength (UTS), and the maximum strain at failure (ε_{max}).
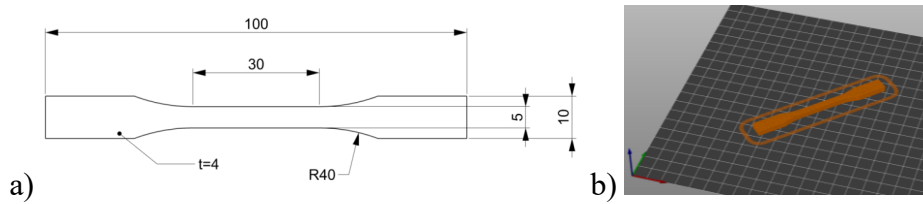
Figure 95. Tensile specimen, 1BA type, according to ISO 527 standard: (a) dimensions, (b) manufacturing orientation with respect to the building plate.

Figure 96 shows one tensile test specimen for each material mixing.

Figure 96. Tensile test samples, from top to bottom: 100% ASA, 75% ASA - 25% TPU, 50% ASA - 50% TPU, 25% ASA - 75% TPU, 100% TPU; 25% PLA - 75% TPU, 50% PLA - 50% TPU, 75% PLA - 25% TPU, 100% PLA.

Figure 97.a shows representative Stress-Strain curves for the different mixing percentages of the PLA – TPU samples, with an enlargement in the first section of the curve (Figure 97.b) to better appreciate the different elastic behaviors. Similarly, Figure 98 shows a representative Stress-Strain curve for each percentage mixing of the ASA – TPU series.
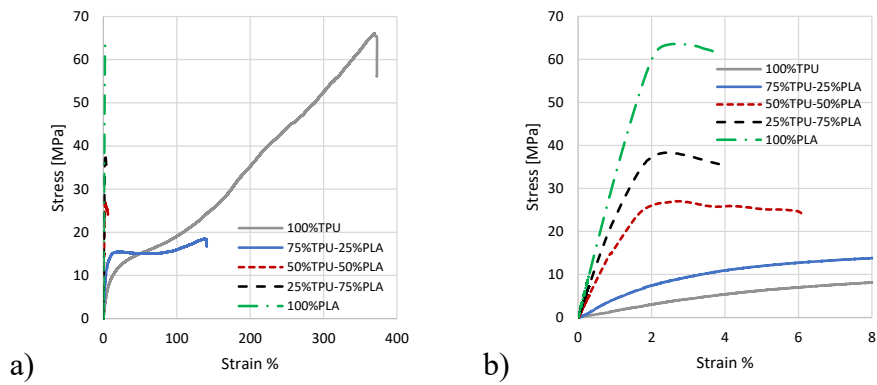
Figure 97. a) Stress – Strain curves for the different PLA – TPU mixes; b) Enlargement of the Stress – Strain curves at low deformation percentages.
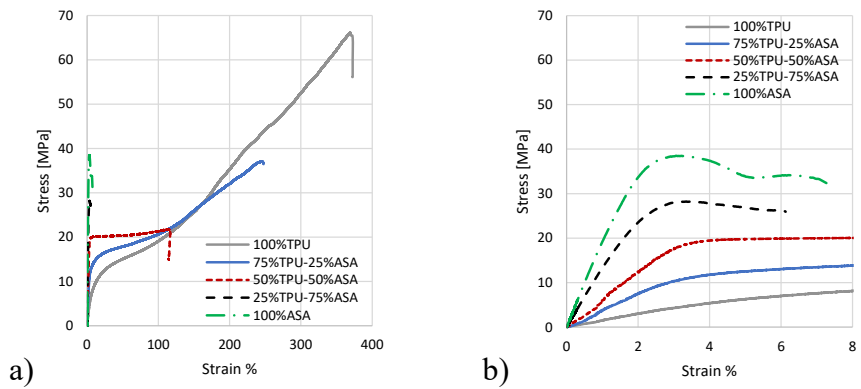
Figure 98. a) Stress – Strain curves for the different ASA – TPU mixes; b) Enlargement of the Stress – Strain curves at low deformation percentages.

The results of the analysis of the Young Modulus, UTS, and maximum strain for the PLA-TPU and ASA-TPU series are summarized in the plots in Figure 99.
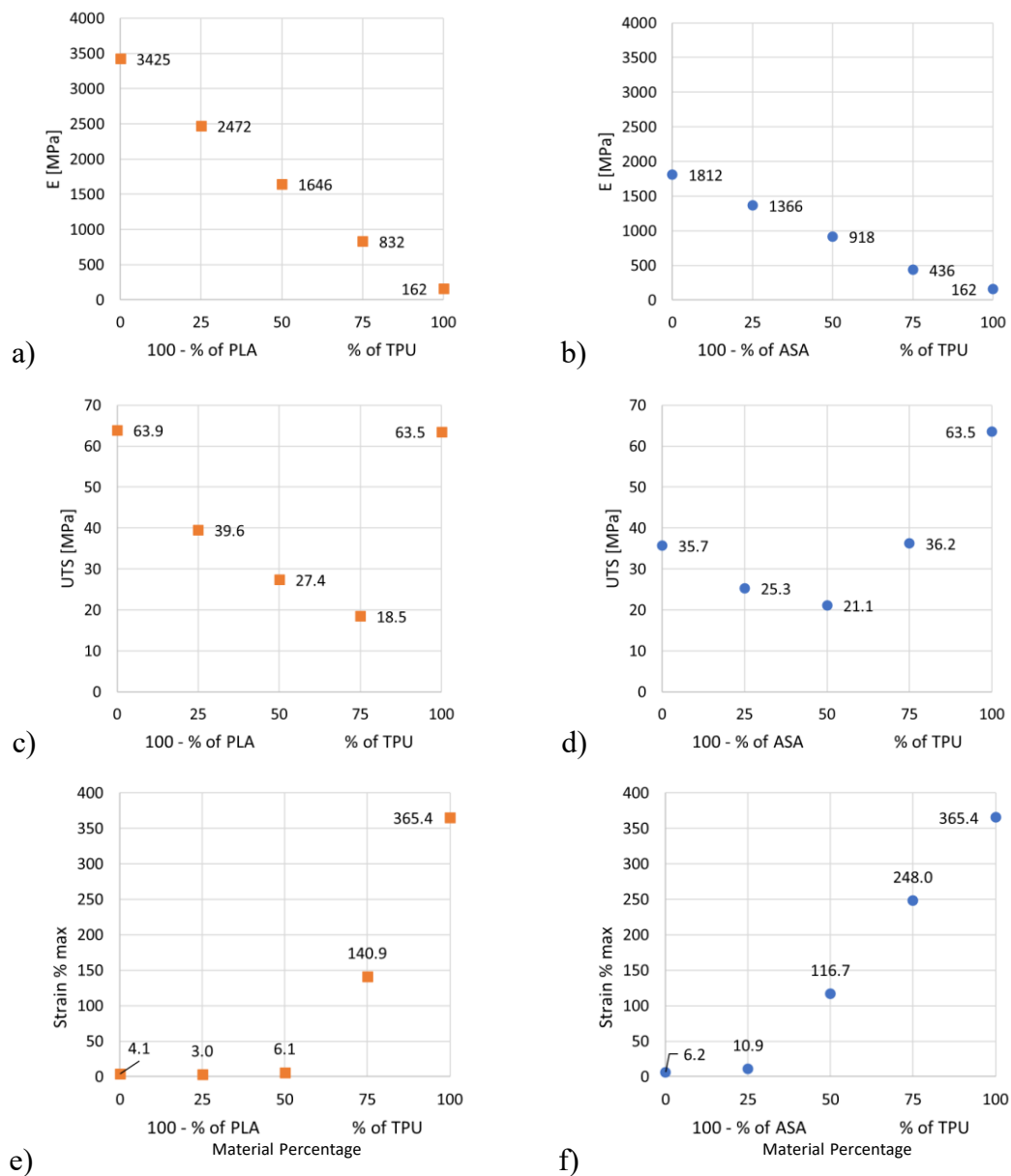
Figure 99. Results of the mechanical tests: (a) Young modulus of the PLA – TPU mixes, (b) Young modulus of the ASA – TPU mixes, (c) Ultimate Tensile Strength of the PLA – TPU mixes, (d) Ultimate Tensile Strength of the ASA – TPU mixes, (e) maximum strain of the PLA – TPU mixes, (f) maximum strain of the ASA – TPU mixes.

The results of the not-mixed materials, i.e., PLA, TPU, and ASA, are in agreement with the data declared by the filament producer [256]. A mismatch is found for the maximum strain of the ASA samples, where the obtained mean value, 6.2%, differs from the datasheet, 35%. Nevertheless, similar maximum strain values of 6 % can be found in the literature; for instance, Vazquez Martinez et al. [270] obtained comparable results by

145

additively manufacturing ASA specimens testing several process parameters combinations. More in general, an agreement is found between the results of the mechanical characterization in the present study with other studies in the literature for PLA [271–273], ASA [270,274], and TPU [275].

Moving to the mixed materials, the Young's modulus displays a similar trend for both PLA–TPU and ASA–TPU series. It consistently decreases with higher TPU percentages. Conversely, the strain at failure tends to increase with higher TPU content, except for the 75% PLA – 25% TPU combination. However, this specific mixture doesn't deviate significantly from the overall trend due to its proximity in values with surrounding combinations. Additionally, up to 50% of PLA, the elongation at failure doesn't show a significant increase. A distinct pattern emerges in the Ultimate Tensile Strength (UTS). The performance of the material blends is generally lower compared to the single materials. The behavior is not linear: UTS decreases for intermediate mixes, reaching its lowest point in the 25% PLA – 75% TPU (18.5 MPa) and 50% ASA – 50% TPU (21.1 MPa) combinations. Then, it begins to rise again, eventually reaching the UTS of pure TPU (63.5 MPa). This trend is attributed to the higher stiffness of PLA and ASA, causing them to bear the load more effectively than TPU. Consequently, at the same level of deformation, the stress is higher in the stiffer material (PLA or ASA), leading to an earlier breakage. As the TPU percentages increase, the sectional area of PLA and ASA decreases, resulting in a sudden failure of the samples. Conversely, at higher fractions of TPU, when PLA and ASA components fracture, the UTS is determined by the sectional area of TPU, consequently increasing.

A comparison can be made with the work of Arifvianto et al. [276] in which PLA and TPU samples produced by AM are compared to a 50/50 mix; as in the present study, the mix presents an intermediate Young modulus, whereas the strain at break does not increase by adding TPU. It must be highlighted that in Arifvianto et al. [276] the samples were not obtained by coextrusion but by adopting a so-called "sandwich structure" where PLA and TPU layers were deposited in an alternating manner and the mechanical properties of the starting materials are different from the one of the present work. More, the results of the UTS value of the 50% PLA – 50% TPU mix (27.4 MPa) are in the range of the ones obtained by Kennedy and Christ [251] (17 MPa ÷ 38 MPa) that tested 50% PLA – 50% TPU blends obtained by "in-situ active mixing" and manufactured tensile

specimens both parallel and perpendicular to the applied test load. The elastic modulus of the present study for a 50/50 mix of PLA and TPU (1646 MPa) is higher than the ones of Kennedy and Christ (889 MPa maximum); this could be explained by different materials, process parameters, and a different material mixing approach.

Figure 100 presents a comparison between the elastic moduli derived from the analytical model and those obtained from the tensile tests. It's important to highlight that the analytical model demonstrates a similar trend for both material combinations. This analytical model serves as a simplified representation of material behavior. Despite the experimental data being collected under varied conditions (such as orientation on the building plate and contour pattern for perimeters), the elastic modulus E_y demonstrates behavior within the range of the model and is closely aligned with linearity.
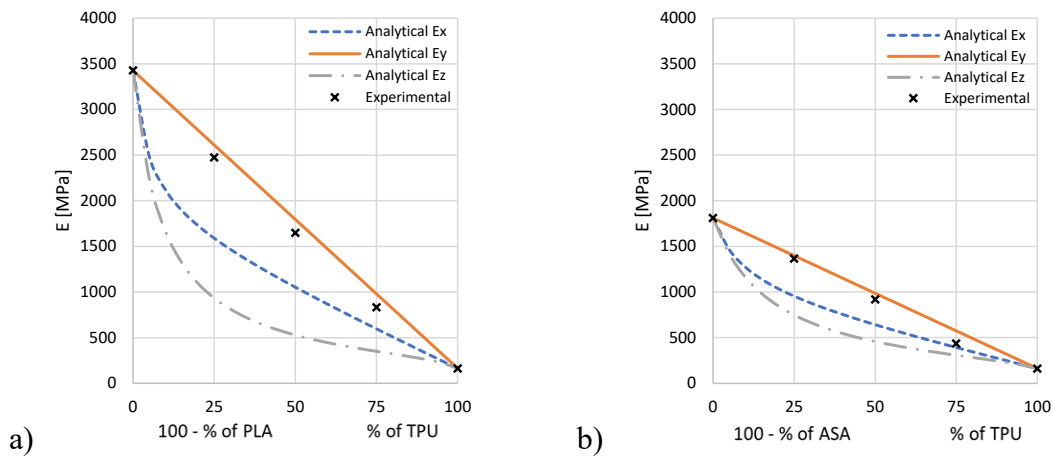
Figure 100. Comparison of the elastic moduli of analytical model and tensile tests for the couples: a) PLA-TPU and b) ASA-TPU.

Further tests should be performed to verify the effectiveness of the model considering also different manufacturing directions.

3.2.2. Porous Bioceramics

Porous bioceramics have garnered substantial interest for their applications in the biomedical field, including as scaffolds for bone grafts [277], bone fillers[278], orbital implants [279], and carriers for drug delivery [280]. Bioactive ceramics are commonly fabricated into three-dimensional porous scaffolds, serving as frameworks that facilitate and guide tissue ingrowth and regeneration [281,282]. The primary challenge in bone tissue engineering lies in crafting porous bioceramics that exhibit both a highly porous

architecture and possess sufficient mechanical strength and bioactivity to effectively address load-bearing bone defects [283]

The production of highly porous bioceramic foams encompasses three primary techniques: the replica method [284], the sacrificial template method [285], and the direct foaming of liquid suspensions or solutions [286]. In the replica method, a polyurethane foam is immersed in a ceramic slurry, yielding a macro-porous structure with evenly distributed pores. Upon high-temperature sintering, the organic components are removed, resulting in a ceramic foam scaffold characterized by interconnected pores [287]. The sacrificial template technique introduces porosity through the addition of fillers (porogens). Additionally, ceramic foams featuring substantial interconnected porosity can be generated by directly foaming a slurry or solution, followed by the solidification of the foamed mixture (achieved through gel casting or cross-linking).

Calcium silicate-based bioceramics, particularly $CaSiO_3$, have garnered substantial attention for their potential in bone tissue regeneration and implant coatings due to their remarkable bioactivity and degradability. However, the rapid dissolution and degradation rates of $CaSiO_3$ ceramics due to chemical instability have restricted their widespread biological applications. To enhance the biological performance of $CaSiO_3$ as a bone substitute material, one approach is to modify its chemical composition. This can be achieved by introducing various elements like Zn, Mg, Ti, Sr, and Zr. This leads to the development of silicate ceramics with distinct degradation rates, altered biological behavior, and modified mechanical properties. The combination of these desirable features positions these ceramics as promising candidates to meet the demanding requirements of medical applications [288].

Hardystonite ($Ca_2ZnSi_2O_7$) is a bioceramic rich in calcium that was developed by introducing zinc (Zn) into the calcium-silicon oxide system to enhance its chemical stability [289]. Ceramics derived from the sol-gel method using hardystonite have shown promise in bone tissue engineering [290,291]. These materials have been proven to accelerate the growth rate of mesenchymal stem cells (MSCs) derived from human bone marrow and encourage their specialization into bone-forming cells [290]. Furthermore, $Ca_2ZnSi_2O_7$ ceramics have demonstrated the ability to facilitate cell attachment, increase cellular proliferation, and enhance differentiation compared to $CaSiO_3$. Additionally,

when in contact with human osteoblast-like (HOB) cells, $Ca_2ZnSi_2O_7$ has been observed to stimulate the expression of alkaline phosphatase (ALP), osteocalcin, and collagen type I [291]. Moreover, hardystonite ceramics possess improved biocompatibility, bending strength, and fracture toughness compared to hydroxyl-apatite (Hap) and $CaSiO_3$ [289,292]. Previous research has also shown that it is possible to develop zinc-containing silicates, such as hardystonite ($Ca_2ZnSi_2O_7$) and willemite (Zn_2SiO_4), by simply incorporating ZnO powders into a bioglass powder (AP40 glass) that crystallizes in the apatite/wollastonite system. Alternatively, they can be embedded in the preceramic polymer as additional fillers, followed by heating at 1000°C. The mechanical properties of the resulting bioceramics were contingent on the crystalline phase composition, with an increase in strength observed when hardystonite was present [288]. These findings suggest that hardystonite ceramics hold significant promise for applications in bone regeneration and hard tissue engineering.

Silicone resins, combined with phosphates and other oxide fillers, have recently emerged as a viable feedstock for producing silicate bioceramics like commercial Biosilicate® glass-ceramics. This combination of silicones and engineered fillers facilitates the creation of innovative carbon-infused Biosilicate-based composites, notably enabling the straightforward application of AM techniques. Masked stereolithography printing was effectively employed with polymer-derived materials resembling Biosilicate® glass-ceramics, achieved through blends of silicone and photocurable acrylates. The more advanced printing technology, combined with ceramic transformation, allowed fabrication of scaffolds with a complex geometry and a distinctive control of overall porosity. The fine-tuning of the silicone/fillers ratio proved crucial in optimizing this specific AM process to produce component that align with the intended phase composition. The transition from a polymeric precursor to a glass-ceramic system interacted with the manufacturing technology. The porosity developed during the ceramic transformation of both the silicone precursor and the fillers compensated for any deviations from the target model porosity that may have arisen during the printing process.

Based on the promising results highlighted in the literature regarding the use of silicone and fillers to produce silicate bioceramics [293], combined with the favorable properties of hardystonite [294], this study conducts a comprehensive comparison involving

different raw materials systems (glass powder and silicone with fillers) and VPP AM technologies.

In the following section it is described the design, manufacturing and testing of highly porous 3D scaffolds based on doped hardystonite as a promising silicate bioceramic glass material for AM of bio-active, bio-resorbable applications. Two different mixtures were investigated, one based on solid solutions and the other on silicone/fillers. The macro porosity was designed by implementing 3D models of gyroids structures corresponding to different relative density (85, 90 and 95%). The 3D models were then printed using two different mixtures with two VPP technologies, i.e., masked Stereolithography (mSLA) and Digital Light Processing (DLP). Geometrical and mechanical characterizations were performed. Shrinkage and porosity were measured on green and fired scaffolds to verify the geometrical fidelity with respect to the designed ones. Mechanical characterization involved the realization of uniaxial compression tests. Porosity and compression strength permitted the comparison between the various samples.

3.2.2.1. Advanced additive manufacturing of silicate bioceramic scaffolds

The utilization of bioceramics porous structures as bone scaffolds serves a dual purpose. It not only offers structural reinforcement and encourages the infiltration of new bone tissue but also furnishes mechanical support during the process of tissue regeneration through mechano-transduction.

From the standpoint of synthetic bone graft engineering, attaining the desired mechanical properties in grafted scaffolds can be a complex task, primarily because of the increased porosity. Nevertheless, the incorporation of multi-scale (hierachical) porosity, spanning from macro to micro and nano levels, within 3D scaffolds presents encouraging avenues [293]. Larger interconnected macropores, exceeding 100 μm in size, serve a pivotal role in promoting bone growth, regeneration, and the transport of essential nutrients. Concurrently, micro- and nano-porosity fosters cell adhesion and proliferation.

In load-bearing areas, a delicate balance between mechanical reinforcement and controlled degradation is paramount. This stability is critical for ensuring a gradual transfer of load to the renewing bone tissue. Therefore, adjusting these features to create

materials with a favorable strength-to-density ratio, coupled with an optimal microstructure, remains a central challenge in the domain of bone tissue engineering.

3.2.2.2. Materials and Methods

The present investigation relates to hardystonite ($Ca_2ZnSi_2O_7$) glass, which is one of the most interesting bioceramic materials studied in recent years. This investigation employed a Sr-doped hardystonite composition. The XRD spectrum showed overlapping peaks between hardystonite and åkermanite, which resulted in the nomenclature hardystonite-åkermanite-Sr (HAS). The chemical formula is $Ca_{1.7}Sr_{0.3}Mg_{0.3}Zn_{0.7}Si_2O_7$.

Two systems were investigated using different raw materials (Figure 101). The first system comprises a combination of modified hardystonite glass powder (particle size <0.025 mm), suspended in a photocurable acrylate resin (PCR) (Though Resin, Prusa Research a.s., Prague, Czech Republic) (Table 18). The mixture was homogenized for 20 min manually (Figure 101.a).
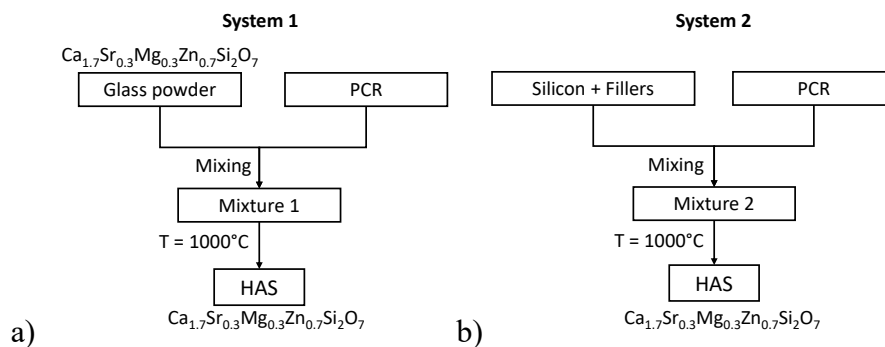
Figure 101. The two mixtures systems: a) System 1: glass powder based mixture, b) System 2: Silicone + Fillers based mixture

The second system consists of a silicone-based blend (Figure 101.b). A commercial solid silicone resin, H44 (Wacker-Chemie GmbH, Munich, Germany), was selected as the silica precursor. The silicone was mixed with the same commercial photocurable acrylate resin (Though Resin, Prusa Research a.s., Prague, Czech Republic), using isopropyl alcohol (IPA) to adjust the viscosity and to match the solid fraction with the first mixture. The mixture underwent manual homogenization for 20 minutes. Fillers were added following the amounts specified in Table 19. Raw materials and compositions for the silicone-based mixture (System 2), and subsequently homogenized in a mixer for another 30 minutes. For fillers, calcium carbonate ($CaCO_3$, <10 μm, industrial grade, Bitossi,

Vinci, Italy), magnesium oxide ($Mg(OH)_2$, <10 μm, reagent grade, Sigma-Aldrich, Germany), strontium carbonate ($SrCO_3$, <10 μm, reagent grade, Sigma-Aldrich, Germany), and zinc oxide (ZnO) were used. The total solid fraction resulted in 37 vol% for both the mixtures.

Table 18. Raw materials and compositions for the glass powder based mixture (System 1)

Raw Materials	Volumetric fraction [vol%]
$Ca_{1.7}Sr_{0.3}Mg_{0.3}Zn_{0.7}Si_2O_7$	0.37
PCR	0.63

Table 19. Raw materials and compositions for the silicone-based mixture (System 2)

Raw Materials	Volumetric fraction [vol%]
H44	0.26
$CaCO_3$	0.08
$Mg(OH)_2$	0.01
$SrCO_3$	0.02
ZnO	0.01
PCR	0.35
IPA	0.27

XRD analyses are performed on the powder of the fired samples to verify the actual composition.

Lattice specimens measuring 10 mm x 10 mm x 10 mm were constructed with gyroid structures, having three different porosity levels: 85%, 90% and 95%, i.e. 15%, 10% and 5% relative density, obtained by modifying the wall thickness. A Gyroid surface is a type of TPMS, which is deinfed by the equation $(2\pi x/L) * cos(2\pi y/L) + sin(2\pi y/L) * cos(2\pi z/L) + sin(2\pi z/L) * cos(2\pi x/L) = 0,$ whereby L represents the cell size. The lattice cell size used was 5 mm x 5 mm x 5 mm, resulting in 2 repetitions for each Cartesian axis. The CAD representation of the structures is displayed in the figures above Table 20. The method detailed in section 3.1.3 was used to model these structures, which results in a uniform file size in .stl format for all 3D models, ensuring a similar number of faces and vertices. The resulting thicknesses utilized were 0.262 mm (85%), 0.176 mm (90%), and 0.087 mm (95%). The specimen volumes decreased uniformly. The porosity

of the models slightly deviated from the design presented in Table 20 using these parameters. In addition, the 95% model had a minimum wall thickness, which is more than three times the maximum size of the glass powder, and around two time the accuracy (pixel size) of the 3D printing machines (Appendix B).

Table 20 Geometric models characteristics

a)   b)   c)
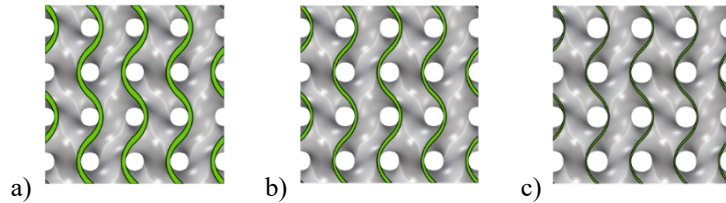
Model Name	Gyr_85_5_10	Gyr_90_5_10	Gyr_95_5_10
Design Porosity [vol%]	85.0	90.0	95.0
Model Porosity [vol%]	85.3	90.1	95.1
Wall Thickness [mm]	0.262	0.176	0.087
Volume [mm^3]	147.29	99.25	49.23
File Size (STL) [MB]	5.142	5.158	5.163

Eight samples are produced using two different VPP technologies. The first technology involves a mSLA desktop printer (Original Prusa SL-1S, Prusa Research a.s., Prague, Czech Republic) operating in the visible light range at 405 nm. The second technology utilizes a DLP industrial machine (Lithoz CeraFab 7500, Lithoz GmbH, Wien, Austria) operating in the same range at 460 nm, which is developed for ceramics materials (see Appendix B).

For the first system using the Prusa SL-1S, the exposure time was set at 13-15 seconds for the first 6 layers and 2.5 seconds for the other layers. The material printing profile, which governs the speed of the vat tilting movement, was set to "fast" (2.5 seconds). For the second system, the exposure time for the first 6 layers was 40 seconds, followed by 7 seconds for the remaining layers. The high-density printing profile (15 seconds) was used. For Lithoz, the default parameters were used for both mixtures since no optimization study has been conducted on them. Unlike Prusa Slicer, Lithoz software provides more parameters, resulting in a finer control of the process. However, exposure time cannot be modified as an explicit parameter when using the proprietary software. The DLP intensity, set at 92.35 mW/cm^2 (DLP Energy = 200 mJ/cm^2), is a related parameter. These

parameters vary slightly between the first five layers and subsequent layers. The rotation speed and angle of rotation, which are related to the machine movement of the vat for active mixing, are set to 150°/s and 360° respectively. This movement is highlighted by the red rounded arrow in the vat in Figure 102, which depicts the rotation movement of the vat. Before commencing the printing process, manual addition of the mixtures directly into the vat is required for both technologies. For both technologies, the samples are printed directly on the platform without the use of a pad, i.e., a basement to improve first layer's adhesion.

Table 21 Parameters used in the production of the Gyroid Lattices: Prusa SL-1S

Prusa SL-1S	System 1	System 2
Layer Thickness [mm]	0.025	0.025
Exposure Time [s]	2.5	7
Exposure Time Initial [s]	13-15	40
Material Printing Profile	Fast (2.5 s)	High Viscosity (15 s)
Others	No Pad	

Table 22 Parameters used in the production of the Gyroid Lattices: Lithoz Cerafab 7500

Lithoz CeraFab 7500	System 1	System 2
Layer Thickness [mm]	0.025	0.025
DLP intensity [mW/cm^2]	92	92
DLP energy [mJ/cm^2]	200	200
Rotation speed [°/s]	150	150
Angle of rotation [°]	360	360
Others	No Pad	

1. Light Source
2. DMD-chip (dynamic mask)
3. Optic
4. Material vat
5. Coating blade
6. Back light
7. Building platform
8. Load cell
9. Manufactured part
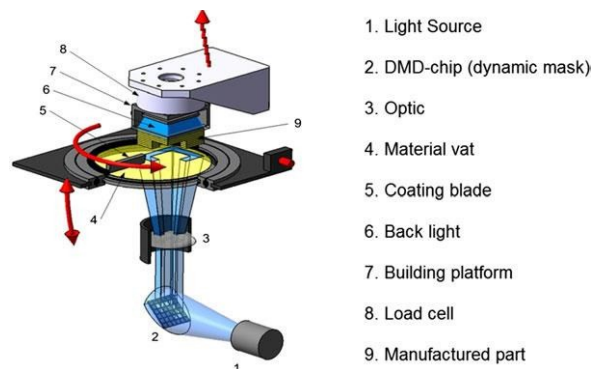
Figure 102. Schematic setup of the Lithoz Cerafab 7500 machine [295].

After printing, the samples underwent cleaning using compressed air and were washed with isopropyl alcohol or ethanol using ultrasound technology. They were then dried and cured for 3 and 5 minutes respectively at 30 °C in a UV chamber (Prusa CW-1S, Prusa Research a.s., Prague, Czech Republic). To complete the process, the scaffolds were subjected to a two-step heat treatment in air, including debinding at a rate of 3 °C/min up to 650 °C for 3 hours and sintering at a rate of 5 °C/min up to 1000 °C for 1 hour. It is worth noting that the polymer-to-ceramic conversion occurs with gas release, volume shrinkage (20–30%, linear shrinkage) and formation of porosity (micro and macro). Here, the debinding rate is intentionally kept relatively low to facilitate the gradual decomposition of the photocurable resin, preventing the formation of cracks resulting from gas release. Higher debinding rates are not recommended, as they can lead to increased distortions in the final ceramic part and the occurrence of macro defects, ultimately compromising mechanical properties. [296]. On the other hand, the debinding rate could be further reduced, however lengthening the time required to obtain the final piece.

The geometrical density of the green and fired samples was measured using a digital caliper and by weighting with an analytical balance. The apparent and true densities of the printed samples were measured by He pycnometry (Ultrapyc Anton Parr Graz, Austria). The total, open, and closed porosities were then calculated based on the density values obtained from the measurements.

Morphological and microstructural characterizations were performed by optical stereomicroscopy (AxioCam ERc 5s Microscope Camera, Carl Zeiss Microscopy, Thornwood, New York, NY, USA) and scanning electron microscopy (SEM) (JEOL 7600 F, JEOL Ltd., Tokyo, Japan) using an accelerating voltage of 20 kV. The mineralogical analysis after firing was conducted by X-ray diffraction (XRD) (Bruker AXS D8 Advance, Bruker, Germany).

The compressive strength σ_c was measured for each combination using a universal material testing machine (Quasar 25, Galdabini S.p.a., Italy) equipped with a 25 kN load cell. The machine operated at a cross-head speed of 1 mm/min, and three fired samples were tested. The specimens were compressed in the z axis, i.e., along the direction of manufacturing. To ensure a more accurate comparison, the solid phase's bending strength

σbend was computed using the reverse version of the Gibson-Ashby relation designed for extremely porous ceramic lattices:

$$\sigma_{bend} = \frac{\sigma_c}{\rho_r^{\frac{3}{2}} \cdot C}$$

where ρ_r is the relative density (ρ_r = 1 – Total Porosity), σ_c is the compressive strength and C is a dimensionless constant (C = 0.2).

3.2.2.3.   Results and discussion

The compositions of the fired samples for both mixtures match the $Ca_{1.7}Sr_{0.3}Mg_{0.3}Zn_{0.7}Si_2O_7$ composition (hardystonite) as visible in the XRD pattern in Figure 103.
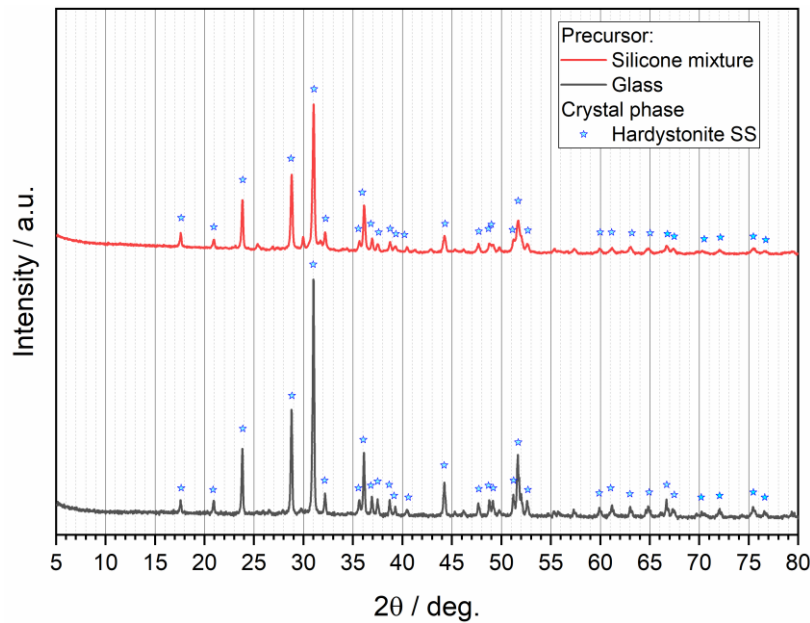
Figure 103. XRD patterns of different the two different mixtures heat treated at 1000 °C: glass powder-based mixture is showed in red color; silicone-based mixture is showed in black color. Hardistonite peaks are identified by the blue star symbol.

The overall dimensions of the three lattice specimens allow for effective printing with both technologies, mitigating the segregation issues observed in powder-based mixtures, particularly for Prusa SL-1S. Notably, the 95% gyroid models were not successfully printed using both mixtures.

The shape of the samples is well-maintained for both green and fired specimens. However, distortions become apparent in the fired samples, contingent on the porosity percentage and the composition of the mixture. As illustrated in Figures 54a, b, and 55b, minor distortions are associated with the 85% porosity samples across all four combinations. Conversely, higher degrees of distortion are more pronounced in the 90% and 95% porosity samples, especially when utilizing the glass powder mixture (see Figure 104.a and b).
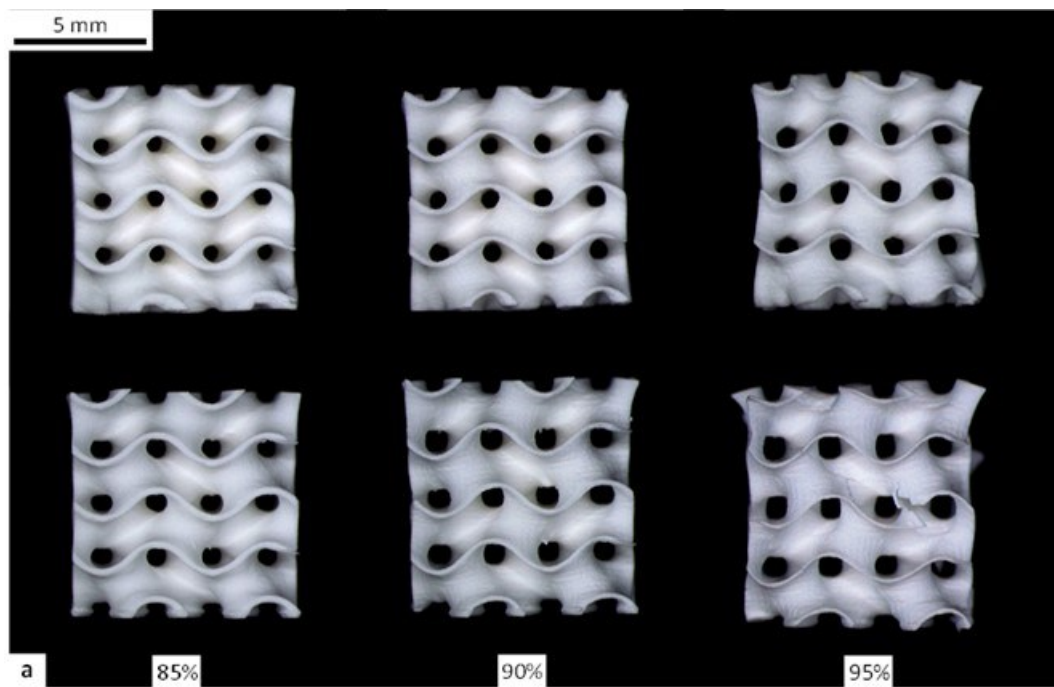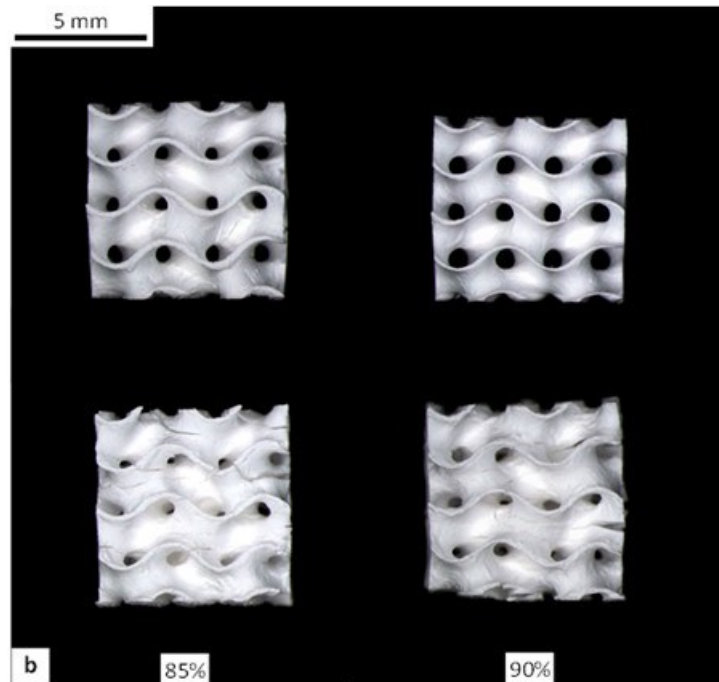
Figure 104. Side view of all the fired samples: a) Glass powder mixture samples, Lithoz on the top side, Prusa on the bottom; b) Silicone-based mixture samples, Lithoz on the top side, Prusa on the bottom.

The samples produced with the powder-based mixture exhibit superior surface finishing and well-defined edges compared to those created with the silicone-based mixture (see Figure 107). No discernible coarsening effects, typically induced by uncontrolled viscous flow in sintered glass-ceramics, are observed. This is crucial, as uncontrolled viscous flow can potentially compromise the three-dimensional structure entirely. The presence of glass powder is evident in the green samples, and layering is more pronounced in the case of samples printed with Prusa (Figure 107.a,c) compared to those produced with Lithoz. After firing, the silicone-based samples exhibit small surface cracks, visible for both technologies (Figure 107.f, h). These cracks are attributed to reactions during the heat treatment, possibly worsened by excess and uncleaned mixture on the walls, particularly in the case of Prusa SL-1S. SEM micrographs better highlight these cracks as visible in Figure 105.e.
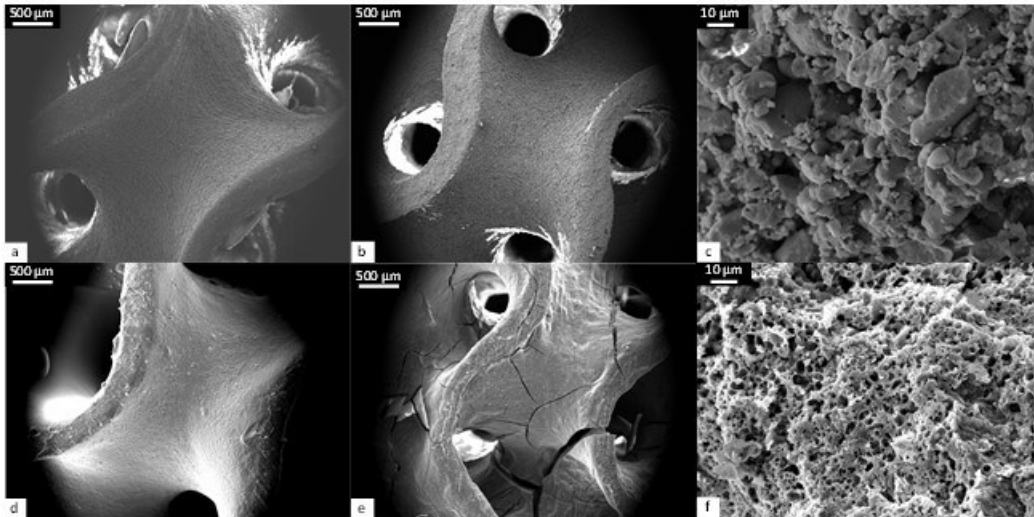
Figure 105. SEM images of green (a,d) and fired (b,c,e,f) samples (85% porosity) for both mixtures (top: glass powder; bottom: silicone) printed with Prusa.

The excess of mixture is prominently visible in the green lattices (Figure 106.b and Figure 107). This excess was not entirely removed from the surface, resulting in a reduction in porosity for this type of green sample. Additionally, the excess mixture on the surface is also attributed to the printing process of the Prusa SL-1S and becomes more noticeable with highly viscous fluids, such as the silicone-based mixture. After each layer, the platform of the Prusa printer goes up slightly, but the sample remains largely immersed in the mixture. In contrast, the Lithoz distributes a thin film of mixture through a rotational movement of the circular vat, facilitated by a coating knife (Figure 102), after every layer. Consequently, the samples are not immersed in the mixture, resulting in a nearly clean surface. This rotational motion, which induces mixing of the mixture after each layer, enhances the stability of mixtures containing suspended powder, as observed in the case of mixture 1. This process helps to mitigate or prevent segregation, which can limit the processability and printing time window, particularly in the case of the Prusa SL-1S.

As previously noted, the 95% gyroid models could not be successfully printed using the silicone-based mixture. This is likely attributed to the low thickness of the lattice walls (0.087mm), which poses challenges in the initial layers' attachment to the platform. Even if the first layers are successful, the high viscosity of the mixture leads to the material adhering to the lattice surface during the printing process. This, in turn, causes the thin

printed walls of the lattice with 95% porosity to collapse under the weight of subsequent layers.
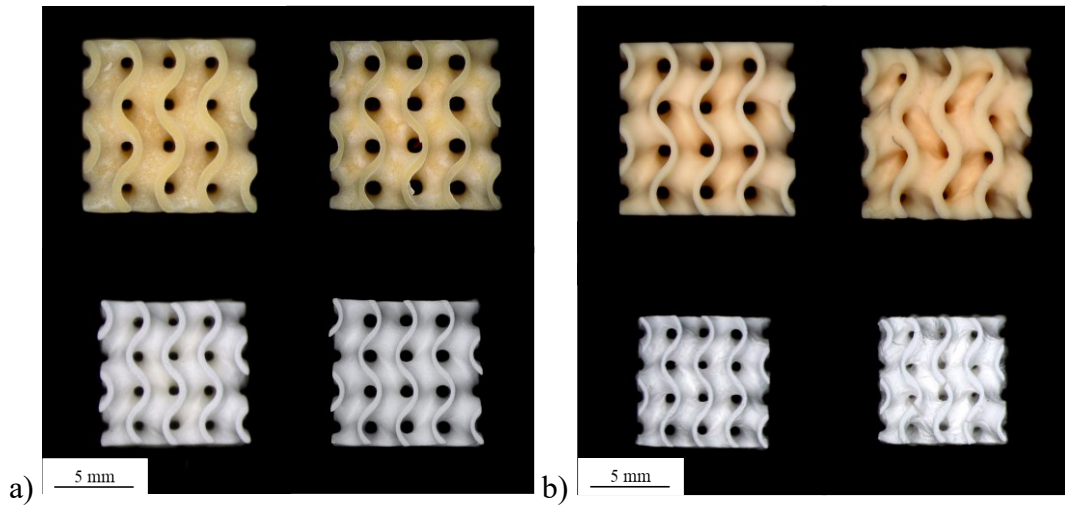
Figure 106. 85% porosity samples (Top View): a) System 1, Prusa - Lithoz, Green and Fired Samples, b) System 2, Prusa - Lithoz, Green and Fired Samples.

The porosities of the geometric models closely align, with slight discrepancies, with the intended design porosity (Table 20). Notably, the size of the STL files diminishes relative to the dimensions of the utilized unit cell. However, the porosity of the printed samples diverges from that of the geometric models, depending on the technology and mixture employed. The relationship between these latter porosities is complex and warrants further discussion. Furthermore, the total porosity aligns with the apparent porosity (P_{app}), as closed porosity is nearly negligible. This is attributed to the behavior of the two mixtures throughout the printing and firing processes, combined with the minimal thickness of the walls in the lattice structures (less than 0.262 mm in the model with 85% porosity, as indicated in Table 20). These factors collectively mitigate the probability of trapped air bubbles within the solid lattice structure.
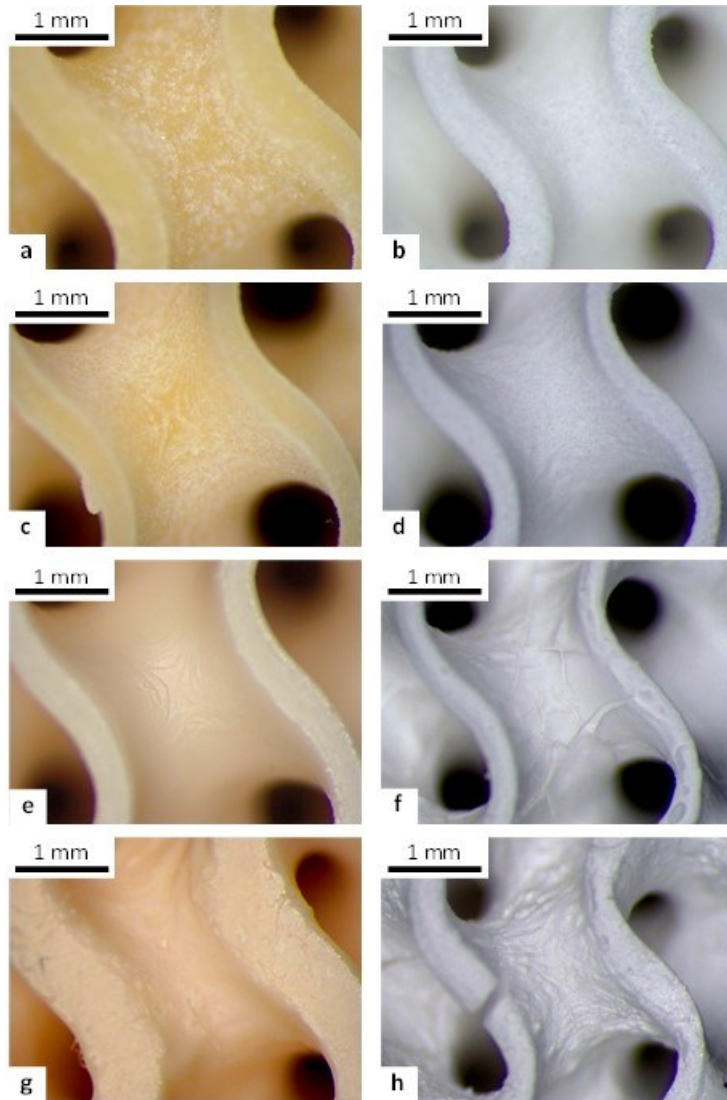
Figure 107. Magnifications of the surface portion (top view) of the 85% green (left side) and fired (right side) samples for all the combinations. a,b,c,d) Glass powder mixture and e,f,g,h) Silicone-based mixture. a,b,e,f) printed with Lithoz CeraFab 7500; c,d,g,h) printed with Prusa SL-1S.

The utilization of glass powder suspensions, as the first mixture, has a detrimental impact on printing resolution when compared to more homogeneous liquid feedstock. This effect arises from the scattering of light by solid particles, which in turn alters the depth of curing. While adjustments in exposure times can mitigate this, it remains possible for the photocurable resin to cure beyond the intended projection area. This leads to a reduction in porosity, as an expanded projected area corresponds to an increased solid occupancy in a printed layer.

In our specific case, a decrease in overall porosity was observed in printed samples created with the glass-powder mixture using Lithoz (see Figure 107.a, b). This outcome was attributed to the elevated DLP energy and intensity applied, resulting in an extension of the projected area and increased scattering. More favorable outcomes were achieved for samples printed with Prusa SL-1S, as the process parameters were finely tuned to better adhere to the intended porosities (see Figure 107.c, d). Additionally, it's noteworthy that the UV LED wavelengths differed between the two technologies.

In the instance of the silicone-based mixture, the thermal conversion of silicone and the interaction between polymer-derived silica and filler counteracted the reduction in porosity. The cured parts were not intended to undergo densification close to conventional sintering. Instead, they were anticipated to transition into porous walls, facilitated by the release of gas from fillers and the polymer matrix during ceramic conversion. As a result, the overall porosity, which is predominantly open, closely aligned with the porosity of the models, mirroring sintered structures. This behavior is prominently demonstrated in Figure 108.b, particularly in the samples fabricated with Prusa SL-1S (Figure 105.f). For instance, in the case of samples designed for 85% porosity, the porosity increased from 56% to 82% after firing. High-viscosity mixtures, such as the silicone-based mixture used, exhibit ease of printing and produce cleaner results with Lithoz. This is attributed to the thin film of mixture distributed in the vat after each layer, which prevents complete immersion of the sample structure during printing. Additionally, the green samples exhibit greater precision as they are devoid of scattering effects (as depicted in Figure 107.e, g).
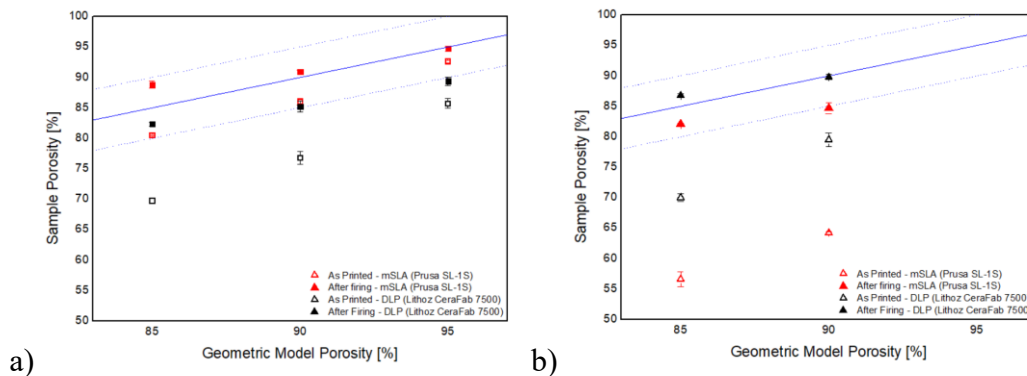
Figure 108. Porosity of samples (after printing and after firing) compared to the design porosity. a) Porosities of the samples printed with the glass powder based mixture; b) Porosities of the samples

A uniform shrinkage is observed in all three directions. For the powder-based mixture, it falls within the range of 10–15% in each direction, whereas for the second mixture, it ranges from 20–25%. Shrinkage is more pronounced in samples printed with the silicone-based mixture, primarily due to volume loss associated with the decomposition of the organic component.

Compressive tests reveal superior values for samples produced with Lithoz for both mixtures. The highest value is attained by the 85% glass powder-based sample, yielding a compressive strength $\sigma_c = 1.73 \pm 0.29$ MPa.

Excellent strength-to-density ratios were achieved, particularly in samples produced with Lithoz. This observation is substantiated by the compressive strength-to-density chart, displayed on a logarithmic scale axis in Figure 109, which provides a comparative overview of all the fired samples. The blue lines in the chart correspond to the model proposed by Gibson and Ashby, encompassing a range of σ_{bend} values from 50 to 250 MPa. Materials represented by points closer to the bottom left corner demonstrate an excellent balance of high compressive strength and low density. In this regard, the top-performing sample is the one with 95% porosity, a powder-based mixture realized with Lithoz.

As previously noted, the actual porosities of the fired samples slightly deviate from the designed values. Generally, samples printed with Lithoz exhibit higher compressive and bending strengths compared to those from Prusa. Furthermore, Lithoz-printed samples more closely adhere to the linear trend indicated by the σ_{bend} lines. All relevant properties are summarized in Table 23, Table 24 and Table 25.
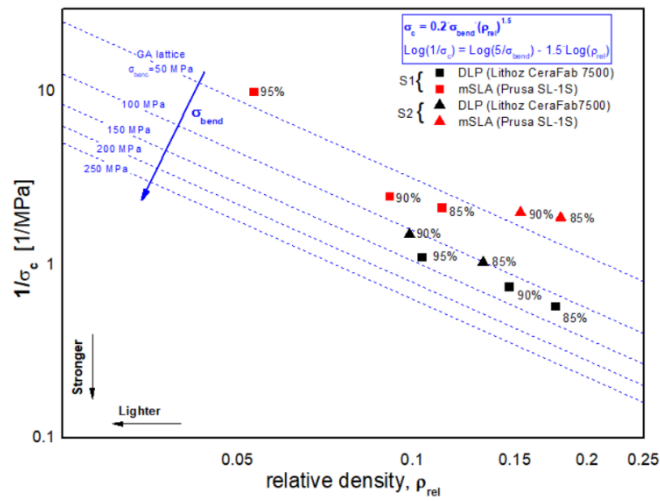
Figure 109. Compressive strength/relative density plot of developed porous materials. Glass powder-based (S1) and silicone-based (S2) mixtures are shown as square and triangle shapes respectively. The two printing technologies, i.e., Prusa and Lithoz, are identified in red and black color.

Table 23. Mechanical Properties, Gyroid Samples 85%

System	Machine	State	ρ_{geo} [g/cm³]	ρ_{app} [g/cm³]	P_{open} [vol %]	σ_c [MPa]	σ_{bend} [MPa]
S1	Lithoz	Green	0.59±0.01	1.97±0.01	69.7±0.4	-	-
S1	Lithoz	Fired	0.59±0.01	3.33±0.01	82.3±0.3	1.73±0.29	116.20
S1	Prusa	Green	0.41±0.02	2.11±0.01	80.5±0.1	-	-
S1	Prusa	Fired	0.37±0.02	3.34±0.01	88.8±0.6	0.47±0.06	62.12
S2	Lithoz	Green	0.47±0.01	1.57±0.01	70.0±0.6	-	-
S2	Lithoz	Fired	0.42±0.01	3.16±0.01	86.8±0.3	0.97±0.06	101.08
S2	Prusa	Green	0.68±0.02	1.56±0.01	56.6±1.2	-	-
S2	Prusa	Fired	0.58±0.03	3.22±0.01	82.1±0.1	0.53±0.06	34.97

Table 24. Mechanical Properties, Gyroid Sample 90%

System	Machine	State	ρ_{geo} [g/cm³]	ρ_{app} [g/cm³]	P_{open} [vol %]	σ_c [MPa]	σ_{bend} [MPa]
S1	Lithoz	Green	0.48±0.02	2.08±0.01	76.8±1.1	-	-
S1	Lithoz	Fired	0.49±0.03	3.32±0.01	85.2±0.9	1.33±0.06	116.91
S1	Prusa	Green	0.31±0.01	2.20±0.01	86.0±0.5	-	-
S1	Prusa	Fired	0.30±0.01	3.31±0.01	90.9±0.3	0.40±0.01	72.52
S2	Lithoz	Green	0.33±0.02	1.60±0.01	79.5±1.1	-	-
S2	Lithoz	Fired	0.31±0.01	3.04±0.01	89.8±0.4	0.67±0.12	102.55
S2	Prusa	Green	0.57±0.03	1.58±0.01	64.2±2.0	-	-

| S2 | Prusa | Fired | 0.48±0.03 | 3.13±0.01 | 84.7±0.9 | 0.50±0.02 | 41.63 |

Table 25. Mechanical Properties, Gyroid Sample 95%

System	Machine	State	ρ_{geo} [g/cm^3]	ρ_{app} [g/cm^3]	P_{open} [vol %]	σ_c [MPa]	σ_{bend} [MPa]
S1	Lithoz	Green	0.31±0.02	2.19±0.01	85.7±0.8	-	-
S1	Lithoz	Fired	0.35±0.02	3.29±0.01	89.4±0.7	0.9±0.2	130.19
S1	Prusa	Green	0.19±0.01	2.55±0.01	92.6±0.2	-	-
S1	Prusa	Fired	0.18±0.01	3.33±0.01	94.7±0.4	0.1±0.0	40.69
S2	Lithoz	Green	n.d.	n.d.	n.d.	-	-
S2	Lithoz	Fired	n.d.	n.d.	n.d.	n.d.	n.d.
S2	Prusa	Green	n.d.	1.57±0.01	n.d.	-	-
S2	Prusa	Fired	n.d.	3.30±0.01	n.d.	0.3±0.0	-

Additional samples were designed and printed with smaller cell sizes to investigate the behavior of the lattice structure while maintaining the same relative density and bioceramic material. The models were gyroid structures with three varying cell sizes: 5, 2.5, and 1.25 mm. The 5 mm cell size was previously discussed. All samples shared an 85% porosity, meaning they occupied the same volume (V = 147.62 mm^3). Consequently, as the cell size decreased, the walls became thinner (Figure 110 and Table 26). These samples were exclusively printed in limited quantities using Prusa SL-1S and the glass powder mixture. Since the samples were printed without pad, which typically aids initial layer adhesion to the platform, having smaller cells was advantageous for attachment, as it increased the contact surface area. The process parameters for printing and thermal treatment reflected those of the previously described samples.

The fired samples exhibit P_{open} that closely align with the designed 85% porosity. Specifically, it is slightly higher for the gyroid with a 5 mm cell size (~88%), quite accurate for the 2.5 mm cell size (~85%), and marginally lower for the 1.25 mm (~79%). This trend is attributed to the increased volume of trapped mixture within the pores and channels of the three structures during the printing process with Prusa SL-1S, as previously exposed. Notably, the pore dimensions for the three structures diminish as the unit cell size decreases (as evident in Figure 110 and Figure 111). Consequently, achieving perfect cleanliness within the inner part of the green lattice structures is challenging due to the intricate shape, resulting in residual trapped mixture that cannot be

entirely eliminated during firing. This phenomenon is particularly pronounced in the 1.25 mm cell size sample.

Regarding mechanical properties, reported in Table 27, both compression and bending strength (σ_c and σ_{bend}) increase as the cell size decreases. The strength progresses from σ_c = 0.47±0.06 MPa for the 5 mm to σ_c = 1.42±0.01 MPa for the 2.5 mm. Although the σ_c of the 1.25 mm sample is better than the one of the 5 mm cell size, and it appears to deviate from the expected positive trend, due to the aforementioned considerations regarding porosity. However, this aspect warrants further investigation in future studies.

Table 26 Geometric Models characteristics

Model	Porosity [vol%]	Volume [mm3]	Wall Thickness [mm]	File Size [MB]
Gyroid85_5	85.3	147.29	0.262	5.142
Gyroid85_2.5	85.2	147.62	0.134	10.363
Gyroid85_1.25	85.2	147.57	0.067	79.678
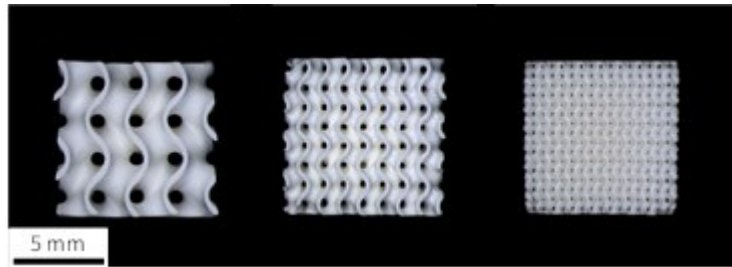
Figure 110. The printed samples with different unit cell size (Top view). From the left, unit cell size = 5 (Gyroid85_5), 2.5 (Gyroid85_2.5)and 1.25 (Gyroid85_1.25) mm. The samples are printed using the glass powder based mixture with Prusa SL-1S.
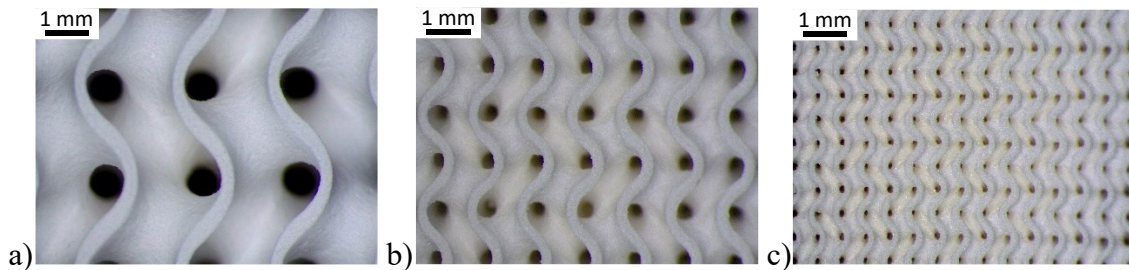
Figure 111. Magnification of the printed samples with different unit cell size (Top view). a) 5 mm, b) 2.5 mm and c) 1.25 mm.

Table 27 Mechanical properties of the fired samples printed with glass powder mixture with

Model	ρ_{geo} [g/cm³]	ρ_{app} [g/cm³]	P_{open} [vol %]	σ_c [MPa]	σ_{bend} [MPa]
Gyroid85_5	0.374±0.021	3.338±0.007	88.8±0.6	0.47±0.06	62.12
Gyroid85_2.5	0.486±0.002	3.307±0.002	85.3±0.2	1.42±0.06	97.74
Gyroid85_1.25	0.697±0.002	3.300±0.002	78.9±0. 2	1.13±0.06	72.10

4. Bio-inspired volumetric geometric modeling methods for AM – Natural Phenomena

In the area of bioinspired design methods simulated by math models, two geometric modeling methods have been implemented. The first concerns the Reaction-Diffusion model and the different patterns that can be generated. As an opening explorative study a method for generating tree-like supports for AM is proposed. The second method relies on another bioinspired model, the differential growth. The implemented method is a curve growing physics-based algorithm that mimics this phenomenon in 3D. Furthermore, this method is used in the design of counter-flow heat exchanger.

4.1. Reaction & Diffusion for AM supports

In this section a 2D implementation of a Reaction-Diffusion based on Gray-Scott model (described in Section 2.3.1) is investigated as a possible tool to generate geometric B-Rep models, due to the extreme variety of patterns that can be produced. Furthermore, a method for generating tree-like supports for AM are developed on top of the Reaction-Diffusion algorithm.

4.1.1. Method and tools

The method is based on a C# implementation by L. Delrieu of the modified Gray-Scott model of Reaction and Diffusion in 2D [297]. Rhinoceros 7 CAD software (McNeel & Associates, USA) and its plugin Grasshopper were the development environment.

The script calculates the concentration of the two species A and B locally for each index i, seen as belonging to a list. Once the loop on the 'layer' is finished, the next external loop is passed, starting to compute the concentrations from the values saved in the previous external loop. Finally, the values created for each external loop and stored in sub-lists equal to the number of steps are returned as output. Here is the pseudocode:

```
Initialize Variables:
n_point = n_x * n_y
Initialize Arrays A, B, Aprime, Bprime with size n_points
Initialize Lists A_stacked, B_stacked

Main Loop:
for i in range(_n_step):
  for j in range(_n_jump):
    for i_x in range(n_x):
```

```
    for i_y in range(n_y):
      Calculate Laplacian (dxA, dxB) based on neighboring pts
      Calculate AB2
      Calculate Aprime and Bprime using RD equation (f,k,dt)
      Update A and B with bounded values
        if j == 0:
          Add values to A_stacked and B_stacked
Finalize A_stacked and B_stacked:
Add 1.0 to A_stacked and B_stacked

Assign Results:
Aout = A
Bout = B
Astack = A_stacked
Bstack = B_stacked
```

In particular, the script has the following input parameters:

- n_x and n_y parameters determine the initial point grid resolution.
- A and B are lists representing the initial concentrations of species A and B respectively.
- Da and Db (Diffusion terms) are constants that affect how the concentrations of A and B change over time.
- f represents the feed rate of species A into the domain and the reduction of B.
- k represents the rate at which species B is reduced in the domain.
- dt is the discrete interval of time.
- n_step defines how many iterations ("layers") the simulation will have.
- n_jump determines how many time intervals the reaction-diffusion process occurs in each layer (sub-iterations).

As input for the concentration of A, a grayscale image is used (8-bit depth), then converted to a list of values in the range [0-1] by sampling the image using the grid points of the initial grid.

The script defines a method named modulo that helps handle boundary conditions when accessing neighboring points in the grid, using i_x + i_y * n, where n = n_y; in this way the 2D domain is wrapped at the boundaries. The script initializes the reaction by adding an artificial value of concentration for both species (A_stacked and B_stacked are initialized with 1.0 for every point). The main calculation loop starts with a loop over layers (n_step), followed by a loop over time intervals within each layer (n_jump). Within these loops, the script iterates over all points in the 2D domain (n_x and n_y). For each

point, it calculates the Laplacian using a convolution matrix. For one, two, or three-dimensional signals, the discrete Laplacian can be calculated by convolution with kernels [298]. The Laplacian calculation involves summing weighted values of neighboring points for both species A and B. The weights in the convolution 3x3 matrix k are defined as:

$$k = \begin{bmatrix} 0.05 & 0.2 & 0.05 \\ 0.2 & -1 & 0.2 \\ 0.05 & 0.2 & 0.05 \end{bmatrix}$$

After calculating the Laplacian, the script computes the changes in concentrations for both species (A' and B') based on the Gray Scott reaction-diffusion equations. The equations for Reaction-Diffusion Gray-Scott model are defined by:

$$A'[i] = A[i] + (D_A[i] * dx_A - A * B^2 + f * (1.0 - A[i])) * dt[i]$$

$$B'[i] = B[i] + (D_B[i] * dx_B + A * B^2 - (k + f) * B[i]) * dt[i]$$

where dx_A, dx_B are the Laplacians, f, k, D_A, D_B are the reaction and diffusion parameters and dt is the time interval; A, B are the concentrations of the two species and A', B' are the new concentrations. The script then enforces constraints on the concentration values to ensure they stay within a valid range (between 0 and 1). The concentrations at each point are added to A_stacked and B_stacked lists, forming a representation of the concentrations over time. Finally, the script appends another artificial value of 1.0 to A_stacked and B_stacked at the end of the simulation. The output parameters (Aout, Bout, A_stack, and B_stack) are assigned their respective values.

The simulation can be extended to form a 3D map of concentrations by stacking layers containing the values of the output lists. The values will be interpreted as sequential layers and then used to create the third dimension, i.e., the time represents the Z-Axis. In such terms, it can be considered a 2.5D algorithm because it works in the XY-plane, and the Z direction is defined asynchronously.

Those values are then associated to a voxel data structure, having the same XY resolution of the starting grid (n_x, n_y) and in Z direction n_step number of voxels, and a surface mesh can be extracted by means of marching cube algorithm by setting a specific isovalue within the domain of A or B concentrations.

Figure 112 shows the resulting patterns using the same concentration of A and B as input. The concentration of A is given as an image in grayscale colors (Figure 112.a) and B = 1 for all the grid points. The image has a resolution of 359x369 pixels in X and Y direction but is sampled using the resolution of the grid for simulation of the RD, in this case 51x51. By slightly modifying the value of k (Figure 112.b,c), the results are completely different: the first pattern is a 'solitons' pattern while the second is a 'stripes' pattern. The mesh surfaces extracted using the same isovalue = 0.3 are also different.
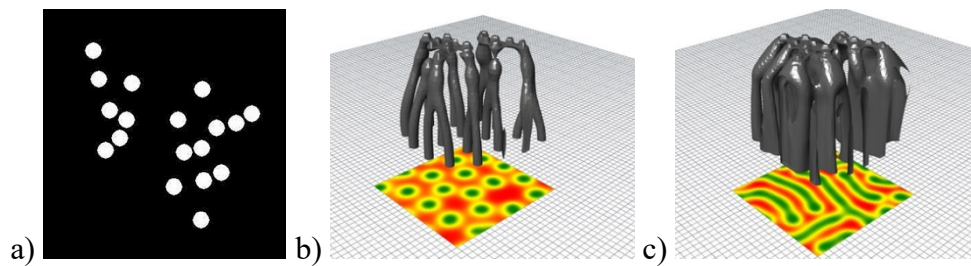
Figure 112. Effects of the variations of some parameters. a) Starting A concentration, as a grayscale image; b) B=1, Da=1, Db=0.3, f=0.05, k=0.064, n step=40, n jump=30, IsoValue=0.35; c) B=1, Da, Db=0.3, f=0.05, k=0.64, n step=40, n jump=30, IsoValue=0.35.

4.1.2. Case study, results and discussion

Considering the potentiality of the scripts, the algorithm is modified to realize tree-like support structures for AM. A specific Reaction-Diffusion (RD) pattern, i.e., a particular combination of f and k is used, to generate a branching structure.

4.1.2.1.   *Support Structures for AM*

Support structures in AM are crucial for ensuring the successful printing of complex parts. They provide support for overhanging features, holes, and bridges, maintaining part manufacturability and aiding in heat management. Not all technologies require supports, but they are essential for processes like FDM and VPP. In some cases, supports are made from a different material and can be easily removed after printing. In Binder Jetting and certain other methods, supports are rarely needed as the powder itself offers sufficient support. Overall, supports play a vital role in achieving accurate and high-quality 3D products.

To minimize the need for supports in AM, strategies fall into two categories: direct and indirect methods [181,299]. Direct methods involve modifying supports within the existing design, such as adjusting object orientation on the print tray or using different support materials for easier removal. Shape and structure optimization of supports is also a direct method. Indirect methods involve redesigning the original part using guidelines like DfAM or employing topology optimization with overhang constraints. While some solutions may require specialized knowledge, optimizing support shape and structure is generally accessible to users. Supports can be created separately, saved as STL models and imported directly into CAM software.

Support structures can be categorized into two groups based on geometry:

1. Simple:
   o Pillars: These are basic vertical structures projected from the build base to support overhangs. They consist of evenly distributed points touching the overhang areas.
   o Surfaces/Walls: Another straightforward approach involves using vertical or sloped walls or shells for support.
2. Complex:
   o Lattices: These structures replace solid bars or walls with a lattice pattern to reduce support volume while maintaining stability.
   o Fractals: Fractals are shapes where a part resembles the whole, regardless of size. They recursively repeat similar patterns.
   o Trees: These supports mimic the structure of trees.
   o Free-form: Generated by bioinspired or optimization algorithms like topology optimization [300], resulting in diverse shapes.

These complex geometries build upon simple shapes, are often generated through algorithms. Tree-like supports offer several advantages: they are easier to remove, cause less damage to the underside of overhangs, and can save up to 75% of material compared to straight vertical supports. However, they are best suited for non-flat overhangs, like nose tips or arches.
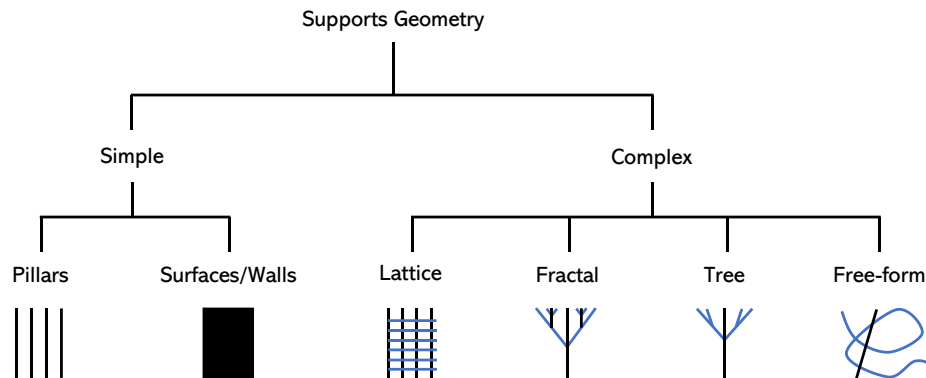
Figure 113. Support Taxonomy based on geometry.

In FDM, supports can take the form of either a lattice, a tree-like structure or even shells. In SLA, supports are thin and minimally touch the part to save material. For metal parts, lattice structures are typically used. Absolutely, free and proprietary 3D printing software, like Autodesk Meshmixer, Materialise E-stage, Autodesk Netfabb, and slicer software for FDM technologies such as Cura, PrusaSlicer, Makerwave, and Ideamaker, now incorporate tools for designing intricate support structures, including tree-like formations.

Figure 114. Various type of three-like supports for FDM.

4.1.2.2. Methods and tools

Figure 115 depicts the methodology for generating the tree supports. The workflow starts with the definition of the Design Space, which boundaries are derived in the three cartesian directions from the surface that needs to be supported. Concurrently the key parameters for the generation of the correct pattern in the RD simulation are set. Tree parameters ('treetrunk height', 'treetrunk size', 'branches inclination and number') are modified in order to control the RD behaviour, i.e., tree shape: 'treetrunk height' controls the relative height of the trunk; 'treetrunk size' controls the diameter of the trunk and 'branches inclination and number' controls both the inclination and the quantity of branches generated. Once the all the parameters are set correctly the simulation is run.

Finally, the mesh model is generated and scaled to correctly adapt to the unsupported surface. The algorithm is developed in Rhinoceros 7 (McNeel & Associates, USA) and its plugin Grasshopper. The algorithm developed in Grasshopper is reported in Appendix A.2.

```
┌─────────────────────┐
│ Define Design Space │┐
├─────────────────────┤│   ┌──────────────────┐   ┌──────────────────┐
│   Set overall RD    ││──▶│ Run RD Simulation│──▶│  Generate Mesh   │
│    Parameters       ││   └──────────────────┘   └──────────────────┘
├─────────────────────┤│
│   Set RD Tree       │┘
│    Parameters       │
└─────────────────────┘
```
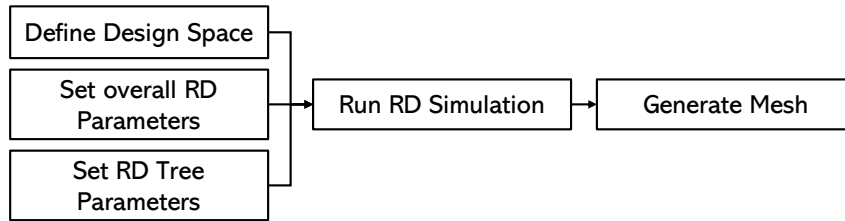
Figure 115. Workflow for the tree supports generation trough RD simulation.

4.1.2.2.1. *Define Design Space*

The initial algorithm worked on a 3D design space defined by the user: n_x, n_y concurrently with n_z (= the number of iterations, n_step), and the spacings can be set arbitrarily to define the overall volume occupied by the simulation. In this case, for the generation of the tree support, the design space must be constructed in relation to the surface to be supported, in terms of position and dimensions. The resulting volume is a 3D space in which the tree will "grow". To create the base of this volume, i.e., the area in which the grid of points for the RD simulation will be defined, the surface to be supported is projected to the XY-plane. The inscribed rectangle with the maximum area is created inside the boundary of the projected surface (Figure 116). The height of the volume is defined by the maximum Z-coordinate of the surface. The resolution of the grid is set arbitrarily as well as the n_z value, while the spacings are calculated from the overall dimension of the volume.
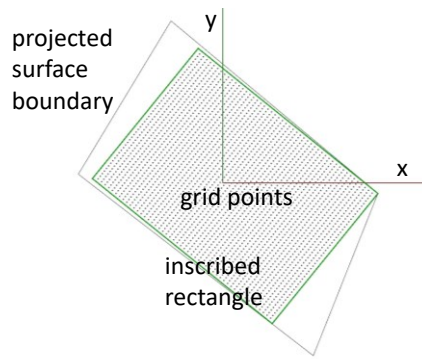
Figure 116. Definition of the base of the DS. Grid points (n_x = n_y = 50) are visualized in black color inside the inscribed rectangle in green color.

4.1.2.2.2. Set overall RD parameters

The overall RD parameters refer to those parameters that in this implementation act indirectly on the tree shape or are constant during the simulation: B, Da, Db, n_jump, f and k. B is set equal to 1 for all the point of the grid. Da, Db can be set as constant values (for instance Da=1, Db = 0.1). Then n_jump, that controls the number of sub-iterations is set arbitrarily. The generation of the correct pattern is a fundamental requirement in order to obtain a branching structure. In this case the solitons pattern (λ) is chosen and is defined by f = 0.025; k = 0.08. Anyhow, all the parameters concur to generate the final pattern (Figure 120).
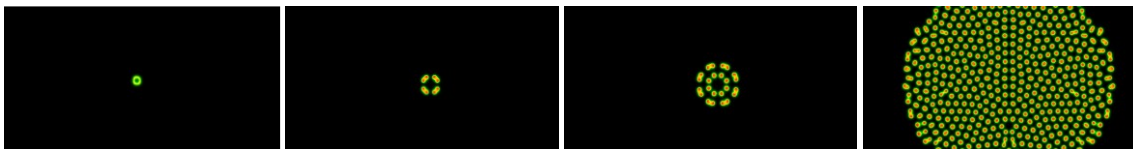
Figure 117. Sequence of the solitons pattern development.

4.1.2.2.3. Set RD Tree parameters

The overall shape of the tree is controlled by tree parameters, 'treetrunk height', 'treetrunk size', 'branches inclination and number', while the position of the tree in the XY-plane is defined manually. 'Treetrunk height' parameter controls the relative height of the trunk. With the 'treetrunk size' parameter it is possible to change the diameter of the trunk. 'Branches inclination and number' controls both the inclination and the quantity of branches generated. All these three parameters act on the dt input, which is a list of n_step values, resulting in deceleration or acceleration of the mitosis process during the

simulation: for the trunk part the dt is set to a very low value (dt = 0.001) while for the branches the dt value is usually higher.
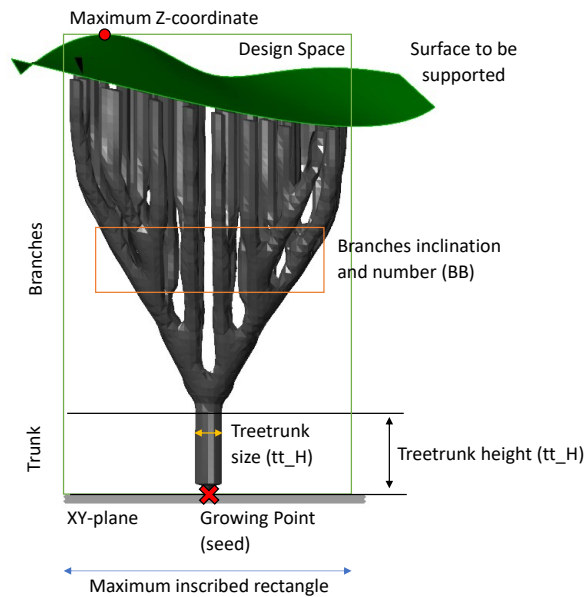
Figure 118. Tree description and final mesh visualization.

Before modifying the three parameters, the initial position (growing point or seed) of the tree (or more than one) needs to be set. This means setting the initial position (in the XY-plane) and the concentration of A species. In the starting script position and concentration are set using a greyscale image, sampled using the grid points in the range of values [0 (black)-1 (white)]. The sampled values are stored into a list, and then used as input for A. So, it is sufficient to replace the image with a list containing 0s and 1s (but in principle, they can be values in between) to trigger the reaction in the same way. The initial A concentration, consisting in a list of 0 values, is modified setting a value of 1 at a specified index. The correct index is identified by placing a 3D point (seed) inside the inscribed rectangle in XY-plane, derived from the surface to be supported. The nearest point in the grid and its index are computed from the seed point, and the 1 value is associated to that index, as is showed in Figure 119 for two seeds highlighted in green with the nearest points in the grid.
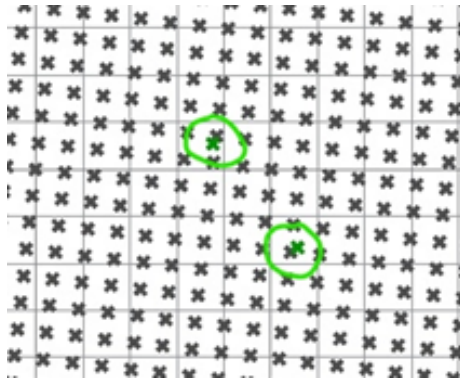
Figure 119. Growing points positioning in the grid.

'Treetrunk height' (tt_H) is a percentage value and represents the relative length of the trunk with respect to the DS height. Higher is the value, bigger is the trunk (Figure 120). The parameter is used to define the number of n_step dedicated to the trunk as $n_{step,trunk} = tt\_H * n\_step$. This value, integer, is used to construct a list with n_step,trunk indices with an associated dt value of dt = dt_min = 0.001. This value regulate the reaction rate and therefore, if this dt tends to zero, the reaction is stopped for the first n_step,trunk indices.
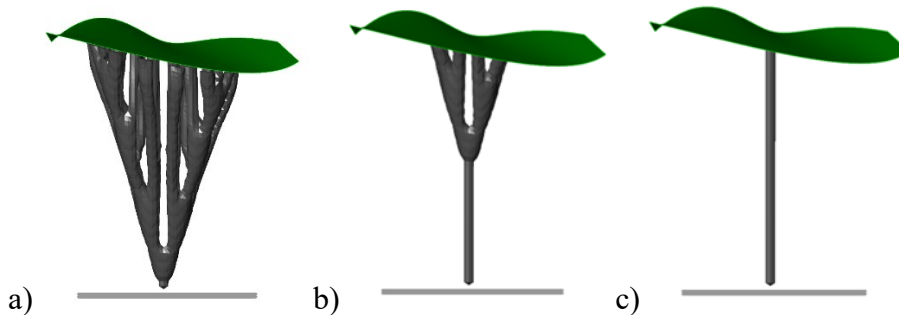
Figure 120. Effects on the variation of the 'treetrunk height' parameter a) 0.01, b) 0.50 and c) 0.99.

'Treetrunk size' (tt_S) is a percentage value and control the 'diameter' of the trunk. It contracts or expands the trunk diameter. It modifies the dt value in the first position of the list (index = 0). The associated value determines how much the diffusion reaction occurs or how much the first soliton grows (without dividing). The trunk, being an extrusion of this, depends directly on it. The dt value is calculated as

$$dt(tt\_S) = (tt\_S * (dt\_max - 0.4))/100 + 0.4$$

where dt_max is the maximum allowed time, which in this implementation is set to 1.
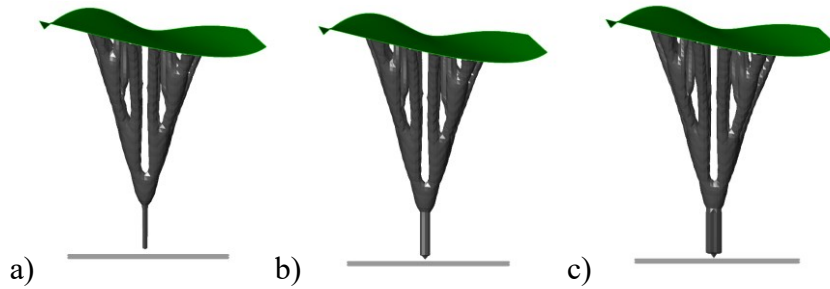
Figure 121. Effect on the variation of the 'treetrunk size' parameter a) 0.01, b) 0.50 and c) 1.

'Branches inclination and number' (BB) is a percentage value and describe the branching behavior of the tree controlling the inclination and the numerosity of the branches. It also affects the input dt. dt is calculated as

$$dt(BB) = BB * dt\_max$$

As BB increases, dt also increases, consequently accelerating the 'mitosis' process. This pertains to both diffusion and reaction, signifying that entities move more within the same layer. In other words, the inclination increases, resulting in the creation of more solitons within the same number of layers, hence leading to an increase in branches. The dt value is then use to fill a list with n_step – n_step,trunk-1 indices. All the dt values calculated are placed at the correct index in a list with n_step places. For instance, in the case of n_step = 9, tt_S = 0.3, tt_H = 0.2 and BB = 0.3; dt(tt_S) = [0.58], dt(tt_H) = [0.001,0.001,0.001] and dt(BB) = [0.3,0.3,0.3,0.3,0.3], so dt = [0.58,0.001,0.001,0.001,0.3,0.3,0.3,0.3,0.3] is the input list to the dt parameter.
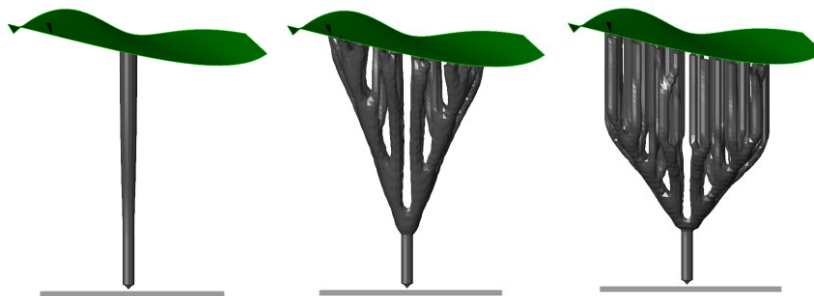
Figure 122. Effect on the variation of the 'branches inclination and number' parameter a) 0.01, b) 0.50 and c) 1.

Additional parameters, discussed in the overall RD parameters section, can influence the eventual tree shape (trunk and branches) and enable fine-tuning. For instance, one

valuable parameter is the sub-iteration for each step (n_jump), which can be adjusted to accelerate the tree's growth. Additionally, the diffusivity parameters Da and Db can be altered to alter the positions of the solitons in the pattern thus the 'movements' of the branches.

The final shape is generated by means of marching cubes algorithm (Appendix A.4). Once the mesh is obtained, it is scaled to correctly fit the space between the ground and the surface. To scale the mesh the vertices are extracted and then projected onto the XY-plane and the surface. The Z-coordinates of the vertices are recalculated accordingly to the distances of the surface from the XY-plane. Finally, the mesh can be reconstructed. This process is depicted in Figure 123 shows the structure of the tree support, with the final mesh and the surface to be supported visualized.
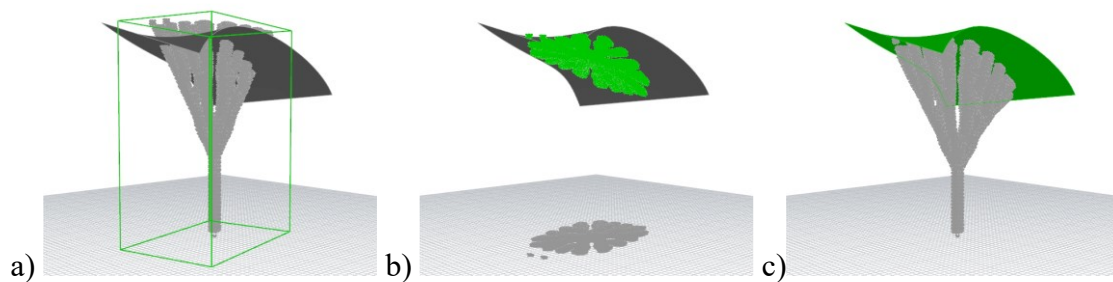
Figure 123. Mesh adaptation process. (a) Initial mesh (grey) inside the DS (wireframe in green); b) Projection of vertices on the XY-plane (grey) and on the surface (green); c) Reconstructed Mesh.

The algorithm is tested on various surface typologies. As a comparison, the cases illustrated in the work by Lantada et al. [301] were chosen because of the range of situations covered. The test cases are architrave, hemisphere, and complex surface.

In the architrave surface, the overall number of branches is similar, despite the left support structure having two primary starting points and four secondary ones (Figure 124.a), while the right side has three primary points(Figure 124.b). The outcome of this process appears somewhat flattened due to the algorithm's current operation on a square domain, later adapted to a rectangle shape (n_x, n_y). This makes it suitable for supporting square or moderately rectangular surfaces. However, if the surfaces are elongated and narrow, some noticeable deformation occurs. Nevertheless, the area is generally covered quite uniformly.

In hemisphere surface, the supports are quite comparable (Figure 124.c,d). It's possible to further refine the result, aiming for slightly sparser branching. The defining box is calculated from the inscribed rectangle, ensuring that contact with the surface occurs in the areas that require support, i.e., those with an inclination greater than 45 degrees.

In complex surface, the algorithm performs quite well, adapting to curvature (Figure 124.e,f). The branching isn't as dense, but it can be increased. The structure is similar, resembling even more the natural appearance of a tree. It's not optimized, but it can be concluded that with further development, achieving a good balance between material usage and support provided is possible.
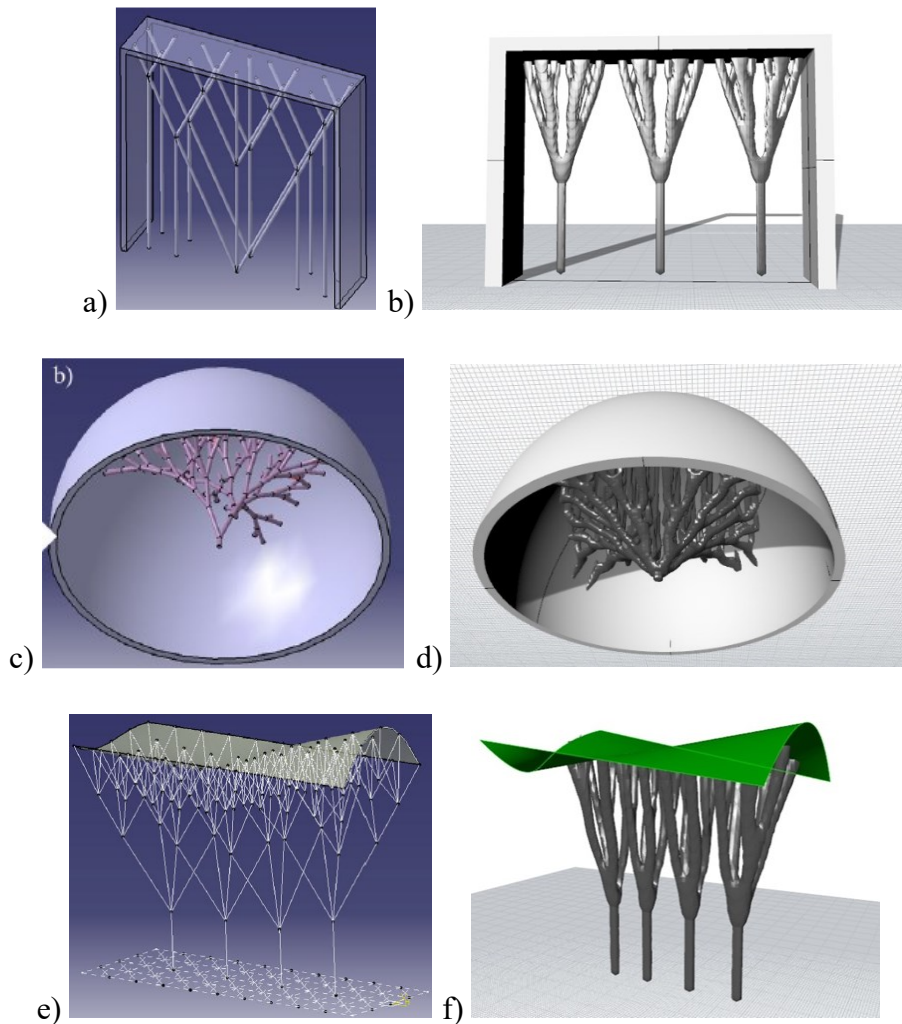
Figure 124. Comparison between the test cases: architrave, hemisphere and complex surface; results of Lantada et al. [301] *(a,c,e) and the proposed method (b,d,f).*

As a result, a tree support generated by the algorithm proposed and printed with FDM technology is showed in Figure 125.

a)   b)
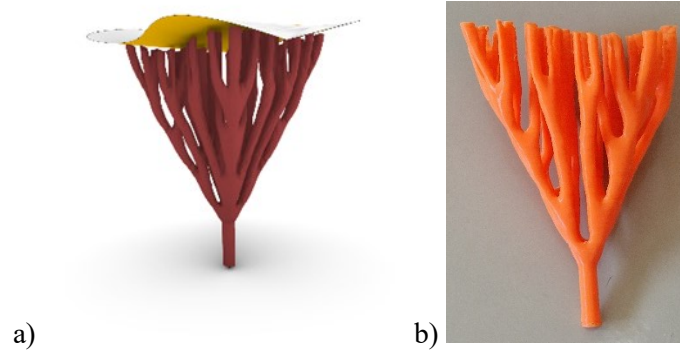
Figure 125 AM supports model and printed result.

4.1.2.2.4.   *Remarks and discussion*

The proposed approach has several limitations and is intended to serve as a preliminary investigation for further improvement. Current slicers software, such as Cura, can generally create tree-like supports faster, and better than our implementation. On the other hand, RD is a very powerful tool generate various type of pattern using only a couple of equations.

Indeed, one limitation lies in the lack of control over the positioning and quantity of points in contact with the surface requiring support. For an improved tree-like support design, it is recommended to initially identify a set of points that are both necessary and adequate for supporting the overhangs effectively. These points would serve as the starting point for branching out the structure, eventually leading to the identification of the trunk. However, in our algorithm, the process unfolds in the reverse order: starting points are chosen, from which the trunk and subsequent branches extend. Therefore, although the structure is tree-like and reminiscent of state-of-the-art supports, the destination points are not controlled, as they depend on the combination of parameters chosen to initiate the reaction, rather than actual structural needs. To overcome this problem, one might consider evolving the system in reverse. Moreover, it is difficult to control the distance between support points. Furthermore, the maximum area covered by supports points is only related to the initial inscribed rectangle, inside the area of the projected surface, thus the entire surface it is not filled with supports. So, to fill the inscribed rectangle, it is better

to increase the BB value, i.e., increase the development of the reaction, taking into account the treetrunk height parameter that effectively control the start of the reaction. However, to cover all the unsupported areas of the surface, a potential geometric solution involves scaling the final mesh appropriately in both the X and Y directions. A similar effect of scaling can also be achieved through the RD simulation by adjusting the _nx and _ny parameters, which essentially changes the spacing of the grid points. When using identical initial conditions and a predetermined set of values for f and k (in the case of the soliton pattern: f = 0.03634, k = 0.06425), the end outcomes consist of smaller 'points' as the resolution increases (Figure 127). The simulations demand additional iterations with escalating resolution to reach an equilibrium state where all motion ceases, and the pattern stabilizes. Moreover, this ensures the entire 2D domain is filled as per the prescribed pattern. Once the space is entirely occupied, solitons tend to reorganize into hexagonal grids. Within this balanced configuration, it becomes feasible to measure the distances (di) between the centers of adjacent solitons. Consequently, this allows for the estimation of an average distance (ds), which can be employed to approximate the quantity of supporting points in a given area (Figure 128).

Another issue arises from the application of boundary conditions to the simulation, i.e., to the grid points. By employing a list and the modulo method to access indices, like in our implementation, the simulation wraps around the boundaries in both the X and Y edges. While this prevents the simulation from being constrained by the edges of the grid, it causes complications when generating the isosurface mesh, resulting in the creation of disjointed meshes, as visible in Figure 133.
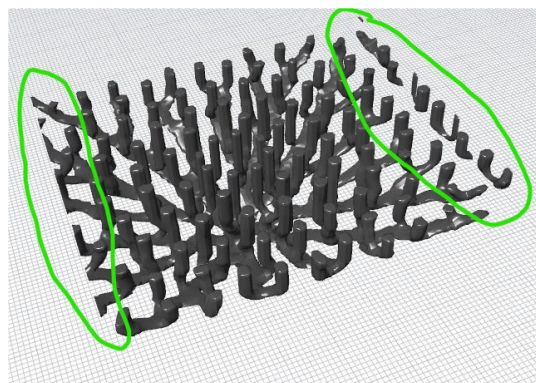
Figure 126. Wrapping effect at the edges and disjoint meshes (highlighted in green).

Future research will focus on generating supports using different patterns. The 'stripes' (κ) pattern, for instance, could be particularly intriguing, not only for supports but also for slicing patterns or applications that require extensive coverage or utilization of high surface areas. Additionally, there will be an exploration into the potential to create and manage gradients of patterns (in space and time), including their three-dimensional shapes, as illustrated in Figure 129 (from solitons (down) to overall B species) .The geometrical characterization of patterns could be another interesting area to potentially enhance the RD algorithm for design purposes.

a) b) c) d)
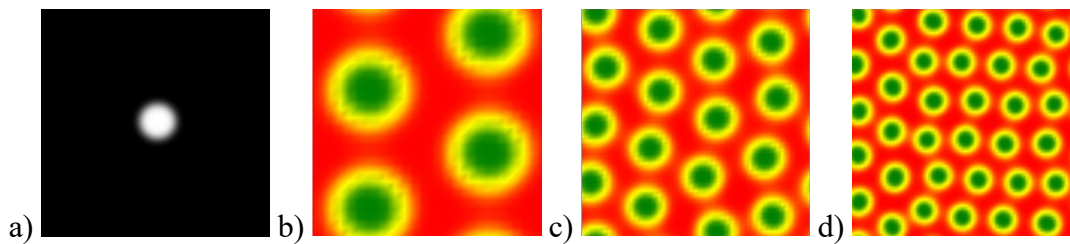
Figure 127. RD simulation using different resolutions and same initial conditions (f = 0.03634, k = 0.06425). a) Initial concentration and position of A species, b) n_x = n_y = 25, spacing = 0.8 mm, n_step = 100 , n_jump = 50, d_s = 11.688 mm, c) n_x = n_y = 50, spacing = 0.4 mm, n_step = 100, n_jump = 50, d_s = 5.354 mm, d) n_x = n_y = 75, spacing = 0.267 mm, n_step = 250, n_jump = 50, d_s = 3.774 mm.
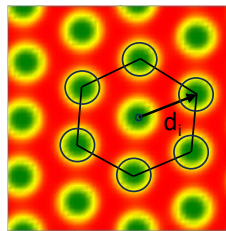
Figure 128. Distance between centers in solitons pattern at equilibrium (n_step >150)
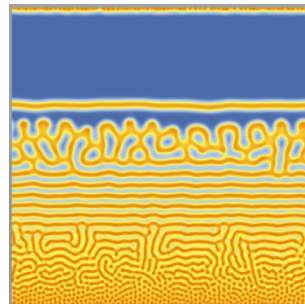
Figure 129. n_x, n_y = 400x400, A = 1, B = parabola equation [0 - 1], Da = 1, Db = linear equation, domain [0.1-1.0], f = 0.045, k = 0.06, dt = 1, n_step = 1, n_jump = 5000.

184

4.2. Differential Curve Growing

Differential growth is a characteristic that biological systems adopt to differentiate parts of themselves to acquire multiple functionalities. It can be modeled by physics-based algorithms, where physical behaviour and constraints are imposed on the geometric entities. In this section, a modeling approach is developed to obtain space-filling and self-avoiding 2D paths, to mimic differential growth in 3D, based on the work by G. Kirdeikis [302].

4.2.1. Method

The computation and the geometric modeling tasks are carried out in Rhinoceros 7 (Robert McNeel & Associates, USA). The algorithm is developed in Grasshopper, a Rhinoceros 7 plugin, using Kangaroo2, Anemone, and other standard components. Kangaroo2 is a library and set of tools of Grasshopper components developed by Daniel Piker for form-finding and physics-based simulations, where the solver works by minimizing the total energy applied to the specific geometric entities of the system (similar to dynamic relaxation) [303–306]. Anemone is a library for Grasshopper developed by Mateusz Zwierzycki which enables the creation of loops in the Grasshopper environment, without scripting [307]. The basic workflow of Anemone relies on two main components: "Loop Start" and "Loop End". Where "Loop End"sends data back to "Loop Start" and the components in the cycle are in between of these two.

This bioinspired behavior is achieved through the application of three constraints on a curve, utilizing the physics-based solver of Kangaroo2. Elastic properties are assigned to the segments L_i of the corresponding polyline, derived from the initial curve by dividing it into a defined number of subdivisions (n). Additionally, a colliding constraint is imposed, simulating the collisions of spheres defined by their centers (p_i) and radii (R_i), positioned at the vertices of the polyline. The curve is further constrained to adhere to a surface with a predefined shape throughout the algorithm's progression. Each constraint (j) is associated with a strength parameter (s_i^j) representing its relative significance. **Errore. L'origine riferimento non è stata trovata.**.a illustrates these key parameters. A series of closed polylines is generated through successive iterations of the initial closed curve (number of iterations = number of curves). At each loop iteration, the solver conducts the simulation without reaching convergence. Simultaneously, the segment

lengths and sphere radii in the constraints are updated by a factor (referred to as the 'growing factor' (GF)). This factor is determined by a function linked to the iteration number and the average length of the initial segments. The choice for the function is arbitrary, and depends on the behavior that the designer what to apply to the growing structure; in this instance, it is defined as:

$$Growing\ factor\ =\ (G(i) * A * k) + c$$

where G(i) is a linear function, G(i) = 0.9*i+1, i represent the iteration index, A is the average initial segments length L in mm, while k and c are two correction factors. This means that in the case of A = 0.2 mm and k = 0 = 0, the Growing factor becomes:

$$GF = (0.9 * i + 1 * 0.2)$$

and

$$for\ i = 0,\ GF = 0.2;\ for\ i = 1,\ GF = 0.236,\ etc \dots$$

The number of iterations is arbitrarily chosen with respect to the growing factor: if it rises slowly the number of curves will be higher and vice versa. Figure 131 shows the workflow for the proposed method. The algorithm, as developed in Grasshopper, is reported in Appendix A.2.. Finally, the set of polylines is turned into NURBS curves, then arranged in the three-dimensional Euclidean space and combined into a NURBS surface using a loft function. Figure 130.b depicts a possible result using a circle as starting curve.
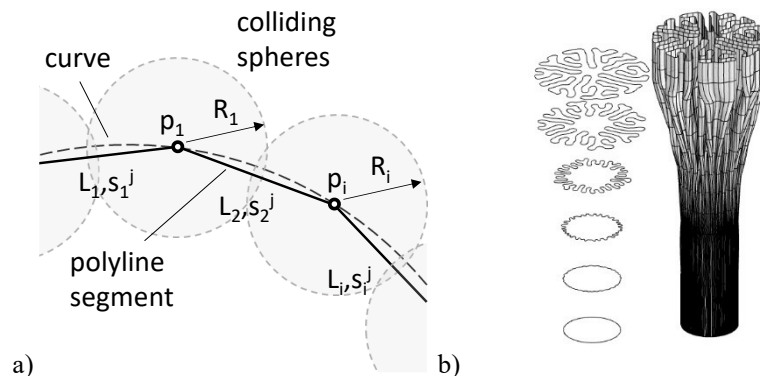
Figure 130. a) Main geometric entities and parameters involved in the geometric modeling method. b) Final results: arranged curves in the space and corresponding surface.
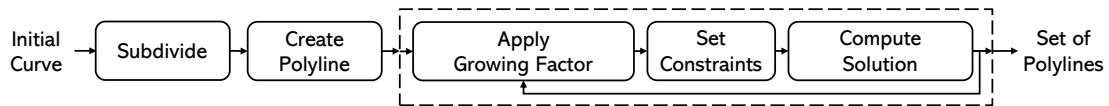
Figure 131. The workflow of the proposed modeling method.

4.2.2. Case study, results and discussion

Bioinspired algorithms are used in combination with AM capabilities to obtain complex and organic shapes, for aesthetic or functional purposes. Common algorithms utilized for the generation of complex geometries are optimization algorithms, such as topology optimization that usually can generate more intricate and lightweight shapes for an original design, or in other cases evolutionary algorithm and swarm intelligence-based algorithms in which the design variants are generated by the imposing rules mimicking nature.

Many prior works demonstrate the potential of AM for complex heat management components, coupled with the use of topology optimization or lattice structures [9], especially using TPMS [10]. Moreover, various examples exist as demonstrators and prototypes realized with metal AM. For instance, NASA, Airbus, and General Electric employed AM in heat exchanger design with the goals of reducing size, mass, and cost while improving part consolidation and durability [308]; two examples are showed in Figure 132.a,b. Among others, the work by Scheitauer et al. [309] presents and explores different ways to design heat exchangers taking into account the possibilities offered by AM, for instance, fractals curves and L-Systems (Figure 132.c).

187

c)
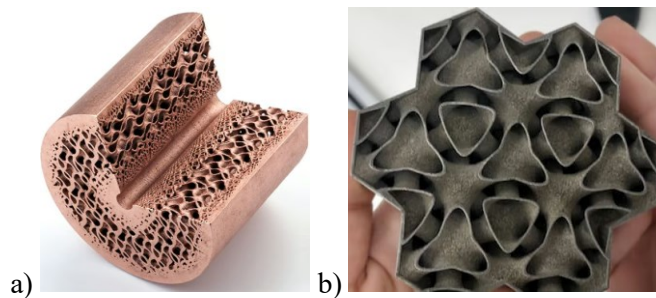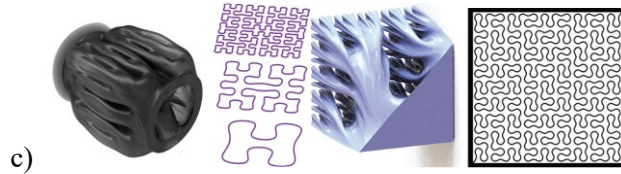
Figure 132 a) 3D printed copper heat exchanger designed by Hyperganic and printed by Heraeus (TPMS Gyroid cell), b) A 3D printed heat exchanger prototype by GE Research called UPHEAT (Ultra Performance Heat Exchanger enabled by Additive Manufacturing) using a lung inspired tri-furcating design (similar to a TPMS Diamond), and c) fractal geometries [309]

In this work the curve growing algorithm is used to design a coaxial counterflow heat exchanger. The model is then numerically analyzed and compared with three different plain pipe versions, considering same length, same surface area, and same temperature difference (ΔT). Finally to show reliability and printability of the internal tube the proposed model is prototyped by FDM technology in white PLA material as shown in Figure 133.

Figure 133. 3D printed prototype (internal tube).

As a design requirement, the inlet and outlet section shapes must be circular. Moreover, the internal areas of the transversal sections of the inner tube are required to remain constant. On the other hand, the outer section is defined by a constant diameter, ensuring a minimum distance from the inner wall. Initially, the algorithm is employed to generate the curves required for subsequent operations. In the heat exchanger modeling process, the number and arrangement of these curves within the Cartesian space are essential considerations. To achieve a tubular shape, the curves are vertically displaced in the z-direction by a specific amount, dz, which can be either a constant or variable value. Furthermore, the curves are mirrored along a plane parallel to the XY plane, with the input curve lying on the XY-plane.

To control the areas, a series of operations are performed for each curve. After the determination of the tube thickness value (t), related to the minimum distance in the curves concavities and the AM process limits, i.e., minimum printable thickness, an inward offset is applied using the value of t. The area of the first curve serves as a threshold and is evaluated accordingly. A scaling operation is employed to adjust each curve to the threshold area in order to obtain the same internal area, followed by an outward offset operation using the thickness value on these scaled curves. If necessary, the equivalent circular sections of the outer tube are obtained by deriving the radius from the curve's area. This ensures that the areas of the inner and annular sections are identical in each section defined by the curves. Then, the surfaces are generated through loft operations, while the solids are created using Boolean differences. This process yields four solid parts consisting of two tubes and two volumes for the fluids. Table 28 reports the values used for each parameter of the algorithm. The model obtained, due to its elongated shape in one direction, can be readily fabricated using AM technologies. When transitioning between different AM technologies, it is crucial to consider printer resolution to accurately determine the minimum thickness that can be employed in the 3D model. Additionally, the surface roughness of the final piece must be taken into account for the specific application, particularly when utilizing metallic materials.

The model, consisting of four solids, is then exported as a parasolid file format (.x_t) for the numerical analyses. Figure 134 shows a cross-section of half of the heat exchanger external tube and the side view of the internal one and 4 significant sections with increasing complexity.

Table 28. Parameters and values adopted in the design of the heat exchanger.

Design parameters	Value
n. of subdivisions	500
n. of iterations	4
s_i^j	2 mm
dz	30 mm

The modeled heat exchanger has an initial inlet diameter of 19 mm while the outer tube has a constant diameter of 34 mm. Both tubes have a thickness of 1 mm. The overall length of the tube is 258 mm. The resulting mid surface of the inner tube has an area of

35248 mm^2 while the correspondent cylinder surface (same inlet and outlet section) presents an area of 15431 mm^2. The lengths of the curves in the section range from 59.7 mm to 244.8 mm.

As a supplementary study, the performance of the heat exchanger is assessed through a Computational Fluid Dynamics (CFD) steady state simulation based on the k − ε model and energy equations in ANSYS Fluent, Release 18.1 (Ansys Inc., USA). As initial conditions, the inlet temperatures are set to 365 K and 280 K respectively for the external (hot) and internal (cold) fluid and the mass flow rate ($\dot{m}$) is 0.1 kg/s. For boundary conditions, the external tube is considered adiabatic. In terms of material selection, aluminum is chosen for the pipes since it is a commonly used material in AM. The thermophysical properties of the fluids and the materials used are reported in Table 29. Temperature difference (ΔT) and pressure drops (Δp) between inlet and outlet sections are obtained as results of the numerical simulations. Δp are a function of the friction factor, which depends on the laminar or turbulent flow [310].
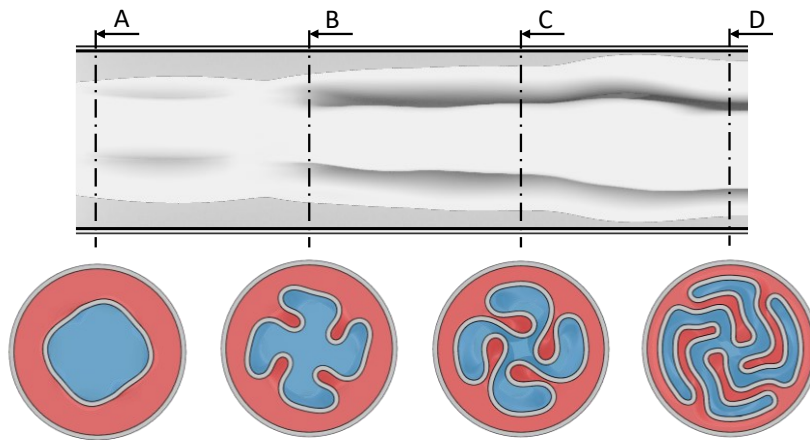
Figure 134. Heat exchanger tubes and sections. Red and blue colors depict hot (external) and cold (internal) fluid regions respectively.

Table 29. Thermophysical properties.

	Type	Specific heat capacity [J/(kg·K)]	Thermal conductivity [W/(m·K)]	Density [kg/m³]
Fluid	Water/Water	4186	0.6	998.2
Tube	Aluminium	871	202.4	2 719

For the four solids, the volumetric mesh is created using the following main settings: tetrahedron elements with 0.7 mm element size; hard behaviour, high smoothing, smooth transition of inflation and tetrahedrons method. The resulting mesh consists of 1587491 nodes and 9159765 tetrahedral elements.

For the proposed solution the numerical analyses results show that for the internal fluid, the temperatures range from 280 K to 295.91 K and from 365 K to 349.96 K for the external fluid, with a $\Delta T = 15.7$ K. The pressure drops (Δp) are measured as 269.2 Pa for the internal fluid and 212.7 Pa for the external one. Figure 135 displays the results of the CFD analysis. Figure 135.a highlights the temperature profile at the contact surface internal fluid/internal tube, showing an increase in temperature towards the outlet section. The velocity vectors are showed in Figure 135.b, highlighting that the velocity is variable, increasing significantly at restrictions; particularly, the velocity vectors are reported not only at the contact surface but also within the fluid field, which is in motion and therefore has non-zero velocities. The shape of the streamline suggests that the motion of the fluid is turbulent. The analytical calculation of the Reynolds number, given the complexity of the geometric model, will be explored in subsequent work.

A comparison is made between the proposed solution and three different plain pipe versions, considering same length, same surface area, and same temperature difference (ΔT) as shown in Table 30.

The plain pipe version with the same length (258 mm) and inlet/outlet sections exhibits a ΔT of 4.1 K and Δp of 4.83 Pa for both the internal fluid. Although it has a lower temperature difference compared to the proposed solution, it has almost negligible pressure drops. The plain pipe with the same surface area (35248 mm^2) has a ΔT of 10.4 K, while the pressure drops are 120.7 Pa for the internal fluid and 80.7 Pa for the external fluid. However, its length is more than doubled (559.43 mm). On the other hand, the plain pipe with the same ΔT is three times longer (774 mm) than the proposed solution, with Δp of 156.2 Pa for the internal fluid and 104.5 Pa for the external fluid. The significant difference in pressure drops is attributed to the greater decrease in temperature, which leads to an increase in water dynamic viscosity and subsequently higher pressure drops.

Table 30. Proposed vs Equivalent Geometric Models Data.

Geometric Model	Length [mm]	Surface Area [mm²]	ΔT [K]	Δp (Internal-External) [Pa]
Proposed Solution	258	35248	15.7	269.2 – 212.7
Same Length	258	15431	4.1	4.83 – 4.90
Same Surface Area	559.4	35248	10.4	120.7 – 80.7
Same ΔT	774	48632	15.7	156.2 – 104.5

a)   b)
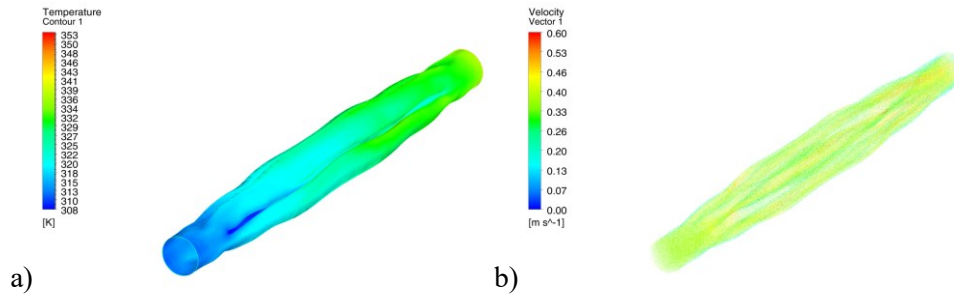
Figure 135. a) Temperature of the contact surface and b) velocity profiles for the internal tube.

The proposed design approach offers notable advantages. It boasts a high area-to-volume ratio, leading to enhanced heat transfer rates compared to conventional coaxial heat exchangers. Additionally, it facilitates greater geometric intricacy and part integration thanks to AM capabilities. This design is particularly fitting for applications demanding efficient heat transfer, limited space, and minimal pressure drops. Examples encompass condensers and evaporators in heat pump systems, along with cutting-edge aerospace components. [311,312].

The modeling process encounters several challenges, particularly related to the complexity of the model, which directly impacts the creation of the finite element (FE) model and computational efforts. Issues such as ensuring a minimum thickness and minimum distance between the "shell" profiles need careful attention. Additionally, special consideration should be given to the NURBS surface, as it may contain self-intersections, which can be addressed by improving the control of the generated curves and the spacing between them during the lofting operation (refer to Figure 136.a). One possible solution is the use of volumetric approaches to create the bioinspired surface as a mesh, similarly to the method proposed in Section 3.1.4.

Another critical aspect is the exchange of files between different software platforms, which becomes necessary when transferring the model from a computer-aided design (CAD) software to FE/CFD software for numerical analysis. It should be noted that different file formats accepted by FE/CFD software may yield varying outcomes for the

same model. Issues such as errors during model generation or non-watertight geometries can arise, as shown in Figure 136.b and c.
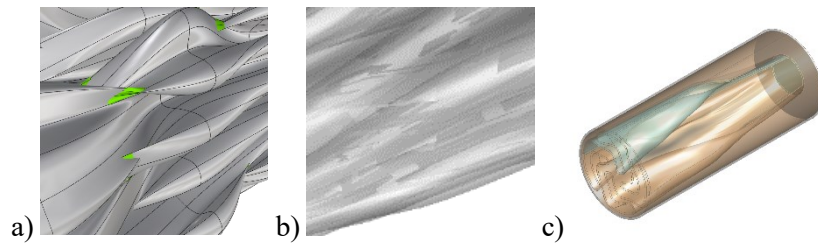
Figure 136. Common issues: a) self-intersections of the surface during the geometric modeling process, b) graphic artefacts, which usually highlights a problem in the imported geometry and then in the mesh generation process, c) not watertight geometries, when solids are not reconstructed correctly in the FEM software and are recognized as separate surfaces.

5. Conclusions

Additive Manufacturing by enabling the creation of objects layer by layer, in contrast to conventional methods that involve material removal has conducted in a new era. This groundbreaking approach allows the production of complex parts with unprecedented shapes, functions, and material combinations. To fully control these new manufacturing capabilities, it is imperative to have design and modeling tools tailored to these novel paradigms. Unfortunately, standard CAD software has proven inadequate for this task, as they were originally designed to represent components produced through traditional processes. Moreover, a broader issue arises from the scarcity of tools tailored for modeling AM-centric, heterogeneous objects.

So, the present research project aimed to overcome these limitations and develop new design and geometric modeling methods and tools suitable for designing parts that fully exploit the possibilities offered by AM.

For reaching the research aim, different topics were addressed regarding two aspects: shape and material complexity; the focus of the work was the development of geometric modeling approaches for graded lattice structures, graded materials and bio-inspired shapes.

Four methods have been developed for the design and modeling of graded lattices structures and two methodologies from natural phenomena models, in particular reaction and diffusion systems and curve growing algorithm. Concerning graded materials, a method to design graded composition for FDM has been proposed, related to the deposition and mechanical characterization of bi-material samples. In addition, bioceramics TPMS lattice structures were designed and tested.

The first method developed allows the fabrication of graded density lattices with FDM AM technology. The key concept of the method is the computation of a specific process parameter, the extrusion parameter E, in the G-code file through the density map generated by a volumetric model, such as, images, topology optimization or CT scans, as highlighted in the related test cases. This method avoids the use of a 3D geometric model of the lattice structures which is a bottleneck of the AM workflow for this type of objects. In addition, this solves another problem: the toolpath generated by a so-called slicer software, that prepared the printing file, is usually not consistent for graded density structures.

A modeling method based on implicit functions has been developed for lattice structures based on TPMS. This method facilitates the modification of lattice parameters such as relative density, cell size, or topology between distinct TPMS cell types by using volumetric maps. The values of the volumetric maps are interpolated into a denser 3D grid. A function with variable parameters is constructed. For every point (x,y,z) within this 3D grid, this function is modified, using the interpolated values, and evaluated, enabling precise local oversight of the resultant value. Isosurface algorithm are then used to extract the surface model.

The third method describes an approach based on subdivisions surfaces offset for geometric modeling of variable thickness TPMS. The approach consists of three main steps: the definition of an initial mesh, the adoption of a subdivision algorithm and the assignment of a variable thickness by a differential offset. The variable thickness values are derived from volumetric density maps. The proposed approach allows obtaining consistent and smooth geometric models improving other critical issues on complex models, such as scalability and automation.

The fourth method relies on the combination of two geometric modeling approaches V-Rep and B-Rep. This combination is employed to geometrically modeling the relative density of lattices through distance functions. The relative density values, coming from a density map, are mapped as distances from a cloud of points representing curves of surfaces, into a voxel data structure. The distance field is evaluated at each point by using the interpolated distance values to generate a isosurface, obtaining a graded density lattice. This method has no highlighted limitations for graded lattices since it relies on an initial geometry that can be obtained in several ways. For this reason, it can be adopted in the realization of different lattice and non-lattice graded structures. The major constraint lies in the computational time, which experiences a significant surge as the mesh resolution increases. Graded lattices based on diamond beam-based and diamond shell-based were manufactured by SLA technologies and the mechanical properties were tested. The results show how the Diamond TPMS lattice specimens exhibited superior flexural strength compared to the Diamond beam-based lattice, while Diamond beam-based specimens are more flexible. The same trend for compression-related properties where the Diamond TPMS lattice specimens outperforms the Diamond beam-based lattice specimens.

The proposed methods, based on implicit functions, surface subdivision, and distance field approaches, are universally applicable across all AM technologies. This is because they generate 3D models as output. Conversely, the G-code modification method is tailored specifically for MEX technologies like FDM or DIW. With some changes, it could potentially be extended to other AM technologies utilizing pathways or material deposition, such as DED. Choosing the appropriate method depends on specific requirements. For flexibility and intuitiveness, the distance fields method is recommended, but put attention on mesh resolution. For TPMS graded lattices with speed and compact file sizes, subdivision surface offset method is ideal. If TPMS advanced gradients are a priority, the method using implicit functions is the more suitable. Finally, for graded density lattices with FDM technologies, consider the G-code modification method.

Similarly, to the first method for graded lattice structures, to generate components with graded material composition a method based on G-code editing has been proposed. The main difference is that works on another process parameter, i.e., the material ratio. In this case the volumetric model represents a material ratio map and the infill pattern is not necessary a lattice. To gain insight into the multimaterial printing, the extrusion and deposition of bi-material blends in FDM technologies was investigated using a series of custom tests. The investigations focused on two key factors: deposition behaviour and the composition percentage of three material pairings. The findings validated the coextrusion behaviour during deposition using a standard nozzle. As the materials were deposited, their relative positions varied depending on the direction of deposition. Additionally, analytical models were proposed to calculate the Young modulus E of these combinations, taking in to account these findings and the experimental E values. The elastic modulus Ey demonstrates a behavior within the range of the model and is closely aligned with linearity.

Highly porous bioceramic scaffolds were produced using two different VPP technologies and two different mixtures. The objective of this investigation was to evaluate both printing accuracy and mechanical strength. The results showed as the good combination of materials, lattice topology and process parameters concur in the improvement of mechanical properties of these advanced materials for biomedical applications. As a final assessment, samples produced with DLP machine (Lithoz), which is designed to manage

advanced materials, present better mechanical properties, with respect to the lattices realized with mSLA (Prusa).

Concerning the bio-inspired models, the focus was on reaction and diffusion systems and differential curve growing. The reaction and diffusion algorithm has been adapted in order to create tree-like supports for AM adopting a particular pattern called "solitons". To realize the tree shape, the evolution of the model acts differently for the trunk and for the branches part. The proposed approach has several limitations and is intended to serve as a preliminary investigation for further improvement. Current slicers software, such as Cura, can generally create tree-like supports faster. On the other hand, RD can be considered a powerful tool generate variety of patterns and thus geometric models using only a couple of equations.

Concerning the differential curve growing, a modeling approach was developed to obtain space-filling and self-avoiding 2D paths, to mimic differential growth in 3D. This bioinspired behaviour is achieved by applying three constraints to a curve applying a physics-based simulation. The algorithm was applied to realize a counterflow heat-exchanger in which a high surface area to volume ratio is required. The results shows that the proposed bio-inspired solution is suitable for applications in small spaces, where a high exchange ratio is required, and pressure drops are neglected.

Summing up, the research project allowed for the implementation of methods for the modeling and optimization of lattice structures, leading to an advancement in the AM field, and overcoming some of the limitations that emerged from the literature. Thanks to the broad versatility of AM, the outcomes of the research can be adopted in different fields. Lattice structures and bioinspired shapes can be used in the automotive, in the aerospace field, in sports apparel. More, graded lattices structures with local controlled shapes (porosity) can be beneficial to the production of patient specific biomedical scaffolds for prothesis. Furthermore, bioinspired shapes can be beneficial in the realization of ergonomic parts for orthosis. The integration of material gradients can further improve their functionalities. The promising results in terms of geometric modeling and printing, related to technology knowledge, show the possibilities to push a little bit far the limit of manufacturable functional components.

Improvements to the presented work are still warranted. In future endeavours, the refinement of the proposed methods and their subsequent validation will be prioritized.

This includes more comprehensive studies on the behavior of multimaterial extrusion and the characterization of multimaterial samples. Moreover, the application of the proposed geometric modeling methodologies to real-world cases will be further developed. Additional investigations will be focused on the bio-inspired aspect of this research; the previously mentioned models (reaction and diffusion, differential growth) will be examined for their potential in shape control. Furthermore, other nature inspired mathematical models will be explored to facilitate the generation of alternative shapes.

Appendix A – Algorithms

Appendix A.1 – Grasshopper Plugin for Volumetric Modeling

Dendro

Dendro (ECR Labs, Los Angeles, USA) is a volumetric modeling plugin for Grasshopper based on the OpenVDB library (Ken Museth, USA). It makes working with volumes no different from handling any other geometry in Grasshopper. It works with many native components, thus avoiding the "blockiness" found in other plugins.

It allows volume objects to be created from meshes, curves or points, and makes it possible to transform a previously designed curved lattice into a volume lattice, with thickness control, surface smoothness and using Boolean operations, thus allowing various operations to be performed on volumes. When working with mesh or B-Rep, these types of operations are often computationally heavy, error-prone, or cannot handle complex geometries. OpenVDB's volume data structures enable faster computation with greater repeatability, allowing more complex operations to be leveraged within Grasshopper:

- Wrapping of meshes, curves, or points

- Fast Boolean operations

- Offsets of complex geometries

- Smoothing operations

- Watertight meshes

- High repeatability

OpenVDB is an open-source C++ library that consists of a new hierarchical data structure for the efficient representation of scattered, time-varying volumetric data discretized on a 3D grid. "VDB," so named because it is a volumetric and dynamic grid that shares several features with B+ trees, exploits the spatial coherence of time-varying data to encode data values and grid topology separately and compactly. VDB models a virtually infinite 3D index space that enables fast and consistent access to data in scattered volumes at high resolution. It imposes no topology restrictions on volumetric data sparsity and supports fast random access patterns (average O(1)) when data are inserted, retrieved, or deleted. This contrasts with most existing sparse volumetric data structures, which

assume a static or multiform topology and require specific data access patterns to compensate for slow random access. Because the VDB data structure is fundamentally hierarchical, it also facilitates adaptive grid sampling, and the inherent acceleration structure leads to fast algorithms that are suitable for simulations.

In most cases, volumetric data are represented on regular, spatially uniform 3D grids, in part because such representations are simple and convenient. In addition, most volumetric algorithms and numerical schemes have a strong preference for uniform sampling. Discretization of differential operators, interpolation, convolution kernels, and other similar techniques can be generalized only with difficulty to nonuniform grids. However, some volumetric applications, such as volumetric modeling and ray marching, benefit from variable-resolution sampling, so it is desirable to employ a data structure that supports both uniform and hierarchical sampling. In addition, many volumetric algorithms such as computational solid geometry (CSG) benefit significantly from a hierarchical data representation. Although dense regular grids are convenient for several reasons, they suffer from at least one serious shortcoming: their memory footprint grows proportionally to the volume of the inclusion space. Since most volumetric applications used in visual effects production do not require that data be sampled uniformly everywhere in a dense grid, the solution is clearly to employ a sparse volumetric data structure. Such a sparse volume should ideally have the advantage that the memory footprint scales only with the number of voxels that contain significant sample values and not with the volume of the dense inclusion space. Although many sparse 3D data structures have been proposed, most are explicitly designed for adaptive sampling, have slow or restrictive data access, do not scale to extreme resolution, or cannot easily handle numerical simulations with dynamic topology. The VDB data structure is memory efficient, supports simulation of time-varying data, can encode arbitrary topology, and facilitates both uniform and adaptive sampling while allowing fast and unrestricted data access.

The typical workflow for the Dendro plugin is to generate a volume, perform operations on it, and then generate the volume as a mesh. Volume objects can be created from meshes, curves or points. The main commands that characterize the plug-in are first illustrated.
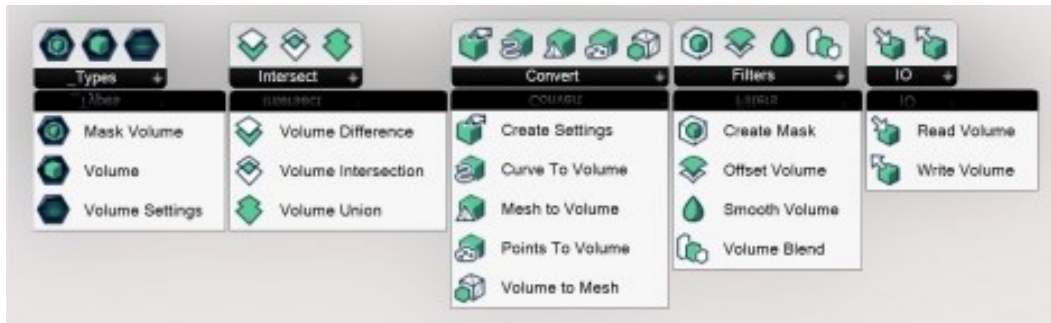
Figure 137 Dendro Components

The Point to Cloud component

The Point Cloud to Volume component generates volumes from point data. This component takes in a radius and creates a volume sphere at each point. You can supply one radius value for everything or provide a list of radius values for each point. This component can be used to replicate the features of the Curve to Volume but with more control. Below you can see what happens as segment increases are applied to a curve with the resulting points used to create a volume. Additionally, the Point Cloud to Volume component can take in a list of radius values, one for each point provided. This allows you to make complex variable volumes from an input curve. In Figure 138 below, points along a curve are given a radius from 0.2 up to 3.0 generating a gradient shape.
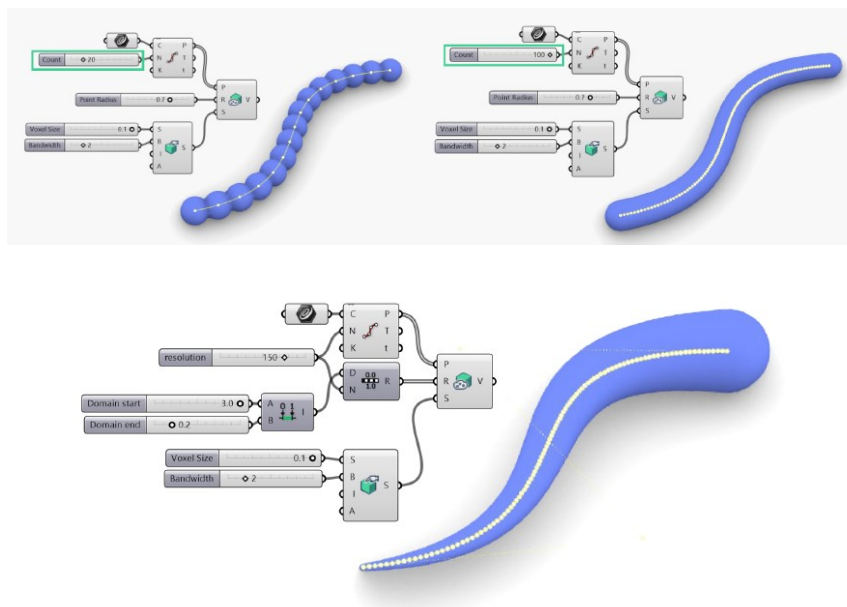
Figure 138. Point to Cloud component

Axolotl

Axolotl (Mathias Bernhard, Zurich) is a plug-in that provides a set of components for volumetric modeling in Grasshopper. They work on the principle of signed distance functions (SDFs). Volumetric modeling, as previously analyzed is also based on the representation of functions (F-Rep). The space is considered a full and continuous field of values. These values can be described by a function so that for any coordinate in a given 3D space, there is a respective value that can be mapped to that coordinate. Instead of defining a 3D object as a collection of polygons or surfaces and curves, it is described in purely mathematical terms as a field of values associated with coordinates.

Many geometric primitives (sphere, cube, cone, cylinder, plane, Platonic solids, ...) can in fact be described not explicitly by placing vertices in space and connecting them with edges and faces, but by a function $v = f(x,y,z)$. In this formula, v is the distance of the point (x,y,z) from the surface of the shape. Point membership depends on the sign of the defining function evaluated at that point. All point positions where this function returns v=0 form the skin of the object, called the isosurface, which unambiguously divides the inside from the outside. All those that give a negative value are inside the object, all those with positive values are outside it. Such a function is called a distance function, and the space is defined as a signed distance field (SDF) (Figure 139).
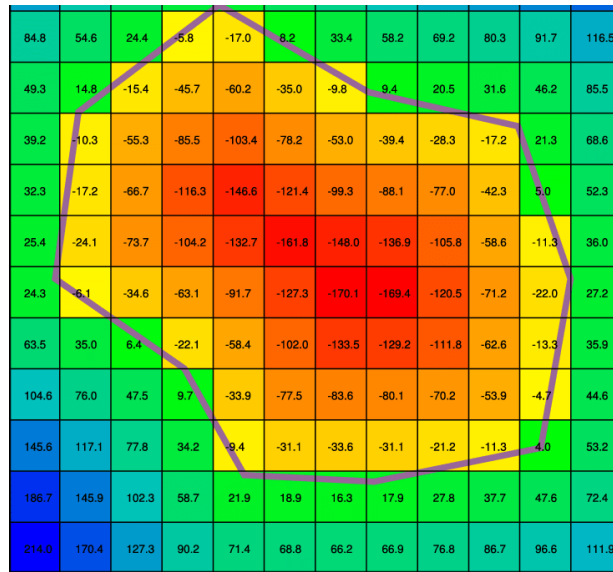
Figure 139. Representation of the distance field with sign of a 2D polygonal obstacle. The space is discretized into cells. Cells storing a negative distance are on the inside of the obstacle; cells with a positive distance are on the outside

The combination of objects is now not a geometric problem of difficult intersection calculations, but purely arithmetic. If object A is defined by a = f(p) and object B by b = g(p), with p ∈ ℝ3, then the Boolean union A∪B is defined as min(a,b), the intersection A∩B as max(a,b), and the subtraction A-B as max(a,-b). Many more combinations with a and b are possible, for example to produce smooth fillets, chamfer angles, stepped transitions or grooves. Of objects is now not a geometric problem of difficult intersection calculations, but purely arithmetic. If object A is defined by a = f(p) and object B by b = g(p), with p ∈ ℝ³, then the Boolean union A∪B is defined as min(a,b), the intersection A∩B as max(a,b), and the subtraction A-B as max(a,-b). Many more combinations with a and b are possible, for example, to produce smooth fillets, bevel angles, stepped transitions, or grooves.

Many operations such as set theory, blending, offsets, projections, nonlinear deformations, sweeping and others have been formulated for this representation in such a way as to produce continuous real-valued functions as outputs, thus guaranteeing the closure property of this representation. The originally introduced R-functions provide C^k continuity for functions that exactly define set theory operations. Because of this property, the result of any supported operation can be considered as input for a subsequent operation; thus, very complex models can be created in this way from a single functional

expression. The F-Rep-based construction treats thickening as the union of multiple cylindrical or spherical features.

A typical workflow with Axolotl is to choose objects from primitives, combine them using, for example, Boolean operations from combinations, make additional modifications if necessary, and finally display the distance object using a component from the meshing tab. In addition, there are several lattice types, some math functions, components to convert Rhino geometry to an SDF, and some SDF analysis utilities (Figure 140).

Axolotl creates isosurfaces via the marching cubes algorithm through different discretization strategies: from a dense grid of voxels, but also from an octree.

The commands "Octree" and "MCubeOctree" create, respectively, an SVO subdivision and a marching cubes isosurface from an octree; "MCubeGrid" and "DenseGrid" create, respectively, a marching cubes isosurface from a dense grid and sample an SDF object in a dense grid. It can then be seen that, to create the mesh, there are various components, depending on whether one wants to create an isosurface from an SVO subdivision or from a dense grid of voxels.

Within the "Lattices" module there are components for creating various cell types and with different coordinate systems. In input it asks for the type of lattices you want to generate, the unit cell size and the thickness of the beam/shell, to output the SDF-based object. Similarly, TPMS can also be created.
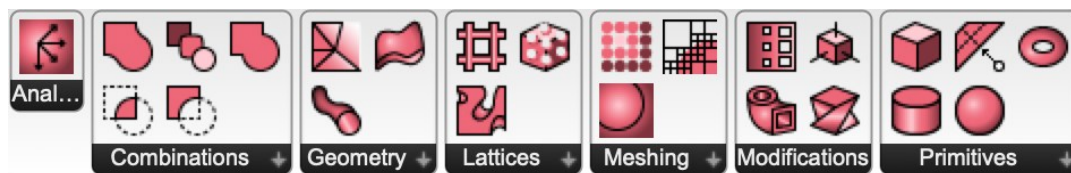
Figure 140. Axolotl Components

Monolith

Monolith is a voxel-based model editor, which uses approaches similar to 2D image editing. It is a research project focused on the development of new digital representations and design workflows that inhabit the space between traditional computer-aided design

(CAD) and voxel-based three-dimensional image processing, with the goal of enabling a very fine level of control over the volumetric distribution of material, especially in light of new multimaterial 3D printing technologies. For conventional manufacturing, choosing the correct voxel size can be ambiguous, especially with solid models with a high degree of curvature. However, for AM, the voxel size need not exceed the tolerance of a 3D printer, as higher voxel resolution would not be feasible (Y. F. Zhao et al., 2021). Voxel-based models offer computational flexibility, enabling operations with 3D matrices. Monolith can be used as a stand-alone program or as an extension to Rhino. This plugin offers a full suite of tools that give the ability to quickly build detailed voxel-based models and visualize them in unique ways using the custom OpenGL rendering pipeline.

To achieve this goal, three problems were addressed by the designers of this plugin. The first is data structures to describe material fields, the second is user interaction and design workflows, and the third is the types of output and processing that could link digital models to AM processes. For data structure, multichannel voxel models are used. Like an image that contains RGB channels, the Monolith data structure contains a series of channels that define different geometric and material properties. Each channel represents a field type that describes a scalar value that changes from point to point in space.

The most basic channel is the shape channel, which determines the solid/vacuum boundary. Two nested isosurfaces are extracted from this field, which will determine the outer and inner boundaries of the solid volume. A second channel determines the mixing ratio of the material and will be interpreted using three-dimensional typographic techniques into a micro-pattern with desired porosity and anisotropy. In essence, this channel describes the mixing ratio of materials at each point in space. Finally, three additional channels describe fields for volumetric texture coordinates (U, V, W) that allow arbitrary flow of micro-patterns within the volume. In addition to this, the data structure is extensible enough to facilitate the exchange of information with simulation modules. For example, additional channels can be added to a voxel model that contains basic geometric information to store the results of a structural analysis simulation.

Each voxel can be used as a drawing context. Operations such as anti-aliasing drawing of lines, points, planes, transformed voxel models and meshes are supported. These

operations use three-dimensional super-sampling to avoid pixelation and aliasing effects along boundaries.

A typical workflow with Monolith starts with the generation of the voxel data structure, model the volumetric data, if many volumetric data are constructed combine them using, for example, Boolean operations, make additional modifications with filters if necessary, and finally extract the V-Rep or B-Rep model.

Figure 141 Monolith components

Among the main components of Monolith is "Construct Base Voxel," which constructs a generic voxel class based on the bounding box, resolution, i.e., setting the size of the smallest voxel in which the model is discretized, and channel designation.

To assign the desired information to the voxels, the "Add Source" command is used: as input there are the voxels to be assigned properties, the shape channel, and, optional, the material ratio channel, which identifies the density of the material or the Red, Green, Blue channels. Two pieces of information are in fact associated with each voxel: the first identifies whether the voxel is "full" or "empty," and the second refers to the materials present.

Once the voxels are obtained, the mesh can be generated with the "Get Iso Mesh" command. You can use the values from a given channel, then using the "Get Channel Names" block. Finally set the chosen isovalue or isovalues for the desired isosurface.

Appendix A.2 – Grasshopper Canvas

Graded Density Lattices by G-code editing

Topology optimization case study
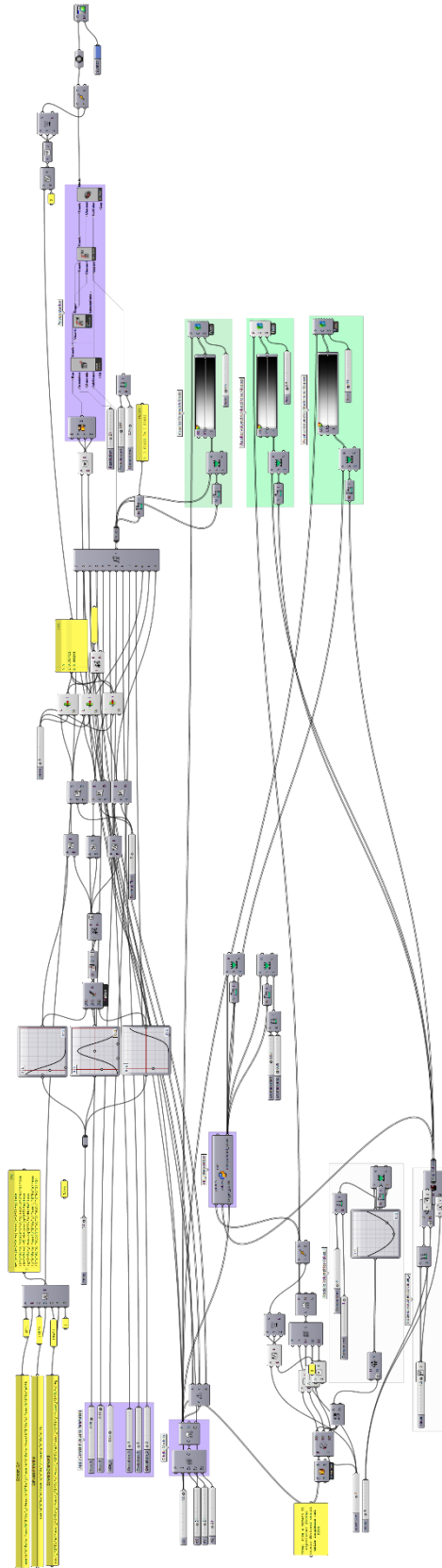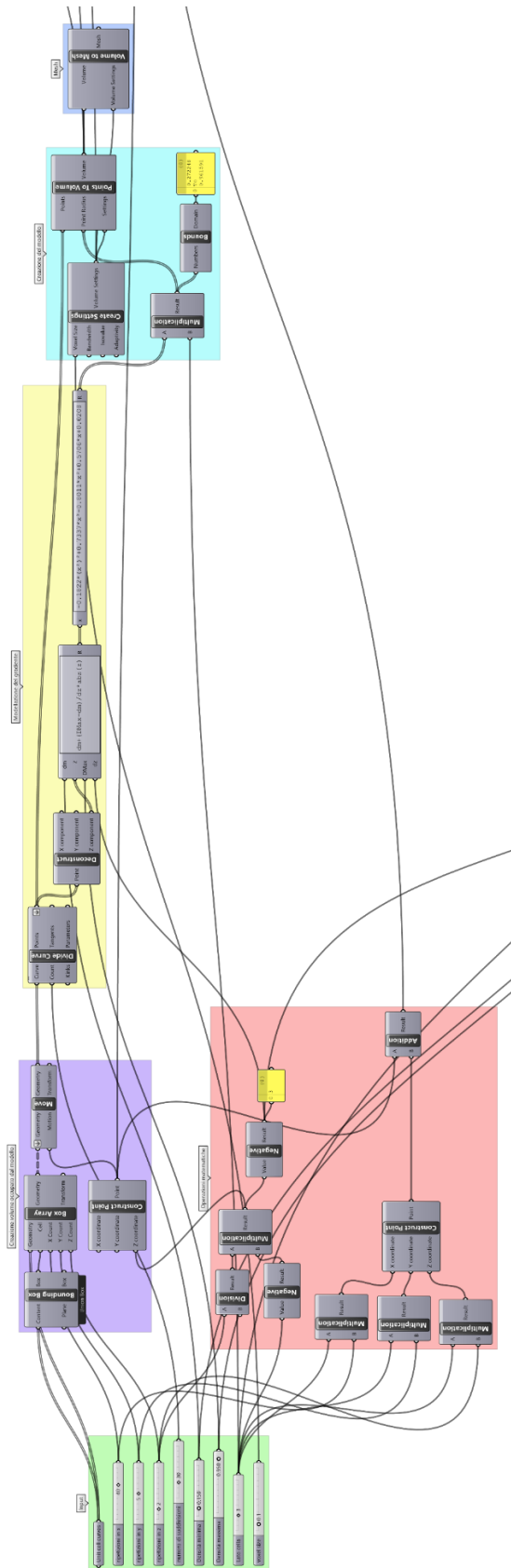
Reaction & Diffusion for AM Supports
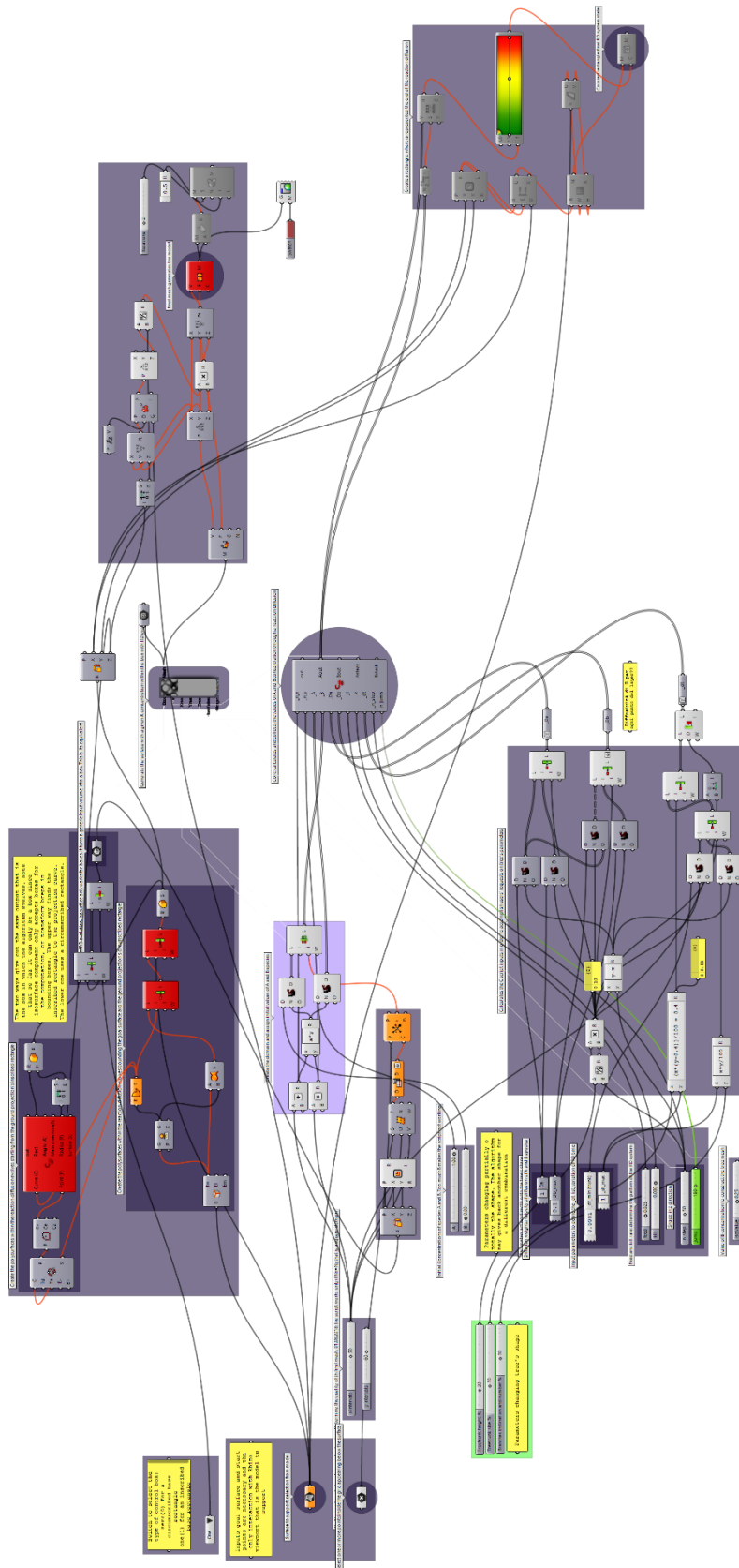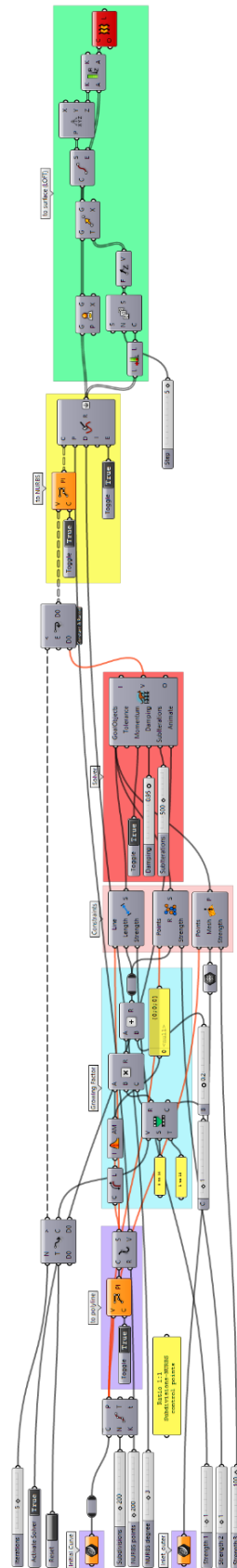
Appendix A.3 – Scripts

Trilinear interpolation

Trilinear interpolation is a method used in computer graphics and numerical analysis to estimate the value of a point within a cube (or a rectangular prism) based on the values at its eight neighbouring vertices. The process involves linearly interpolating along each of the three axes independently. Here's a breakdown:

- Interpolation along the X-axis: First, the value along the x-axis is linearly interpolated between the two vertices on one face of the cube.
- Interpolation along the Y-axis: Next, the interpolated values from step 1 are used to linearly interpolate along the y-axis on both the top and bottom faces of the cube.
- Interpolation along the Z-axis: Finally, the values obtained from step 2 are used to linearly interpolate along the z-axis to find the final interpolated value.

Trilinear interpolation provides a smooth transition between the eight corner points of the cube, allowing for a more accurate representation of the function within the cube than a simple linear interpolation. This technique is widely used in computer graphics for tasks like texture mapping, where it helps to determine the colour or other attributes of a point on a textured surface. It's also employed in various scientific and engineering simulations, such as fluid dynamics and medical imaging, where estimating values within a three-dimensional space is crucial.

Python Script for Grasshopper

```python
import rhinoscriptsyntax as rs
import math

def Trilineare(x,y,z,n,n2,nx,ny,nz,VoxelSizeX,VoxelSizeY,VoxelSizeZ,Vdata):
# Voxel Anisotropo
    #INPUT:
        # x, y, z: coordinates of point to interpolate
        # n, n2: indices that tell me when it works or when I have problems with the trilinear
        # nx, ny, nz: repetitions of the voxel in the 3 directions (x,y,z)
        # VoxelSizeX, VoxelSizeY, VoxelSizeZ: size of the voxel in the 3 directions (x,y,z)
        # Vdata: list of the input scalar values from volumetric model
    #OUTPUT:
        # n, n2: indices that tell me when it works or when I have problems with trilinear
        # de_interp: interpolated value at the i-th point in space after trilinear

        d3D=[[[0 for col in range(nz)]for row in range(ny)] for tre in range(nx)]

        n=0
        for k in range(nz):
            for j in range(ny):
                for i in range(nx):
                    d3D[i][j][k]=Vdata[n]
                    n=n+1
```

```python
        n=0
        n2=0
    nnx,rx1=divmod((x-VoxelSizeX/2),VoxelSizeX)
    nny,ry1=divmod((y-VoxelSizeY/2),VoxelSizeY)
    nnz,rz1=divmod((z-VoxelSizeZ/2),VoxelSizeZ)

    try:
        if nnx<0:
            v1x=0
            v2x=1
            rx1=rx1-VoxelSizeX
        elif nnx==nx-1:
            v1x=nx-1
            v2x=nx-2
        else:
            v1x=int(nnx)
            v2x=v1x+1

        if nny<0:
            v1y=0
            v2y=1
            ry1=ry1-VoxelSizeY
        elif nny==ny-1:
            v1y=ny-1
            v2y=ny-2
        else:
            v1y=int(nny)
            v2y=v1y+1

        if nnz<0:
            v1z=0
            v2z=1
            rz1=rz1-VoxelSizeZ
        elif nnz==nz-1:
            v1z=nz-1
            v2z=nz-2
        else:
            v1z=int(nnz)
            v2z=v1z+1

        #prendo il valore dalla matrice tridimensionale de3D
        v1=de3D[v1x][v1y][v1z]
        v2=de3D[v2x][v1y][v1z]
        v3=de3D[v1x][v2y][v1z]
        v4=de3D[v2x][v2y][v1z]
        v5=de3D[v1x][v1y][v2z]
        v6=de3D[v2x][v1y][v2z]
        v7=de3D[v1x][v2y][v2z]
        v8=de3D[v2x][v2y][v2z]

        rx2=rx1-VoxelSizeX
        ry2=ry1-VoxelSizeY
        rz2=rz1-VoxelSizeZ

        #interpolo
        de_interp=-(rz2*(ry2*(rx2*v1-rx1*v2)-ry1*(rx2*v3-rx1*v4))-rz1*(ry2*(rx2*v5-rx1*v6)-
ry1*(rx2*v7-rx1*v8)))
        CellSize=1
        de_interp= de_interp*CellSize/4

        n=n+1
    except:
        de_interp= 0.05
        n2=n2+1
        print "Eccezione"
        rs.AddPoint(x,y,z)
        print "of non calcolato",x,y,z
    return de_interp,n,n2
```

Radial Basis function (RBF) interpolation

Radial Basis Function (RBF) interpolation is a technique used in numerical analysis and computer graphics for approximating a function from a set of scattered data points. It relies on the concept of radial basis functions, which are mathematical functions that depend only on the distance from a given point (the center) to other points in the dataset. The basic idea behind RBF interpolation is to represent the target function as a weighted sum of these radial basis functions. The weights are determined by solving a system of linear equations that arises from the interpolation problem. This approach is particularly useful when the relationships between data points are not easily captured by traditional polynomial or spline interpolations. The choice of radial basis function is crucial in RBF interpolation, as different functions can lead to different results. Commonly used radial basis functions include Gaussian, multiquadric, inverse multiquadric, and thin plate spline functions, among others. The Gaussian function is one of the most popular choices due to its flexibility and smoothness. Advantages of RBF interpolation include its ability to handle irregularly spaced data points and its inherent smoothness, which can be beneficial for approximating functions with complex or noisy behaviour. However, RBF interpolation can be computationally expensive, especially when dealing with large datasets, as it requires the solution of a system of linear equations. Overall, Radial Basis Function interpolation is a powerful tool for approximating functions from scattered data and finds applications in various fields such as computer graphics, geostatistics, machine learning, and numerical analysis.

Python Script for Grasshopper

```python
import rhinoscriptsyntax as rs
import math

#INPUT:
# points: points of input volumetric model, sparse
# values: list of the input scalar values from volumetric model
# target points: point to interpolate
#OUTPUT:
# interpolated values: list of the interpolated scalar values to the target points

def gaussian_rbf(x, epsilon):
    return math.exp(-(epsilon * x)**2)
def multiquadric_rbf(x, epsilon):
    return math.sqrt(1 + (epsilon * x)**2)

def interpolate_rbf(points, values, target_points, epsilon):
    interpolated_values = []

    for target_point in target_points:
        weighted_sum = 0.0
        weight_sum = 0.0
```

```
        for i in range(len(points)):
            dist = rs.Distance(points[i], target_point)
            weight = gaussian_rbf(dist, epsilon)

            weighted_sum += weight * values[i]
            weight_sum += weight

        interpolated_value = weighted_sum / weight_sum if weight_sum != 0 else 0.0
        interpolated_values.append(interpolated_value)

    return interpolated_values

epsilon = 0.3

interpolated_values = interpolate_rbf(points, values, target_points, epsilon)
```

Reaction and Diffusion Script

$$A' = A + \left(D_A \nabla^2 A - A B^2 + f(1-A) \right) \Delta t$$
$$B' = B + \left(D_B \nabla^2 B + A B^2 - (k+f)B \right) \Delta t$$

New values

Previous values

Feed: at rate *f*, scaled by (1-A) so A doesn't exceed 1.0

"Delta t" is the change in time for each iteration. All the terms get scaled by this.

Diffusion: rates for A and B

These are 2D Laplacian functions, which give the difference between the average of nearby grid cells and this cell. This simulates diffusion because A and B become more like their neighbors.

Kill: this term is subtracted to remove B and scaled by B so it doesn't go below 0. *f* is added to *k* here so the resulting kill rate is never less than the feed rate.

Reaction: the chance that one A and two B will come together is *A x B x B*. A is converted to B so this amount is subtracted from A and added to B.

Figure 142. Reaction Diffusion Equations (discrete version)

As written in the C# component of Grasshopper

```
//Number of points/vertex in the mesh
int n_points;
n_points = _n * _n;

double[] A = new double[n_points];
double[] B = new double[n_points];
double[] Aprime = new double[n_points];
double[] Bprime = new double[n_points];
List<double> A_stacked = new List<double>();
List<double> B_stacked = new List<double>();

A = _A.ToArray();
B = _B.ToArray();

double dxA;
double dxB;
double AB2;
int i_point;

for (int i_p = 0; i_p < n_points; i_p++)
{
  A_stacked.Add(1.0);
  B_stacked.Add(1.0);
}

for (int i = 0; i < _n_step; i++)
```

```
{
  for (int j = 0; j < _n_jump; j++)
  {
    for (int i_x = 0; i_x < _n; i_x++)
    {
      for (int i_y = 0; i_y < _n; i_y++)
      {
        //Laplacian calculation using convolution Matrix
        dxA = 0.0;
        dxB = 0.0;

        dxA = dxA + 0.05 * A[modulo(i_x - 1 + (i_y - 1) * _n, n_points)];
        dxB = dxB + 0.05 * B[modulo(i_x - 1 + (i_y - 1) * _n, n_points)];
        dxA = dxA + 0.20 * A[modulo(i_x - 0 + (i_y - 1) * _n, n_points)];
        dxB = dxB + 0.20 * B[modulo(i_x - 0 + (i_y - 1) * _n, n_points)];
        dxA = dxA + 0.05 * A[modulo(i_x + 1 + (i_y - 1) * _n, n_points)];
        dxB = dxB + 0.05 * B[modulo(i_x + 1 + (i_y - 1) * _n, n_points)];

        dxA = dxA + 0.2 * A[modulo(i_x - 1 + (i_y ) *_n, n_points)];
        dxB = dxB + 0.2 * B[modulo(i_x - 1 + (i_y ) *_n, n_points)];
        dxA = dxA - 1.0 * A[modulo(i_x - 0 + (i_y ) *_n, n_points)];
        dxB = dxB - 1.0 * B[modulo(i_x - 0 + (i_y ) *_n, n_points)];
        dxA = dxA + 0.2 * A[modulo(i_x + 1 + (i_y ) *_n, n_points)];
        dxB = dxB + 0.2 * B[modulo(i_x + 1 + (i_y ) *_n, n_points)];

        dxA = dxA + 0.05 * A[modulo(i_x - 1 + (i_y + 1) * _n, n_points)];
        dxB = dxB + 0.05 * B[modulo(i_x - 1 + (i_y + 1) * _n, n_points)];
        dxA = dxA + 0.20 * A[modulo(i_x - 0 + (i_y + 1) * _n, n_points)];
        dxB = dxB + 0.20 * B[modulo(i_x - 0 + (i_y + 1) * _n, n_points)];
        dxA = dxA + 0.05 * A[modulo(i_x + 1 + (i_y + 1) * _n, n_points)];
        dxB = dxB + 0.05 * B[modulo(i_x + 1 + (i_y + 1) * _n, n_points)];
        //Reaction-diffusion equation
        i_point = modulo(i_x + i_y * _n, n_points);
        AB2 = A[i_point] * B[i_point] * B[i_point];
        Aprime[i_point] = A[i_point] + (_Da * dxA - AB2 + _f * (1.0 -
A[i_point])) * _dt;
        Bprime[i_point] = B[i_point] + (_Db[i_point] * dxB + AB2 - (_k + _f)
* B[i_point]) * _dt;
      }
    }
    for (int i_p = 0; i_p < n_points; i_p++)
    {
      A[i_p] = Math.Min(Math.Max(Aprime[i_p], 0.0), 1.0);
      B[i_p] = Math.Min(Math.Max(Bprime[i_p], 0.0), 1.0);
    }
    if (j == 0)
    {
      for (int i_p = 0; i_p < n_points; i_p++)
      {
        A_stacked.Add(A[i_p]);
        B_stacked.Add(B[i_p]);
      }
    }
  }
}

for (int i_p = 0; i_p < n_points; i_p++)
{
  A_stacked.Add(1.0);
  B_stacked.Add(1.0);
}
Aout = A;
Bout = B;
Astack = A_stacked;
Bstack = B_stacked;
```

Appendix A.4 – Polygonization algorithms

Here are reported a brief descriptions of two techniques for polygonizing isosurfaces, i.e. surfaces which are a level-set of some function f(x,y,z); the surface is the set of points {(x,y,z) | t = f(x,y,z)} for some value t. t is usually called the isovalue.

Marching Cubes

The Marching Cubes algorithm is a computational technique used in computer graphics and computer-aided design (CAD) to create a 3D surface mesh from a 3D scalar field (a volume of data). It was developed by W. Lorensen and H. Cline in 1987 [160].
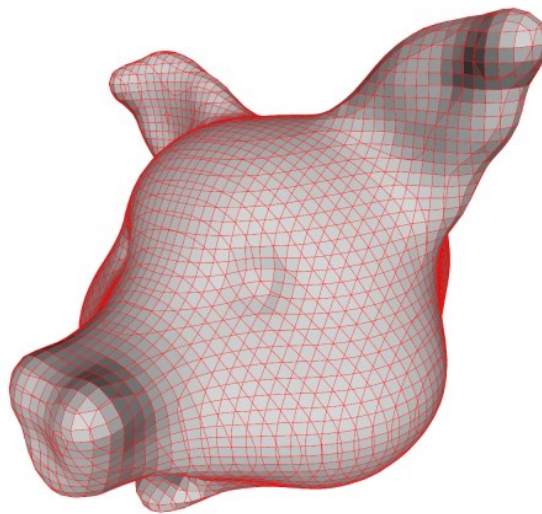
Figure 143. Surface mesh generated by marching cubes algorithm, with its typical surface pattern [238].

Here's a basic overview of how the algorithm works:

- **Scalar Field and Grid**: The algorithm starts with a three-dimensional grid, where each grid cell contains a scalar value. This scalar value could represent various properties like density, temperature, or other attributes.
- **Isosurface Extraction**: The algorithm aims to extract an isosurface, which is a surface that represents points where the scalar value is constant. In simpler terms, it identifies a surface that divides regions with different scalar values.
- **Marching Cube Approach**:
  - o For each grid cell, the algorithm considers the scalar values at its eight corners.
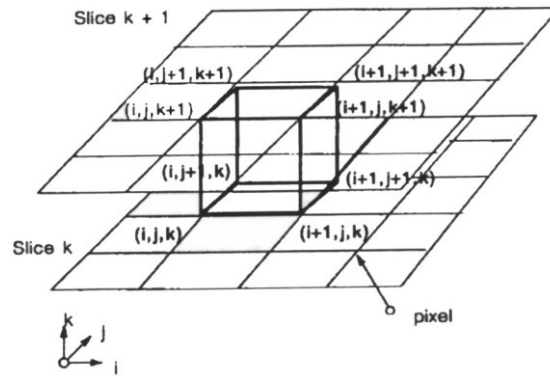
Figure 144. Marching Cube [160].

    o   It then generates a unique 8-bit index based on whether the scalar value at each corner is above or below a chosen threshold value.

    o   This index is then used to look up a pre-computed set of triangles ($2^8 =$ 256 possible configurations) that approximate the surface within the cube.
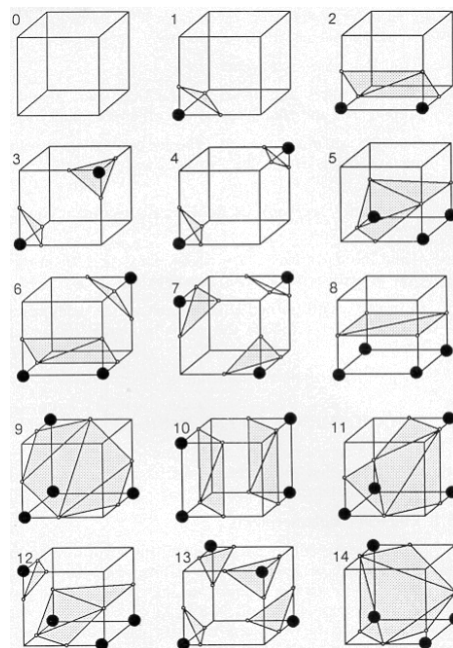
Figure 145. Triangulated Cubes [160].

- **Repeat for Each Cube**: This process is repeated for each grid cell in the volume. The resulting triangles are then combined to form a surface mesh.

The Marching Cubes algorithm is widely used in fields like medical imaging, scientific visualization, and computer graphics. It's particularly useful in situations where the

underlying data is in the form of a 3D grid with scalar values (such as in MRI or CT scans), and there's a need to visualize or analyse surfaces within that data.

There are variations and improvements of the Marching Cubes algorithm, such as Dual Marching Cubes, Extended Marching Cubes, and others, which aim to address specific limitations or improve performance in certain scenarios.

Dual Contouring

Dual Contouring is an algorithm used for generating high-quality, smooth surface meshes from volumetric data, often obtained from techniques like medical imaging or simulations. It was introduced by T. Ju et al. [313] in 2002.
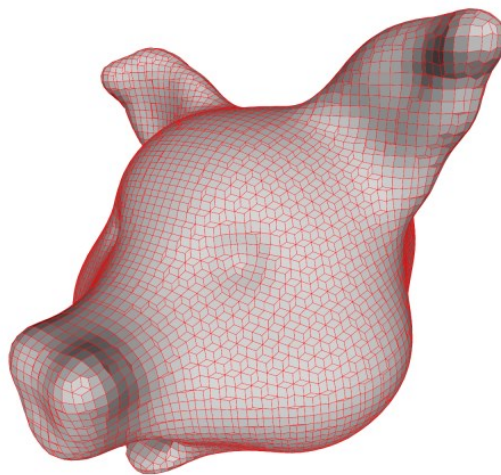
Figure 146. Surface mesh generated by dual contouring algorithm, with its typical surface pattern [238].

Here's a basic overview of how the Dual Contouring algorithm operates:

- **Scalar Field and Octree**: Like Marching Cubes, Dual Contouring starts with a three-dimensional grid, where each grid cell contains a scalar value. It also employs an octree data structure to efficiently represent the volume.

- **Dual Points**: In Dual Contouring, the algorithm identifies "dual points" within each grid cell. These points lie on the isosurface and are used to determine the topology of the surface.

- **Constructing Dual Contours**:
  - For each grid cell, the algorithm generates a set of dual points.

o These points are positioned based on a minimization of a quadratic error function that measures the difference between the actual isosurface and the linear approximation that could be constructed using just the corner points.

- **Edge Reconstruction**: Dual Contouring doesn't explicitly generate triangles like Marching Cubes. Instead, it utilizes edge intersections to construct a surface mesh. It reconstructs the surface between the dual points along edges in the octree.

- **Smoothing and Optimization**: The algorithm applies smoothing and optimization techniques to improve the quality of the resulting mesh.

- **Repeat for Each Cell**: This process is repeated for each grid cell in the volume.

The advantage of Dual Contouring over Marching Cubes is that it tends to produce smoother and more accurate surfaces, especially in regions with high curvature or narrow features. It also handles sharp features and T-junctions more naturally. However, implementing Dual Contouring is more complex than Marching Cubes due to the optimization step and the need to handle the octree structure. Nevertheless, it can be very effective for applications where high-quality surface reconstruction is essential.

Appendix A.5 – Marlin Firmware configuration and G-Code Commands for multimaterial extrusion in FDM technologies

To enable multimaterial extrusion with a single nozzle, the configuration.h file must be adapted. `MIXING_EXTRUDER` must be enabled (uncommented) and the correct number of mixing stepper needs to be set. All the various commands can be enabled to depending on the necessity.

```
#define MIXING_EXTRUDER
#if ENABLED(MIXING_EXTRUDER)
// Number of steppers in your mixing extruder
  #define MIXING_STEPPERS 3
// Use the Virtual Tool method with M163 and M164
  #define MIXING_VIRTUAL_TOOLS 16
  // Allow ABCDHI mix factors in G1 movement commands
  #define DIRECT_MIXING_IN_G1
// Support for gradient mixing with M166 and LCD
//#define GRADIENT_MIX
 #if ENABLED(GRADIENT_MIX)
// Add M166 T to use a V-tool index as a Gradient alias
   #define GRADIENT_VTOOL
  #endif
#endif
```

A single extruder must be defined in `EXTRUDERS`

```
#define EXTRUDERS 1.
```

Finally `SINGLENOZZLE` must be disabled.

```
// #define SINGLENOZZLE
```

Here is reported the description and the implementation of Marlin firmware for the commands used in the G-code to realize multiple material extrusion: M163, M164, M165 and M166.

Reference: https://github.com/bigtreetech/BIQU-Legend/blob/master/Firmware/Marlin-2.0/Marlin/src/gcode/feature/mixing/M163-M165.cpp

```
/**
 * Marlin 3D Printer Firmware
 *Copyright(c)2019Marlin Firmware
[https://github.com/MarlinFirmware/Marlin]
 *
 * Based on Sprinter and grbl.
 * Copyright (c) 2011 Camiel Gubbels / Erik van der Zalm
 *
 * This program is free software: you can redistribute it and/or
modify
```

```
#include "../../../inc/MarlinConfig.h"

#if ENABLED(MIXING_EXTRUDER)

#include "../../gcode.h"
#include "../../../feature/mixing.h"

/**
 * M163: Set a single mix factor for a mixing extruder
 *       This is called "weight" by some systems.
 *       Must be followed by M164 to normalize and commit them.
 *
 *   S[index]   The channel index to set
 *   P[float]   The mix value
 */
void GcodeSuite::M163() {
  const int mix_index = parser.intval('S');
  if (mix_index < MIXING_STEPPERS)
    mixer.set_collector(mix_index, parser.floatval('P'));
}

/**
 * M164: Normalize and commit the mix.
 *
 *   S[index]   The virtual tool to store
 *              If 'S' is omitted update the active virtual tool.
 */
void GcodeSuite::M164() {
  #if MIXING_VIRTUAL_TOOLS > 1
    const int tool_index = parser.intval('S', -1);
  #else
    constexpr int tool_index = 0;
  #endif
  if (tool_index >= 0) {
    if (tool_index < MIXING_VIRTUAL_TOOLS)
      mixer.normalize(tool_index);
  }
  else
    mixer.normalize();
}

#if ENABLED(DIRECT_MIXING_IN_G1)
```

224

```
   /**
    * M165: Set multiple mix factors for a mixing extruder.
    *        Omitted factors will be set to 0.
    *        The mix is normalized and stored in the current virtual
tool.
    *
    *   A[factor] Mix factor for extruder stepper 1
    *   B[factor] Mix factor for extruder stepper 2
    *   C[factor] Mix factor for extruder stepper 3
    *   D[factor] Mix factor for extruder stepper 4
    *   H[factor] Mix factor for extruder stepper 5
    *   I[factor] Mix factor for extruder stepper 6
    */
  void GcodeSuite::M165() {
    // Get mixing parameters from the GCode
    // The total "must" be 1.0 (but it will be normalized)
    // If no mix factors are given, the old mix is preserved
    const char mixing_codes[] = { 'A', 'B'
      #if MIXING_STEPPERS > 2
        , 'C'
        #if MIXING_STEPPERS > 3
          , 'D'
          #if MIXING_STEPPERS > 4
            , 'H'
            #if MIXING_STEPPERS > 5
              , 'I'
            #endif // MIXING_STEPPERS > 5
          #endif // MIXING_STEPPERS > 4
        #endif // MIXING_STEPPERS > 3
      #endif // MIXING_STEPPERS > 2
    };
    uint8_t mix_bits = 0;
    MIXER_STEPPER_LOOP(i) {
      if (parser.seenval(mixing_codes[i])) {
        SBI(mix_bits, i);
        mixer.set_collector(i, parser.value_float());
      }
    }
    // If any mixing factors were included, clear the rest
    // If none were included, preserve the last mix
    if (mix_bits) {
      MIXER_STEPPER_LOOP(i)
        if (!TEST(mix_bits, i)) mixer.set_collector(i, 0.0f);
      mixer.normalize();
    }
  }

#endif // DIRECT_MIXING_IN_G1

#endif // MIXING_EXTRUDER
```

Appendix B – AM technologies datasheet

In the following the main AM technologies used in the thesis work are reported

Formlabs Form 3

Vat photopolymerization > Stereolithography (SLA) > Low Force Stereolithography (LFS)

Laser: Light Processing Unit (LPU)

Power: 250 mW,

Wavelength: 405 nm

Build Volume: 145 x 145 x 185 mm

Z-Layer Resolution: range [25 – 300] microns

XY Resolution: 25 microns

Materials: Formlabs resin cartridges

Software: PreForm

Dimensions: 405 x 375 x 530 mm

Lithoz Cerafab 7500

Vat photopolymerization > Digital Light Processing (DLP) > Lithography-based Ceramic Manufacturing (LCM)

Mask: DMD chip

      Size   76.8 mm, 43.2 mm

      Physical resolution   1920 X 1080 Y pixels (bit depth 1)

      Pixel Size   0.040 mm in X, 0.040 mm in Y (Min. Feature Size) 635 dpi

Light Source: UV LED

      Wavelength   460 nm

      Energy   5 - 1000 mJ/cm^2

      Intensity   0.5 - 92.35 mW/cm^2

Build dimensions	76 × 43 × 170 mm
Build volume	0.56 L
Tank shape	Circle
Movement	Rotation (Knife, Coating) and Tilting
Layer thickness	0.01 – 0.5 mm
File Input	.stl
Software:	Lithoz Cerafab Control

Prusa SL-1S

Vat photopolymerization > masked Stereolithography (mSLA)

Mask: LCD

Size	128 mm X 81 mm Y (125.44,79.38)	
Physical resolution	1620 X 2560 Y pixels (bit depth 8)	
Pixel Size	0.049 mm in X, 0.049 mm in Y (Min. Feature Size)	

Light Source: UV LED

Wavelength	405 nm
Energy	n.d.
Intensity	2.2 mW/cm^2

Build dimensions:	127 × 80 × 150 mm
Build volume:	1.22 L – 0.00122 m^3
Tank shape:	Rectangular
Movement:	Tilting (one direction)
Layer thickness:	0.025 - 0.1 mm
Input file:	.stl
Software:	Prusa Slicer

Appendix C – Materials datasheet

Here are reported the characteristics for the materials adopted in section 3.2.1 and section 3.1.4.2 for the preparation of the samples.

Fillamentum – PLA Extrafill

Datasheet

fillamentum
addi(c)tive polymers

PLA Extrafill

Description:

Fillamentum PLA Extrafill is a material for the FFF (also known as FDM) 3D printing technology.

The advantage of this material is that it can be used in 3D printers easily, that it allows a high quality of printing even in tricky details and an excellent lamination of the printed object.

PLA filament is made of natural ingredients and is easily biodegradable by composting. It complies with the requirements for food contact.

The material may be used for production of electrical and electronic equipment. It doesn't contain the restricted substances.

Fillamentum guarantees high precision of filament dimensions within the tolerance of +/- 0,05 mm, which is strictly controlled throughout the production.

Printing filaments reported on the marked under the trademark Fillamentum are produced in a wide variety of colours in accordance with the colour charts RAL and Pantone, and also in own unique colour ranges.

Physical properties	Typical Value	Test Method	Test Condition
Material density	1,24 g/cm³	ASTM D792	
Melt flow index	6 g/10 min	ASTM D1238	210 °C, 2,16 kg
Diameter tolerance	± 0,05 mm		
Weight	750 g of filament (+ 250 g spool)		

Mechanical properties	Typical Value	Test Method	Test Condition
Tensile strength	60 MPa	ASTM D882	at yield
	53 MPa	ASTM D882	at break
Elongation at break	6 %	ASTM D882	
Tensile modulus	3600 MPa	ASTM D882	
Flexural strength	83 MPa	ASTM D790	
Flexural modulus	3800 MPa	ASTM D790	
Izod impact strength	16 J/m	ASTM D256	23 °C, notched

Thermal properties	Typical Value	Test Method	Test Condition
Glass transition temperature	55-60 °C	ASTM D3418	
Heat distortion temperature	55 °C	ASTM E2092	0,45 MPa

Printing properties	Recommended	Notes
Print temperature	190-210 °C	Recommended settings! It may differ according to the printer and the object. Try your own settings before printing.
Hot pad	50-60 °C	
Bed adhesive	Magigoo	

Workability of 3D printing filament is at least 12 months from delivery.
The information was processed with the best knowledge of the manufacturer and it is for information only.

Fillamentum Manufacturing Czech s.r.o.
nam. Miru 1217, 768 24 Hulin
Czech Republic

(+420) 720 060 947
helpdesk@fillamentum.com
www.fillamentum.com

Datasheet

<img>fillamentum
addi(c)tive polymers</img>
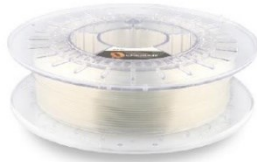
Flexfill TPU 98A

Description:

Flexfill TPU 98A is semi-flexible filament that offers specific mechanical properties. High tear and tensile strength guarantee the durability of 3D printed products.

The material is based on polyurethane, which offers highly reversible deformation, resistance to ozone, oils and greases and good transparency. Properties are stable also thanks to improved UV stability. It has high abrasion resistance and rebound resilience. Printing with 100% infill insures tough object. Material has resistance to wide range of temperatures.

This material is ideal for dynamically stressed parts, for example belts, shoe outsoles, wheels, grippers, flexible covers.

It can be used for production of electrical and electronic equipment. It doesn't contain the restricted substances. The use of the material in the food or medical industry is not recommended.

For flexible materials, Fillamentum can guarantee maximum deviation of diameter +/- 0,10 mm. During the production, filament is made with the best stability of diameter, roundness and colour.

Physical properties	Typical Value	Test Method	Test Condition
Material density	1,23 g/cm³	ISO 1183-1	
Diameter tolerance	± 0,10 mm		
Weight	500 g of filament (+ 250 g spool)		

Mechanical properties	Typical Value	Test Method	Test Condition
Tensile strength	53,7 MPa	DIN 53504	at break, 200 mm/min
Tensile stress	12,1 MPa	DIN 53504	10% elongation, 200 mm/min
	22,1 MPa	DIN 53504	50% elongation, 200 mm/min
	28,4 MPa	DIN 53504	100% elongation, 200 mm/min
	37,8 MPa	DIN 53504	300% elongation, 200 mm/min
Elongation at break	318 %	DIN 53504	200 mm/min
Hardness	98 Shore A	ISO 7619-1	
	60 Shore D	ISO 7619-1	
Tear strength	170 kN/m	ISO 34-1	500 mm/min
Abrasion	23 mm³	ISO 4649	method A

Chemical properties	Typical Value	Test Method	Test Condition
Polymer base	polyurethane		
Oils, greases and ozone resistance	good		25 °C
Water, acetone, acids, alkalis, alcohols and car fluids resistance	bad		25 °C

Printing properties	Recommended	Notes
Print temperature	220-240 °C	Recommended settings! It may differ according to the printer and the object. Try your own optimization before printing.
Hot pad	50-60 °C	
Bed adhesive	Magigoo	For easy removing of the object.
Speed of printing	20-30 mm/s	
Fan speed	70-100 %	

Workability of 3D printing filament is at least 12 months from delivery.
The information was processed with the best knowledge of the manufacturer and it is for information only.

Datasheet

fillamentum
addi(c)tive polymers

ASA Extrafill

Description:

Thanks to mechanical properties is ASA filament ideal for the production of the first samples before serial production for functional prototyping, manufacturing tools, but also for the production of goods for everyday usage including outdoor applications.

The advantage of this material is its excellent weather resistance, high retention of physical features and low level of yellowing.

ASA has a higher rigidity than ABS and thus it is suitable for demanding applications. Another advantage is its good dimensional stability.

This material can be used for production of electrical and electronic equipment. It doesn't contain the restricted substances. The use of the material in the food or medical industry is not recommended.

Fillamentum guarantees precision of filament dimensions within the tolerance of +/- 0,05 mm, which is strictly controlled throughout the production.
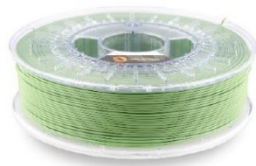
Physical properties	Typical Value	Test Method	Test Condition
Material density	1,07 g/cm³	ASTM D792	
Melt flow index	5 g/10 min		220 °C, 10 kg
Diameter tolerance	± 0,05 mm		
Weight	750 g of filament (+ 250 g spool)		

Mechanical properties	Typical Value	Test Method	Test Condition
Tensile strength	40 MPa	ASTM D638	50 mm/min
Elongation at break	35 %	ASTM D638	50 mm/min
Tensile modulus	1726 MPa	ASTM D638	1 mm/min
Flexural strength	62 MPa	ASTM D790	at yield, 15 mm/min
Flexural modulus	1814 MPa	ASTM D790	15 mm/min
Izod impact strength	441 J/m	ASTM D256	23 °C, 1/8"
Rockwell hardness	92	ASTM D785	R-Scale

Thermal properties	Typical Value	Test Method	Test Condition
Heat distortion temperature	86 °C	ASTM D648	1,8 MPa
	96 °C	ASTM D648	0,45 MPa
Vicat softening temperature	94 °C	ASTM D1525	50 °C/h, 5 kg

Printing properties	Recommended	Notes
Print temperature	240-255 °C	Recommended settings! It may differ according to the printer and the object. Try your own settings before printing.
Hot pad	90-105 °C	
Bed adhesive	3Dlac, glue stick	

Workability of 3D printing filament is at least 12 months from delivery.
The information was processed with the best knowledge of the manufacturer and it is for information only.

Fillamentum Manufacturing Czech s.r.o.
nam. Miru 1217, 768 24 Hulin
Czech Republic

(+420) 720 060 947
helpdesk@fillamentum.com
www.fillamentum.com

Formlabs - White Resin (Standard)

Material Properties Data

The following material properties are comparable for all Formlabs Standard Resins.

	METRIC[1]		IMPERIAL[1]		METHOD
	Green[2]	Post-Cured[3]	Green[2]	Post-Cured[3]	
Tensile Properties					
Ultimate Tensile Strength	38 MPa	65 MPa	5510 psi	9380 psi	ASTM D 638-10
Tensile Modulus	1.6 GPa	2.8 GPa	234 ksi	402 ksi	ASTM D 638-10
Elongation at Failure	12 %	6.2 %	12 %	6.2 %	ASTM D 638-10
Flexural Properties					
Flexural Modulus	1.25 GPa	2.2 GPa	181 ksi	320 ksi	ASTM C 790-10
Impact Properties					
Notched IZOD	16 J/m	25 J/m	0.3 ft-lbf/in	0.46 ft-lbf/in	ASTM D 256-10
Temperature Properties					
Heat Deflection Temp. @ 264 psi	42.7 °C	58.4 °C	108.9 °F	137.1 °F	ASTM D 648-07
Heat Deflection Temp. @ 66 psi	49.7 °C	73.1 °C	121.5 °F	163.6 °F	ASTM D 648-07

[1] Material properties can vary with part geometry, print orientation, print settings, and temperature.

[2] Data was obtained from green parts, printed using Form 2, 100 µm, Clear settings, washed and air dried without post cure.

[3] Data was obtained from parts printed using Form 2, 100 µm, Clear settings, and post-cured with 1.25 mW/cm² of 405 nm LED light for 60 minutes at 60 °C.

Solvent Compatibility

Percent weight gain over 24 hours for a printed and post-cured 1 x 1 x 1 cm cube immersed in respective solvent:

Solvent	24 Hour Weight Gain (%)	Solvent	24 Hour Weight Gain (%)
Acetic Acid, 5 %	<1	Hydrogen Peroxide (3 %)	<1
Acetone	sample cracked	Isooctane	<1
Isopropyl Alcohol	<1	Mineral Oil, light	<1
Bleach, ~5 % NaOCl	<1	Mineral Oil, heavy	<1
Butyl Acetate	<1	Salt Water (3.5 % NaCl)	<1
Diesel	<1	Sodium hydroxide (0.025 %, pH = 10)	<1
Diethyl glycol monomethyl ether	1.7	Water	<1
Hydrolic Oil	<1	Xylene	<1
Skydrol 5	1	Strong Acid (HCl Conc)	distorted

FORMLABS MATERIAL PROPERTIES – STANDARD: Photopolymer Resin for Form 2 3D Printers

Appendix D – Mechanical Testing Machines

Here are reported the main testing machines adopted in the realization of mechanical experiments.

MTS Acumen 3 Electrodynamic Test System

Reference: https://www.mts.com/it/products/materials/dynamic-materials-test-systems/acumen-electrodynamic

Altezza minima dello spazio di prova[3]	A	26 mm (1.02 in)
Altezza massima dello spazio di prova[4]	A	819 mm (32.24 in)
Altezza di lavoro[5]	B	133 mm (5.24 in)
Larghezza spazio di prova (misurato tra le colonne)	C	460 mm (18.11 in)
Design della piastra di base		T-Slot (standard del settore: 8 mm)
Diametro colonna	D	63.5 mm (2.5 in)
Larghezza dell'ingombro del telaio	E	634 mm (24.96 in)
Profondità dell'ingombro del telaio[6]	F	501 mm (19.72 in)
Larghezza totale[6] (con controller montato su telaio)	G	764 mm (30.08 in)
Altezza totale[7]	H	1726 mm (67.95 in)
Peso		188 kg (415 lb)

a)   b)

Specifications:

- Dynamic force: 3.000 N (670 lbf)
- Static Force: 2.000 N (450 lbf)
- Actuator Length: 70 mm (2.75 in)
- Dynamic Momentum: +/-30 Nm (265 in-lb)
- Static Momentum: +/- 21 Nm (185 in-lb)

Galdabini Quasar 25

Reference: https://www.galdabini.it/datasheets/quasar-25

Capacity of frame and max allowed load	25,000 N
Load cell nominal size (tensile & compression)	25,000 N
Testing area depth	Unlimited
Power Rating	700 W
Machine weight (without accessories)	160 kg
Height	1548 mm
Width	730 mm
Depth	700 mm

Appendix E – AM international standards

American Society for Testing and Materials (ASTM) and the International Organization for Standardization (ISO) started publishing AM related standards.

For what concerns the international organizations, both ASTM and ISO have technical committees working on AM-related standards. ASTM Committee F42 on AM technologies was established in 2009 and has 8 technical subcommittees [314]. ISO Technical Committee 261 was established in 2011 [315] and soon after its creation, in September 2011, ISO and ASTM signed a cooperative agreement to adopt and jointly develop international standards on the AM subject. In their "Joint Plan for Additive Manufacturing Standards Development" [316] a hierarchy of AM standards based on three levels was proposed (Figure 147):

1. General standards: standards that specify general concepts, common requirements, or are generally applicable to most types of AM materials, processes, and applications.

2. Category standards: standards that specify requirements that are specific to a material category or process category.

3. Specialized standards: standards that specify requirements that are specific to a material, process, or application.
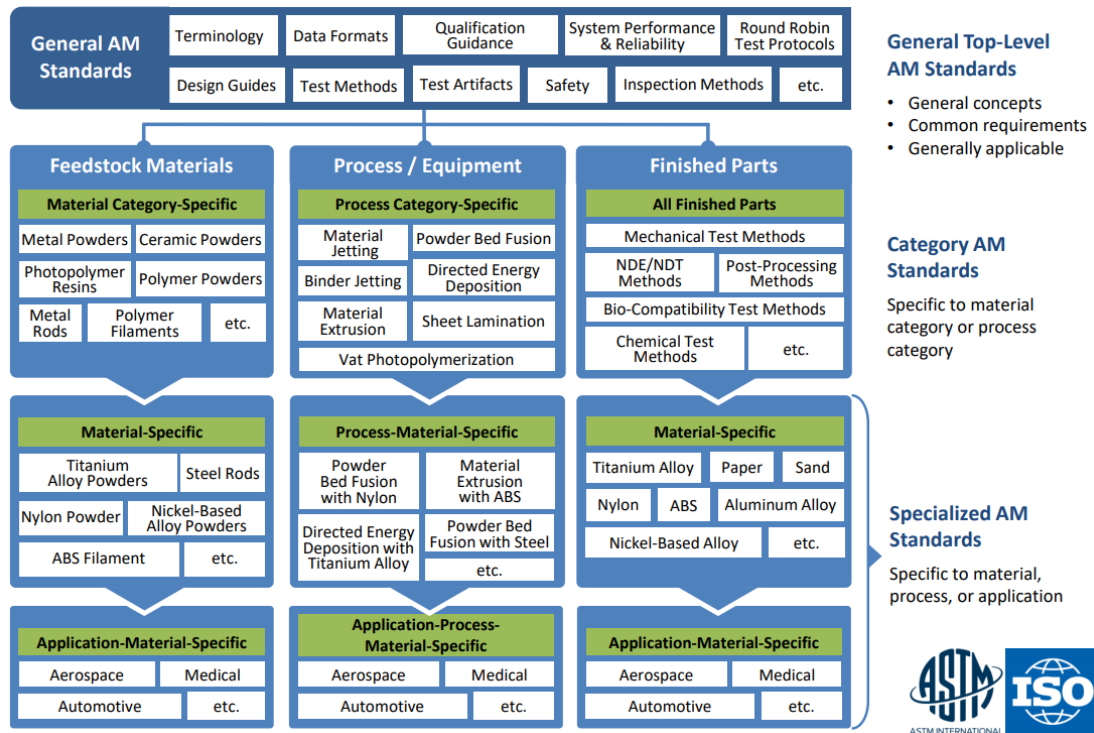
Figure 147. Three-levels hierarchy AM standard structure proposed by ISO and ASTM organizations
[317].

ISO declares that, including the updates, 19 standards have been published under the direct responsibility of ISO/TC 261, whereas 37 standards are under development. Among them, some of the most significant published ones are:

- ISO/ASTM 52900:2015 - Additive manufacturing — General principles — Terminology, where all the definitions of AM-related terms are given.

- ISO/ASTM 52902:2019 - Additive manufacturing — Test artifacts — Geometric capability assessment of AM systems, where benchmarking test piece geometries are described, and directions are given to perform quantitative and qualitative measurements. The results can be used to evaluate the capability and/or to calibrate the AM systems.

- ISO/ASTM 52911-1:2019 - Additive manufacturing — Design — Part 1: Laser-based powder bed fusion of metals, where design recommendations are given to avoid poor quality features or failure of the build when metal PBF technologies are used.

- ISO/ASTM 52911-2:2019 - Additive manufacturing — Design — Part 2: Laser-based powder bed fusion of polymers, where design recommendations are given to avoid poor quality features or failure of the build when polymers PBF technologies are used.

- ISO/ASTM TR 52912:2020 - Additive manufacturing — Design — Functionally graded additive manufacturing, which is more a technical report and presents a state of the art of functionally graded AM, dealing with the current manufacturing approaches, potentialities, and limitations.

- ISO/ASTM 52915:2020 - Specification for additive manufacturing file format (AMF) Version 1.2, where the requirements for the preparation, display, and transmission for the AMF are given.

- ISO/ASTM 52921:2013 - Standard terminology for additive manufacturing — Coordinate systems and test methodologies, where directions are given to define a coordinate system for the AM machines that is also used to identify the test specimen orientation.

- ISO 17296-3:2014 - Additive manufacturing — General principles — Part 3: Main characteristics and corresponding test methods, that will be replaced by ISO/ASTM 52927, where the principal requirements applied for testing parts manufactured by additive manufacturing processes are covered. The main quality characteristics of parts, the appropriate test procedures, and the scope and content of test and supply agreements are specified.

References

[1] ISO/ASTM, ISO/ASTM 52900:2015 (ASTM F2792) - Additive manufacturing -- General principles -- Terminology, (2015). file:///C:/Users/Administrator/AppData/Local/Mendeley Ltd./Mendeley Desktop/Downloaded/ISOASTM - 2015 - ISOASTM 529002015 (ASTM F2792) - Additive manufacturing -- General principles -- Terminology.pdf.

[2] ASTM F2792-09, Standard Terminology for Additive Manufacturing Technologies, ASTM Int. (2009) 1–3. https://doi.org/10.1520/F2792-09.

[3] I. Gibson, D. Rosen, B. Stucker, M. Khorasani, Additive Manufacturing Technologies, 3rd ed., Springer, Cham, Cham, 2021. https://doi.org/10.1007/978-3-030-56127-7.

[4] A.D. Lantada, P.L. Morgado, Rapid Prototyping for Biomedical Engineering: Current Capabilities and Challenges, Annu. Rev. Biomed. Eng. 14 (2012) 73–96. https://doi.org/10.1146/annurev-bioeng-071811-150112.

[5] D. Brackett, I. Ashcroft, R. Hague, Topology optimization for additive manufacturing, in: 22nd Annu. Int. Solid Free. Fabr. Symp. - An Addit. Manuf. Conf., Austin,Texas, 2011: pp. 348–362.

[6] A. Kudzal, B. McWilliams, C. Hofmeister, F. Kellogg, J. Yu, J. Taggart-Scarff, J. Liang, Effect of scan pattern on the microstructure and mechanical properties of Powder Bed Fusion additive manufactured 17-4 stainless steel, Mater. Des. 133 (2017) 205–215. https://doi.org/10.1016/J.MATDES.2017.07.047.

[7] Z. Wang, T.A. Palmer, A.M. Beese, Effect of processing parameters on microstructure and tensile properties of austenitic stainless steel 304L made by directed energy deposition additive manufacturing, Acta Mater. 110 (2016) 226–235. https://doi.org/10.1016/J.ACTAMAT.2016.03.019.

[8] G.H. Loh, E. Pei, D. Harrison, M.D. Monzón, An overview of functionally graded additive manufacturing, Addit. Manuf. (2018). https://doi.org/10.1016/j.addma.2018.06.023.

[9] T.S. Srivatsan, Materials Processing Handbook , Joanna R. Groza, James F. Shackelford, Enrique J. Lavernia, and Michael T. Powers, Editors, Mater. Manuf. Process. 27 (2012) 1146–1147. https://doi.org/10.1080/10426914.2012.689459.

[10] P.K. Gokuldoss, S. Kolla, J. Eckert, Additive manufacturing processes: Selective laser melting, electron beam melting and binder jetting-selection guidelines, Materials (Basel). 10 (2017) 672. https://doi.org/10.3390/ma10060672.

[11] M. Ziaee, N.B. Crane, Binder jetting: A review of process, materials, and methods, Addit. Manuf. 28 (2019) 781–801. https://doi.org/10.1016/j.addma.2019.05.031.

[12] A. Dass, A. Moridi, State of the art in directed energy deposition: From additive manufacturing to materials design, Coatings. 9 (2019) 418. https://doi.org/10.3390/COATINGS9070418.

[13] T.J. Gordelier, P.R. Thies, L. Turner, L. Johanning, Optimising the FDM additive manufacturing process to achieve maximum tensile strength: a state-of-the-art review, Rapid Prototyp. J. 25 (2019) 953–971. https://doi.org/10.1108/RPJ-07-2018-0183.

[14] R.J. Zaldivar, T.D. Mclouth, G.L. Ferrelli, D.N. Patel, A.R. Hopkins, D. Witkin, Effect of initial filament moisture content on the microstructure and mechanical performance of ULTEM ® 9085 3D printed parts, Addit. Manuf. 24 (2018) 457–466. https://doi.org/10.1016/j.addma.2018.10.022.

[15] T. Hofstätter, D.B. Pedersen, G. Tosello, H.N. Hansen, State-of-the-art of fiber-reinforced polymers in additive manufacturing technologies:, Http://Dx.Doi.Org/10.1177/0731684417695648. 36 (2017) 1061–1073. https://doi.org/10.1177/0731684417695648.

[16] D. Chimene, R. Kaunas, A.K. Gaharwar, Hydrogel Bioink Reinforcement for Additive Manufacturing: A Focused Review of Emerging Strategies, Adv. Mater. 32 (2020) 1902026. https://doi.org/10.1002/ADMA.201902026.

[17] L.J. Tan, W. Zhu, K. Zhou, Recent Progress on Polymer Materials for Additive Manufacturing, Adv. Funct. Mater. (2020) 2003062. https://doi.org/10.1002/adfm.202003062.

[18] H. Fayazfar, F. Liravi, U. Ali, E. Toyserkani, Additive manufacturing of high loading concentration zirconia using high-speed drop-on-demand material jetting, Int. J. Adv. Manuf. Technol. 2020 1099. 109 (2020) 2733–2746. https://doi.org/10.1007/S00170-020-05829-2.

[19] W.E. Frazier, Metal additive manufacturing: A review, J. Mater. Eng. Perform. 23 (2014) 1917–1928. https://doi.org/10.1007/s11665-014-0958-z.

[20] W.E. King, A.T. Anderson, R.M. Ferencz, N.E. Hodge, C. Kamath, S.A. Khairallah, A.M. Rubenchik, Laser powder bed fusion additive manufacturing of metals; physics, computational, and materials challenges, Appl. Phys. Rev. 2 (2015) 041304. https://doi.org/10.1063/1.4937809.

[21] C.A. Chatham, T.E. Long, C.B. Williams, A review of the process physics and material screening methods for polymer powder bed fusion additive manufacturing, Prog. Polym. Sci. 93 (2019) 68–95. https://doi.org/10.1016/j.progpolymsci.2019.03.003.

[22] N. Hopkinson, P. Erasenthiran, High speed sintering—early research into a new rapid manufacturing process, in: Solid Free. Fabr. Symp., 2004: pp. 312–320.

[23] B. Khoshnevis, B. Asiabanpour, M. Mojdeh, K. Palmer, SIS - A new SFF method based on powder sintering, Rapid Prototyp. J. 9 (2003) 30–36. https://doi.org/10.1108/13552540310455638.

[24] C. Cai, W.S. Tey, J. Chen, W. Zhu, X. Liu, T. Liu, L. Zhao, K. Zhou, Comparative study on 3D printing of polyamide 12 by selective laser sintering and multi jet fusion, J. Mater. Process. Technol. 288 (2021) 116882. https://doi.org/10.1016/j.jmatprotec.2020.116882.

[25] S. Dadbakhsh, L. Verbelen, O. Verkinderen, D. Strobbe, P. Van Puyvelde, J.-P. Kruth, Effect of PA12 powder reuse on coalescence behaviour and microstructure of SLS parts, Eur. Polym. J. 92 (2017) 250–262. https://doi.org/https://doi.org/10.1016/j.eurpolymj.2017.05.014.

[26] G. V. Salmoria, J.L. Leite, R.A. Paggi, The microstructural characterization of PA6/PA12 blend specimens fabricated by selective laser sintering, Polym. Test. 28 (2009) 746–751. https://doi.org/10.1016/j.polymertesting.2009.06.010.

[27] B. Van Hooreweder, F. De Coninck, D. Moens, R. Boonen, P. Sas, Microstructural characterization of SLS-PA12 specimens under dynamic tension/compression excitation, Polym. Test. 29 (2010) 319–326. https://doi.org/10.1016/j.polymertesting.2009.12.006.

[28] S. Yuan, F. Shen, J. Bai, C.K. Chua, J. Wei, K. Zhou, 3D soft auxetic lattice structures fabricated by selective laser sintering: TPU powder evaluation and process optimization, Mater. Des. 120 (2017) 317–327. https://doi.org/10.1016/J.MATDES.2017.01.098.

[29] L.J. Tan, W. Zhu, K. Sagar, K. Zhou, Comparative study on the selective laser sintering of polypropylene homopolymer and copolymer: processability, crystallization kinetics, crystal phases

and mechanical properties, Addit. Manuf. 37 (2021) 101610. https://doi.org/10.1016/J.ADDMA.2020.101610.

[30]   M. Schmidt, D. Pohle, T. Rechtenwald, Selective laser sintering of PEEK, CIRP Ann. - Manuf. Technol. 56 (2007) 205–208. https://doi.org/10.1016/j.cirp.2007.05.097.

[31]   C.Y. Yap, C.K. Chua, Z.L. Dong, Z.H. Liu, D.Q. Zhang, L.E. Loh, S.L. Sing, Review of selective laser melting: Materials and applications, Appl. Phys. Rev. 2 (2015) 041101. https://doi.org/10.1063/1.4935926.

[32]   L.E. Murr, S.M. Gaytan, D.A. Ramirez, E. Martinez, J. Hernandez, K.N. Amato, P.W. Shindo, F.R. Medina, R.B. Wicker, Metal Fabrication by Additive Manufacturing Using Laser and Electron Beam Melting Technologies, J. Mater. Sci. Technol. 28 (2012) 1–14. https://doi.org/10.1016/S1005-0302(12)60016-4.

[33]   J. Romano, L. Ladani, J. Razmi, M. Sadowski, Temperature distribution and melt geometry in laser and electron-beam melting processes – A comparison among common materials, Addit. Manuf. 8 (2015) 1–11. https://doi.org/10.1016/J.ADDMA.2015.07.003.

[34]   M. Rombouts, J.P. Kruth, L. Froyen, P. Mercelis, Fundamentals of Selective Laser Melting of alloyed steel powders, CIRP Ann. 55 (2006) 187–192. https://doi.org/10.1016/S0007-8506(07)60395-3.

[35]   J. Zhang, B. Song, Q. Wei, D. Bourell, Y. Shi, A review of selective laser melting of aluminum alloys: Processing, microstructure, property and developing trends, J. Mater. Sci. Technol. 35 (2019) 270–284. https://doi.org/10.1016/J.JMST.2018.09.004.

[36]   S. Leuders, M. Thöne, A. Riemer, T. Niendorf, T. Tröster, H.A. Richard, H.J. Maier, On the mechanical behaviour of titanium alloy TiAl6V4 manufactured by selective laser melting: Fatigue resistance and crack growth performance, Int. J. Fatigue. 48 (2013) 300–307. https://doi.org/10.1016/j.ijfatigue.2012.11.011.

[37]   B. Vandenbroucke, J.P. Kruth, Selective laser melting of biocompatible metals for rapid manufacturing of medical parts, Rapid Prototyp. J. 13 (2007) 196–203. https://doi.org/10.1108/13552540710776142.

[38]   D. Ahn, J.H. Kweon, J. Choi, S. Lee, Quantification of surface roughness of parts processed by laminated object manufacturing, J. Mater. Process. Technol. 212 (2012) 339–346. https://doi.org/10.1016/J.JMATPROTEC.2011.08.013.

[39]   T. Himmer, T. Nakagawa, M. Anzai, Lamination of metal sheets, Comput. Ind. 39 (1999) 27–33. https://doi.org/10.1016/S0166-3615(98)00122-5.

[40]   R.J. Friel, R.A. Harris, Ultrasonic Additive Manufacturing – A Hybrid Production Process for Novel Functional Products, Procedia CIRP. 6 (2013) 35–40. https://doi.org/10.1016/J.PROCIR.2013.03.004.

[41]   C.W. Hull, Apparatus for production of three-dimensional objects by stereolithography, U.S. Patent 4,575,330, 1986.

[42]   S. Maruo, O. Nakamura, S. Kawata, Three-dimensional microfabrication with two-photon-absorbed photopolymerization, Opt. Lett. 22 (1997) 132. https://doi.org/10.1364/OL.22.000132.

[43]   J. Crivello, Photoinitiators for free radical cationic and anionic photopolymerization, Surf. Coatings Technol. 168 (1998).

[44]   A. Nazir, O. Gokcekaya, K. Md Masum Billah, O. Ertugrul, J. Jiang, J. Sun, S. Hussain, Multi-material additive manufacturing: A systematic review of design, properties, applications, challenges, and 3D printing of materials and cellular metamaterials, Mater. Des. 226 (2023) 111661. https://doi.org/10.1016/j.matdes.2023.111661.

[45]   N. Shamsaei, A. Yadollahi, L. Bian, S.M. Thompson, An overview of Direct Laser Deposition for additive manufacturing; Part II: Mechanical behavior, process parameter optimization and control, Addit. Manuf. 8 (2015) 12–35. https://doi.org/10.1016/j.addma.2015.07.002.

[46]   J. Wang, Z. Pan, Y. Ma, Y. Lu, C. Shen, D. Cuiuri, H. Li, Characterization of wire arc additively manufactured titanium aluminide functionally graded material: Microstructure, mechanical properties and oxidation behaviour, Mater. Sci. Eng. A. 734 (2018) 110–119. https://doi.org/10.1016/j.msea.2018.07.097.

[47]   X. Zhang, C. Wei, Y.H. Chueh, L. Li, An integrated dual ultrasonic selective powder dispensing platform for three-dimensional printing of multiple material metal/glass objects in selective laser melting, J. Manuf. Sci. Eng. Trans. ASME. 141 (2019). https://doi.org/10.1115/1.4041427.

[48]   M. Rafiee, R.D. Farahani, D. Therriault, Multi-Material 3D and 4D Printing: A Survey, Adv. Sci. 7 (2020) 1902307. https://doi.org/10.1002/advs.201902307.

[49]   Prusa Research, Original Prusa i3 Multi Material 2.0 - Prusa3D - 3D Printers from Josef Průša, (2021).

[50]   Mosaic Manufacturing, Palette 2S, (n.d.).

[51]   N. Oxman, E. Tsai, M. Firstenberg, Digital Anisotropy, J. Virtual Phys. Prototyp. 4 (2011) 261–274.

[52]   Stratasys, PolyJet Technology for 3D Printing, (2021).

[53]   J.-W. Choi, H.-C. Kim, R. Wicker, Multi-material stereolithography, J. Mater. Process. Technol. 211 (2011) 318–328. https://doi.org/10.1016/j.jmatprotec.2010.10.003.

[54]   Lithoz, CeraFab Multi 2M30, (n.d.). https://lithoz.com/en/3d-printer/cerafab-multi/.

[55]   G. Boothroyd, P. Dewhurst, W.A. Knight, Product Design for Manufacture and Assembly, Third Edition (Manufacturing Engineering and Ma..., (2010).

[56]   D.W. Rosen, Computer-Aided Design for Additive Manufacturing of Cellular Structures, Comput. Aided. Des. Appl. 4 (2007) 585–594. https://doi.org/10.1080/16864360.2007.10738493.

[57]   S. Hällgren, L. Pejryd, J. Ekengren, 3D Data Export for Additive Manufacturing-Improving Geometric Accuracy, in: Procedia CIRP, Elsevier, 2016: pp. 518–523. https://doi.org/10.1016/j.procir.2016.05.046.

[58]   ISO International Organization for Standardization, ISO 10303-242:2020 - Industrial automation systems and integration — Product data representation and exchange — Part 242: Application protocol: Managed model-based 3D engineering, (2020) 11.

[59]   AP 242 Edition 2 capabilities for Additive Manufacturing interoperability, (2020).

[60]   ISO International Organization for Standardization ASTM American Society for Testing and Materials, ISO/ASTM 52915:2020 - Specification for additive manufacturing file format (AMF) Version 1.2, (2020).

[61]   Enabling the full potential of 3D printing - 3MF Consortium, (2020).

[62]   Shapeways, Shapeways Launches SVX, a Voxel Based File Format for 3D Printing - Shapeways Blog, (2014).

[63]   G. Savio, R. Meneghello, S. Rosso, G. Concheri, 3D Model Representation and Data Exchange for Additive Manufacturing, in: 2019: pp. 412–421. https://doi.org/10.1007/978-3-030-12346-8_40.

[64]   X.Y.Y. Kou, S.T.T. Tan, Heterogeneous object modeling: A review, CAD Comput. Aided Des. 39 (2007) 284–301. https://doi.org/10.1016/j.cad.2006.12.007.

[65]   G.K. Sharma, B. Gurumoorthy, Modelling multiply connected heterogeneous objects using mixed-dimensional material reference features, J. Comput. Des. Eng. 6 (2019) 337–347. https://doi.org/10.1016/j.jcde.2018.11.003.

[66]   M.E. Mortenson, Geometric Modeling, I, Wiley, 1985.

[67]   A. Bacciaglia, A. Ceruti, A. Liverani, Additive Manufacturing Challenges and Future Developments in the Next Ten Years, in: 2020: pp. 891–902. https://doi.org/10.1007/978-3-030-31154-4_76.

[68]   J. Ahern, A. DiCarlo, Computationally engineered advanced manufacturing of parts, in: 2016 IEEE Aerosp. Conf., IEEE, 2016: pp. 1–8. https://doi.org/10.1109/AERO.2016.7500892.

[69]   R.G. Miyamoto, Y., Kaysser, W.A., Rabin, B.H., Kawasaki, A., Ford, Functionally Graded Materials: Design, Processing and Applications (Materials Technology Series), Springer Science & Business Media, 1999.

[70]   R.M. Mahamood, E.T. Akinlabi, M. Shukla, S. Pityana, Functionally graded material: An overview, in: Lect. Notes Eng. Comput. Sci., 2012: pp. 1593–1597. https://www.scopus.com/inward/record.uri?eid=2-s2.0-85013851127&partnerID=40&md5=7526c74fa5bdab6b998da01ba1f6239d.

[71]   Y.-S. Leung, T.-H. Kwok, X. Li, Y. Yang, C.C.L. Wang, Y. Chen, Challenges and Status on Design and Computation for Emerging Additive Manufacturing Technologies, J. Comput. Inf. Sci. Eng. 19 (2019). https://doi.org/10.1115/1.4041913.

[72]   A. Garland, G. Fadel, Optimal Design of Topology and Gradient Orthotropic Material, in: Vol. 2A 43rd Des. Autom. Conf., American Society of Mechanical Engineers, 2017. https://doi.org/10.1115/DETC2017-67852.

[73]   A. Garland, G. Fadel, Design and Manufacturing Functionally Gradient Material Objects With an Off the Shelf Three-Dimensional Printer: Challenges and Solutions, J. Mech. Des. 137 (2015). https://doi.org/10.1115/1.4031097.

[74]   C. Zhang, F. Chen, Z. Huang, M. Jia, G. Chen, Y. Ye, Y. Lin, W. Liu, B. Chen, Q. Shen, L. Zhang, E.J. Lavernia, Additive manufacturing of functionally graded materials: A review, Mater. Sci. Eng. A. 764 (2019) 138209. https://doi.org/10.1016/j.msea.2019.138209.

[75]   G. Fadel, S. Morvan, Multi-material representation and design issues, in: I. Gibson (Ed.), Softw. Solut. Rapid Prototyp., Wiley, 2002: pp. 155–224.

[76]   A. Paolini, S. Kollmannsberger, E. Rank, Additive manufacturing in construction: A review on processes, applications, and digital planning methods, Addit. Manuf. 30 (2019) 100894. https://doi.org/10.1016/j.addma.2019.100894.

[77]   T.R. Jackson, Analysis of functionally graded material object representation methods, Massachusetts Institute of Technology, 2000. http://hdl.handle.net/1721.1/9032.

[78] G. Savio, R. Meneghello, S. Rosso, G. Concheri, 3D model representation and data exchange for additive manufacturing, Lect. Notes Mech. Eng. (2019) 412–421. https://doi.org/10.1007/978-3-030-12346-8_40.

[79] A. Blouin, B. Combemale, B. Baudry, O. Beaudoux, Kompren: modeling and generating model slicers, Softw. Syst. Model. 14 (2015) 321–337. https://doi.org/10.1007/s10270-012-0300-x.

[80] A. Pasko, V. Adzhiev, A. Sourin, V. Savchenko, Function representation in geometric modeling: concepts, implementation and applications, Vis. Comput. 11 (1995) 429–446. https://doi.org/10.1007/BF02464333.

[81] F. Massarwi, G. Elber, A B-spline based framework for volumetric object modeling, CAD Comput. Aided Des. 78 (2016) 36–47. https://doi.org/10.1016/j.cad.2016.05.003.

[82] W. Martin, E. Cohen, Representation and extraction of volumetric attributes using trivariate splines, in: Proc. Sixth ACM Symp. Solid Model. Appl. - SMA '01, ACM Press, New York, New York, USA, 2001: pp. 234–240. https://doi.org/10.1145/376957.376984.

[83] E.L. Doubrovski, E.Y. Tsai, D. Dikovsky, J.M.P. Geraedts, H. Herr, N. Oxman, Voxel-based fabrication through material property mapping: A design method for bitmap printing, Comput. Des. 60 (2015) 3–13. https://doi.org/10.1016/j.cad.2014.05.010.

[84] R. Bidarra, K.J. De Kraker, W.F. Bronsvoort, Representation and management of feature information in a cellular model, CAD Comput. Aided Des. 30 (1998) 301–313. https://doi.org/10.1016/S0010-4485(97)00070-5.

[85] M. Panagiotis, A.O. Payne, Monolith, (2019). http://www.monolith.zone (accessed November 27, 2019).

[86] P. Michalatos, A. Payne, Monolith : The Biomedical Paradigm and the Inner Complexity of Hierarchical Material Design, in: Complex. Simplicity - Proc. 34th ECAADe Conf., Oulu School of Architecture, August 22nd – 26th 2015, Oulu, Finland, 2016: pp. 445–454.

[87] P.-A. Fayolle, L. McLoughlin, M. Sanchez, G. Pasko, A. Pasko, Modeling and Visualization of Multi-material Volumes, Sci. Vis. 13 (2021). https://doi.org/10.26583/sv.13.2.09.

[88] A. Tereshin, A. Pasko, O. Fryazinov, V. Adzhiev, Hybrid function representation for heterogeneous objects, Graph. Models. 114 (2021) 101098. https://doi.org/10.1016/j.gmod.2021.101098.

[89] A. Biswas, V. Shapiro, I. Tsukanov, Heterogeneous material modeling with distance fields, Comput. Aided Geom. Des. 21 (2004) 215–242. https://doi.org/10.1016/j.cagd.2003.08.002.

[90] M.W. Jones, J.A. Baerentzen, M. Sramek, 3D distance fields: a survey of techniques and applications, IEEE Trans. Vis. Comput. Graph. 12 (2006) 581–599. https://doi.org/10.1109/TVCG.2006.56.

[91] K. Takayama, O. Sorkine, A. Nealen, T. Igarashi, Volumetric modeling with diffusion surfaces, in: ACM SIGGRAPH Asia 2010 Pap. - SIGGRAPH ASIA '10, ACM Press, New York, New York, USA, 2010: p. 1. https://doi.org/10.1145/1866158.1866202.

[92] H. PFISTER, Hardware-Accelerated Volume Rendering, in: Vis. Handb., Elsevier, 2005: pp. 229–258. https://doi.org/10.1016/B978-012387582-2/50013-7.

[93] B. Preim, C. Botha, Visual Computing for Medicine. Theory, Algorithms, and Applications, 2nd ed., Elsevier, 2014. https://doi.org/10.1016/C2011-0-05785-X.

[94] NEMA, DICOM PS3.1 2021e - Introduction and Overview, (n.d.) 1–34.

[95] L.J. Gibson, M.F. Ashby, Cellular Solids, Cambridge University Press, Cambridge, 1997. https://doi.org/10.1017/CBO9781139878326.

[96] G. Savio, S. Rosso, R. Meneghello, G. Concheri, Geometric Modeling of Cellular Materials for Additive Manufacturing in Biomedical Field: A Review, Appl. Bionics Biomech. 2018 (2018) 1–14. https://doi.org/10.1155/2018/1654782.

[97] G.J. Tattersall, D. V. Andrade, A.S. Abe, Heat exchange from the toucan bill reveals a controllable vascular thermal radiator, Science (80-.). 325 (2009) 468–470. https://doi.org/10.1126/science.1175553.

[98] M. Lai, A.N. Kulak, D. Law, Z. Zhang, F.C. Meldrum, D.J. Riley, Profiting from nature: Macroporous copper with superior mechanical properties, Chem. Commun. (2007) 3547–3549. https://doi.org/10.1039/b707469g.

[99] K.F. Leong, C.M. Cheah, C.K. Chua, Solid freeform fabrication of three-dimensional scaffolds for engineering replacement tissues and organs, Biomaterials. 24 (2003) 2363–2378. https://doi.org/10.1016/S0142-9612(03)00030-9.

[100] A. Kantaros, N. Chatzidai, D. Karalekas, 3D printing-assisted design of scaffold structures, Int. J. Adv. Manuf. Technol. 82 (2016) 559–571. https://doi.org/10.1007/s00170-015-7386-6.

[101] Y. Tang, A. Kurtz, Y.F. Zhao, Bidirectional Evolutionary Structural Optimization (BESO) based design method for lattice structure to be fabricated by additive manufacturing, CAD Comput. Aided Des. 69 (2015) 91–101. https://doi.org/10.1016/j.cad.2015.06.001.

[102] Y. Tang, Y.F. Zhao, A survey of the design methods for additive manufacturing to improve functional performance, Rapid Prototyp. J. 22 (2016) 569–590. https://doi.org/10.1108/RPJ-01-2015-0011.

[103] H. Wang, Y. Chen, D.W. Rosen, A Hybrid Geometric Modeling Method for Large Scale Conformal Cellular Structures, in: Vol. 3 25th Comput. Inf. Eng. Conf. Parts A B, ASMEDC, Long Beach, CA, 2005: pp. 421–427. https://doi.org/10.1115/DETC2005-85366.

[104] A.P. Roberts, E.J. Garboczi, Elastic moduli of model random three-dimensional closed-cell cellular solids, Acta Mater. 49 (2001) 189–197. https://doi.org/10.1016/S1359-6454(00)00314-1.

[105] M.H. Luxner, J. Stampfl, H.E. Pettermann, Finite element modeling concepts and linear analyses of 3D regular open cell structures, in: J. Mater. Sci., 2005: pp. 5859–5866. https://doi.org/10.1007/s10853-005-5020-y.

[106] V.S. Deshpande, N.A. Fleck, M.F. Ashby, Effective properties of the octet-truss lattice material, J. Mech. Phys. Solids. 49 (2001) 1747–1769. https://doi.org/10.1016/S0022-5096(01)00010-2.

[107] J.C. Wallach, L.J. Gibson, Mechanical behavior of a three-dimensional truss material, Int. J. Solids Struct. 38 (2001) 7181–7196. https://doi.org/10.1016/S0020-7683(00)00400-5.

[108] A.P. Roberts, E.J. Garboczi, Elastic properties of model random three-dimensional open-cell solids, J. Mech. Phys. Solids. 50 (2002) 33–55. https://doi.org/10.1016/S0022-5096(01)00056-4.

[109] E.A. Lord, A.L. Mackay, Periodic minimal surfaces of cubic symmetry, Curr. Sci. 85 (2003) 346–362.

[110] F.S.L. Bobbert, K. Lietaert, A.A. Eftekhari, B. Pouran, S.M. Ahmadi, H. Weinans, A.A. Zadpoor,

Additively manufactured metallic porous biomaterials based on minimal surfaces: A unique combination of topological, mechanical, and mass transport properties, Acta Biomater. 53 (2017) 572–584. https://doi.org/10.1016/j.actbio.2017.02.024.

[111] W. Li, G. Yu, Z. Yu, Bioinspired heat exchangers based on triply periodic minimal surfaces for supercritical CO2 cycles, Appl. Therm. Eng. 179 (2020) 115686. https://doi.org/10.1016/J.APPLTHERMALENG.2020.115686.

[112] V.S. Deshpande, M.F. Ashby, N.A. Fleck, Foam topology: bending versus stretching dominated architectures, Acta Mater. 49 (2001) 1035–1040. https://doi.org/10.1016/S1359-6454(00)00379-7.

[113] M.F. Ashby, The properties of foams and lattices, Philos. Trans. R. Soc. A Math. Phys. Eng. Sci. 364 (2006) 15–30. https://doi.org/10.1098/rsta.2005.1678.

[114] C.R. Calladine, Buckminster Fuller's "Tensegrity" structures and Clerk Maxwell's rules for the construction of stiff frames, Int. J. Solids Struct. 14 (1978) 161–172. https://doi.org/10.1016/0020-7683(78)90052-5.

[115] N.A. Fleck, V.S. Deshpande, M.F. Ashby, Micro-architectured materials: Past, present and future, in: Proc. R. Soc. A Math. Phys. Eng. Sci., Royal Society, 2010: pp. 2495–2516. https://doi.org/10.1098/rspa.2010.0215.

[116] T. Maconachie, M. Leary, B. Lozanovski, X. Zhang, M. Qian, O. Faruque, M. Brandt, SLM lattice structures: Properties, performance, applications and challenges, Mater. Des. 183 (2019) 108137. https://doi.org/10.1016/j.matdes.2019.108137.

[117] L.J. Gibson, M.F. Ashby, Cellular Solids: Structure and Properties, 2nd ed., Cambridge University Press, Cambridge, 1997. https://doi.org/10.1017/CBO9781139878326.

[118] Y. Tang, A. Kurtz, Y.F. Zhao, Bidirectional Evolutionary Structural Optimization (BESO) based design method for lattice structure to be fabricated by additive manufacturing, CAD Comput. Aided Des. 69 (2015) 91–101. https://doi.org/10.1016/j.cad.2015.06.001.

[119] P. Zhang, J. Toman, Y. Yu, E. Biyikli, M. Kirca, M. Chmielus, A.C. To, Efficient design-optimization of variable-density hexagonal cellular structure by additive manufacturing: Theory and validation, J. Manuf. Sci. Eng. Trans. ASME. 137 (2015). https://doi.org/10.1115/1.4028724.

[120] C.H.P. Nguyen, Y. Kim, Y. Choi, Design for Additive Manufacturing of Functionally Graded Lattice Structures: A Design Method with Process Induced Anisotropy Consideration, Int. J. Precis. Eng. Manuf. - Green Technol. 8 (2021) 29–45. https://doi.org/10.1007/s40684-019-00173-7.

[121] G.H. Song, S.K. Jing, F.L. Zhao, Y.D. Wang, H. Xing, L.F. Qie, Design of Lattice Structures Using Local Relative Density Mapping Method, Chinese J. Mech. Eng. (English Ed. 31 (2018) 89. https://doi.org/10.1186/s10033-018-0289-3.

[122] G. Savio, R. Meneghello, G. Concheri, Design of variable thickness triply periodic surfaces for additive manufacturing, Prog. Addit. Manuf. 4 (2019) 281–290. https://doi.org/10.1007/s40964-019-00073-x.

[123] G. Dong, Y. Tang, Y.F. Zhao, A Survey of Modeling of Lattice Structures Fabricated by Additive Manufacturing, J. Mech. Des. 139 (2017) 100906–100913. https://doi.org/10.1115/1.4037305.

[124] M. Alzahrani, S.K. Choi, D.W. Rosen, Design of truss-like cellular structures using relative density mapping method, Mater. Des. 85 (2015) 349–360. https://doi.org/10.1016/j.matdes.2015.06.180.

[125] Y. Tang, Y.F. Zhao, Multifunctional design of heterogeneous cellular structures, Struct.

Multidiscip. Optim. 58 (2018) 1121–1138. https://doi.org/10.1007/s00158-018-1956-9.

[126] F. Leonardi, S. Graziosi, R. Casati, F. Tamburrino, M. Bordegoni, Additive Manufacturing of Heterogeneous Lattice Structures: An Experimental Exploration, Proc. Des. Soc. Int. Conf. Eng. Des. 1 (2019) 669–678. https://doi.org/10.1017/dsi.2019.71.

[127] PD CEN/TR/ISO/ASTM 52912:2020, Additive manufacturing — Design — Functionally graded additive manufacturing, (2020).

[128] A. Panesar, M. Abdi, D. Hickman, I. Ashcroft, Strategies for functionally graded lattice structures derived using topology optimisation for Additive Manufacturing, Addit. Manuf. 19 (2018) 81–94. https://doi.org/10.1016/j.addma.2017.11.008.

[129] Luca Grigolato, Stefano Rosso, Roberto Meneghello, Gianmaria Concheri, Gianpaolo Savio, Heterogeneous objects representation for Additive Manufacturing: a review, Instant J. Mech. Eng. (2019) 14–23. https://doi.org/10.36811/ijme.2019.110002.

[130] G. Savio, R. Meneghello, G. Concheri, Geometric modeling of lattice structures for additive manufacturing, Rapid Prototyp. J. 24 (2018) 00–00. https://doi.org/10.1108/RPJ-07-2016-0122.

[131] G. Savio, R. Meneghello, G. Concheri, Geometric modeling of lattice structures for additive manufacturing, Rapid Prototyp. J. 24 (2018) 351–360. https://doi.org/10.1108/RPJ-07-2016-0122.

[132] I. Maskery, L.A. Parry, D. Padrão, R.J.M. Hague, I.A. Ashcroft, FLatt Pack: A research-focussed lattice design program, Addit. Manuf. 49 (2022) 102510. https://doi.org/10.1016/j.addma.2021.102510.

[133] O. Al-Ketan, D.-W. Lee, R. Rowshan, R.K. Abu Al-Rub, Functionally graded and multi-morphology sheet TPMS lattices: Design, manufacturing, and mechanical properties, J. Mech. Behav. Biomed. Mater. 102 (2020) 103520. https://doi.org/10.1016/j.jmbbm.2019.103520.

[134] N. Novak, O. Al-Ketan, M. Borovinšek, L. Krstulović-Opara, R. Rowshan, M. Vesenjak, Z. Ren, Development of novel hybrid TPMS cellular lattices and their mechanical characterisation, J. Mater. Res. Technol. 15 (2021) 1318–1329. https://doi.org/10.1016/j.jmrt.2021.08.092.

[135] A. Pasko, O. Fryazinov, T. Vilbrandt, P.-A. Fayolle, V. Adzhiev, Procedural function-based modelling of volumetric microstructures, Graph. Models. 73 (2011) 165–181. https://doi.org/10.1016/j.gmod.2011.03.001.

[136] D. Popov, E. Maltsev, O. Fryazinov, A. Pasko, I. Akhatov, Efficient contouring of functionally represented objects for additive manufacturing, Comput. Des. 129 (2020) 102917. https://doi.org/10.1016/j.cad.2020.102917.

[137] E. Maltsev, D. Popov, S. Chugunov, A. Pasko, I. Akhatov, An Accelerated Slicing Algorithm for Frep Models, Appl. Sci. 11 (2021) 6767. https://doi.org/10.3390/app11156767.

[138] S.M. Giannitelli, D. Accoto, M. Trombetta, A. Rainer, Current trends in the design of scaffolds for computer-aided tissue engineering, Acta Biomater. 10 (2014) 580–594. https://doi.org/10.1016/j.actbio.2013.10.024.

[139] H. Zeinalabedini, Y.O. Yildiz, P. Zhang, K. Laux, M. Kirca, A.C. To, Homogenization of additive manufactured polymeric foams with spherical cells, Addit. Manuf. 12 (2016) 274–281. https://doi.org/10.1016/j.addma.2016.04.008.

[140] F. Gagliardi, L. De Napoli, L. Filice, D. Umbrello, A comparison among FE models to simulate metallic foams forming – An experimental validation, Mater. Des. 30 (2009) 1282–1287.

https://doi.org/10.1016/J.MATDES.2008.06.051.

[141] A. Ceruti, R. Ferrari, A. Liverani, Design for additive manufacturing using LSWM: A CAD tool for the modelling of lightweight and lattice structures, in: Smart Innov. Syst. Technol., 2017: pp. 756–765. https://doi.org/10.1007/978-3-319-57078-5_71.

[142] V. Shapiro, Theory of R-functions and Applications: A Primer, (1991).

[143] A.O. Aremu, J.P.J. Brennan-Craddock, A. Panesar, I.A. Ashcroft, R.J.M. Hague, R.D. Wildman, C. Tuck, A voxel-based method of constructing and skinning conformal and functionally graded lattice structures suitable for additive manufacturing, Addit. Manuf. 13 (2017) 1–13. https://doi.org/10.1016/j.addma.2016.10.006.

[144] M.K. Thompson, G. Moroni, T. Vaneker, G. Fadel, R.I. Campbell, I. Gibson, A. Bernard, J. Schulz, P. Graf, B. Ahuja, F. Martina, Design for Additive Manufacturing: Trends, opportunities, considerations, and constraints, CIRP Ann. - Manuf. Technol. 65 (2016) 737–760. https://doi.org/10.1016/j.cirp.2016.05.004.

[145] Ansys, Ansys SpaceClaim, (2021).

[146] Siemens, Design for Additive Manufacture, (2021).

[147] Dassault Systèmes, The 3DEXPERIENCE platform, a Game Changer for Business and Innovation, (2021).

[148] Altair, Accelerate Simulation-driven Design | Altair Inspire, (2021).

[149] Materialise, 3-matic Lattice Structures Module, (2021).

[150] Materialise, Structures Module | Materialise Magics | 3D Printing Software, (2021).

[151] PTC, Creo CAD Software: Enable the Latest in Design, (n.d.).

[152] Autodesk, Fusion 360 - Volumetric Lattice, (n.d.). https://help.autodesk.com/view/fusion360/ENU/?guid=SLD-VOLUMETRIC-PROPERTIES (accessed November 5, 2023).

[153] Robert McNeel & Associates, Rhino - Rhinoceros 3D, (2021).

[154] S. Davidson, Grasshopper - algorithmic modeling for Rhino, (2021).

[155] General Lattice, GL Software, (n.d.).

[156] ADML Lab - McGill Univeristy, INTRA|LATTICE, (n.d.).

[157] A. Porterfield, Crystallon, (2019).

[158] Ecrlabs, Dendro, (n.d.).

[159] Bespoke geometry, Cocoon, (2015).

[160] W.E. Lorensen, H.E. Cline, MARCHING CUBES: A HIGH RESOLUTION 3D SURFACE CONSTRUCTION ALGORITHM., Comput. Graph. 21 (1987) 163–169. https://doi.org/10.1145/37402.37422.

[161] Jellyfish, (n.d.). https://www.food4rhino.com/en/app/jellyfish.

[162] M. Bernhard, M. Bolhassani, M. Akbarzadeh, Performative Porosity – adaptive infills for architectural elements, in: Proc. IASS Annu. Symp. 2020/21 7th Int. Conf. Spat. Struct. Inspiring

Next Gener., 2021: pp. 1–14. https://par.nsf.gov/biblio/10209908.

[163]   GrammaCAD, (n.d.). https://www.igd.fraunhofer.de/en/products/information-technology/grammacad---graded-multi-material-cad.html.

[164]   nTopology, Next-Generation Design & Engineering Software | nTopology, (2021).

[165]   J.C. Hart, Sphere tracing: A geometric method for the antialiased ray tracing of implicit surfaces, Vis. Comput. 12 (1996) 527–545. https://doi.org/10.1007/s003710050084.

[166]   O. Al-Ketan, R.K. Abu Al-Rub, MSLattice: A free software for generating uniform and graded lattices based on triply periodic minimal surfaces, Mater. Des. Process. Commun. 3 (2021). https://doi.org/10.1002/mdp2.205.

[167]   A. Gleadall, FullControl GCode Designer: Open-source software for unconstrained design in additive manufacturing, Addit. Manuf. 46 (2021) 102109. https://doi.org/10.1016/j.addma.2021.102109.

[168]   A. Moetazedian, A.S. Budisuharto, V. V. Silberschmidt, A. Gleadall, CONVEX (CONtinuously Varied EXtrusion): A new scale of design for additive manufacturing, Addit. Manuf. 37 (2021) 101576. https://doi.org/10.1016/j.addma.2020.101576.

[169]   A. Holloway, A. Mamou-Mani, K. Kjelstrup-Johnson, Project Silkworm, (n.d.). https://projectsilkworm.com/ (accessed February 23, 2021).

[170]   M. Wheadon, Velocity Painting, (2017). https://github.com/MarkWheadon/velocity-painting (accessed December 15, 2021).

[171]   A. Nazir, K.M. Abate, A. Kumar, J.Y. Jeng, A state-of-the-art review on types, design, optimization, and additive manufacturing of cellular structures, Int. J. Adv. Manuf. Technol. 104 (2019) 3489–3510. https://doi.org/10.1007/s00170-019-04085-3.

[172]   J. Feng, J. Fu, Z. Lin, C. Shang, B. Li, A review of the design methods of complex topology structures for 3D printing, Vis. Comput. Ind. Biomed. Art. 1 (2018) 5. https://doi.org/10.1186/s42492-018-0004-3.

[173]   Y. Tang, G. Dong, Q. Zhou, Y.F. Zhao, Lattice Structure Design and Optimization With Additive Manufacturing Constraints, IEEE Trans. Autom. Sci. Eng. 15 (2018) 1546–1562. https://doi.org/10.1109/TASE.2017.2685643.

[174]   L. Riva, P.S. Ginestra, E. Ceretti, Mechanical characterization and properties of laser-based powder bed–fused lattice structures: a review, Int. J. Adv. Manuf. Technol. (2021) 1–23. https://doi.org/10.1007/s00170-021-06631-4.

[175]   C. Yan, L. Hao, A. Hussein, D. Raymont, Evaluations of cellular lattice structures manufactured using selective laser melting, Int. J. Mach. Tools Manuf. 62 (2012) 32–38. https://doi.org/10.1016/j.ijmachtools.2012.06.002.

[176]   G. Savio, R. Meneghello, G. Concheri, Optimization of lattice structures for Additive Manufacturing Technologies, in: B. Eynard, V. Nigrelli, S.M. Oliveri, G. Peris-Fajarnes, S. Rizzuti (Eds.), Adv. Mech. Des. Eng. Manuf. Lect. Notes Mech. Eng., Springer, Cham, Cham, 2017: pp. 213–222. https://doi.org/10.1007/978-3-319-45781-9_22.

[177]   F. Calignano, Design optimization of supports for overhanging structures in aluminum and titanium alloys by selective laser melting, Mater. Des. 64 (2014) 203–213. https://doi.org/10.1016/j.matdes.2014.07.043.

[178] A. Hussein, L. Hao, C. Yan, R. Everson, P. Young, Advanced lattice support structures for metal additive manufacturing, J. Mater. Process. Technol. 213 (2013) 1019–1026. https://doi.org/10.1016/j.jmatprotec.2013.01.020.

[179] Z.D. Zhang, O. Ibhadode, U. Ali, C.F. Dibia, P. Rahnama, A. Bonakdar, E. Toyserkani, Topology optimization parallel-computing framework based on the inherent strain method for support structure design in laser powder-bed fusion additive manufacturing, Int. J. Mech. Mater. Des. 16 (2020) 897–923. https://doi.org/10.1007/s10999-020-09494-x.

[180] A.T. Gaynor, J.K. Guest, Topology optimization considering overhang constraints: Eliminating sacrificial support material in additive manufacturing through design, Struct. Multidiscip. Optim. 54 (2016) 1157–1172. https://doi.org/10.1007/s00158-016-1551-x.

[181] J. Jiang, X. Xu, J. Stringer, Support Structures for Additive Manufacturing: A Review, J. Manuf. Mater. Process. 2 (2018) 64. https://doi.org/10.3390/jmmp2040064.

[182] L. Cheng, A. To, Part-scale build orientation optimization for minimizing residual stress and support volume for metal additive manufacturing: Theory and experimental validation, CAD Comput. Aided Des. 113 (2019) 1–23. https://doi.org/10.1016/j.cad.2019.03.004.

[183] M. Langelaar, Combined optimization of part topology, support structure layout and build orientation for additive manufacturing, Struct. Multidiscip. Optim. 57 (2018) 1985–2004. https://doi.org/10.1007/s00158-017-1877-z.

[184] S. Le Roux, M. Salem, A. Hor, Improvement of the bridge curvature method to assess residual stresses in selective laser melting, Addit. Manuf. 22 (2018) 320–329. https://doi.org/10.1016/j.addma.2018.05.025.

[185] O. Diegel, J. Schutte, A. Ferreira, Y.L. Chan, Design for additive manufacturing process for a lightweight hydraulic manifold, Addit. Manuf. 36 (2020) 101446. https://doi.org/10.1016/j.addma.2020.101446.

[186] F. Tamburrino, S. Graziosi, M. Bordegoni, The Design Process of Additively Manufactured Mesoscale Lattice Structures: A Review, J. Comput. Inf. Sci. Eng. 18 (2018). https://doi.org/10.1115/1.4040131.

[187] L. Yang, C. Yan, C. Han, P. Chen, S. Yang, Y. Shi, Mechanical response of a triply periodic minimal surface cellular structures manufactured by selective laser melting, Int. J. Mech. Sci. 148 (2018) 149–157. https://doi.org/10.1016/j.ijmecsci.2018.08.039.

[188] G. Barile, A. Leoni, M. Muttillo, R. Paolucci, G. Fazzini, L. Pantoli, Fused-Deposition-Material 3D-Printing Procedure and Algorithm Avoiding Use of Any Supports, Sensors. 20 (2020) 470. https://doi.org/10.3390/s20020470.

[189] M. Wüthrich, M. Gubser, W.J. Elspass, C. Jaeger, A Novel Slicing Strategy to Print Overhangs without Support Material, Appl. Sci. 11 (2021) 8760. https://doi.org/10.3390/app11188760.

[190] M. Galati, P. Minetola, Analysis of density, roughness, and accuracy of the atomic diffusion additive manufacturing (ADAM) process for metal parts, Materials (Basel). 12 (2019). https://doi.org/10.3390/ma1224122.

[191] A. Watson, J. Belding, B.D. Ellis, Characterization of 17-4 PH Processed via Bound Metal Deposition (BMD), in: 2020: pp. 205–216. https://doi.org/10.1007/978-3-030-36296-6_19.

[192] J. Duro-Royo, L. Mogas-Soldevila, N. Oxman, Flow-based fabrication: An integrated

computational workflow for design and digital additive manufacturing of multifunctional heterogeneously structured objects, Comput. Des. 69 (2015) 143–154. https://doi.org/10.1016/j.cad.2015.05.005.

[193]   P.A.G.S. Giachini, S.S. Gupta, W. Wang, D. Wood, M. Yunusa, E. Baharlou, M. Sitti, A. Menges, Additive manufacturing of cellulose-based materials with continuous, multidirectional stiffness gradients, Sci. Adv. 6 (2020). https://doi.org/10.1126/sciadv.aay0929.

[194]   P. Gray, S.K. Scott, Autocatalytic reactions in the isothermal, continuous stirred tank reactor, Chem. Eng. Sci. 38 (1983) 29–43. https://doi.org/10.1016/0009-2509(83)80132-8.

[195]   G. Adomian, Fisher-Kolmogorov equation, Appl. Math. Lett. 8 (1995) 51–52. https://doi.org/10.1016/0893-9659(95)00010-N.

[196]   A.M. Turing, The chemical basis of morphogenesis, Philos. Trans. R. Soc. Lond. B. Biol. Sci. 237 (1952) 37–72. https://doi.org/10.1098/rstb.1952.0012.

[197]   R. Munafo, Pearson's classification (extended) of Gray-Scott system parameter values, (n.d.). http://mrob.com/pub/comp/xmorphia/pearson-classes.html.

[198]   J.E. Pearson, Complex Patterns in a Simple System, Science (80-.). 261 (1993) 189–192. https://doi.org/10.1126/science.261.5118.189.

[199]   H. Wang, B. Chen, T. Qiu, J. Zhao, A New Biochemical Fermentation Process Design Method Considering Bifurcations and Oscillations, in: 2015: pp. 145–172. https://doi.org/10.1016/B978-0-444-63472-6.00006-9.

[200]   A.T. Winfree, The prehistory of the Belousov-Zhabotinsky oscillator, J. Chem. Educ. 61 (1984) 661. https://doi.org/10.1021/ed061p661.

[201]   K. Sims, Kars Sims, (n.d.). https://www.karlsims.com/index.html.

[202]   K. Sims, Reaction-Diffusion Tutorial, (n.d.). https://www.karlsims.com/rd.html.

[203]   SASAM, Additive Manufacturing: SASAM Standardisation Roadmap, 2015.

[204]   FoFAM, Additive Manufacturing roadmap: gaps and actions on market driven value chains, 2016.

[205]   America Makes, ANSI, Standardization Roadmap for Additive Manufacturing - Version 2.0, 2018.

[206]   S. Rosso, F. Uriati, L. Grigolato, R. Meneghello, G. Concheri, G. Savio, An Optimization Workflow in Design for Additive Manufacturing, Appl. Sci. 11 (2021) 2572. https://doi.org/10.3390/app11062572.

[207]   M. Kumke, H. Watschke, T. Vietor, A new methodological framework for design for additive manufacturing, Virtual Phys. Prototyp. 11 (2016) 3–19. https://doi.org/10.1080/17452759.2016.1139377.

[208]   C.C. Seepersad, Challenges and Opportunities in Design for Additive Manufacturing, 3D Print. Addit. Manuf. 1 (2014) 10–13. https://doi.org/10.1089/3dp.2013.0006.

[209]   A. Bacciaglia, A. Ceruti, A. Liverani, A systematic review of voxelization method in additive manufacturing, Mech. Ind. 20 (2019) 630. https://doi.org/10.1051/meca/2019058.

[210]   F. Calignano, M. Lorusso, I. Roppolo, P. Minetola, Investigation of the mechanical properties of a carbon fibre-reinforced nylon filament for 3d printing, Machines. 8 (2020) 1–13. https://doi.org/10.3390/machines8030052.

[211] G. Allevi, L. Capponi, P. Castellini, P. Chiariotti, F. Docchio, F. Freni, R. Marsili, M. Martarelli, R. Montanini, S. Pasinetti, A. Quattrocchi, R. Rossetti, G. Rossi, G. Sansoni, E.P. Tomasini, Investigating Additive Manufactured Lattice Structures: A Multi-Instrument Approach, IEEE Trans. Instrum. Meas. 69 (2020) 2459–2467. https://doi.org/10.1109/TIM.2019.2959293.

[212] S. Raghavendra, A. Molinari, M. Dallago, G. Zappini, F. Zanini, S. Carmignato, M. Benedetti, Uniaxial static mechanical properties of regular, irregular and random additively manufactured cellular materials: Nominal vs. real geometry, Forces Mech. 2 (2021) 100007. https://doi.org/10.1016/j.finmec.2020.100007.

[213] M. Benedetti, A. du Plessis, R.O. Ritchie, M. Dallago, S.M.J. Razavi, F. Berto, Architected cellular materials: A review on their mechanical properties towards fatigue-tolerant design and fabrication, Mater. Sci. Eng. R Reports. 144 (2021) 1–40. https://doi.org/10.1016/j.mser.2021.100606.

[214] R. Ponche, O. Kerbrat, P. Mognol, J.Y. Hascoet, A novel methodology of design for Additive Manufacturing applied to Additive Laser Manufacturing process, Robot. Comput. Integr. Manuf. 30 (2014) 389–398. https://doi.org/10.1016/j.rcim.2013.12.001.

[215] P. Cicconi, M. Mandolini, C. Favi, F. Campi, M. Germani, Metal Additive Manufacturing for the Rapid Prototyping of Shaped Parts: A Case Study, Comput. Aided. Des. Appl. 18 (2021) 1061–1079. https://doi.org/10.14733/cadaps.2021.1061-1079.

[216] A. Ranellucci, Slic3r, (n.d.). https://slic3r.org/ (accessed January 14, 2020).

[217] G. Hodgson, A. Ranellucci, J. Moe, Slic3r Manual - Flow Math, (n.d.). https://manual.slic3r.org/advanced/flow-math (accessed August 1, 2021).

[218] M200 - Set Filament Diameter, (n.d.).

[219] B. N. Turner, R. Strong, S. A. Gold, A review of melt extrusion additive manufacturing processes: I. Process design and modeling, Rapid Prototyp. J. 20 (2014) 192–204. https://doi.org/10.1108/RPJ-01-2013-0012.

[220] P. Carrier, 3D Printer Print Speed Calculation: How to find the optimal speed for reliable and constant print quality, (2018). https://dyzedesign.com/2018/07/3d-print-speed-calculation-find-optimal-speed/ (accessed December 10, 2021).

[221] Y. Tlegenov, W.F. Lu, G.S. Hong, A dynamic model for current-based nozzle condition monitoring in fused deposition modelling, Prog. Addit. Manuf. 4 (2019) 211–223. https://doi.org/10.1007/s40964-019-00089-3.

[222] L.K. Platzman, J.J. Bartholdi, Spacefilling curves and the planar travelling salesman problem, J. ACM. 36 (1989) 719–737. https://doi.org/10.1145/76359.76361.

[223] GE jet engine bracket challenge, GrabCAD, (n.d.).

[224] S. Khaleghi, F.N. Dehnavi, M. Baghani, M. Safdari, K. Wang, M. Baniassadi, On the directional elastic modulus of the TPMS structures and a novel hybridization method to control anisotropy, Mater. Des. 210 (2021) 110074. https://doi.org/10.1016/j.matdes.2021.110074.

[225] M. Panagiotis, K. Sawako, Millipede, (n.d.). http://www.sawapan.eu/ (accessed February 25, 2020).

[226] M.P. Bendsøe, O. Sigmund, Topology Optimization, 2nd ed., Springer Berlin Heidelberg, Berlin, 2004. https://doi.org/10.1007/978-3-662-05086-6.

[227] P. Allisy-Roberts, J. Williams, Computed tomography, in: Farr's Phys. Med. Imaging, Elsevier, 2008: pp. 103–119. https://doi.org/10.1016/B978-0-7020-2844-1.50011-9.

[228] 3D Slicer User Guide - Volumes, (n.d.). https://slicer.readthedocs.io/en/latest/user_guide/modules/volumes.html.

[229] knee and bones 1.0.0, (n.d.). https://www.embodi3d.com/files/file/19722-knee-and-bones/ (accessed February 10, 2022).

[230] E. Catmull, J. Clark, Recursively generated B-spline surfaces on arbitrary topological meshes, Comput. Des. 10 (1978) 350–355. https://doi.org/10.1016/0010-4485(78)90110-0.

[231] M. Bernhard, M. Hansmeyer, B. Dillenburger, Volumetric modelling for 3D printed architecture, AAG - Adv. Archit. Geom. (2018) 392–415. https://research.chalmers.se/en/publication/504188.

[232] ISO International Organization for Standardization, ISO 527-1:2012 - Plastics -- Determination of tensile properties -- Part 1: General principles, (2012).

[233] F.C. Manager, Density engineering resin, (n.d.). https://forum.formlabs.com/t/density-engineering-resin/24998.

[234] S. Solhjoo, S. Khoddam, Evaluation of barreling and friction in uniaxial compression test: A kinematic analysis, Int. J. Mech. Sci. 156 (2019) 486–493. https://doi.org/10.1016/j.ijmecsci.2019.04.007.

[235] B.N. Turner, S.A. Gold, A review of melt extrusion additive manufacturing processes: II. Materials, dimensional accuracy, and surface roughness, Rapid Prototyp. J. 21 (2015) 250–261. https://doi.org/10.1108/RPJ-02-2013-0017.

[236] Slic3r Manual – Modifier Meshes, (n.d.).

[237] S. Rosso, A. Curtarello, F. Basana, L. Grigolato, R. Meneghello, G. Concheri, G. Savio, Modeling Symmetric Minimal Surfaces by Mesh Subdivision, in: 2021: pp. 249–254. https://doi.org/10.1007/978-3-030-70566-4_40.

[238] A. Bærentzen, Isosurface Polygonization, (n.d.). http://www.imm.dtu.dk/~janba/gallery/polygonization.html.

[239] S. Hällgren, L. Pejryd, J. Ekengren, 3D Data Export for Additive Manufacturing - Improving Geometric Accuracy, Procedia CIRP. 50 (2016) 518–523. https://doi.org/10.1016/j.procir.2016.05.046.

[240] C. Bader, D. Kolb, J.C. Weaver, S. Sharma, A. Hosny, J. Costa, N. Oxman, Making data matter: Voxel printing for the digital fabrication of data across scales and domains, Sci. Adv. 4 (2018). https://doi.org/10.1126/sciadv.aas8652.

[241] M.A. Skylar-Scott, J. Mueller, C.W. Visser, J.A. Lewis, Voxelated soft matter via multimaterial multinozzle 3D printing, Nature. 575 (2019) 330–335. https://doi.org/10.1038/s41586-019-1736-8.

[242] C. Bader, D. Kolb, J.C. Weaver, N. Oxman, Data-Driven Material Modeling with Functional Advection for 3D Printing of Materially Heterogeneous Objects, 3D Print. Addit. Manuf. 3 (2016) 71–79. https://doi.org/10.1089/3dp.2016.0026.

[243] A. Kaufman, D. Cohen, R. Yagel, Volume graphics, Computer (Long. Beach. Calif). 26 (1993) 51–64. https://doi.org/10.1109/MC.1993.274942.

[244] L. Grigolato, S. Rosso, R. Meneghello, G. Concheri, G. Savio, Design and manufacturing of graded density components by material extrusion technologies, Addit. Manuf. 57 (2022) 102950. https://doi.org/10.1016/j.addma.2022.102950.

[245] M163 - Set Mix Factor, (n.d.).

[246] Select Tool, (n.d.).

[247] M. Firmware, M165 - Set Mix, (n.d.). https://marlinfw.org/docs/gcode/M165.html.

[248] E. Brancewicz-Steinmetz, J. Sawicki, P. Byczkowska, The Influence of 3D Printing Parameters on Adhesion between Polylactic Acid (PLA) and Thermoplastic Polyurethane (TPU), Materials (Basel). 14 (2021) 6464. https://doi.org/10.3390/ma14216464.

[249] D. Rahmatabadi, I. Ghasemi, M. Baniassadi, K. Abrinia, M. Baghani, 3D printing of PLA-TPU with different component ratios: Fracture toughness, mechanical properties, and morphology, J. Mater. Res. Technol. 21 (2022) 3970–3981. https://doi.org/10.1016/j.jmrt.2022.11.024.

[250] A. Żur, P. Żur, P. Michalski, A. Baier, Preliminary Study on Mechanical Aspects of 3D-Printed PLA-TPU Composites, Materials (Basel). 15 (2022) 2364. https://doi.org/10.3390/ma15072364.

[251] Z.C. Kennedy, J.F. Christ, Printing polymer blends through in situ active mixing during fused filament fabrication, Addit. Manuf. 36 (2020) 101233. https://doi.org/10.1016/j.addma.2020.101233.

[252] X. Yao, S.K. Moon, G. Bi, J. Wei, A multi-material part design framework in additive manufacturing, Int. J. Adv. Manuf. Technol. 99 (2018) 2111–2119. https://doi.org/10.1007/s00170-018-2025-7.

[253] P. Muller, P. Mognol, J.Y. Hascoet, Functionally graded material (FGM) parts: From design to the manufacturing simulation, in: ASME 2012 11th Bienn. Conf. Eng. Syst. Des. Anal. ESDA 2012, 2012: pp. 123–131. https://doi.org/10.1115/ESDA2012-82586.

[254] SHENZHEN GETECH TECHNOLOGY CO. LTD, Guide of Color Mixer Software, (n.d.).

[255] R. Sponchiado, S. Rosso, P.D. Fabbro, L. Grigolato, H. Elsayed, M. Maltauro, F. Uccheddu, R. Meneghello, G. Concheri, G. Savio, Modeling materials coextrusion in polymers additive manufacturing, Mater. MDPI. (n.d.) 1–25.

[256] Data Sheets & 3D Printing Guides, (n.d.).

[257] V.S. Vakharia, L. Kuentz, A. Salem, M.C. Halbig, J.A. Salem, M. Singh, Additive manufacturing and characterization of metal particulate reinforced polylactic acid (Pla) polymer composites, Polymers (Basel). 13 (2021). https://doi.org/10.3390/polym13203545.

[258] R.T.L. Ferreira, I.C. Amatte, T.A. Dutra, D. Bürger, Experimental characterization and micrography of 3D printed PLA and PLA reinforced with short carbon fibers, Compos. Part B Eng. 124 (2017) 88–100. https://doi.org/10.1016/j.compositesb.2017.05.013.

[259] Y.L. Yap, W. Toh, R. Koneru, Z.Y. Chua, K. Lin, K.M. Yeoh, C.M. Lim, J.S. Lee, N.A. Plemping, R. Lin, T.Y. Ng, K.I. Chan, H. Guang, W.Y.B. Chan, S.S. Teong, G. Zheng, Finite element analysis of 3D-Printed Acrylonitrile Styrene Acrylate (ASA) with Ultrasonic material characterization, Int. J. Comput. Mater. Sci. Eng. 08 (2019) 1950002. https://doi.org/10.1142/S2047684119500027.

[260] W. Cahyadi, Mechanical Properties of 3D Printed Acrylonitrile Styrene Acrylate, South Dakota State University, 2018. https://doi.org/https://openprairie.sdstate.edu/etd/3187 This.

[261] H.J. Qi, M.C. Boyce, Stress-strain behavior of thermoplastic polyurethanes, Mech. Mater. 37 (2005) 817–839. https://doi.org/10.1016/j.mechmat.2004.08.001.

[262] Y.X. Xu, J.Y. Juang, Measurement of nonlinear poisson's ratio of thermoplastic polyurethanes under cyclic softening using 2d digital image correlation, Polymers (Basel). 13 (2021). https://doi.org/10.3390/polym13091498.

[263] N.A.M. Radzuan, A.B. Sulong, A. Verma, N. Muhamad, Layup sequence and interfacial bonding of additively manufactured polymeric composite: A brief review, Nanotechnol. Rev. 10 (2021) 1853–1872. https://doi.org/10.1515/ntrev-2021-0116.

[264] H. Gonabadi, Y. Chen, A. Yadav, S. Bull, Investigation of the effect of raster angle, build orientation, and infill density on the elastic response of 3D printed parts using finite element microstructural modeling and homogenization techniques, Int. J. Adv. Manuf. Technol. 118 (2022) 1485–1510. https://doi.org/10.1007/s00170-021-07940-4.

[265] F. Tamburrino, S. Graziosi, M. Bordegoni, The influence of slicing parameters on the multi-material adhesion mechanisms of FDM printed parts: an exploratory study, Virtual Phys. Prototyp. 14 (2019) 316–332. https://doi.org/10.1080/17452759.2019.1607758.

[266] P. Dal Fabbro, A. La Gala, W. Van De Steene, D.R. D'hooge, G. Lucchetta, L. Cardon, R. Fiorio, Influence of machine type and consecutive closed-loop recycling on macroscopic properties for fused filament fabrication of acrylonitrile-butadiene-styrene parts, Rapid Prototyp. J. 27 (2021) 268–277. https://doi.org/10.1108/RPJ-03-2020-0060.

[267] R. Freund, H. Watschke, J. Heubach, T. Vietor, Determination of influencing factors on interface strength of additively manufactured multi-material parts by material extrusion, Appl. Sci. 9 (2019). https://doi.org/10.3390/app9091782.

[268] ISO/ASTM, ISO/ASTM DIS 52927: Additive manufacturing — General principles — Main characteristics and corresponding test methods, (2022).

[269] ISO/ASTM, ISO/ASTM 52903-2:2020: Additive manufacturing — Material extrusion-based additive manufacturing of plastic materials — Part 2: Process equipment, (2020).

[270] J.M. Vázquez Martínez, D. Piñero Vega, J. Salguero, M. Batista, Evaluation of the printing strategies design on the mechanical and tribological response of acrylonitrile styrene acrylate (ASA) additive manufacturing parts, Rapid Prototyp. J. 28 (2022) 479–489. https://doi.org/10.1108/RPJ-05-2021-0108.

[271] A. Rodríguez-Panes, J. Claver, A.M. Camacho, The influence of manufacturing parameters on the mechanical behaviour of PLA and ABS pieces manufactured by FDM: A comparative analysis, Materials (Basel). 11 (2018) 1333. https://doi.org/10.3390/ma11081333.

[272] A. Lanzotti, M. Grasso, G. Staiano, M. Martorelli, The impact of process parameters on mechanical properties of parts fabricated in PLA with an open-source 3-D printer, Rapid Prototyp. J. 21 (2015) 604–617. https://doi.org/10.1108/RPJ-09-2014-0135.

[273] J.M. Chacón, M.A. Caminero, E. García-Plaza, P.J. Núñez, Additive manufacturing of PLA structures using fused deposition modelling: Effect of process parameters on mechanical properties and their optimal selection, Mater. Des. 124 (2017) 143–157. https://doi.org/10.1016/j.matdes.2017.03.065.

[274] S. Raam Kumar, S. Sridhar, R. Venkatraman, M. Venkatesan, Polymer additive manufacturing of ASA structure: Influence of printing parameters on mechanical properties, in: Mater. Today Proc.,

Elsevier, 2020: pp. 1316–1319. https://doi.org/10.1016/j.matpr.2020.04.500.

[275] B. Adrover-Monserrat, J. Llumà, R. Jerez-Mesa, J.A. Travieso-Rodriguez, Study of the Influence of the Manufacturing Parameters on Tensile Properties of Thermoplastic Elastomers, Polymers (Basel). 14 (2022) 576. https://doi.org/10.3390/polym14030576.

[276] B. Arifvianto, B.E. Satiti, U.A. Salim, Suyitno, A. Nuryanti, M. Mahardika, Mechanical properties of the FFF sandwich-structured parts made of PLA/TPU multi-material, Prog. Addit. Manuf. (2022) 1–11. https://doi.org/10.1007/s40964-022-00295-6.

[277] J.R. Jones, L.L. Hench, Regeneration of trabecular bone using porous ceramics, Curr. Opin. Solid State Mater. Sci. 7 (2003) 301–307. https://doi.org/10.1016/j.cossms.2003.09.012.

[278] F. Barrère, C.A. van Blitterswijk, K. de Groot, Bone regeneration: Molecular and cellular interactions with calcium phosphate ceramics, Int. J. Nanomedicine. 1 (2006) 317–332.

[279] S. Woottichaiwat, S. Puajindanetr, S.M. Best, Fabrication of porous hydroxyapatite through combination of sacrificial template and direct foaming techniques, Eng. J. 15 (2011) 1–15. https://doi.org/10.4186/ej.2011.15.2.1.

[280] D. Loca, J. Locs, K. Salma, J. Gulbis, I. Salma, L. Berzina-Cimdina, Porous hydroxyapatite bioceramic scaffolds for drug delivery and bone regeneration, IOP Conf. Ser. Mater. Sci. Eng. 18 (2011). https://doi.org/10.1088/1757-899X/18/19/192019.

[281] Q. Chen, J. A. Roether, A. R. Boccaccini, Tissue Engineering Scaffolds from Bioactive Glass and Composite Materials, Top. Tissue Eng. 4 (2008).

[282] X. Chatzistavrou, P. Newby, A.R. Boccaccini, Bioactive glass and glass-ceramic scaffolds for bone tissue engineering, Bioact. Glas. Mater. Prop. Appl. (2011) 107–128. https://doi.org/10.1533/9780857093318.2.107.

[283] M.M. Stevens, Biomaterials for bone tissue engineering, Mater. Today. 11 (2008) 18–25. https://doi.org/10.1016/S1369-7021(08)70086-5.

[284] Roger Narayan Paolo Colombo Dileep Singh Jonathan Salem, Advances in Bioceramics and Porous Ceramics II, (2009) 344.

[285] D. Mohamad Yunos, O. Bretcanu, A.R. Boccaccini, Polymer-bioceramic composites for tissue engineering scaffolds, J. Mater. Sci. 43 (2008) 4433–4442. https://doi.org/10.1007/s10853-008-2552-y.

[286] J.R. Jones, L.M. Ehrenfried, L.L. Hench, Optimising bioactive glass scaffolds for bone tissue engineering, Biomaterials. 27 (2006) 964–973. https://doi.org/10.1016/j.biomaterials.2005.07.017.

[287] D. Desimone, W. Li, J.A. Roether, D.W. Schubert, M.C. Crovace, A.C.M. Rodrigues, E.D. Zanotto, A.R. Boccaccini, Biosilicate®-gelatine bone scaffolds by the foam replica technique: Development and characterization, Sci. Technol. Adv. Mater. 14 (2013). https://doi.org/10.1088/1468-6996/14/4/045008.

[288] H. Elsayed, A. Zocca, E. Bernardo, C.M. Gomes, J. Günster, P. Colombo, Development of bioactive silicate-based glass-ceramics from preceramic polymer and fillers, J. Eur. Ceram. Soc. 35 (2015) 731–739. https://doi.org/10.1016/j.jeurceramsoc.2014.09.020.

[289] C. Wu, J. Chang, W. Zhai, A novel hardystonite bioceramic: Preparation and characteristics, Ceram. Int. 31 (2005) 27–31. https://doi.org/10.1016/j.ceramint.2004.02.008.

[290] Hongxu Lu, N. Kawazoe, T. Tateishi, Guoping Chen, Xiaogang Jin, Jiang Chang, In vitro Proliferation and Osteogenic Differentiation of Human Bone Marrow-derived Mesenchymal Stem Cells Cultured with Hardystonite (Ca 2 ZnSi 2 O 7) and β-TCP Ceramics, J. Biomater. Appl. 25 (2010) 39–56. https://doi.org/10.1177/0885328209342469.

[291] Y. Ramaswamy, C. Wu, H. Zhou, H. Zreiqat, Biological response of human bone cells to zinc-modified Ca-Si-based ceramics, Acta Biomater. 4 (2008) 1487–1497. https://doi.org/10.1016/j.actbio.2008.04.014.

[292] K. Lin, W. Zhai, S. Ni, J. Chang, Y. Zeng, W. Qian, Study of the mechanical property and in vitro biocompatibility of CaSiO3 ceramics, Ceram. Int. 31 (2005) 323–326. https://doi.org/10.1016/j.ceramint.2004.05.023.

[293] P. Ożóg, H. Elsayed, L. Grigolato, G. Savio, J. Kraxner, D. Galusek, E. Bernardo, Engineering of silicone-based blends for the masked stereolithography of biosilicate/carbon composite scaffolds, J. Eur. Ceram. Soc. 42 (2022) 6192–6198. https://doi.org/10.1016/j.jeurceramsoc.2022.06.057.

[294] H. Elsayed, M. Secco, F. Zorzi, K. Schuhladen, R. Detsch, A.R. Boccaccini, E. Bernardo, Highly Porous Polymer-Derived Bioceramics Based on a Complex Hardystonite Solid Solution, Materials (Basel). 12 (2019) 3970. https://doi.org/10.3390/ma12233970.

[295] P. Tesavibul, R. Felzmann, S. Gruber, R. Liska, I. Thompson, A.R. Boccaccini, J. Stampfl, Processing of 45S5 Bioglass® by lithography-based additive manufacturing, Mater. Lett. 74 (2012) 81–84. https://doi.org/10.1016/j.matlet.2012.01.019.

[296] P. Colombo, G. Mera, R. Riedel, G.D. Sorarù, Polymer-Derived Ceramics: 40 Years of Research and Innovation in Advanced Ceramics, J. Am. Ceram. Soc. 93 (2010) 1805–1837. https://doi.org/10.1111/j.1551-2916.2010.03876.x.

[297] L. Delrieu, 2D Reaction Diffusion to 3D, (2015).

[298] W. Waheed, G. Deng, B. Liu, Discrete Laplacian Operator and Its Applications in Signal Processing, IEEE Access. 8 (2020) 89692–89707. https://doi.org/10.1109/ACCESS.2020.2993577.

[299] Z. Wang, Y. Zhang, S. Tan, L. Ding, A. Bernard, Support point determination for support structure design in additive manufacturing, Addit. Manuf. 47 (2021) 102341. https://doi.org/10.1016/j.addma.2021.102341.

[300] G. Allaire, B. Bogosel, Optimizing supports for additive manufacturing, Struct. Multidiscip. Optim. 58 (2018) 2493–2515. https://doi.org/10.1007/s00158-018-2125-x.

[301] A. Díaz Lantada, A. de Blas Romero, Á. Sánchez Isasi, D. Garrido Bellido, Design and Performance Assessment of Innovative Eco-Efficient Support Structures for Additive Manufacturing by Photopolymerization, J. Ind. Ecol. 21 (2017) S179–S190. https://doi.org/10.1111/jiec.12660.

[302] Gediminas Kirdeikis, How to: Simple Growth Simulation (Grasshopper), (2020). https://www.youtube.com/watch?v=viEpaivq9A0 (accessed March 10, 2023).

[303] D. Piker, Kangaroo - Form Finding With Computational Physics, (2013) 136–137.

[304] D. Piker, Kangaroo 2.4.2 Release notes, (2017).

[305] Daniel Piker, How does Kangaroo solver work?, (2019). https://discourse.mcneel.com/t/how-does-kangaroo-solver-work/92075/2.

[306] M. Biedermann, Automated Design of Additive Manufactured Flow Components, ETH Zurich, 2022. https://doi.org/10.3929/ethz-b-000587405.

[307] Mateusz Zwierzycki, Anemone, (2013). https://www.grasshopper3d.com/group/anemone.

[308] S. Goguelin, Better Heat Exchangers with Additive Manufacturing, (2021). https://all3dp.com/1/better-heat-exchangers-with-additive-manufacturing/.

[309] U. Scheithauer, R. Kordaß, K. Noack, M. F. Eichenauer, M. Hartmann, J. Abel, G. Ganzer, D. Lordick, Potentials and Challenges of Additive Manufacturing Technologies for Heat Exchanger, in: Adv. Heat Exch., IntechOpen, 2019. https://doi.org/10.5772/intechopen.80010.

[310] L. Doretti, F. Martelletto, S. Mancin, Numerical analyses of concrete thermal energy storage systems: effect of the modules' arrangement, Energy Reports. 6 (2020) 199–214. https://doi.org/10.1016/j.egyr.2020.07.002.

[311] L. Huang, V. Aute, R. Radermacher, A finite volume coaxial heat exchanger model with moving boundaries and modifications to correlations for two-phase flow in fluted annuli, Int. J. Refrig. 40 (2014) 11–23. https://doi.org/10.1016/j.ijrefrig.2013.11.012.

[312] B. Blakey-Milner, P. Gradl, G. Snedden, M. Brooks, J. Pitot, E. Lopez, M. Leary, F. Berto, A. du Plessis, Metal additive manufacturing in aerospace: A review, Mater. Des. 209 (2021) 110008. https://doi.org/10.1016/j.matdes.2021.110008.

[313] T. Ju, F. Losasso, S. Schaefer, J. Warren, Dual contouring of hermite data, in: Proc. 29th Annu. Conf. Comput. Graph. Interact. Tech., ACM, New York, NY, USA, 2002: pp. 339–346. https://doi.org/10.1145/566570.566586.

[314] ASTM, Committee F42 on Additive Manufacturing Technologies, (2021).

[315] ISO, ISO/TC 261 on Additive Manufacturing, (2021).

[316] ISO/TC 261, ASTM-F24, Joint Plan for Additive Manufacturing Standards Development, (2013).

[317] ASTM, F42 AM Standards Structure And Primer, (n.d.).